

# A microfabricated dielectrophoretic trapping array for cell-based biological assays

by

Joel Voldman

B.S., University of Massachusetts at Amherst, 1995  
S.M. Massachusetts Institute of Technology, 1997

Submitted to the Department of Electrical Engineering and Computer Science in partial fulfillment of the requirements for the degree of

Doctor of Philosophy

at the

MASSACHUSETTS INSTITUTE OF TECHNOLOGY  
June 2001

© 2001 Massachusetts Institute of Technology  
All rights reserved

Signature of Author.....  
Department of Electrical Engineering and Computer Science  
May 20, 2001

Certified by.....  
Martin A. Schmidt  
Professor of Electrical Engineering  
Thesis Supervisor

Certified by.....  
Martha L. Gray  
Edward Hood Taplin Professor of Medical & Electrical Engineering  
Thesis Supervisor

Certified by.....  
Mehmet Toner  
Associate Professor of Bioengineering  
Harvard Medical School  
Thesis Supervisor

Accepted by.....  
Arthur C. Smith  
Chairman, Department Committee on Graduate Students



# A microfabricated dielectrophoretic trapping array for cell-based biological assays

by

Joel Voldman

Submitted to the Department of Electrical Engineering and Computer Science on May 20, 2001  
in partial fulfillment of the requirements for the degree of Doctor of Philosophy in Electrical  
Engineering and Computer Science

## ABSTRACT

This thesis presents the development of a small planar array of microfabricated traps for holding single cells and performing assays on them. The traps use the phenomenon of dielectrophoresis—the force on polarizable bodies in a non-uniform electric field—to make potential energy wells. These potential energy wells are electrically switchable, arrayable, and amenable to batch fabrication. The trapping arrays have potential use as a cytometer for monitoring the dynamics of populations of single cells and then sorting those cells based upon those dynamics.

To design such traps, I have developed a modeling environment that can absolutely predict the ability of DEP-based traps to hold particles against liquid flows, which are the dominant destabilizing force in these systems. I have used the common easy-to-fabricate planar quadrupole trap to verify the accuracy of these modeling tools, and in the process determined why planar quadrupole traps behave as they do.

I next used the modeling tools to design an improved quadrupole trap—the extruded quadrupole—that has the potential to hold particles 10x-100x stronger. The extruded quadrupole trap consists of a set of microfabricated gold posts arranged in a trapezoidal fashion, to ease trap loading, and includes metal substrate shunts to improve performance. The fabrication process for small arrays of these traps uses electroplating of gold into an SU-8 mold to achieve the required geometries.

The final section of the thesis details experiments using small arrays of these extruded quadrupole traps. Experiments were performed with beads to verify the strong nature of the trap and then with cells to demonstrate qualitative operation of the arrays and the ability to perform dynamic fluorescent assays on multiple single cells followed by sorting. The technology is now well poised to enable the development of biological assays that are currently unavailable.

Thesis Supervisor: Martin A. Schmidt  
Title: Professor of Electrical Engineering and Computer Science

Thesis Supervisor: Martha L. Gray  
Title: Edward Hood Taplin Professor of Medical & Electrical Engineering

Thesis Supervisor: Mehmet Toner  
Title: Associate Professor of Bioengineering, Harvard Medical School

## Acknowledgements

Many people have helped make my time at MIT an enjoyable one. I want to first thank Marty for allowing me to join the group 6 years ago, when all I knew about MEMS was that they were cool. It was certainly a risk, but one that I think has paid off well. Marty not only let me join the group, he also allowed me to indulge my interest in BioMEMS, which I thought was the coolest part of MEMS. Our plundering through that field, resulted in this thesis, and it's been a fun journey. All through it, Marty had genuine concern for my well-being and what was best for me. He never micromanaged, allowing me to make my own mistakes.

Early on we decided to collaborate with Martha, and she quickly became not just a collaborator but also a bona-fide 2<sup>nd</sup> advisor. Her perspective from the bio end of things ensured that the project would not just be cool, but actually useful. In addition, her outlook on the process and perspective on academia did much to shape my views.

At the start of my Ph.D., we all wanted to work with Mehmet, since he was such a nice, fun guy with neat ideas. I have really appreciated his many ideas and enthusiasm about science. He has also proved exceptionally gifted as a career counselor, both in the advice he dispenses and his candor in dispensing it. Plus, he reads stuff really quickly.

I'd like to also thank some other professors at MIT with whom I have had contact. I've appreciated SDS' ability to quickly divine the good from the crap, and also the career advice he has given me. I've enjoyed my numerous chats with Tayo and his enthusiasm as we were both going through MIT's growth process.

The staff at the MTL helped me get this stuff done. Central to this is Vicky, who is responsible for running the place but still has the courage to say and do what's right even if it's risky; JoeD, for his warmth; Kurt, for having no boundaries on how he can help; Debb, for her attitude and for treating me like I deserve; and Pat and Anne, for their help in navigating the intricacies of MIT beaurocracy.

As much as my advisors, the group of students and postdocs that I have been surrounded with have really helped bring me through these six years. Certainly, at least half of what I learned has been from these folks. It's a resource that cannot be overstated. Central to it all has been the past and present Schmidt group, whose members helped me both intellectually and emotionally. A few people deserve special mention—LP, my first mentor, a stellar example, and knower of all things; Shipreck, for his advice, his superb scientific wit, his opinions on everything, and his stories; Dr. Folch, for his arguments with Shipreck, his hatred of cheese, and his take on biomems; Dr. J, for her accent, tea breaks, and ability to listen to my whining; jowu, for more tea breaks and Japanese mania; Christine, who has intellectually blossomed in the past 3 years, and agreed to take over as lab czar; fujimori, for yet even more tea breaks, good advice, and ruminations; boss, for all the office conversations and general heehaw good times; and of course Samara, my partner in hell for these six years, who not only is extremely sharp, but has good manners.

Finally, I'd like to thank my friends and family, for their support, and Jenny, for everything.

# Contents

Chapter 1 : Introduction .....	13
1.1 Bio-microsystems.....	13
1.2 The $\mu$ DAC.....	14
1.2.1 Overview .....	14
1.2.2 Applications .....	15
1.3 Micron-sized particle manipulation .....	18
1.4 Dielectrophoresis.....	19
1.4.1 Physics: dipole approximation.....	19
1.4.2 Physics: Multipolar theory .....	23
1.4.3 Microscale DEP: separation systems .....	24
1.4.4 Microscale DEP: traps.....	25
1.4.5 Other microscale electromechanics.....	26
1.5 Electric fields and cells .....	27
1.5.1 Current-induced heating.....	27
1.5.2 Direct electric-field interactions.....	27
1.6 Scope of the thesis.....	30
Chapter 2 : Modeling environment .....	31
2.1 Motivation.....	31
2.2 Overview .....	31
2.2.1 Model Parameters.....	33
2.2.2 Electric field calculation.....	33
2.2.3 DEP force calculation.....	35
2.2.4 Other forces .....	36
2.2.5 Holding point determination .....	38
2.2.6 Holding force simulation.....	42
2.2.7 Effect of particle density and fluid flow on isosurfaces.....	43
2.3 Discussion .....	46
2.3.1 Modeling environment.....	46
2.3.2 Parameter-space exploration .....	47
2.3.3 Limitations .....	47
2.4 Conclusion.....	48
Chapter 3 : Holding forces of the planar quadrupole .....	49
3.1 Experimental vehicle—the planar quadrupole.....	49
3.2 Experimental methods—fab, packaging, test setup, methodology .....	49
3.2.1 Stock Solutions.....	49
3.2.2 Beads .....	49
3.2.3 Electrode Traps .....	50
3.2.4 Packaging .....	50
3.2.5 Chamber height measurement.....	51
3.2.6 Electrical Excitation .....	51
3.2.7 Fluidics.....	51
3.2.8 Optics .....	51
3.2.9 Release flowrate measurements .....	51
3.2.10 Modeling .....	51

3.3 Results .....	52
3.3.1 Single-bead holding.....	52
3.3.2 Release flowrate as the voltage is varied—the holding characteristic .....	53
3.3.3 Holding characteristic as the particle diameter is varied.....	56
3.3.4 Holding characteristic changes with frequency .....	57
3.4 Discussion .....	58
3.4.1 DEP force measurements .....	58
3.4.2 Shear flow approximation to Poiseuille flow.....	60
3.4.3 Agreement between predictions and experiments.....	60
3.4.4 Forces responsible for anomalous frequency effects .....	61
3.5 Conclusion.....	62
Chapter 4 : Extruded trap design.....	63
4.1 Materials and Methods.....	63
4.1.1 Modeling .....	63
4.2 The extruded trap - introduction.....	63
4.2.1 Electrode number .....	64
4.2.2 Electrode shape/arrangement .....	66
4.3 The extruded trap—optimization .....	66
4.3.1 Electrode height.....	67
4.3.2 Electrode arrangement/diameter .....	67
4.3.3 Trap switching.....	68
4.3.4 Wiring.....	69
4.4 System-level design.....	72
4.4.1 Fill time .....	73
4.4.2 Shear on cells .....	73
4.4.3 Transmembrane potential.....	74
4.5 Final design .....	76
4.6 Conclusion.....	79
Chapter 5 : Array fabrication, packaging & test setup.....	81
5.1 Fabrication.....	81
5.1.1 Substrate interconnect .....	81
5.1.2 SU-8 mold deposition.....	82
5.1.3 Electroplating the electrodes .....	85
5.1.4 SU-8 mold removal.....	86
5.1.5 Titanium adhesion-layer removal.....	88
5.1.6 Forming the SU-8 channel .....	89
5.1.7 Final fabrication .....	90
5.2 Packaging .....	90
5.2.1 Assembling the package.....	91
5.3 Test setup.....	93
5.4 Conclusion.....	94
Chapter 6 : Trap validation.....	95
6.1 Materials and Methods.....	95
6.1.1 Materials.....	95
6.1.2 Test methodology.....	95
6.1.3 Modeling .....	95

6.2 As-fabricated geometries.....	95
6.2.1 Trap geometry .....	96
6.2.2 Chamber geometry .....	98
6.3 Results .....	98
6.3.1 Trap switching.....	98
6.3.2 Holding characteristics with beads.....	98
6.3.3 Holding characteristics with cells .....	101
6.4 Discussion .....	101
6.4.1 Model and trap validation .....	101
6.4.2 Deviation between model and experiment.....	102
6.4.3 Comparison to existing traps.....	104
6.4.4 Holding forces .....	106
6.4.5 Outlook for future trap design.....	107
6.5 Conclusion.....	108
Chapter 7 : Cell-based operation.....	109
7.1 Materials and Methods.....	109
7.1.1 Cell culture .....	109
7.1.2 Assay buffer .....	109
7.1.3 Cell assay preparation .....	109
7.1.4 Calcein labeling.....	109
7.1.5 Electrode Traps .....	110
7.1.6 Chamber purging and cleaning .....	110
7.1.7 Optics .....	110
7.1.8 Image analysis.....	110
7.1.9 Release flowrate measurements .....	111
7.1.10 Modeling .....	111
7.2 Results .....	111
7.2.1 Qualitative operation.....	111
7.2.2 Quantitative operation.....	115
7.3 Discussion .....	126
7.3.1 Single-cell manipulation .....	126
7.3.2 Lag time to stimulus entry.....	127
7.3.3 Dynamic assays.....	128
7.4 Conclusions .....	129
Chapter 8 : Conclusions .....	131
8.1 Thesis contributions .....	131
8.2 Outlook, challenges and future work .....	132
Appendix A : Derivation of the DEP force on a homogenous sphere .....	137
Appendix B : Fabrication Process flow.....	141
References .....	143

# List of Figures

FIGURE 1-1: SYSTEM DIAGRAM OF THE $\mu$ DAC. ....	15
FIGURE 1-2: DIELECTROPHORESIS.....	20
FIGURE 1-3: CM FACTOR FOR THREE SITUATIONS.....	22
FIGURE 1-4: N-DEP TRAPPING STRUCTURES .....	25
FIGURE 1-5: ELECTRICAL MODEL OF THE CELL .....	28
FIGURE 2-1: OVERVIEW OF MODELING ENVIRONMENT, SHOWING THE MAJOR STEPS .....	32
FIGURE 2-2: SCHEMATIC OF SIMULATED PLANAR QUADRUPOLE GEOMETRY .....	33
FIGURE 2-3: PLOTS OF THE ELECTRIC FIELD INTENSITY FOR THE QUADRUPOLE GEOMETRY .....	34
FIGURE 2-4: PLOTS OF THE DEP FORCE (UP TO $n=2$ ) IN THE $x$ - $y$ PLANE DERIVED FROM THE ELECTRIC FIELD PICTURED IN FIGURE 2-3 .....	37
FIGURE 2-5: ZERO-FORCE ISOSURFACES .....	39
FIGURE 2-6: BOUNDING BOX ALGORITHM IN TWO DIMENSIONS.....	40
FIGURE 2-7: SCHEMATIC OF POINT-IN-POLYGON TESTS.....	41
FIGURE 2-8: FLOWCHART FOR HOLDING FORCE PROGRAM.....	43
FIGURE 2-9: FLOWCHART FOR RELAXATION PROGRAM.....	43
FIGURE 2-10: THE EFFECT OF PARTICLE DENSITY ON THE HOLDING POINTS .....	44
FIGURE 2-11: EFFECT OF FLOW ON THE HOLDING POINTS.....	45
FIGURE 3-1: (A) PHOTOGRAPH OF THE COMPLETED QUADRUPOLE ELECTRODES. (B) SCHEMATIC OF PACKAGING ASSEMBLY. (C) SCHEMATIC OF FLUIDIC SUBSYSTEM.....	50
FIGURE 3-2: (A) SCHEMATIC OF FLOW CHAMBER. (B) RELEASE FLOWRATE AND HOLDING FORCE MEASUREMENTS .....	52
FIGURE 3-3: SCHEMATIC SHOWING HOW THE NUMBER OF PARTICLES PER TRAP VARIES WITH APPLIED FLOW .....	53
FIGURE 3-4: EXPERIMENTAL ( $\circ$ ) AND SIMULATED ( $\text{—}$ ) HOLDING CHARACTERISTICS FOR BEADS IN THE PLANAR QUADRUPOLE TRAP OF FIGURE 3-1A AS THE BEAD DIAMETER WAS VARIED .....	54
FIGURE 3-5: EXPLANATION OF HOLDING CHARACTERISTICS AS VOLTAGE IS VARIED .....	55
FIGURE 3-6: COMPARISON OF EXTRACTED EXPERIMENTAL ( $\circ$ ) AND SIMULATED ( $\text{—}$ ) PEAK VOLTAGE (A), PEAK RELEASE FLOWRATE (B), AND BASELINE RELEASE FLOWRATE (C). .....	56
FIGURE 3-7: CALCULATED CM FACTOR (DIPOLE TERM) FOR A POLYSTYRENE BEAD IN SALT SOLUTION.....	57
FIGURE 3-8: EXPERIMENTAL ( $\circ$ ) AND SIMULATED ( $\text{—}$ ) HOLDING CHARACTERISTICS FOR 10.00 $\mu\text{m}$ BEADS FOR THREE DIFFERENT FREQUENCIES AT SOLUTION CONDUCTIVITIES OF 0.01 S/M (A-C) AND 0.75 mS/M (D-F) .....	59
FIGURE 4-1: DEP HOLDING IN ONE DIMENSION.....	64
FIGURE 4-2: DEP HOLDING IN TWO DIMENSIONS .....	65
FIGURE 4-3: EVOLUTION OF THE EXTRUDED TRAP .....	66
FIGURE 4-4: COMPARISON OF $x$ -DIRECTED BARRIERS FOR TWO TRAP GEOMETRIES .....	67
FIGURE 4-5: RESULTS OF TRAP OPTIMIZATION SIMULATIONS .....	69
FIGURE 4-6: TRAP SWITCHING VIA ONE ELECTRODE.....	70
FIGURE 4-7: HOLDING CHARACTERISTIC OF THE SINGLE-WIRE TRAP.....	71
FIGURE 4-8: RESULTS FROM VARIOUS WIRING SCHEMES.....	71
FIGURE 4-9: IN-PLANE HOLDING OF SELECTED WIRING SCHEME.....	72

FIGURE 4-10: (A) TRANSMEMBRANE POTENTIAL OF HL-60 CELLS. (B) THE DIPOLE TERM OF THE CM FACTOR FOR THE SAME CELLS .....	74
FIGURE 4-11: SYSTEM-LEVEL DESIGN OF CHAMBER HEIGHT .....	76
FIGURE 4-12: SCHEMATIC OF A 1X8 ARRAY OF TRAPS, SHOWING THE INTERCONNECTS AND POSTS. ....	77
FIGURE 4-13: HOLDING CHARACTERISTIC FOR FINAL TRAP .....	77
FIGURE 4-14: COMPARISON OF THE HOLDING CHARACTERISTICS OF THE FINALIZED TRAP DESIGN WITH THE PLANAR QUADRUPOLE OF CHAPTER 3 FOR 10.0- $\mu\text{M}$ BEADS .....	78
FIGURE 5-1: FABRICATION PROCESS FLOW FOR THE EXTRUDED TRAPS. ....	81
FIGURE 5-2: TOP-DOWN VIEW OF THE SUBSTRATE INTERCONNECT FOLLOWING AU ETCHING .....	82
FIGURE 5-3: DEKTAK MEASUREMENTS OF THE EDGE BEAD FROM SU-8 COATING WITHOUT (A) AND WITH (B) A FINAL HIGH-SPEED SPIN .....	83
FIGURE 5-4: DEKTAK MEASUREMENTS OF THE SU-8 EDGE BEAD FOLLOWING PGMEA TREATMENT OF THE EDGE .....	84
FIGURE 5-5: IMAGE OF A 1X8 ARRAY AFTER SU-8 DEVELOPMENT AND ASHING. ....	85
FIGURE 5-6: SCHEMATIC OF THE ELECTROPLATING SETUP. ....	85
FIGURE 5-7: ELECTROPLATING & SU-8 STRIPPING PROCESS .....	87
FIGURE 5-8: ELECTRODES AFTER TITANIUM REMOVAL .....	88
FIGURE 5-9: FINAL FABRICATION STEPS .....	89
FIGURE 5-10: FINAL SEMs OF THE COMPLETED CHIPS. ....	90
FIGURE 5-11: PACKAGING OF THE EXTRUDED ARRAY .....	91
FIGURE 5-12: ASSEMBLING THE PACKAGING .....	91
FIGURE 5-13: THE ALUMINUM FLUIDIC CARRIER AND PRINTED CIRCUIT BOARD .....	92
FIGURE 5-14: ELECTRICAL DRIVING CIRCUIT. ....	93
FIGURE 5-15: PHOTOGRAPHS OF THE TEST SETUP .....	93
FIGURE 6-1: (A) SEM OF A COMPLETED TRAP OVERLAID WITH THE MASK DRAWING. (B) SEM OF A FALLEN POST .....	96
FIGURE 6-2: TOP-DOWN SEMs OF TWO POSTS .....	97
FIGURE 6-3: MOVIE FRAMES SHOWING ELECTRICAL CONTROL OF THE TRAPS .....	98
FIGURE 6-4: SUPERIMPOSED DATA FOR HOLDING CHARACTERISTICS .....	99
FIGURE 6-5: MODEL PREDICTIONS OF THE HOLDING CHARACTERISTICS .....	100
FIGURE 6-6: EXTRACTED HOLDING FORCES OF THE EXTRUDED QUADRUPOLE TRAPS .....	101
FIGURE 6-7: SIMULATED HOLDING CHARACTERISTICS FOR HL-60 CELLS IN THE FINALIZED TRAPS .....	102
FIGURE 6-8: PREDICTED PARTICLE LOCATIONS AT RELEASE USING THE INTERPOLATED RESULTS .....	103
FIGURE 6-9: COMPARISON BETWEEN THE SIMULATED HOLDING CHARACTERISTICS OF BEADS IN TRAPS WITH 3.5- $\mu\text{M}$ (—) AND 4.0- $\mu\text{M}$ (---) ELECTRODE TAPERS .....	104
FIGURE 6-10: DEPICTION OF DRAG FORCE ON PARTICLES IN THE CHAMBER .....	106
FIGURE 6-11: HOLDING FORCES IN EXTRUDED TRAPS .....	107
FIGURE 7-1: LOADING A 1X8 ARRAY OF TRAPS WITH CALCEIN-LABELED HL-60 CELLS .....	112
FIGURE 7-2: SINGLE-CELL DISCRIMINATION .....	113
FIGURE 7-3: INDEPENDENT TRAP CONTROL .....	114
FIGURE 7-4: RESULTS OF CELL-HOLDING EXPERIMENTS AT VARIOUS FREQUENCIES .....	115
FIGURE 7-5: CM FACTOR FOR 9.3- $\mu\text{M}$ HL-60 CELLS WHEN THE MEMBRANE CAPACITANCE IS 1.6 $\mu\text{F}/\text{CM}^2$ (—) AND 4.0 $\mu\text{F}/\text{CM}^2$ (—) .....	116

FIGURE 7-6: CM FACTOR HL-60 CELLS WITH THE APPROXIMATIONS FOR THE VARIOUS FREQUENCY DEPENDENCIES INDICATED .....	117
FIGURE 7-7: EFFECTS OF CHANGES IN THE MEMBRANE CAPACITANCE ON THE PREDICTED HOLDING CHARACTERISTICS OF 9.3- $\mu\text{M}$ HL-60 CELLS.....	117
FIGURE 7-8: CELL HOLDING DATA OVERLAID WITH A PATCH (LIGHT GRAY) DENOTING THE EXTENTS OF THE PREDICTED PARAMETERS.....	118
FIGURE 7-9: 10 $\mu\text{M}$ CALCEIN LOADING OF HL-60 CELLS.....	119
FIGURE 7-10: CALCEIN LOADING AT 10 $\mu\text{M}$ .....	121
FIGURE 7-11: EFFECT OF CHANGING THE CAMERA SENSITIVITY ON THE EXTRACTED PARAMETERS .....	122
FIGURE 7-12: CALCEIN LOADING AT 1 $\mu\text{M}$ .....	123
FIGURE 7-13: CALCEIN LEAKAGE AT 100 $\mu\text{G/ML}$ .....	125
FIGURE A-1: FORCE ON A UNIFORM SPHERE IN A NON-UNIFORM ELECTRIC FIELD .....	137
FIGURE A-2: FORCE ON AN X-ORIENTED DIPOLE IN AN X-DIRECTED NON-UNIFORM ELECTRIC FIELD. ....	139

# List of Tables

TABLE 4-1: MATRIX FOR TRAP OPTIMIZATION .....	68
TABLE 4-2: SYSTEM-LEVEL SPECIFICATIONS OF THE $\mu$ DAC. ....	73
TABLE 4-3: FINAL SYSTEM-LEVEL DESIGN PARAMETERS .....	78
TABLE 6-1: COMPARISON BETWEEN AS-DESIGNED AND AS-FABRICATED GEOMETRIES .....	96
TABLE 6-2: COMPARISON OF HOLDING AGAINST FLOW BETWEEN THE OPPOSED OCTOPOLE AND THE EXTRUDED QUADRUPOLE TRAP FOR BEADS .....	105

# List of Symbols

<u>Symbol</u>	<u>Units</u>	<u>Description</u>	<u>Symbol</u>	<u>Units</u>	<u>Description</u>
$A_n, B_n, C_n, D_n$	1/m	Plane-determination coefficients	$r$	m	Post diameter
$A$	mm <sup>2</sup>	Cross-sectional area	$R$	μm	Particle radius
$C_m$	F/cm <sup>2</sup>	Cell membrane capacitance	Re	–	Reynolds number
$CM$	–	Clausius-Mossotti factor	$t_f$	s	Chamber fill time
$d$	μm	Distance between entrance and exit electrodes	$U$	mm/s	Linear flowrate
$D$	cm <sup>2</sup> /s	Diffusivity	$U_c$	mm/s	Centerline fluid velocity
$\mathbf{D}$	C/m <sup>2</sup>	Electric displacement field	$U_{dep}$	N	DEP potential energy
$E, \mathbf{E}$	V/m	Electric field	$V$	V	Voltage
$E_i, E_m, E_n$	V/m	Electric field in $i$ -, $m$ -, $n$ -th directions	$V_0$	mm <sup>3</sup>	Tubing void volume
$E_0$	V/m	Constant electric field	$V_{tm}$	V	Transmembrane voltage
$E_{tm}$	V/m	Cell membrane electric field	$w$	mm	Chamber width
$E_x, E_y, E_z$	V/m	Electric field components	$x, y, z$	m	Spatial coordinates
$F$	Hz	Frequency	$x_i, x_m, x_n$		
$F_{dep}, \mathbf{F}_{dep}$	N	Dielectrophoretic force			
$\mathbf{F}_{dep}^{(n)}$	N	$n$ -th order DEP force	$\alpha$	μl/min- V <sup>2</sup>	Fitting parameter
$F_{drag}$	N	Hydrodynamic drag force	$\Delta$	nm 1/m	Membrane thickness; Determinant of A,B,C,D coefficients
$F_{drag}^*$	-	Non-dimensional drag with wall effects	$\epsilon$	F/m	Permittivity
$F_{grav}$	N	Gravitational force	$\epsilon_{cyto}$	F/m	Cytoplasmic permittivity
$F_i^{(n)}$	N	$n$ -th order DEP force in $i$ -th direction	$\epsilon_p$	F/m	Particle permittivity
$F_x, F_y, F_z$	N	Force components	$\epsilon_p'$	F/m	Effective particle permittivity
$g$	m/s <sup>2</sup>	Gravitational force constant	$\epsilon_m$	F/m	Medium permittivity
$G_m$	S/cm <sup>2</sup>	Cell membrane conductance	$\epsilon_s$	F/m	Membrane permittivity
$h$	μm	Chamber height	$\phi$	rad	Aximuthal angle
$h_0$	μm	Nominal chamber height	$\Phi$	V	Electrical potential
$\hat{i}_x, \hat{i}_y, \hat{i}_z$	m	Unit vectors	$\eta$	Pa-s	Fluid viscosity
$K$	cm <sup>2</sup> /s	Dispersion coefficient	$\rho_p$	g/cm <sup>3</sup>	Particle density
$l$	mm	Chamber length	$\rho_m$	g/cm <sup>3</sup>	Medium density
$l_d$	mm	Dispersion length	$\rho_{cyto}$	Ω-m	Cytoplasmic resistivity
$l_1$	μm	Entrance electrode separation	$\rho_{med}$	Ω-m	Medium resistivity
$l_2$	μm	Exit electrode separation	$\sigma$	S/m	Conductivity
$L$	mm	Tubing length			
$n$	-	DEP force order;	$\sigma_{cyto}$	S/m	Cytoplasmic conductivity
$n$	-	Number of data points taken;			
$n$	-	# of electrodes/dimension	$\sigma_m$	S/m	Medium conductivity
$\mathbf{n}$	m	Vector normal	$\sigma_p$	S/m	Particle conductivity
$n_{max}$	-	Maximum DEP force order	$\sigma_s$	S/m	Membrane conductivity
$p, \mathbf{p}$	C-m	Dipole moment	$\tau$	sec; Pa	Time constant; Shear stress
$\mathbf{p}, \mathbf{p}_1, \mathbf{p}_2, \mathbf{p}_3$	-	Points in polygon	$\tau_{MW}$	sec	Maxwell-Wagner time constant
Pe	–	Peclet number	$\omega$	rad/sec	Radian frequency
$Q$	μl/min	Volume flowrate			
$Q_{rf}$	μl/min	Release flowrate			
$r, \mathbf{r}$	m	Spatial coordinate			

# Chapter 1: Introduction

This thesis describes the development of arrays of microfabricated electric-field traps for holding single bioparticles—beads and cells. The traps use dielectrophoretic forces to hold particles in a non-contact fashion and can be individually toggled to release selected particle subpopulations.

In this chapter I will begin with an overview of microsystem technology as applied to bioscience. This will lead to an introduction to the overall project goal—a cytometer for probing the dynamic behavior of many single cells. The cytometer consists in large part of a planar array of traps, and so I will then discuss the physics behind these traps and how they fit into their field. I will conclude the chapter with an overview of the effects of electric fields on cells and an outline of the rest of the thesis.

## 1.1 *Bio-microsystems*

Microsystems have great potential to affect bioscience. The first applications arose in the 1970s, beginning with the development of cortical implants at the University of Michigan [1] and the commercialization of intravenous blood-pressure sensors [2]. One way to examine where bioscience and microsystems intersect is to look at the properties of microsystems that suite them for application to bioscience [3]. When applied in the right instances to exploit these properties, microsystems can significantly enhance existing devices or even enable entirely new ones.

The most obvious property of microsystems is their intrinsically small size. For clinical applications, this can allow the development of point-of-care devices for use “at the bedside” rather than at a central facility, reducing the time it takes to get results [4]. The small size of microsystems also means that small volumes of samples and reagents are necessary. This decreases costs, reduces waste, and increases the number of assays that can be performed with expensive chemical libraries [5].

Another useful property of microsystems is their high surface-area-to-volume ratio, which enhances processes that are dominated by surfaces—such as heat transfer. This allows microfabricated chambers for polymerase chain reactions to ramp temperatures very quickly [6]. Integration with electronic components such as circuits can buffer and amplify low-level electrical signals, such as those recorded from neurons [7], making them easier to detect. Parallelization of microsystems allows for high throughput, which is crucial for such technologies as DNA sequencing [8]. The geometrical control inherent in microfabrication technology allows one to make structures that can constrain diffusion of components [9] or control cell-cell interactions [10]. Finally, batch processing, common in the semiconductor industry, has the potential to reduce the costs and increase the homogeneity of microsystems, allowing them to be disposable. This property is important for clinical applications because there is no need to resterilize devices and also for analytical assays to eliminate issues of sample carryover. In addition, batch fabrication is important for lithographically defined DNA chips, where it enables the creation of highly dense arrays of nucleic acids [11].

A different way to look at the intersection of microsystems and bioscience is by examining where in bioscience the applications have been. Examining the literature reveals that the most interest to date has been in molecular biology and biochemistry. There are several

reasons for this. First, and most importantly, the Human Genome Project has resulted in great need for high-throughput technologies for sequencing DNA and analyzing the RNA transcripts in cells. This led to the development of capillary electrophoresis [12]—and its subsequent miniaturization [13]—and DNA chips [11]. In addition, molecular biology and biochemistry, as opposed to cell biology, do not entail working with living cells, which adds a layer of complexity.

Working at the cellular level is an area that has lagged behind in comparison to the research at the molecular level and microfluidics applications. While examples exist of excellent recent research in this field, the integration of living cells into microsystems (or microdevices) is still in its infancy. With this knowledge in mind, our research group has been interested in developing tools to manipulate multiple single cells.

## **1.2 The $\mu$ DAC**

### **1.2.1 Overview**

The motivation behind developing arrays of single-particle traps is a system for monitoring the dynamics of biological cells and sorting them based on those dynamics. This system, called the “ $\mu$ DAC” (microfabrication-based dynamic array cytometer), combines the strengths of two established biological instruments—the microscope and flow cytometer—to yield a device capable of performing biological assays that are currently unavailable. Microscopy enables researchers to study the dynamic response of cells in a field of view to a stimulus. A common example is monitoring the concentration of intracellular  $\text{Ca}^{2+}$  with a fluorescent dye as a cell-membrane receptor-mediated pathway is provoked [14]. While one can measure fast dynamics (<seconds) with sub-cellular resolution, it is difficult to measure the dynamics of many cells using microscopy. This is due to the limited field of view of microscope objectives coupled with the fact that cell location is not known and so must be determined via software. In addition, removing the cells after analysis is tedious. Flow cytometry can perform similar analyses on large numbers of cells, but only tracks each cell at one time point. Dynamic analyses can be performed by exposing a cell population to a stimulus and looking at the cells one at a time over time, but this assumes a homogeneous population, and sorting based upon those dynamics is still a challenge.

The area of analysis missing from both flow cytometry and microscopy is the ability to look at many cells, each individually, over time, and sort them using dynamic response as a sort variable. This is the goal of the  $\mu$ DAC.

As shown in Figure 1-1, the system will consist of four parts: 1) a microfabricated chip (cell-array chip) that will capture and hold many cells (e.g., 10,000) in an array; 2) a fluidic system to introduce the cells and stimuli to the chip, and to collect released cells with fraction collectors; 3) an optical system to fluorescently interrogate the cell array and record an ensemble of single-cell data; and 4) a control system to selectively release those cells that display a given behavior or signal pattern.

Although both the optical system and the cell-array chip present significant engineering challenges, this thesis concerns the implementation of the cell-array chip, which will capture, hold, and selectively release the cells. This chip contains a two-dimensional planar array of single-cell traps, each of which must be individually addressable to have the ability to turn on and off. Traps in general are potential energy wells, and I use electrical potential energy via the phenomenon of dielectrophoresis to construct these wells.

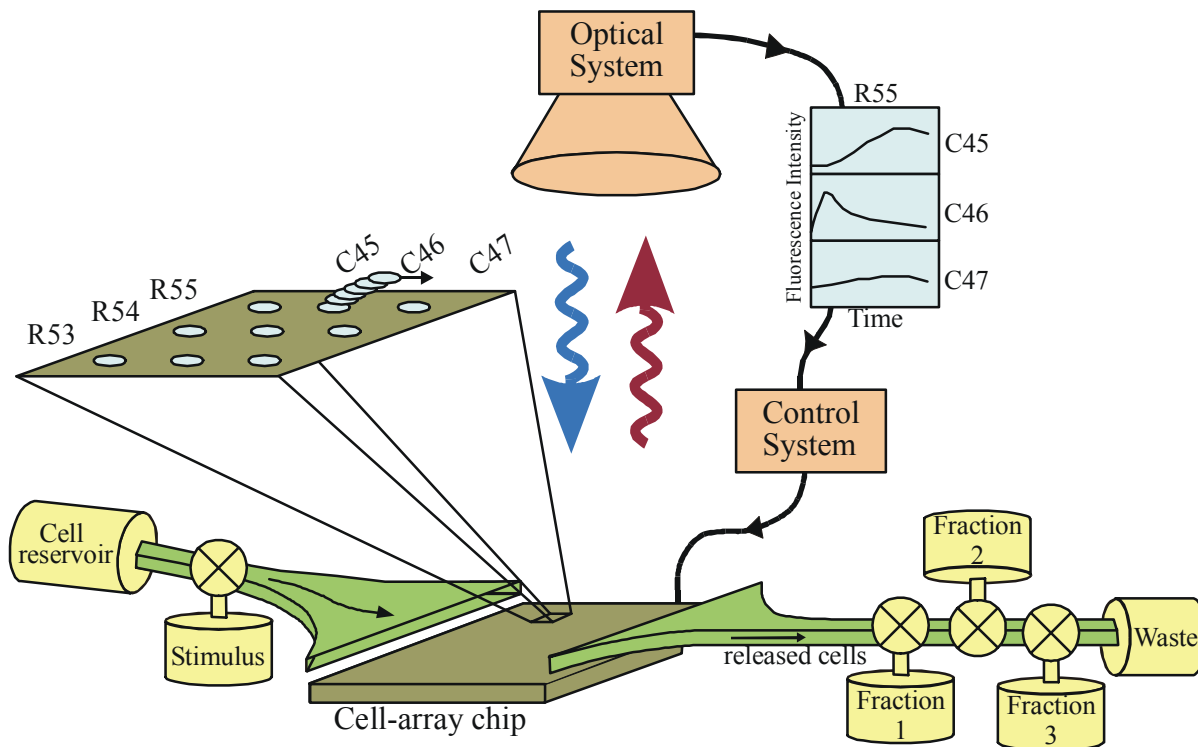


**Figure 1-1:** System diagram of the  $\mu$ DAC.

## 1.2.2 Applications

The  $\mu$ DAC will be useful for luminescence-based single-cell assays that measure the dynamics of many cells individually and sort those cells into arbitrary sub-populations based upon those dynamics (or any other response). The basic premise underlying its development is that information is encoded into the dynamics of cellular behavior—not just the steady-state values—and that tools designed to investigate those dynamics can probe that information. It is possible to imagine applications that utilize part of the  $\mu$ DAC’s capabilities—e.g., observing differential dynamics but not sorting, or sorting based upon single time-point responses. The most powerful assays, of course, will be those that combine all these capabilities.

Applications can be roughly divided into basic cell-biological studies to elucidate cell behavior and applied technological uses, such as for drug discovery. Both of these applications will likely involve single-cell-based reporter gene assays, in which the gene product of interest is monitored, or “reported”, by a visible protein that is either fused to the protein of interest or under the same regulatory control [15]. Examples of reporter proteins include GFP [16], luciferase [17], and  $\beta$ -lactamase [18]. One can investigate many different cellular pathways in this way, especially for drug discovery applications [19, 20]. A challenge for the  $\mu$ DAC is that while many reporter proteins exist, fewer are amenable to single-cell use, either because of sensitivity requirements or difficulty in assaying with intact cells [21].

For basic cell biology, the  $\mu$ DAC can be used to investigate how differences in genotypes affect the dynamics of phenotypic response, especially as applied to cellular signaling pathways. One example is the aforementioned  $\text{Ca}^{2+}$  response assay [14]. In such an assay, one might discover that a statistically significant subpopulation of cells had a lag in the calcium response to an upstream agonist. By sorting out this subpopulation and sequencing the DNA

encoding for the proteins in that pathway, one could investigate the gene mutations that may be responsible for the dynamical changes. Then one could go back and introduce those mutations into new populations to begin to determine what is happening in the cell. The key part, though, is the assay to probe this information, which is enabled by the  $\mu$ DAC.

One might envision performing such an assay with a system like the Laser Scanning Cytometer (LSC), which uses a scanned laser to record fluorescence data from cells on a slide, forming a planar cytometer [22]. Cells, distributed randomly on the slide, are located via software from a minimum fluorescence intensity value. The LSC has been used for many applications, including cancer research [23], apoptosis [24], and cytogenetics [25]. Two problems present themselves, however. First, one cannot sort with the LSC, as the cells are attached to the substrate and there is no way to selectively remove subpopulations. Thus, it would be difficult to select the interesting subpopulation for further analysis. Second, the scan time limits dynamic analyses ( $<100$  cells/second [26]). The  $\mu$ DAC, because all the cells are precisely registered to the substrate, has the potential for a simpler and thereby much faster optical subsystem.

Another alternative for dynamic assays is to use a flow cytometer. Flow cytometers currently (and for the foreseeable future) have the highest throughput for any single cell-based sorting device. Researchers have investigated the use of flow cytometers for dynamic assays. One system, described by Dunne in 1992, describes modifications to a conventional flow cytometer that allows sorting based upon dynamic responses for general applications [27]. His system modifies a conventional flow cytometer, adding a reference bead solution to precisely calibrate the stimulus time ( $t=0$ ) and a delay line so that he can precisely vary the transit time to the detector, thus removing the time uncertainties involved in stimulating cells with conventional flow cytometric setups. He performed proof-of-concept assays, such as stimulating a responsive subclone of rat pheochromocytoma PC12 with bradykinin and measuring the calcium response dynamics. This system, though, and all other flow-based systems can only view cells at one time point, and so the sort is based upon the premise that the population is homogeneous, which is the exact opposite premise envisioned for the calcium-response assay. Thus, flow cytometry is not appropriate for this assay.

Other interesting problems in basic cellular signaling could be investigated with the  $\mu$ DAC. For instance, there is much current interest in constructing and analyzing genetic regulatory networks [28-30]. In endogenous regulatory networks, there is interest in determining the origin of heterogeneity across cell populations. For instance, researchers have investigated different models to explain the whether the distribution in T-cell division rates across populations following stimulation with the cytokine IL-2 is due to stochastic mechanisms in a homogeneous population or due to heterogeneity in either genotype or expression levels of cell-cycle regulating proteins [31]. For cell-cycle induction by IL-2, at least, the differences are due to differential expression of the IL-2 receptor, rather than stochastic differences. The  $\mu$ DAC could be used with the appropriate reporter to investigate such pathways because of its ability to see acquire dynamic data on statistically significant cell populations with single-cell resolution. For instance, one could look for subpopulations that displayed significantly different kinetics in response to IL-2 and then determine whether those differences were due to varying genotypes that could be reconciled with the model.

The  $\mu$ DAC could also be used as a convenient platform to investigate exogenous regulatory networks, such as the recently introduced genetic toggle switch [30]. In these systems, researchers introduce complete regulatory networks that exhibit some predicted

dynamic behavior, in this case bistability. Assays could be performed with the  $\mu$ DAC to both test the predicted responses and to sort cells into subpopulations depending on their responses for further study. As the complexity of these regulatory networks increases, the uses for a platform capable of dynamic assay followed by selection will increase.

Other assays could be used to investigate how differential time responses of cells affect downstream fates, such as differentiation. For instance, it is known that treatment of the PC12 cell line with nerve growth factor (NGF) leads to differentiation while treatment with epidermal growth factor (EGF) leads to cell proliferation, even though the two growth factors excite the same intracellular signaling pathway [32]. The difference in response to the two growth factors is thought to lie in the dynamics of activation of an intermediate signaling protein—extracellular signal-regulated kinase (ERK). Specifically, NGF leads to sustained ( $\sim$ hrs) activation of ERK, while EGF leads to transient activation ( $<1$  hr). Thus, the information determining the fate of the cell is encoded in the dynamic response of ERK. Using the  $\mu$ DAC, one could fluorescently monitor intracellular ERK levels and therefore have an assay for this signaling system. Researchers could then, for example, investigate how mutations in the upstream signaling proteins affect the dynamics of ERK activation, thus gaining insight into exactly how a dynamic signal is encoded and translated by the cell.

This assay also bridges into possible drug discovery applications. For instance, a company might be interested in finding a small molecule that will affect the fates of cells. A simplistic example would be to search for ligands that would send cells into their differentiated states, such as to develop tissues for tissue engineering applications. By monitoring an intermediate messenger (such as an ERK- $\beta$ -lactamase fusion) whose dynamics determines whether a cell will differentiate or not, one could test for drugs that induced differentiation without waiting for the cell to actually differentiate.

Other assays with both drug discovery and basic cell biology applications include mapping the kinetics of a signaling pathway, thus gaining insight into how to perturb it to exert therapeutic influences. IL-2 has shown promise in treating AIDS and as an adjuvant in cancer therapy [33]. However, the systemic doses needed to exert therapeutic effects can cause toxicity. Mapping the kinetics of IL-2 and its receptor has led to specific insight into that pathway as well as generic insight into how to design drugs that exert maximum therapeutic effect by optimizing their binding properties to receptors [33]. Another example is determining drug resistance in tumor cells by examining uptake and efflux rates of anti-cancer agents [34]. This assay can be performed with flow cytometry, but using the  $\mu$ DAC eliminates the homogeneous population assumption. This makes it possible to search for cell subpopulations within a tumor that are drug resistant and would not be affected by the anti-cancer agent. Both of these examples involve mapping of kinetic parameters involving dynamic assays. The  $\mu$ DAC provides an alternative platform for performing such experiments and additionally for selecting mutants that display interesting dynamic behaviors.

Another generic assay is the use of  $\beta$ -lactamase as a reporter for drug discovery applications, because it can be easily detected in single cells. This reporter system has already been used to monitor gene induction dynamics in single living cells and perform clonal selection [18]. It has also been used for genome-wide gene trapping, whereby promoterless  $\beta$ -lactamase is randomly inserted into the genome to find genes that are activated by specific signaling pathways, their case T-cell activation [35]. One could use the same system with the  $\mu$ DAC to investigate the dynamics of different pathways, identifying promoters and genes that display differential dynamic responses.

In related work, several companies are interested in high-throughput cell-based assays for drug discovery, such as could be performed by the  $\mu$ DAC. Biolog ([www.biolog.com](http://www.biolog.com)) makes a set of Phenotype MicroArrays™ that can probe several hundred metabolic phenotypes of *E. coli*. However, these are not single-cell assays and cannot be sorted, and so do not replace the  $\mu$ DAC. Another company, Cellomics, is developing assay technology for both single- and multi-cellular assays. The idea here is to monitor the intracellular behavior of multiple single cells patterned on a substrate—as opposed to a bulk parameter on an aliquot of cells—to extract “high content information” from cellular assays [36, 37]. While they can monitor dynamics, and are moving towards a microfabricated format, they cannot sort cells with their method nor have they established methods for use with non-adherent cells in their approach.

Finally, one could approach the  $\mu$ DAC simply as a microfabricated cell sorter. It could conceivably compete with the throughput of other microfabricated cell sorters, which tend to be extremely slow ( $\sim$ cells/sec), although it is doubtful that it could compete with conventional flow-activated cell sorters, which have very high throughputs ( $\sim 10^4$  cells/sec). Thus, the value-added by the  $\mu$ DAC will most likely be the combination of cell sorting *with* dynamic assays [38-40].

In summary, the  $\mu$ DAC has many potential uses for basic and applied cell biology, most likely for assays that probe the dynamics of signaling pathways in single cells and then sort those cells into subpopulations based upon those dynamics.

### **1.3 Micron-sized particle manipulation**

One might envision several methods to position cells in a planar array, such as is needed for the  $\mu$ DAC. Among the forces most suitable for positioning micron-sized particles are acoustic, optical, physical, and electrical forces. Ultrasonic fields use acoustical energy to either trap particles at field nulls [41, 42] or to actually levitate small volumes of liquids in air with one or a few cells inside [43]. Ultrasonic particle manipulation, however, suffers from problems of arrayability and sufficient localization to trap single particles and is thus unsuitable for our application.

Optical tweezers use optical gradient forces to trap particles at the focal point of strongly focused laser beams [44, 45]. Optical tweezers can be used to manipulate single particles in three-dimensions and allow concurrent imaging, but they do not scale well—manipulation of two particles requires two beams, and so on. Recent work has tried to overcome this limitation by either scanning the beam [46] or manipulating its phase in the Fourier plane [47, 48]. The work is still preliminary, in that it is unclear whether truly real-time manipulations and trap toggling is possible and whether the laser power scales favorably with the number of traps. In addition, such systems are limited in the area they can occupy because they require the use of high numerical aperture (and thus high magnification) objectives, which do not cover a large area; the possibility of a 1cm x 1cm array of optical traps is doubtful.

Nonetheless, researchers have attempted to use optical tweezers to develop an automated planar cytometer [49]. The idea here was to use imaging algorithms to determine cell locations on a coverslip in a field of view and then use optical tweezers to automatically move cells of interest to specified locations. The system, however, to my knowledge was never developed beyond the proof-of-concept stage. Other researchers have used optical tweezers with low-NA objectives, to attain only radial confinement and thus propel cells along the beam axis [50]. Using this apparatus they were able to pattern  $\sim 100$ 's of cells into arbitrary geometries. However, the current throughput is very low ( $\sim 2.5$  cells/min) and there is no way to remove cells following assay.

Another particle-manipulation technology is simply to use physical forces to contain particles. This can take the form of arrays of microfabricated wells into which particles can be deposited and shielded from destabilizing fluid flows, thus effecting trapping [51, 52]. These methods cannot effect sorting, however, as they use passive holding. Active release mechanisms, such as by using microbubbles, could be implemented, but the research is still preliminary [51]. Alternatively, researchers have used electrically responsive polymers to grab 100- $\mu\text{m}$ -sized beads and move them around [53]. The applicability of this work to cells is doubtful at best, because 1) it is unclear if the technology can be used to hold cells, which are generally smaller (e.g.,  $<20\text{-}\mu\text{m}$ ), and 2) the method is user-intensive and unlikely to be scalable. In addition, all physical trapping techniques may cause contact-induced cellular responses that may interfere with assay results [54].

Electrical forces are well suited for manipulating cells and for the  $\mu\text{DAC}$  in general. Electric fields can be used to manipulate cells either by a Coulomb force on a particle's charge or a dielectrophoretic (DEP) force on a particle's dipole. To create stable traps, however, only the dielectrophoretic forces can be used, as it is impossible to stably trap charges in an electroquasistatic field. DEP-based particle traps have many advantages over the aforementioned forces for manipulating micron-sized particles. First, they are amenable to microfabrication, meaning that they have the potential to be arrayed and thus scale well. Second, they can trap particles of various sizes—sub-micron to tens of microns in diameter—depending on the trap geometry. In addition, since they are active traps, they can be turned off, releasing particles and effecting sorting. Finally, because they are electrical, they can be individually addressed, as needed for the  $\mu\text{DAC}$ . Because of these advantages, I have chosen to use DEP-based particle traps in this thesis.

## **1.4 Dielectrophoresis**

Having chosen dielectrophoresis (DEP) as the trapping force, in this section I will describe the physics behind this phenomenon and give an overview of the field.

### **1.4.1 Physics: dipole approximation**

Dielectrophoresis refers to the action of a body in a non-uniform electric field when the body and the surrounding medium have different polarizabilities. DEP is easiest illustrated with reference to Figure 1-2. On the left side of Figure 1-2, a charged body and a neutral body (with different permittivity than the medium) are placed in a uniform electric field. The charged body feels a force, but the neutral body, while experiencing a dipole moment, does not feel a net force. This is because each half of the induced dipole feels opposite and equal forces, which cancel. On the right side of Figure 1-2, this same body is placed in a non-uniform electric field. Now the two halves of the induced dipole experience a different force magnitude and thus a net force is produced. This is the dielectrophoretic force.

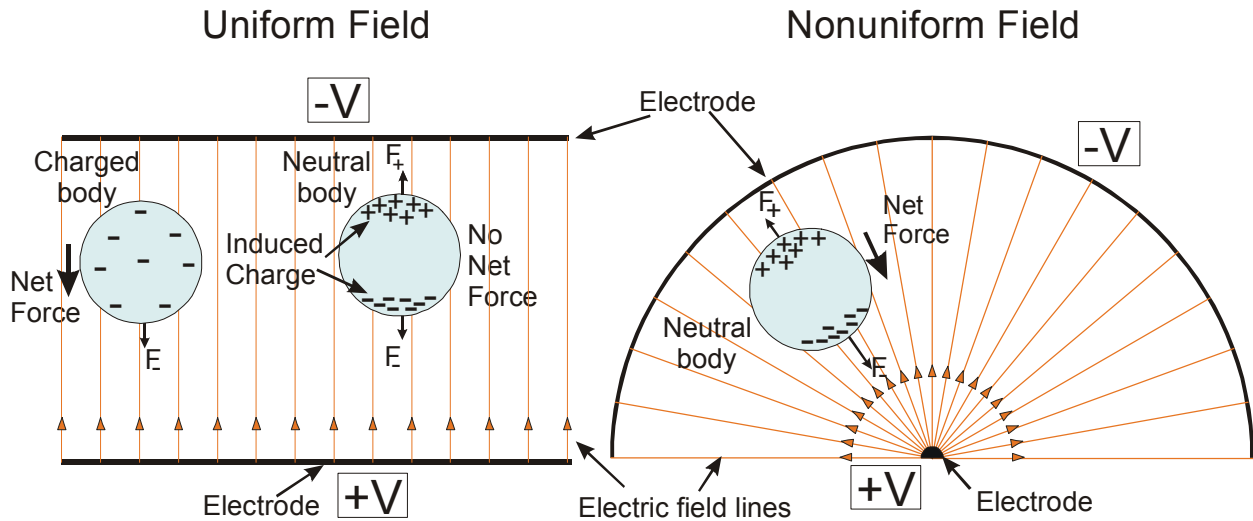


**Figure 1-2:** Dielectrophoresis. The left panel shows the behavior of particles in uniform electric fields, while the right panel shows the net force experienced in a non-uniform electric field.

Depending on the relative polarizabilities of the particle and the medium, the body will feel a force that propels it toward field maxima (termed positive DEP) or field minima (negative DEP). If one sets up a situation with negative DEP (n-DEP) then one can make stable trapping structures to trap particles [55]. In addition, the direction of the force is independent of the polarity of the applied voltage; switching the polarity of the voltage does not change the direction of the force—it is still towards the field maximum. Thus DEP works equally well with both DC and AC fields.

DEP should be contrasted with electrophoresis, where one manipulates charged particles in a dissipative medium with electric fields [56], as there are several important differences. First, DEP does not require the particle to be charged in order to manipulate it; the particle must only differ electrically from the medium that it is in. Second, DEP works with AC fields, whereas no net electrophoretic movement occurs in such a field. Thus, with DEP one can avoid problems such as electrode polarization effects [57] and electrolysis at electrodes. Even more importantly, the use of AC fields reduces membrane charging of biological cells. While explained fully in §1.5.2, membrane charging is due to the potential developed across cell membranes in electric fields. This potential, which can impact cell physiology, can be diminished by the application of high-frequency fields. Third, electrophoretic systems cannot create stable traps, as opposed to DEP—one needs electromagnetic fields to trap charges. Finally, DEP forces increase with the square of the electric field (described below), whereas electrophoretic forces increase linearly with the electric field.

This is not to say that electrophoresis is without applicability. It is excellent for transporting charged particles across large distances, which is difficult with DEP. Second, many molecules are charged and are thus movable with this technique. Third, when coupled with electroosmosis, electrophoresis makes a powerful separation system. However, for trapping particles in place, DEP is the method of choice.

The force in Figure 1-2, where an induced dipole is affected by a non-uniform electric field, is given by ([58] & Appendix A)

$$\mathbf{F}_{dep} = 2\pi\epsilon_m R^3 \text{Re}[\underline{CM}(\omega) \cdot \nabla|\mathbf{E}|^2(\mathbf{r})] \quad (1-1)$$

where  $\underline{\epsilon}_m$  is the permittivity of the medium surrounding the particle,  $R$  is the radius of the particle,  $\omega$  is the radian frequency of the applied field,  $\mathbf{r}$  refers to the spatial coordinate, and  $\underline{\mathbf{E}}$  is the complex applied electric field.

The Clausius-Mossotti factor ( $CM$ )—CM factor—gives the frequency ( $\omega$ ) dependence of the force, and its sign determines whether the particle experiences positive or negative DEP. The Clausius-Mossotti factor comes from solving Laplace's equation and matching the boundary conditions for the electric field at the surface of the particle (Appendix A). For a homogeneous spherical particle in an electric field, the CM factor is given by

$$CM = \frac{\underline{\epsilon}_p - \underline{\epsilon}_m}{\underline{\epsilon}_p + 2\underline{\epsilon}_m}, \quad (1-2)$$

where  $\underline{\epsilon}_m$  and  $\underline{\epsilon}_p$  are the complex permittivities of the medium and the particle, respectively, and are each given by  $\underline{\epsilon} = \epsilon + \sigma/(j\omega)$ , where  $\epsilon$  is the permittivity of the medium or particle,  $\sigma$  is the conductivity of the medium or particle, and  $j$  is  $\sqrt{-1}$ .

Other CM factors can be derived for spherical shells (to approximate white blood cells) and oblate spheroids (to approximate red blood cells) [58]. When working with shells, one solves for boundary conditions at all the interfaces, generating a CM factor with the same form as (1-2) but with an effective permittivity  $\underline{\epsilon}'_p$  in place of  $\underline{\epsilon}_p$ , where  $\underline{\epsilon}'_p$  contains the multi-layer information. For cells with a membrane (but no cell wall), this effective permittivity can be derived as [58]

$$\underline{\epsilon}'_p = \frac{\underline{C}_m R \underline{\epsilon}_m}{\underline{C}_m R + \underline{\epsilon}_m}, \quad (1-3)$$

where the membrane is described as a shell with a complex surface capacitance  $\underline{C}_m = C_m + G_m/j\omega$ .  $C_m$  and  $G_m$  are the surface capacitance and conductance, respectively, given by  $C_m = \epsilon_s/\Delta$  and  $G_m = \sigma_s/\Delta$ , where  $\Delta$  is the membrane thickness and the  $\epsilon_s$  and  $\sigma_s$  are the permittivity and conductivity of the membrane.

There are several important elements to Eqn. (1-1). First, the frequency dependence of the force resides solely in the CM factor, while the spatial dependence resides in the electric field term. Thus, investigations into the spatial and frequency dependencies of the DEP force only need to examine those terms. Second, the specific properties of the particle only emerge through the CM factor, so determining the force on different types of particles only involves recalculating the CM factor (and the  $R^3$  factor, of course). Third, the force increases with  $R^3$  and so is strongly dependent on the particle size.

Much insight into the frequency dependence of the force can be gained by examining the CM factor for a homogeneous sphere. First, the CM factor can only vary between +1 ( $\underline{\epsilon}_p \gg \underline{\epsilon}_m$ , e.g., the particle is much *more* polarizable than the medium) and -0.5 ( $\underline{\epsilon}_p \ll \underline{\epsilon}_m$ , e.g., the particle is much *less* polarizable than the medium). Thus n-DEP can only be half as strong as p-DEP. Second, by taking the appropriate limits, one finds that at low frequency the CM factor (Eqn. (1-2)) reduces to

$$CM_{\omega \rightarrow 0} = \frac{\sigma_p - \sigma_m}{\sigma_p + 2\sigma_m} \quad (1-4)$$

while at high frequency it is

$$CM = \frac{\epsilon_p - \epsilon_m}{\epsilon_p + 2\epsilon_m} \quad (1-5)$$

Thus, similar to many electroquasistatic systems, the CM factor will be dominated by relative permittivities at high frequency and conductivities at low frequencies; the induced dipole varies between a free charge dipole and a polarization dipole. The relaxation time separating the two regimes is

$$\tau_{MW} = \frac{\epsilon_p + 2\epsilon_m}{\sigma_p + 2\sigma_m} \quad (1-6)$$

and is denoted  $\tau_{MW}$  to indicate that the physical origin is Maxwell-Wagner interfacial polarization [59].

This Maxwell-Wagner interfacial polarization causes the frequency variations in the CM factor. It is due to the competition between the charging processes in the particle and medium, resulting in charge buildup at the particle/medium interface. If the particle and medium are both non-conducting, then there is no charge buildup and the CM factor will be constant with no frequency dependence (Figure 1-3A). Adding conductivity to the system results in a frequency dispersion in the CM factor due to the differing rates of interfacial polarization at the sphere surface (Figure 1-3B). A spherical shell electrically approximates a membrane-bound cell. Since it has two interfaces, there are two dispersions in its CM factor, as shown in Figure 1-3C. In general, all three situations depicted in Figure 1-3 can result in p-DEP or n-DEP at various frequencies depending on the sign of the CM factor.

Combining the  $-0.5$  limit of the CM factor with the results of Eqn's (1-4) & (1-5), one sees that maximizing n-DEP requires a particle that is much less conductive or polarizable than

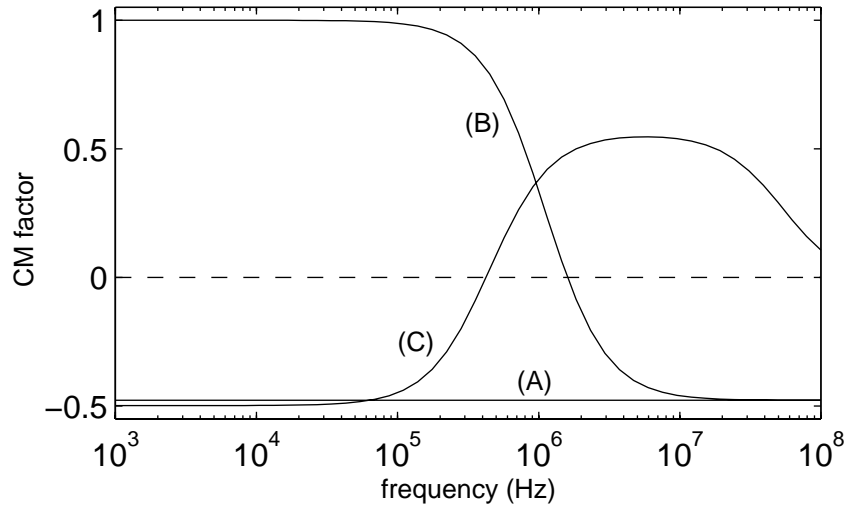


**Figure 1-3:** CM factor for three situations. (A) a non-conducting uniform sphere with  $\epsilon_p=2.4$  in non-conducting water ( $\epsilon_m=80$ ). The water is much more polarizable than the sphere, and thus the CM factor is  $\sim -0.5$ . (B) The same sphere, but with a conductivity  $\sigma_p=0.01$  S/m in non-conducting water. Now there is one dispersion—at low frequencies the bead is much more conducting than the water & hence there is p-DEP, while at high frequencies the situation is as in (A). (C) A spherical shell (approximating a cell), with ( $\epsilon_{cyl0}=75$ ,  $C_m=1$   $\mu\text{F}/\text{cm}^2$ ,  $\sigma_{cyl0}=0.5$  S/m,  $G_m=5$  mS/cm<sup>2</sup>) in a 0.1 S/m salt solution, calculated using results from [58]. Now there are two interfaces and thus two dispersions. Depending on the frequency, the shell can experience n-DEP or p-DEP.

its medium at some frequency. Latex beads in salt water easily meet this requirement as they are electrically insulating and have lower permittivities than the high ( $\epsilon_{water} \sim 80$ ) permittivity of water. Cells are more complicated because they are multi-walled structures, but are essentially bags of salt water. The membrane insulates the cell at low frequencies, but at medium and high frequencies the cell properties are dominated by either the cytoplasmic conductivity or permittivity, respectively. Since these are both high and similar to salt water, it is difficult to get n-DEP and large CM factors in this frequency range. However, one needs to work in this frequency range to minimize membrane charging. Thus, to get trapping of cells in this frequency range one needs to work in medium that is more conductive than the cytoplasm ( $\sim 0.5$  S/m), such as saline ( $\sigma \sim 1$  S/m). This leads to need for microscaling of DEP traps, as I will explain below.

### 1.4.2 Physics: Multipolar theory

Although the DEP force can be obtained using Eqn. (1-1), the force calculated using that expression assumes that only a dipole is induced in the particle. In fact, arbitrary multipoles can be induced in the particle, depending on the spatial variation of the field that it is immersed in. Specifically, the dipole approximation will become invalid when the field non-uniformities become great enough to induce significant higher-order multipoles in the particle. This can easily happen in microfabricated electrode arrays, where the size of the particle can become equal to characteristic field dimensions. In addition, in some electrode geometries there exists field nulls. Since the induced dipole is proportional to the electric field, the dipole approximation to the DEP force is zero there. Thus at least the quadrupole moment must be taken into account to correctly model these forces.

Multipole DEP theory has recently been developed, by two groups of researchers, to address the limitations of the dipole theory. One group has used an effective moment approach to calculate all the induced moments and the forces on them [60-63]. The other group has taken a more rigorous approach using Maxwell's stress tensor [64]. Fortunately, both sets of results are identical, meaning that it is now possible to calculate the DEP forces on lossy particles in arbitrarily polarized non-uniform electric fields. A compact tensor representation of the final result in a form similar to Eqn. (A-11) is

$$\mathbf{F}_{\text{dep}}^{(n)} = \frac{\overset{\cdot\cdot\cdot}{p}^{(n)} [\cdot]^n (\nabla)^n \mathbf{E}}{n!} \quad (1-7)$$

where  $n$  refers to the force order ( $n=1$  is the dipole,  $n=2$  is the quadrupole, etc.),  $\overset{\cdot\cdot\cdot}{p}^{(n)}$  is the multipolar induced-moment tensor, and  $[\cdot]^n$  and  $(\nabla)^n$  represent  $n$  dot products and gradient operations. Thus one sees that the  $n$ -th force order is given by the interaction of the  $n$ -th-order multipolar moment with the  $n$ -th gradient of the electric field. For  $n=1$  the result reverts to the force on a dipole (Eqn. (A-11)).

A more explicit version of this expression for the time-averaged force in the  $i$ -th direction (for sinusoidal excitation) is

$$\begin{aligned}
\langle F_i^{(1)} \rangle &= 2\pi\epsilon_m R^3 \operatorname{Re} \left[ \underline{CM}^{(1)} \underline{E}_m \frac{\partial}{\partial x_m} \underline{E}_i^* \right] \\
\langle F_i^{(2)} \rangle &= \frac{2}{3} \pi\epsilon_m R^5 \operatorname{Re} \left[ \underline{CM}^{(2)} \frac{\partial}{\partial x_m} \underline{E}_n \frac{\partial^2}{\partial x_n \partial x_m} \underline{E}_i^* \right] \\
&\vdots
\end{aligned} \tag{1-8}$$

for the dipole ( $n=1$ ) and quadrupole ( $n=2$ ) force orders [61]. The Einstein summation convention has been applied in Eqn. (1-8). I will use this formulation in later chapters to calculate the DEP forces given the electric fields. The multipolar CM factor for a uniform lossy dielectric sphere is given by

$$\underline{CM}^{(n)} = \frac{\underline{\epsilon}_p - \underline{\epsilon}_m}{n\underline{\epsilon}_p + (n+1)\underline{\epsilon}_m} \tag{1-9}$$

It has the same form as the dipolar CM factor (Eqn. (1-2)) but has smaller limits. The quadrupolar CM factor ( $n=2$ ), for example, can only vary between  $+1/2$  and  $-1/3$ .

### 1.4.3 Microscale DEP: separation systems

DEP has been increasingly coupled with microfabrication for a variety of reasons. First, the surface-area-to-volume ratio of the system increases as the electrodes are scaled down, enhancing the ability of the system to remove heat generated by ohmic conduction in the media. This enables the use of DEP with cells at high frequencies. As explained above, such use entails operation in highly conductive saline ( $\sim 1$  S/m), which leads to high power densities ( $\sigma E^2 \sim 10^9$  W/m<sup>3</sup>). Were it not for the high surface-area-to-volume ratio, the temperatures created in these systems would prohibit their use with live cells.

Second, reducing the size of structures reduces the applied voltage and slew rates needed to obtain certain electric fields/gradients, thus allowing the use of less expensive driving electronics. Third, microfabrication allows the creation of almost any two-dimensional extruded geometry, which is useful for electrode design. Fourth, microscale electrodes produce forces in a range well suited for cell manipulation. General reviews of microscale DEP are found in [65-67].

One main thrust of published microscale DEP research has been to make devices that can separate cells into subpopulations based upon differences in their electrical properties (manifested thru the CM factor). The separations are achieved using two different methods. The first method finds operating conditions where one subpopulation experiences p-DEP and the other n-DEP. In such a situation, the p-DEP subpopulation will be attracted to the electrodes whereas the n-DEP subpopulation will be pushed away. Since particles under p-DEP can experience a stronger DEP force, one can then impose a fluid flow to remove only the n-DEP subpopulation, effecting a separation. The other major class of separations is based upon differing DEP force magnitudes, due to either differences in particle radius or some electrical property. In this case, the force magnitudes are of the same sign, but of differing strength, allowing separation.

Using the first method, researchers have separated many types of cells, including HeLa cells from blood cells [68], human breast cancer cells from blood cells [69], yeast based upon viability [70-72], CD34<sup>+</sup> stem cells from bone marrow and peripheral blood cells [70, 73], and bacteria from blood cells [71, 74]. One group has been using DEP to separate very small particles such as viruses and sub-micron beads [75-78].

The other separation method has not seen as extensive use. It has been coupled with field-force fractionation to separate different sized beads and HL-60 cells from peripheral blood mononuclear cells [79-82] and to perform differential analysis of leukocyte subpopulations [83]. Here, the differing electrical properties result in different levitation heights, which exposes the sub-populations to dissimilar hydrodynamic drag forces, effecting separation. Size-based separation using a chaotic ratchet effect with dielectrophoresis has also been demonstrated [84].

Using a different approach, Fielder et al., have created a dielectrophoretic cell sorter that operates by switching DEP forces to propel incoming cells into one of two output channels [85].

#### 1.4.4 Microscale DEP: traps

The other main thrust of DEP research has been to make particle traps. Almost any electrode arrangement, operated in a suitable fashion, can make a rudimentary particle trap. Much of the early work used non-microfabricated electrodes to levitate air bubbles and cells in either a n-DEP situation [55, 86] or feedback-controlled p-DEP [87, 88], with the primary focus being the validation of the dipole theory (Eqn. (1-1)). One can also trap particles at electrode surfaces using p-DEP [89], although it is difficult to subsequently remove them (i.e., turn the trap off) and they are subjected to extremely high electric fields there; this technique is thus seldom used with cells, although it has been used to trap DNA [90] and proteins [91].

Probably the first major reports of microscale n-DEP traps appeared in 1992 & 1993 by the group at the Institute for Biology at Humboldt University in Germany [92, 93]. They motivated the use of the opposed octopole (Figure 1-4A) to make a strong DEP trap and have used it almost exclusively since then. Other electrode geometries, such as interdigitated electrodes or castellated electrodes ([75], Figure 1-4B) can make rudimentary traps, although these are usually used for particle separation rather than particle trapping.

Other research has investigated the particle-size limits of DEP traps. As the particle size decreases, the DEP force decreases as  $R^3$  (Eqn. (1-1)) while Brownian motion increases with the inverse of the radius [94]. Thus, there should exist a minimum particle size that can be trapped in a given field. Much work has focused on determining these limits [95-97], with the confounding issue being that other trapping forces, most notably electrohydrodynamic flows [77], make it difficult to determine the actual trapping mechanism. Current results indicate that trapping of sub-100-nm particles is possible solely with n-DEP forces [78].

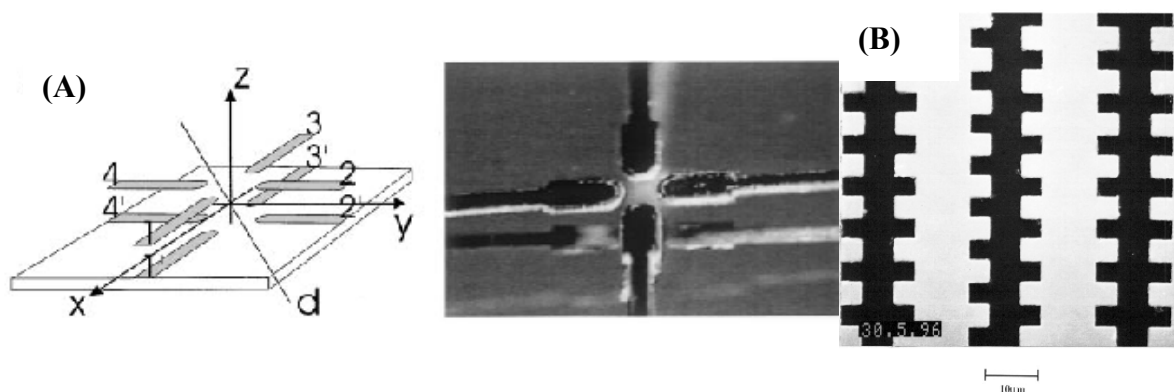


**Figure 1-4:** n-DEP trapping structures. (A) A diagram and photograph of a three-dimensional opposed octopole (from [98]). The octopole consists of two planar quadrupoles on substrates placed apart (and often slightly rotated) from each other. (B) An SEM of a castellated electrode structure (from [75]).

Quantifying the forces in DEP traps is a necessary prerequisite to designing stronger ones. Besides the early quantification work mentioned above [55, 86-88], other researchers have also explored DEP forces in a quantitative manner. While the frequency dependence included in the Clausius-Mossotti factor has long been verified, analyses of the magnitude of the DEP forces in various geometries is a less mature field. The group at Humboldt university have performed semi-quantitative analyses of the DEP force contours on their structures [92, 93]. These researchers, using the same structures, have also measured particle height to infer DEP force trends, although no quantitative agreement was shown. Bahaj and Bailey measured levitation heights of divinyl benzene particles in macroscale ring-disc geometries to attempt to match the DEP forces to theory [99]. Results only marginally agreed with predictions, probably due to the approximations in the calculations of the electric field and the lack of knowledge of the bead properties. X.-B. Wang et al., used spiral electrodes and measured radial velocity and levitation height of breast cancer cells as they varied frequency, particle radius, and medium conductivity [100]. They then matched the data to DEP theory, using fitting parameters to account for unknown material properties, and obtained good agreement. This same set of researchers performed similar analyses using erythroleukemia cells in interdigitated electrode geometries, again obtaining good fits of the data to the theory [101]. One issue with both of these studies is that use of fitting parameters may make it easier to force data to agree with theory. While the above-mentioned work does begin to provide a quantitative basis for DEP forces, a system that can quantitatively predict how well DEP traps of arbitrary geometry can hold cells is lacking. Such a system would be particularly valuable as a design tool.

#### **1.4.5 Other microscale electromechanics**

Still other examples use dielectrophoretic forces in manners different than described above. For example, Washizu has used p-DEP to move isolated water droplets on a hydrophobic surface [102]. Desai et al. used traveling-wave DEP forces to move solid micron-sized particles in air above a surface, the stated application being to concentrate airborne particles [103].

Several other techniques closely related to DEP can induce microscale manipulations. Besides generating forces on an induced dipole, one can generate torques on the dipole by placing it in a rotating electric field. This technique is called electrorotation [104]. Measuring the particle rotation rate as the field frequency changes can be used to determine the electrical properties of micron-sized particles.

Pearl chains are strings of particles that can be produced when the induced dipoles generated by electric fields interact [58]. At certain frequency ranges the induced dipoles from neighboring particles will attract each other, forming long chains of particles resembling pearl necklaces.

In addition, induced dipoles can cause electrodeformation of the cells, either contractile or tensile, depending upon the sign of the CM factor [105, 106]. If the forces are large enough, they can be used to cause cell fission and budding of membrane vesicles [107].

Electrohydrodynamic forces are another microscale electromechanical technique that can be used to induce particle motion, this time by dragging induced dipoles or charges through a fluid, entraining the fluid and thus causing pumping. Pump can be made by varying the phase on a series of interdigitated electrodes to induce either particle or fluid transport [94, 108].

Finally, a number of electrical techniques specifically for use with cells deserve mention. Electroporation (also known as electroporation or electroinjection) uses large (kV/cm)

electric-field pulses ( $\mu\text{s}$ - $\text{ms}$ ) to reversibly permeabilize cell membranes, allowing the transport of reagents into and out of the cell [105, 106, 109]. Application of the pulses, usually by parallel-plate electrodes, causes reversible short-term ( $\sim\text{sec}$ ) permeabilization of the membrane when the transmembrane potential reaches  $\sim 1\text{V}$ . Electrofusion uses similar electric field pulses, but can cause two cells to fuse when they are brought into contact [106, 110]. Electrofusion is often coupled with DEP and pearl chain formation to align and bring the cell populations into contact.

## **1.5 Electric fields and cells**

Since dielectrophoresis involves manipulating cells in strong electric fields, one needs to know how these electric fields might affect cell physiology. Ideally, one would like to determine the conditions under which the electric fields will not affect the cells. Of course, cells are complex systems and thus extra caution needs to be exercised for any device that uses electric fields to manipulate cells in order to prevent or minimize any potential influences of the electric fields on the cells. The physiological impact of fields on the cells can be split into the effects due to current flow, which causes heating, and direct interactions of the fields with the cell. I'll consider each of these in turn.

### **1.5.1 Current-induced heating**

Electric fields in a conductive medium will cause power dissipation in the form of Joule heating. The induced temperature changes can have many effects on cell physiology. As mentioned in §1.4.3, microscale DEP is advantageous in that it minimizes temperature rises due to dissipated power. However, because cells can be very sensitive to temperature changes, it is not assured that any temperature rises will be inconsequential. In this thesis I have not specifically examined the temperature distributions caused by DEP traps. Performing a quantitative analysis would involve solving for the temperature distribution caused by the electric field-induced Joule heating, taking into account the perturbation of the fields by the cells.

Temperature is a potent affecter of cell physiology [111-114]. Very high temperatures ( $>4\text{ }^\circ\text{C}$  above physiological) are known to lead to rapid cell death, and research has focused on determining how to use such knowledge to selectively kill cancer cells [115]. Less-extreme temperature excursions also have physiological effects, possibly due to the exponential temperature dependence of kinetic processes in the cell [116]. One well-studied response is the induction of the heat-shock proteins [113, 117]. These proteins are molecular chaperones, one of their roles being to prevent other proteins from denaturing when under environmental stresses.

While it is still unclear as to the minimum temperature excursion needed to induce responses in the cell, one must try to minimize any such excursions. A common rule of thumb is to keep variations to  $<1\text{ }^\circ\text{C}$ , which is the approximate daily variation in body temperature [116]. Alternatively, one could determine by experiments that imposed temperature loads do not affect the particular pathway being investigated.

### **1.5.2 Direct electric-field interactions**

Electric fields can also directly affect the cells. A simple electrical model of the cell describes it as a membrane-covered sphere consisting of the cytoplasm and the cell membrane (Figure 1-5) [59, 118-121]. The cytoplasm is modeled as a uniform medium with some permittivity and conductivity, while the membrane is described as a shell with the surface electrical properties defined in Eqn. (1-3).

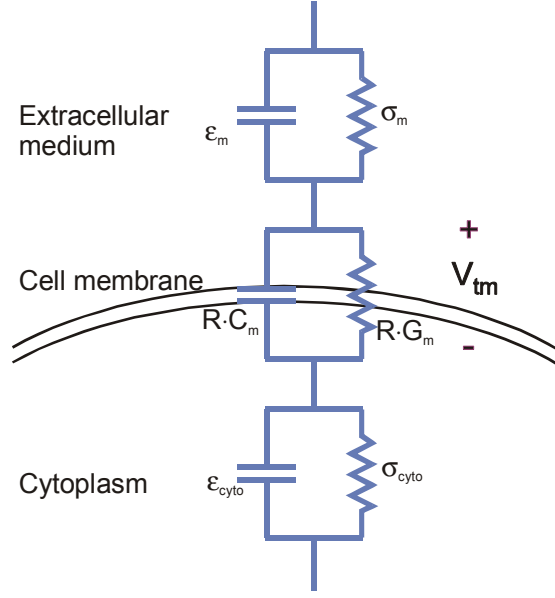


**Figure 1-5:** Electrical model of the cell. The model consists of three capacitor-resistor pairs in series representing the cytoplasm, cell membrane, and extracellular medium. The transmembrane voltage is equivalent to the voltage across the middle capacitor.

By determining where the fields exist in the cell as the frequency is varied, one can determine likely pathways by which the fields could impact physiology. In the model shown in Figure 1-5, the imposed fields can exist across the cell membrane or the cytoplasm. The qualitative electrical behavior of the cell can be explained with reference to this model. The conductance of the cell membrane is usually much smaller than that of the medium and cytoplasm, while the RC-pairs of the medium and cytoplasm usually have similar values. At low frequencies (<MHz) the circuit looks like a resistive divider and because the membrane resistance is large the voltage is primarily dropped across it. This voltage is distinct from the endogenous transmembrane potential that exists in the cell. Rather, it represents the voltage derived from the externally applied field. The total potential difference across the cell would be given by the sum of the imposed and endogenous potentials.

At higher frequencies the impedance of the membrane capacitor comes into play and the voltage across the membrane starts to decrease. Finally, at very high frequencies (100's MHz) the model looks like a capacitive divider and the membrane voltage saturates.

Quantitatively, the imposed transmembrane voltage can be derived as [59]

$$|V_{tm}| = \frac{1.5|\mathbf{E}|R}{\sqrt{1 + (\omega\tau)^2}} \quad (1-10)$$

where  $\omega$  is the radian frequency of the applied field and  $\tau$  is the time constant given by

$$\tau = \frac{RC_m(\rho_{cyto} + 1/2\rho_{med})}{1 + RG_m(\rho_{cyto} + 1/2\rho_{med})} \quad (1-11)$$

where  $\rho_{cyto}$  and  $\rho_{med}$  are the cytoplasmic and medium resistivities ( $\Omega\cdot\text{m}$ ). At low frequencies  $|V_{tm}|$  is constant at  $1.5|\mathbf{E}|R$  but decreases above the characteristic frequency ( $1/\tau$ ). This model does not take into account the high-frequency saturation of the voltage.

At the frequencies used in DEP—10's kHz to 10's MHz—the most probably route of interaction between the electric fields and the cell is at the membrane [122]. There are several

reasons for this. First, electric fields already exist at the cell membrane, leading to transmembrane voltages in the 10's of millivolts ( $V_{tm}$  in Figure 1-5). Changes in these voltages could affect voltage-sensitive proteins, such as voltage-gated ion channels [123]. Second, the electric field across the membrane is greatly amplified over that in solution. From Eqn. (1-10) one gets that at low frequencies

$$|V_{tm}| = \frac{1.5|\mathbf{E}|R}{\sqrt{1+(\omega\tau)^2}} \approx 1.5|\mathbf{E}|R \quad (1-12)$$

$$|E_{tm}| \approx |V_{tm}|/\Delta = (1.5R/\Delta) \cdot |\mathbf{E}|$$

and thus the transmembrane field ( $E_{tm}$ ) is multiplied by a factor of  $1.5R/\Delta$  ( $\sim 1000$ ), which can lead to quite large membrane fields. This does not preclude effects due to cytoplasmic electric fields. However, these effects have not been as intensely studied, perhaps because 1) those fields will induce current flow and thus heating, which is not a direct interaction, 2) the fields are not localized to an area (e.g., the membrane) that is likely to have field-dependent proteins, and 3) unlike the membrane fields, the cytoplasmic fields are not amplified.

Several studies have investigated possible direct links between electric fields and cells. At low frequencies, much investigation has focused on 60-Hz electromagnetic fields and their possible effects, although the studies thus far are inconclusive [124]. DC fields have also been investigated, and have been shown to affect cell growth [125] as well as reorganization of membrane components [126]. At high frequencies, research has focused on the biological effects of microwave radiation, again inconclusively [127].

In the frequency ranges involved in DEP, there has been much less research. Tsong has provided evidence that some membrane-bound ATPases respond to fields in the kHz-MHz range, providing at least one avenue for interaction [122]. Electroporation and electrofusion are other obvious, although more violent, electric field-membrane coupling mechanisms [106].

Still other research has been concerned specifically with the effects of DEP on cells, and has investigated several different indicators of cell physiology to try to elucidate any effects. One of the first studies was by the Fuhr et al., who investigated viability, anchorage time, motility, cell growth rates, and lag times after subjecting L929 and 3T3 fibroblast cells in HBSS to short and long (up to 3 days) exposure to 30-60 kV/m fields at 10-40 MHz near planar quadrupoles [131]. They estimated that the transmembrane load was  $<20$  mV. The fields had no discernable effect.

Another study investigated changes in cell growth rate, glucose uptake, lactate and monoclonal antibody production in CHO & HFN 7.1 cells on top of interdigitated electrodes excited at 10 MHz with  $\sim 10^5$  V/m in DMEM (for the HFN 7.1 cells) or serum-free medium (for the CHO cells) [128]. Under these conditions they observed no differences in the measured properties between the cells and control populations.

Archer et al. subjected fibroblast-like BHK 21 C13 cells to p-DEP forces produced by planar electrodes arranged in a sawtooth configuration [129]. They used low-conductivity (10 mS/m) isoosmotic solutions and applied fields of  $\sim 10^5$  V/m at 5 MHz. They monitored cell morphology, cell doubling time, oxidative respiration (mitochondrial stress assay), alterations in expression of the immediate-early protein fos, and non-specific gene transcription directly after a 15 minute exposure and after a 30-min time delay. They observed 20-30% upregulation of fos expression and a upregulation of a few unknown genes (determined via mRNA analysis). Measured steady-state temperatures near the cells were  $<1$  °C above normal, and their calculated

transmembrane voltage under their conditions was  $<100 \mu\text{V}$ , which should be easily tolerable. The mechanism—thermal or electrical—of the increased gene expression was left unclear. It is possible that artifacts from p-DEP attraction of the cells to the electrodes led to observed changes. Either way, this study certainly demonstrates the possibility that DEP forces could affect cell physiology.

Glasser and Fuhr attempted to differentiate between heating and electric-field effects on L929 mouse fibroblast cells in RPMI to the fields from planar quadrupoles [130]. They imposed  $\sim 40 \text{ kV/m}$  fields of between 100 kHz and 15 MHz for 3 days and observed monolayers of cells near the electrodes with a video microscopy setup, similar to their previous study [131]. They indirectly determined that fields of  $\sim 40 \text{ kV/m}$  caused an  $\sim 2 \text{ }^\circ\text{C}$  temperature increase in the cells, but did not affect cell-division rates. They found that as they increased field frequency (from 500 kHz to 15 MHz) the maximum tolerable field strength (before cell-division rates were altered) increased. This is consistent with a decrease in the transmembrane load with increasing frequency.

Wang et al. studied DS19 murine erythroleukemia cells exposed to fields ( $\sim 10^5 \text{ V/m}$ ) of 1 kHz-10 MHz in low-conductivity solutions for up to 40-min [132]. They found no effects due to fields above 10 kHz. They determined that hydrogen peroxide produced by reactions at the electrode interfaces for 1 kHz fields caused changes in cell growth lag phase, and that removal of the peroxide restored normal cell growth.

In summary, studies specifically interested in the effects of kHz-MHz electroquasistatic fields on cells thus far demonstrate that choosing conditions under which the transmembrane loads and cell heating are small—e.g.,  $> \text{MHz}$  frequencies, and fields in  $\sim 10^5 \text{ kV/m}$  range—can obviate any gross effects. Subtler effects, such as upregulation of certain genetic pathways or activation of membrane-bound components could still occur, and thus DEP, as with any other assay technique, must be used with care.

## **1.6 Scope of the thesis**

The primary concern of this thesis is the development of methods to design DEP traps and implementation of these methods in a proof-of-concept small array as a demonstration of the  $\mu\text{DAC}$ . I have not concerned myself with the other substantial problems involved in developing the cytometer—imaging the cytometer, scaling up the number of traps, or designing the control systems to operate the traps. These are whole theses unto themselves.

In Chapter 2 I will describe the modeling tools that I developed to enable the quantitative design of DEP traps, such as for the  $\mu\text{DAC}$ , as well as the reasoning behind their development. In Chapter 3 I'll present experiments that I performed on a specific trap design—the planar quadrupole—to validate the modeling tools and investigate how that trap works. Once this is done, in Chapter 4 I will demonstrate one use of these modeling tools—for designing trap arrays that can meet the requirements of the cytometer. Chapter 5 describes how I fabricated and packaged these improved trap arrays as well as the setup used for testing them. In Chapter 6 I'll describe experiments with beads designed to validate the extruded trap performance, while in Chapter 7 I'll describe exploratory assays with cells meant to show proof-of-concept operation of the cytometer. I will finish in Chapter 8 with remarks on the significance of the thesis as well as directions for future work.

## Chapter 2: Modeling environment

Now that I have presented an overview of the  $\mu$ DAC project and DEP-based traps, I will describe in this chapter the modeling tools that I developed to allow for quantitative trap design. Most of the description in this and the next chapter will be directed toward planar quadrupole traps as this was the vehicle with which I initially validated the modeling. I will first motivate the need for modeling and then describe the modeling program and some results in detail.

Throughout the chapter there will be references to Matlab commands and the m-files that comprise the modeling environment. They will be displayed in this font.

### 2.1 Motivation

Much DEP-based-trap design to date has been of a qualitative nature, for a variety of reasons. One reason is that many current microscale DEP traps are meant to capture many particles at once. The electrostatic interactions between the many particles in such a trap make it very difficult to quantitatively analyze—although Schnelle et al. [93] performed pioneering work on the validation of the shape of the force fields in these systems. Additionally, traps for large particles (such as cells) are "easy" to make—many electrode configurations and experimental conditions will generate some sort of trapping, and thus detailed analysis may not be necessary. The maturation of microscale DEP-based systems, however, has led to the need for microscale DEP-based systems that effect quantitative functions, such as precise single-cell holding and manipulation. For these applications—such as the  $\mu$ DAC—one needs to *quantitatively understand and design* DEP-based traps.

In order to understand and predict the interaction of forces on particles in these microsystems, I have developed this modeling environment to quantitatively predict the behavior of single particles in DEP-based systems, with particular emphasis on predicting the "strength" of DEP-based cell traps at steady state. *Strength is defined as the ability of a trap to hold a single particle against a fluid flow.* It is the destabilizing flow that will be encountered in our cytometer, and is likely to be the destabilizing force in many cell-based microsystems.

Furthermore, the modeling environment allows for the investigation of multipolar DEP forces (Eqn. (1-7)). Most previous analyses incorporate only the dipole approximation to the DEP force [71, 89], which, while dominating the responses of many systems, does not adequately describe the physical situation at electric-field nulls or where the particle size becomes significant compared to electric field non-uniformities. An important exception is work by Washizu and Jones [133], who used the quadrupolar force order to explain particle size-dependent levitation in quadrupole traps. To extend this work, I have implemented in the modeling environment an iterative algorithm to compute the multipolar DEP forces, trivializing the ability to compute these higher-order force terms, which can now accurately describe the DEP forces in arbitrary electrode geometries.

### 2.2 Overview

An overview of the modeling environment is given in Figure 2-1. It has been written using the Matlab computing environment (R13, The Mathworks, Inc., Natick, MA) to take advantage of the diverse numerical and visualization algorithms available within. The modeling

has undergone approximately five major algorithmic revisions since its inception. Only the final state is detailed here. I originally also wrote code to analyze 2D geometries, but have not continued developing it to the sophistication of the 3D program described herein. The 2D program is simpler and faster to run, however, and could be resurrected if needed.

The modeling environment, though general, has been written expressly to analyze the problem encountered in microscale DEP traps—that of single particles held in such traps against fluid flows, as illustrated in Figure 2-2. In this chapter I will describe its application to planar quadrupole traps. I will show the actual use of this modeling environment for *a priori* trap design in Chapter 4.

The model takes electric-field data and other experimental parameters and computes the total force on the particle everywhere in space. From this, zero-force isosurfaces are constructed, one for each force component, to determine where the forces in each direction are zero. (An isosurface is the three-dimensional equivalent of a contour line.) The modeling environment then looks for intersections of these three zero-force isosurfaces, which correspond to locations where the total force on the particle is zero and thus where the particle can be held. These points are called holding points and by varying the applied flowrate for a given experimental condition, the modeling environment can determine when the holding points cease to exist and therefore the strength of the DEP particle trap.

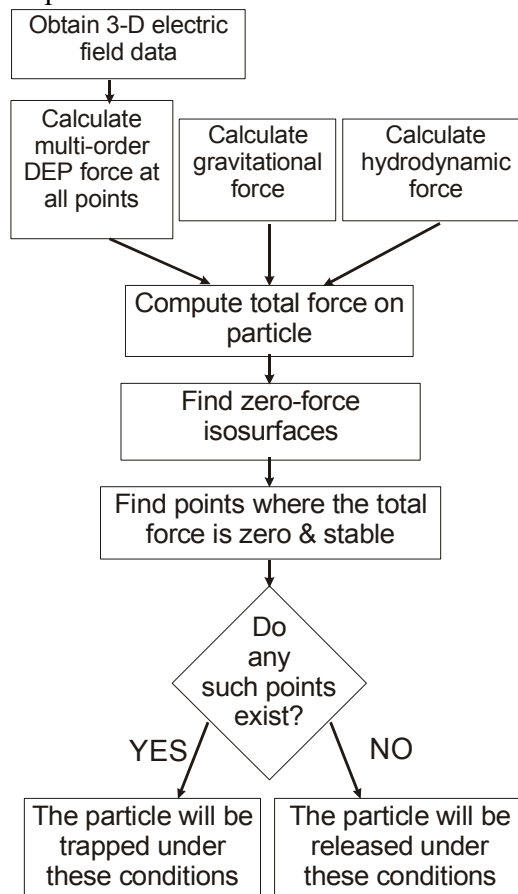


**Figure 2-1:** Overview of modeling environment, showing the major steps. From user-provided electric field data and other experimental parameters, the forces on the particle (DEP, HD drag, and gravitation) are computed in all space and the zero-force isosurfaces are determined. Following this, points of zero net force are searched for. If they exist, they can represent holding points for particles in traps.

## 2.2.1 Model Parameters

Unless specified otherwise, all simulations performed in this chapter had the following parameters. The voltage was 1 V, the particles were beads with a density of  $1.062 \text{ gm/cm}^3$ , the solution relative permittivity was 80 (water), the solution conductivity was  $0.01 \text{ S/m}$ , the bead relative permittivity was 2.5, the bead conductivity was  $0.2 \text{ mS/m}$ , the bead radius was  $5 \text{ }\mu\text{m}$ , the flow chamber height was  $0.73 \text{ mm}$  and its width was  $7 \text{ mm}$ . These parameters approximate the situation used in the validation experiments of Chapter 3.

## 2.2.2 Electric field calculation

Many methods exist to calculate electric fields in electroquasistatic systems. Some of the commonly used electrode geometries have analytical solutions, such as the point quadrupole and octopole, the cone-plate geometry [87], and the polynomial electrodes [134]. Other commonly used geometries, such as the interdigitated electrodes, have been solved using commercial field solvers [75]. Still other approaches have involved developing efficient algorithms to calculate the electric fields in two and three dimensions [71, 89, 135-137]. Due to the diversity of methods available to obtain the electric fields in these systems, I have developed the modeling tools to "assume" that the fields are known, and therefore allow the user to calculate the electric fields any way they wish.

The modeling environment computes all quantities on a regularly spaced grid, and so requires that electric field data be given in a regularly spaced grid in all space. The field data can be obtained from any source that can generate such data. Since the DEP force calculations involves taking multiple derivatives of the field variables (Eqn. (1-8)), care must be taken to obtain fine-enough simulation results in order to minimize errors.

I have successfully used field data from both the commercial FEM solver Maxwell 3D (Ansoft, Pittsburgh, PA) and the commercial BEM solver Coulomb3D (Integrated Engineering Software, Winnipeg, Canada). For the planar quadrupole electrode structure shown in Figure 2-2 (discussed in this and the next chapter) I used results from Maxwell 3D. Using this simulator, one can export field solutions into an ASCII file and use subroutines to massage the data into a matrix form that the program can handle (dload3). I simulate only the upper-half of the trap, using symmetry boundary conditions at the glass substrate. Field data from the central portion of

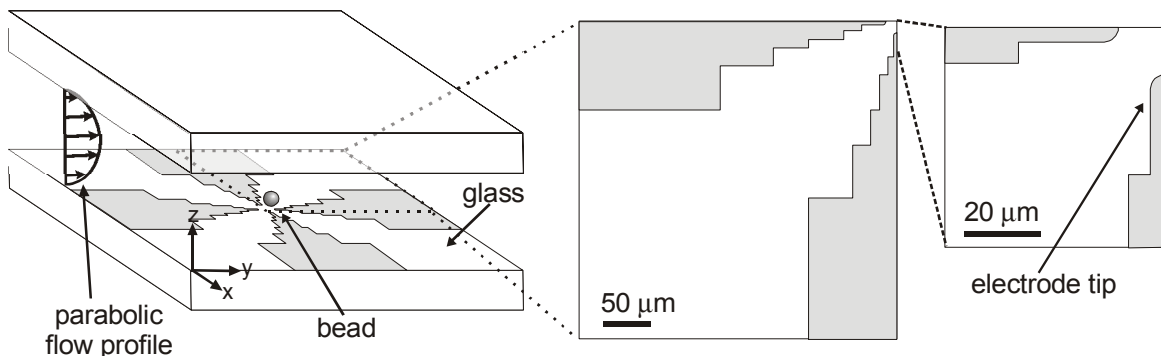


**Figure 2-2:** Schematic of simulated planar quadrupole geometry. Shown is central portion of the planar quadrupole, which is driven with 180-degree out-of-phase alternating voltages on adjacent electrodes. The gap between opposite electrodes is  $24 \text{ }\mu\text{m}$ , while the radius of curvature of the electrode tip is  $4 \text{ }\mu\text{m}$ . The electrodes increase in width away from the electrode tip to reduce resistive losses, with a final width of  $500 \text{ }\mu\text{m}$ . A bead, trapped at the electrode gaps, will experience the DEP forces, HD drag forces from the parabolic flow profile, a gravitational force due to its weight, and, if it is on the substrate surface, an upward force due to the substrate.

the quadrupole is written to a grid, using a grid spacing of 0.5-2  $\mu\text{m}$ , and smoothed using a Gaussian low-pass filter. Simulations are run using a 1V potential difference between electrodes and field results for other voltage differences are obtained by linearly scaling the electric field to different voltages, using the linearity of the electric field with voltage.

In Figure 2-3 I plot the electric field intensity at various heights above the substrate. One sees the circular contours of the familiar quadrupole field near the origin and its perturbation near the electrodes, which lessens as the height above the substrate is increased.

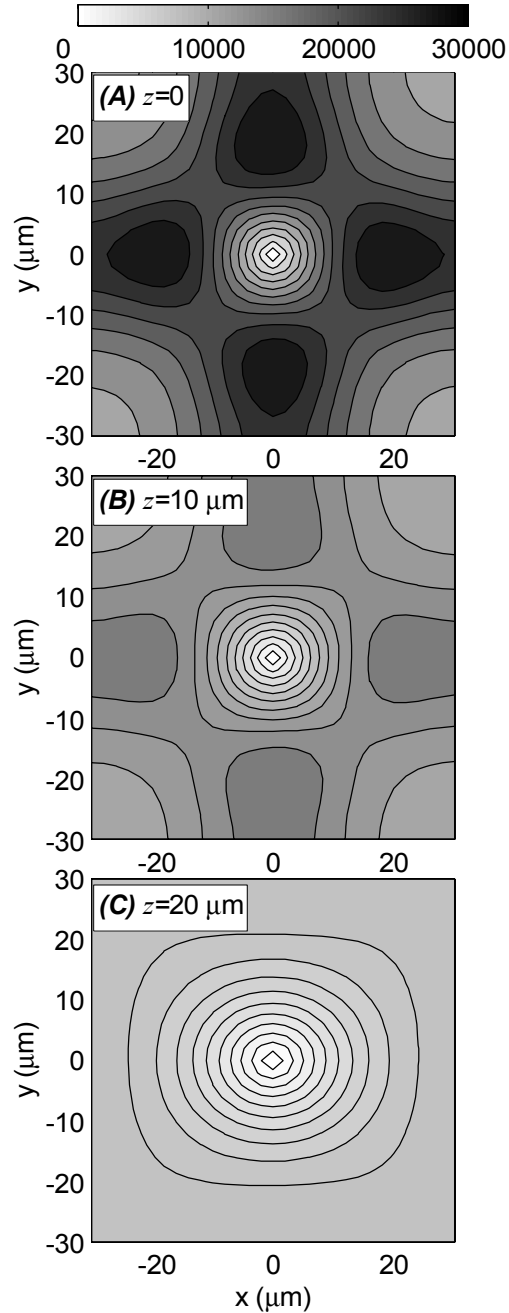


**Figure 2-3:** Plots of the electric field intensity for the quadrupole geometry shown in Figure 2-2 at various heights above the substrate for 1 V applied to the electrodes. The heights are 0 (A), 10  $\mu\text{m}$  (B), and 20  $\mu\text{m}$  (C).

### 2.2.3 DEP force calculation

To calculate the full multipolar DEP force, the program (depforce3) uses the induced-multipole theory developed by Jones and Washizu [61] and shown in Eqns. (1-7) and (1-8). The CM-factor is calculated using the solutions for either a solid dielectric sphere (Eqn. (1-9))—to model plastic beads—or a dielectric shell—to model cells—using expressions from the literature [58].

To allow for an iterative force calculation algorithm, I need to catalog the multiple derivatives of the electric field, which are evaluated using nested loops. I do this with 6-dimensional matrices for the electric field and its derivatives arranged as  $E(x,y,z,p,q,r)$  where  $p$ ,  $q$ , and  $r$  correlate to the number of derivatives of the electric field taken in the  $x$ ,  $y$ , and  $z$  directions, respectively. Since Matlab only allows non-zero addressing into matrices, the following scheme is used

$$\begin{aligned}
 E(x,y,z,2,1,1) &= E_x \\
 E(x,y,z,1,2,1) &= E_y \\
 E(x,y,z,1,1,2) &= E_z \\
 E(x,y,z,2,2,1) &= \frac{\partial E_x}{\partial y} = \frac{\partial E_y}{\partial x} \\
 E(x,y,z,3,1,2) &= \frac{\partial^2 E_x}{\partial x \partial z} = \frac{\partial^2 E_z}{\partial x^2} \\
 &\vdots
 \end{aligned} \tag{2-1}$$

The algorithm for generating the field derivatives is

```

for in=2:nmax
  for p=1:in
    for q=1:(in-p+1)
      r = in - (q + p) + 2;
      [E(:,:,,p+1,q,r),E(:,:,,p,q+1,r),E(:,:,,p,q,r+1)] = gradient(E(:,:,,p,q,r),dx,dy,dz);
    end
  end
end

```

Here,  $n_{max}$  refers to the number of force orders to calculate, and  $dx$ ,  $dy$ , and  $dz$  refer to the spacing of the field grid.

The DEP force calculation algorithm is given by

$$\begin{aligned}
F_0^{(n)} &= \frac{2}{(n-1)!(2n-1)!!} \pi \epsilon_1 R^{2n+1} \operatorname{Re}[CM^{(n)}] \\
\langle F_1^{(i)} \rangle, \langle F_2^{(i)} \rangle, \langle F_3^{(i)} \rangle &= 0 \\
\text{for } i &= 1 \text{ to } n \\
\text{for } p &= 0 \text{ to } n \\
\text{for } q &= 0 \text{ to } (i-p) \\
r &= i - (p + q) \\
\langle F_1^{(i)} \rangle &= \langle F_1^{(i)} \rangle + F_0^{(i)} E(x, y, z, p+1, q+1, r+1) E(x, y, z, p+2, q+1, r+1) \\
\langle F_2^{(i)} \rangle &= \langle F_2^{(i)} \rangle + F_0^{(i)} E(x, y, z, p+1, q+1, r+1) E(x, y, z, p+1, q+2, r+1) \\
\langle F_3^{(i)} \rangle &= \langle F_3^{(i)} \rangle + F_0^{(i)} E(x, y, z, p+1, q+1, r+1) E(x, y, z, p+1, q+1, r+2) \\
\text{end; end; end}
\end{aligned} \tag{2-2}$$

where  $F_0^{(n)}$  is a constant calculated once. For the systems described in this thesis, the electric fields are real and so I do not need to worry about complex values except for the CM factor. The resulting forces are stored in five-dimensional arrays.

This iterative DEP force calculation is one of the strengths of the modeling environment because it makes it simple to compute multipolar DEP forces in all space. From the electric field data in Figure 2-3 I can easily obtain the vector force field plots of Figure 2-4, which show the in-plane components of the calculated DEP forces on a polystyrene bead, up to  $n=2$ , at the same heights as Figure 2-3. One can see that a particle will be brought to and trapped at the  $z$ -axis (with no fluid flow) as long as it is brought within a certain distance ( $\sim 20 \mu\text{m}$  for Figure 2-4B) of the origin.

## 2.2.4 Other forces

The modeling includes three other forces—the gravitational force, the hydrodynamic (HD) drag force on the particle, and a rigid substrate bottom boundary. The magnitude of the gravitational force is given by

$$F_{grav} = \frac{4}{3} \pi R^3 (\rho_p - \rho_m) g \tag{2-3}$$

where  $\rho_m$  and  $\rho_p$  refer to the densities of the medium and the particle, respectively, and  $g$  is the gravitational acceleration constant. Cells and beads are denser than the medium and thus have a net downward force.

The HD drag force imposed on a stationary particle by a moving fluid is governed by the creeping flow approximation because of the small dimensions and low flow rates involved in these microsystems. For these simulations I have used a self-consistently solved analytical formulation for the drag force on a stationary sphere in shear flow [138] or plane Poiseuille flow [139]. Other solved flow profiles could be implemented. Although parabolic Poiseuille flow (from parallel-plate flow chambers) is often used with DEP traps, the shear flow approximation is justified when the levitation height and particle radius are much less than the height of the chamber. The HD drag force has the general form of the Stokes drag on a sphere

$$F_{drag} = 6\pi\eta R \cdot (4U_c/h) \cdot F_{drag}^* \cdot z \tag{2-4}$$

where  $\eta$  is the viscosity of the fluid,  $U_c$  is the fluid velocity at the channel midline,  $h$  is the channel height,  $F_{drag}^*$  is a non-dimensional factor incorporating the wall effects, and  $z$  is the height of the center of the sphere. I also calculate flow-induced lift forces on the particle, although I do not incorporate them into the force balance because they are much smaller than other forces in this system. It would be trivial to incorporate them for other system designs.

The final "force" is the implementation of a rigid bottom boundary defined by the substrate. This lets me simulate particles sitting on the substrate surface. To do this I automatically adjust the  $z$ -directed total force on the particle so that it is zero (or positive) when

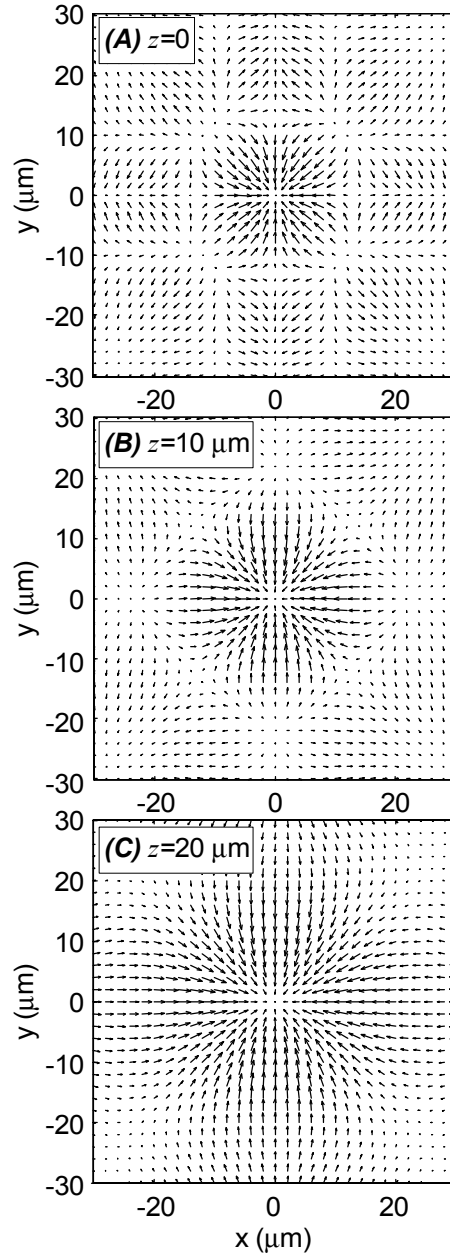


**Figure 2-4:** Plots of the DEP force (up to  $n=2$ ) in the  $x$ - $y$  plane derived from the electric field pictured in Figure 2-3 at heights of 0 (A), 10  $\mu\text{m}$  (B), and 20  $\mu\text{m}$  (C). The  $z$ -directed DEP forces are not shown here (for clarity). Note that the arrow length in each plot is scaled independently.

the particle is sitting on the substrate.

### 2.2.5 Holding point determination

At this point, I have calculated the total force experienced by the particle in all of space for a given electrode geometry and a given set of conditions (Figure 2-1). Now I must determine whether the particle can indeed be held by the trap in this circumstance. To do this, the program must find points in space (called holding points) where the particle experiences zero net force. These are the only points where one can expect to find a particle (at steady state). If I then increase the destabilizing fluid forces and determine when the holding points cease to exist, I can compute the strength of the trap.

The algorithm proceeds as follows. For each of the three total-force components ( $F_x$ ,  $F_y$ ,  $F_z$ ) the program finds the surface where that force component is zero—the zero-force isosurface. Once it has the three isosurfaces, it must find where they intersect to find points where the net force is zero—holding points. I implement this by checking for three-way intersections among the polygons comprising the surfaces. Since the majority of the polygons comprising each surface will be too far away from each other to possibly intersect, the program first does a quick check to exclude such pairings. This reduces the number of computationally intensive operations. The program performs this quick check by first looking for possible intersections between polygons comprising the isosurfaces of two force components. Then it takes the polygons of those two isosurfaces that might be intersecting and checks them against the third isosurface. This produces a set of polygons that represent areas where the three surfaces might be intersecting. It then performs computations on this set of polygons to determine whether any three-way intersection points actually exist and whether they are stable holding points.

#### *Finding zero-force isosurfaces (asspol)*

The isosurfaces are easily computed in Matlab using the `isosurface` command. This returns a set of triangles (known as patches) that comprise the surface. To keep the number of triangles reasonable, I first limit the volume within which the isosurfaces are computed with the `reducevolume` command. This requires knowing where the surfaces are likely to intersect, i.e., where the region of interest is. This is not usually a problem—one simply runs coarse simulations covering the full volume and then refines. The second tactic that I use to limit the number of triangles is to limit the number of faces in the surface with the `reducepatch` command. This command reforms the isosurface with fewer patches while trying to minimize any errors. I usually use 700 patches (triangles) per isosurface.

Examples of the three isosurfaces for the planar quadrupole are shown in Figure 2-5. The  $F_x=0$  (Figure 2-5A) and  $F_y=0$  (Figure 2-5B) isosurfaces are predominately composed of planes at  $x=0$  and  $y=0$ , respectively. In fact, due to the symmetry of this electrode configuration, the two isosurfaces are the same, just rotated 90-degrees with respect to each other. This makes sense in the context of Figure 2-4 where one sees that the  $x$ -directed DEP force is zero at the  $x=0$  plane, and that the  $y$ -directed DEP force is zero at the  $y=0$  plane. The symmetry in the  $F_x=0$  and  $F_y=0$  isosurfaces will disappear when an  $x$ -directed flow is imposed. The other parts of the isosurfaces in these plots represent other regions where those force components are zero. However, subsequent analysis, such as by examining Figure 2-4, shows that these correspond to unstable force minima; particles at those points would not be stably held. Figure 2-5C shows the  $F_z=0$  isosurface, which is cone-shaped. In Figure 2-5D one sees a closeup of the three isosurfaces superimposed, showing the putative holding point located at  $(x,y,z) = (0,0,12 \mu\text{m})$ .

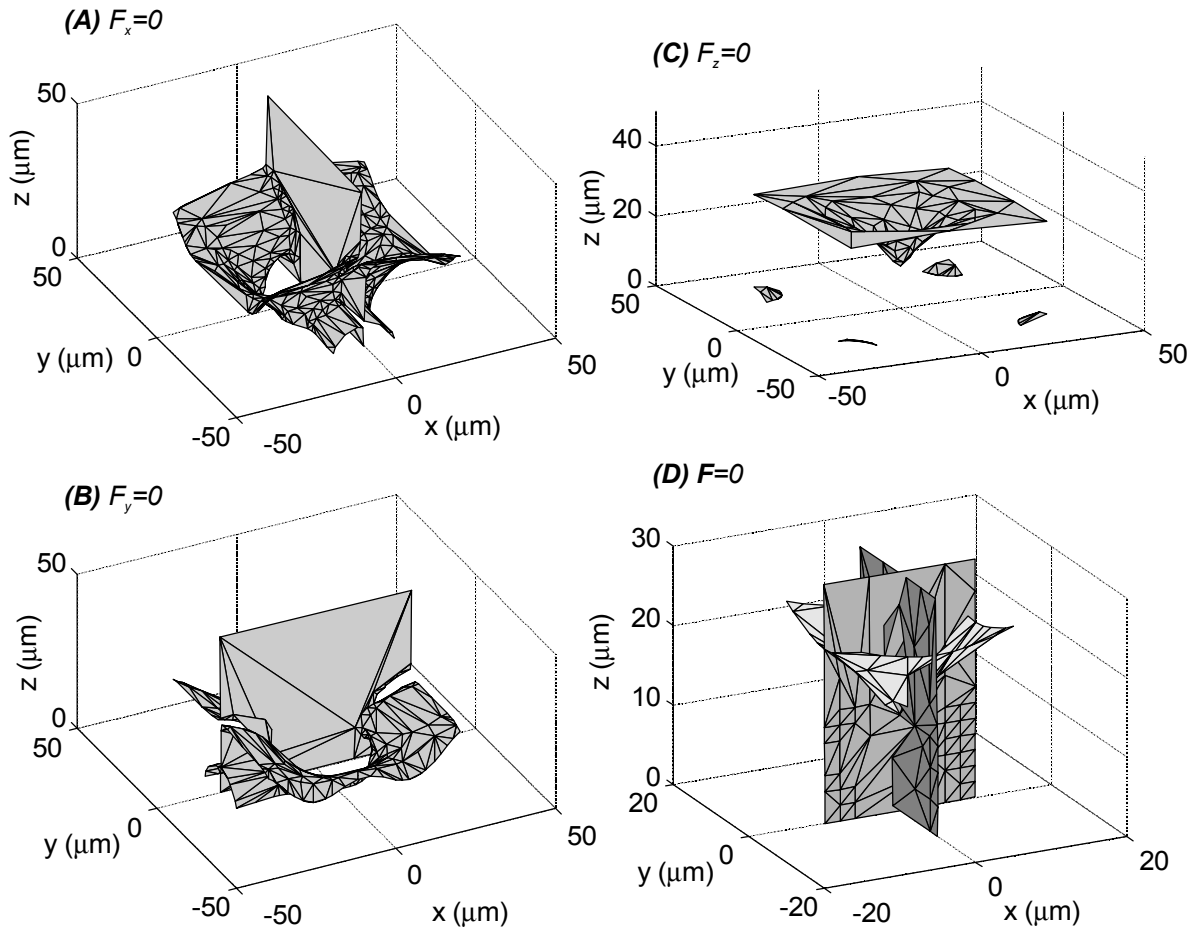


**Figure 2-5:** Zero-force isosurfaces. Shown are the three isosurfaces corresponding to the  $F_x=0$  (A),  $F_y=0$  (B), and  $F_z=0$  (C) isosurfaces calculated from the electric fields in Figure 2-3, when no flow is applied. Panel D shows a close-up of the intersection of the three isosurfaces, illustrating the existence of a holding point at  $(x,y,z)=(0,0,12 \mu\text{m})$ .

#### *Finding possible two-way intersections (asspol)*

Now that the three isosurfaces have been computed, I need to check them against each other to find the intersection point. As stated above, this is first done by performing a quick check for possible intersections and then checking those possible intersection points. The first stage of the quick check is to check two surfaces against each other (checkpol2). Since the vast majority of the patches making up the two sets of isosurfaces won't intersect, I first do a gross test to winnow down the list of possibly intersecting patches (checkpol, minmax). This test, called a bounding box test, is well known in computer graphics and is illustrated in two dimensions in Figure 2-6. Basically, if two patches' bounding boxes do not intersect, then the two patches cannot intersect.

To optimize the algorithm for Matlab, I tried to remove for loops and replace them with vectorized operations. In addition, keeping all variable sizes small enough to fit into memory (without writing to disk) keeps the algorithm fast. My approach was to create large matrices—called minmax matrices—representing all possible two-way combinations from a pair of surfaces. Thus, if one surface had  $n$  triangles and the other had  $m$  triangles then each matrix (one for each surface) would have  $m \cdot n$  rows. Each row contains the extreme coordinates of each

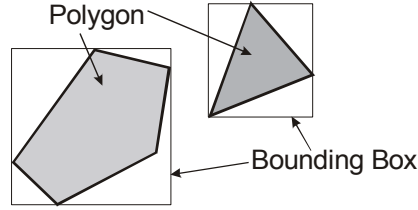


**Figure 2-6:** Bounding box algorithm in two dimensions. If the bounding boxes of the two patches do not intersect, then the patches cannot intersect. Extension to three dimensions only involves checking one more dimension. In the program, the two polygons are actually both triangles.

triangle—e.g., the maximum  $x$ -coordinate of the triangle, the minimum  $x$ -coordinate of the triangle, etc. Since these matrices could get very large, the program can chop up the surfaces to make smaller comparisons if necessary. These minmax matrices are set up in such a way as adding two corresponding rows together and checking the sign of the result performs the bounding box comparison. The final step is to look through the list of comparisons to find ones that meet the test, and export those as a new matrix ready for the set of three-way comparisons.

*Finding possible three-way intersections (asspol)*

At this point I have a matrix where each row is a pair of possibly intersecting patches. The first patch of each pair is compared against the third isosurface using the bounding-box algorithms to find possible three-way intersections. The result is a matrix where each row contains the coordinates of triangles that might intersect.

*Finding intersection points (findint)*

The final step is to check if these possible intersections actually intersect. Using the bounding-box algorithms to minimize the number of intersections that actually need to be checked greatly reduces execution time since this final step is computationally intensive. Essentially, the algorithm finds the intersection point of the three triangles and determines whether the intersection point actually lies within all three triangles. Only points that lie within all three triangles represent zero-force points.

The intersection point of three planes is given by [140]

$$\begin{aligned}
 \text{plane 1: } & A_1x + B_1y + C_1z + D_1 = 0 \\
 \text{plane 2: } & A_2x + B_2y + C_2z + D_2 = 0 \\
 \text{plane 3: } & A_3x + B_3y + C_3z + D_3 = 0
 \end{aligned}$$

$$x = -\frac{1}{\Delta} \begin{vmatrix} D_1 & B_1 & C_1 \\ D_2 & B_2 & C_2 \\ D_3 & B_3 & C_3 \end{vmatrix}, y = -\frac{1}{\Delta} \begin{vmatrix} A_1 & D_1 & C_1 \\ A_2 & D_2 & C_2 \\ A_3 & D_3 & C_3 \end{vmatrix} \tag{2-5}$$

$$z = -\frac{1}{\Delta} \begin{vmatrix} A_1 & B_1 & D_1 \\ A_2 & B_2 & D_2 \\ A_3 & B_3 & D_3 \end{vmatrix}, \Delta = \begin{vmatrix} A_1 & B_1 & C_1 \\ A_2 & B_2 & C_2 \\ A_3 & B_3 & C_3 \end{vmatrix}$$

$\Delta$  will be zero if the three planes intersect in a straight line or not at all.

For each polygon, the code takes the three vertices and computes the  $A$ ,  $B$ ,  $C$ , and  $D$  coefficients for the plane formed by those vertices. The conversion between the  $A$ ,  $B$ ,  $C$ , and  $D$  coefficients and the coordinates is given by

$$A = \begin{vmatrix} y_1 & z_1 & 1 \\ y_2 & z_2 & 1 \\ y_3 & z_3 & 1 \end{vmatrix}, B = \begin{vmatrix} z_1 & x_1 & 1 \\ z_2 & x_2 & 1 \\ z_3 & x_3 & 1 \end{vmatrix}, C = \begin{vmatrix} x_1 & y_1 & 1 \\ x_2 & y_2 & 1 \\ x_3 & y_3 & 1 \end{vmatrix}, D = - \begin{vmatrix} x_1 & y_1 & z_1 \\ x_2 & y_2 & z_2 \\ x_3 & y_3 & z_3 \end{vmatrix} \quad (2-6)$$

where  $x_n$ ,  $y_n$ , and  $z_n$  refer to the coordinates of each vertex. This generates three planes (one for each polygon).

The program then computes  $\Delta$  and checks to see if it is zero. If it is not zero, it calculates the intersection point. The task now is to find the subset of intersection points that lie within all three polygons; only these represent intersections between the zero-force isosurfaces. Checking whether a point is in a polygon is another classic computational geometry problem. The particular algorithm I use was obtained from [141] (pnpoly2). As shown in Figure 2-7, the algorithm goes around the polygon and checks to see if the point is always on the same side of each line segment. For convex polygons, this will be true if the point is inside the polygon. Practically, this is done by computing the cross product between the line segment of the polygon and the vector formed by the point and one of the line segment's vertices. If this cross product always has the same sign, then the point is inside the polygon.

Unfortunately, the point-in-polygon test will not necessarily judge points on the vertices or sides of the polygon to be inside the polygon. Therefore, if a point is deemed to not be in the polygon, the program tests to see if the point is "near" the polygon. The near distance is set to  $10^{-4} \mu\text{m}$ . The code determines the perpendicular distance from the point to each line segment, makes sure that this perpendicular intersection point is "within" the line segment, and then uses the perpendicular distance to see if the point is "close" to the line segment. If it is, then the point is deemed inside the polygon.

The point-in-polygon routine only works in two dimensions. To account for this, I wrote a set of operations to rotate each polygon and point onto the  $xy$ -plane to remove the 3<sup>rd</sup> dimension (rotatept). This is done by picking the three vertices and computing the surface normal and tangent. Each point is then transformed according to the following

$$\mathbf{n} = \frac{(\mathbf{p3} - \mathbf{p2}) \times (\mathbf{p3} - \mathbf{p1})}{|(\mathbf{p3} - \mathbf{p2}) \times (\mathbf{p3} - \mathbf{p1})|}$$

$$\mathbf{x}_p = \frac{\mathbf{p3} - \mathbf{p1}}{|\mathbf{p3} - \mathbf{p1}|} \quad (2-7)$$

$$\mathbf{y}_p = \mathbf{n} \times \mathbf{x}_p$$

$$\mathbf{p}' = [\mathbf{x}_p \quad \mathbf{y}_p \quad \mathbf{n}] [\mathbf{p}]$$

where  $\mathbf{p1}$ ,  $\mathbf{p2}$ , and  $\mathbf{p3}$  are the three points in the polygon,  $\mathbf{p}$  are all the points in the polygon, and

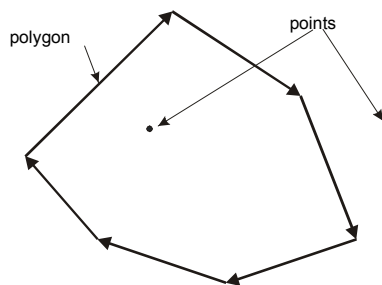


**Figure 2-7:** Schematic of point-in-polygon tests. The point inside the polygon is always to the right of the vectors, whereas the point outside the polygon is sometimes to the left and sometimes to the right.

$\mathbf{p}'$  are the rotated points.

The code finally returns a set of points describing the intersection of the three isosurfaces. Due to the way in which the bounding-box comparisons were made earlier, the intersection-finding routine often generates multiple identical points. Another m-file (expts) takes these points and returns only unique points.

The last important thing to check is whether the zero-force points represent stable force minima (minpts). To check this, I have implemented an algorithm that determines whether  $\mathbf{F} \cdot d\mathbf{r} < 0$  for each direction away from a putative holding point [142]. This essentially checks whether the particle needs to perform work on the system in order to move away from the zero-force point, in which case the point is stable. Other more heuristic methods, such as volume exclusion, are also used.

## 2.2.6 Holding force simulation

An overall program (hforce3) is wrapped around the above code to determine the end variable—usually the flowrate needed to release the particle, which I call the release flowrate. The program varies the flowrate in the model to find the threshold where no holding points exist. That threshold flowrate is the release flowrate and is found using a simple relaxation algorithm. The holding force can then be easily extracted from the release flowrate.

A schematic of the algorithm is shown in Figure 2-8. The code involves two loops, one inside the other, letting me cycle through two sets of initial conditions—for instance, sweeping the bead diameter while also varying the applied voltage. The program only increments to the next set of conditions when the current set has converged. For each set of conditions, it goes through a loop, guessing at the release flowrate until it finds it. The first time through the loop, the program calculates all the field variables, while it only calculates the variables that change with flowrate during subsequent iterations. Also during subsequent iterations, the program only looks for three-way possibly intersecting polygons—it reuses the two-way polygons from the non-changing force directions ( $F_y$  and  $F_z$ ). Both of these strategies greatly diminish the execution time. After all field variables are calculated and possibly intersecting polygons found, the program finds the holding points, if any exist. Then the program takes this information and feeds it to the relaxation algorithm, which decides if this is indeed the release flowrate. If it is then the program records interesting values and increments to the next set of conditions. If not, the relaxation algorithm generates a new guess to try the next time.

The relaxation program (relax) implements a simple bisection algorithm with some modifications. The program asks a series of questions to determine the particular situation that it is in and then takes appropriate action (Figure 2-9). First, it tests to see if it has found the release flowrate by looking at the current and previous guesses and seeing if they are close enough to each other (within some tolerance). If it has converged, then all is well and it tells that to the holding force program. If it hasn't, then it must decide whether it has overshoot or undershot the release flowrate. This is done by looking to see if there are any holding points. If there are, then it means that the flowrate is not high enough. If there aren't any, then it means that it has overshoot the flowrate. Once it knows if it is too high or too low, it must determine a new suitable guess. It does this by first looking to see if there is a "good" previous guess. If so, then it means that the actual answer lies somewhere between the current guess and the previous guess. It simply bisects the two for the next guess. If it has never found a good guess, then it means that it hasn't approached the critical region yet, and so must keep hunting. If it is too high, it divides the previous guess by a factor, usually between 1.3 and 2. If it is too low, then it multiplies by

the same factor. If it is too high, it also must check to make sure that it is at a reasonable value. If it falls below some absolute minimum, then it means that for this particular situation, no holding force exists. In this case, the program just moves to the next set of conditions. This most often happens at the voltage extremes, depending on the geometry.

### 2.2.7 Effect of particle density and fluid flow on isosurfaces

To illustrate the use of the modeling environment for understanding physical phenomena in these microsystems, I address two trends—changes in particle density and the addition of fluid flow (HD drag forces). Figure 2-10 shows the effect of particle density (and thus weight) on the  $F_z=0$  isosurface (which is the only one affected). As the particle density is increased from 1.020 g/cm<sup>3</sup> (Figure 2-10A) to 1.250 g/cm<sup>3</sup> (Figure 2-10C), the particle weight would increase, and from Eqn. (2-3), one would expect the particle to be levitated at lower heights. Observing Figure 2-10, one sees that this is indeed the case. Two important features are apparent. First, the whole isosurface decreases in height, corresponding to lower levitation heights, as expected. Second, at some critical particle density, the cone of the isosurface will reach  $z=5 \mu\text{m}$  (and flatten), whereupon the particle (with  $R=5 \mu\text{m}$ ) will no longer be levitated (Figure 2-10C). This shows

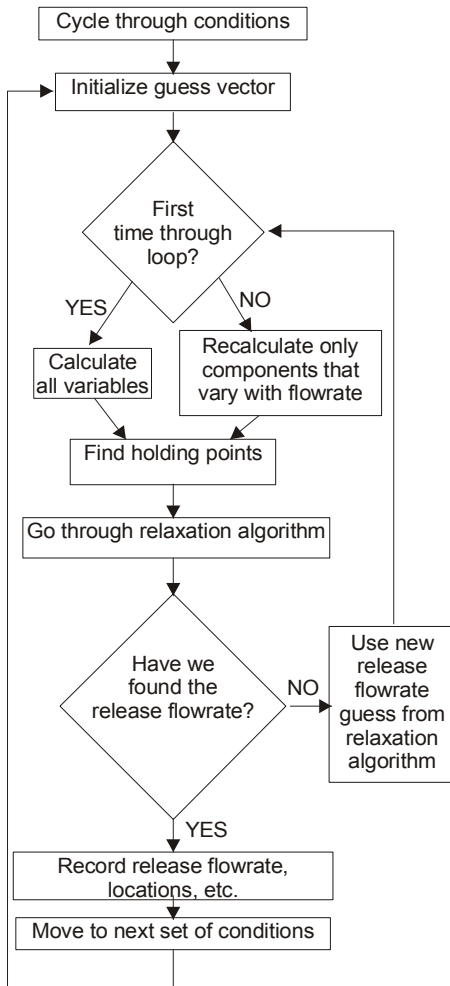


Figure 2-8: Flowchart for holding force program.

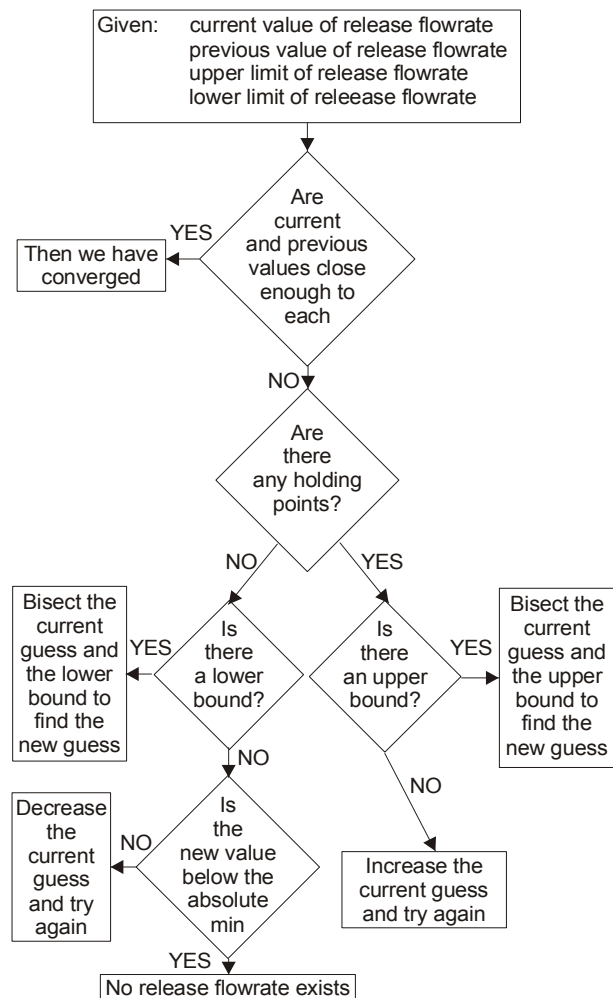
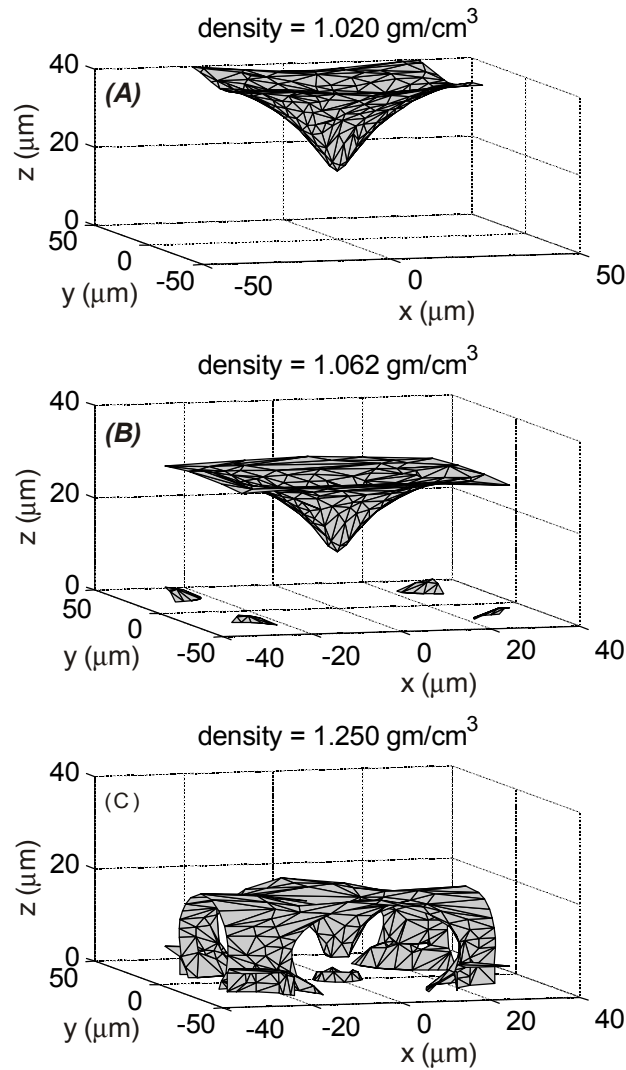


Figure 2-9: Flowchart for relaxation program.

the effect of the bottom boundary “force” that I have implemented.

One also sees that a sharp edge is produced where the  $F_z=0$  isosurface cone flattens into a plane in Figure 2-10C. This will cause difficulties in the holding point extraction, as discussed below.

The effect of fluid flow is important to understanding how these traps work, as fluid flow is *the* destabilizing force that encountered in most DEP-based traps. When fluid flow in the  $x$ -direction is imposed, only the  $F_x=0$  isosurface is affected. In Figure 2-11 I show the effect of fluid flow by examining the intersection of the  $F_x=0$  and  $F_z=0$  isosurfaces as the flowrate is increased. In Figure 2-11A, I show the isosurfaces under conditions of no flow. This is similar to the situation depicted in Figure 2-5D, except that now the  $F_y=0$  isosurface is not shown because it will consist of an  $x$ - $z$  plane at  $y=0$  that will be unaffected by changes in an  $x$ -directed HD drag force. One sees that the  $F_x=0$  isosurface “bends” over as the flow is increased (Figure 2-11B-C), because the HD drag force increases with height (see Eqn. (2-4)), causing the region where  $F_x=0$  to move to  $x>0$ . However, for moderate flows (Figure 2-11B), the two



**Figure 2-10:** The effect of particle density on the holding points. Shown are the results of three simulations where the particle density is varied from 1.020 gm/cm<sup>3</sup> (A) to 1.062 gm/cm<sup>3</sup> (B) to 1.250 gm/cm<sup>3</sup> (C). Only the  $F_z=0$  isosurface is shown.

isosurfaces (and also the  $F_y=0$  isosurface) will still intersect, and thus a holding point will exist and the particle will be held. At a certain threshold flowrate, the  $F_x=0$  isosurface will "bend" over so far as to no longer intersect the  $F_z=0$  isosurface (Figure 2-11C). At this point, no three-way isosurface intersections will exist. Thus, no holding points will exist and the particle will be liberated from the trap. This is the release flowrate, and the corresponding force is the holding force of the trap.

In the case illustrated one sees that the release flowrate is  $\sim 10 \mu\text{l}/\text{min}$  (Figure 2-11C). If I vary the applied voltage the release flowrate will vary because the DEP forces and levitation height will both vary. Predicting and the measuring the relationship between the applied voltage

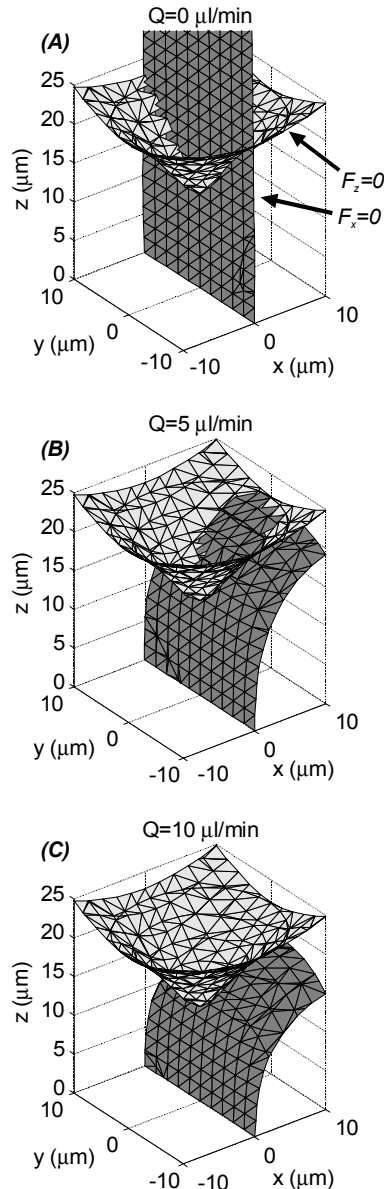


**Figure 2-11:** The effect of flow on the holding points. Shown are the results of three simulations where the volume flow rate ( $Q$ ) is varied from  $0 \mu\text{l}/\text{min}$  (A) to  $5 \mu\text{l}/\text{min}$  (B) to  $10 \mu\text{l}/\text{min}$  (C). Only the  $F_x=0$  and  $F_z=0$  isosurfaces are shown because the  $F_y=0$  isosurface is a flat sheet in the  $y$ - $z$ -plane at  $x=0$  (see Figure 2-5B) and does not vary with applied flow. The highest flowrate (C) corresponds to the release flowrate, since it is the threshold at which the three isosurfaces no longer intersect and thus no longer generate holding points.

and the release flowrate forms a good method to validate the model, which is what I have done in Chapter 3.

## **2.3 Discussion**

### **2.3.1 Modeling environment**

The various manipulations performed, starting with the electric field and experimental parameters, show the utility of the type of integration that I have chosen for these simulations and the suitability of the modeling environment for the design of microscale DEP-based traps. With this design tool, I can now quickly evaluate different designs using a combination of interactive and automatic means.

The interactivity comes from the combination of Matlab's numerical and visualization capabilities with the modeling environment, and lets me simultaneously investigate the various fields and forces on particles. One can, for instance, jump quickly from the zero-force isosurfaces (Figure 2-5) to the force plots (Figure 2-4) to determine whether zero-force points represent holding points by examining the directions of the force arrows around the zero-force points.

In addition to these interactive possibilities, the automatic computation of the release flowrate allows one to run comparative analyses of different traps rather easily. In large measure, this is enabled by the iterative DEP force calculation, which trivializes the ability to compute multipolar DEP forces in all space. This is needed for either highly symmetric, small, or complicated trap geometries. Highly symmetric traps, such as the quadrupole described here, have symmetries that necessitate higher-order moments to properly explain levitation, even in the limit of large traps, as was recognized in 1993 [133]. This is illustrated in the cone-shaped  $F_z=0$  isosurface of Figure 2-5C. The isosurface minimum at the origin corresponds to the field null, where the dipole term in the DEP force goes to zero and the quadrupolar force order dominates. Computing only the dipole force order would give an  $F_z=0$  isosurface that instead of being cone-shaped would look like a cylinder near the origin and never intersect the  $z$ -axis; such an isosurface would not predict levitation.

While highly symmetric traps always need multipolar force calculations, the modeling environment enables the designer to design arbitrary traps—unencumbered by the need to keep the particle much smaller than the field non-uniformities. Analytical approaches, such as undertaken by Washizu and Jones [133], while effective for the simple quadrupole geometry and providing analytical representations of the various parameter dependencies, would be difficult to extend to these situations. Arbitrary trap design has two benefits. One is for single-cell traps. As traps are scaled down to the size necessary to trap single cells, the cells invariably become a significant fraction of any characteristic dimension, and thus quadrupolar and higher-order moments may come into play. The other is for non-analytical electrode geometries, which can shape the electric field or introduce steric effects for more effective trapping. Both of these approaches could be implemented with extruded quadrupole traps. Non-analytical effects are even seen in the planar quadrupole structures, which, although well approximated near the origin by four point charges, deviate significantly from the point-charge quadrupole away from the origin, especially near the plane of the substrate (Figure 2-3A).

In addition to arbitrary trap design, there is a direct extension from the beads modeled here to more complex and biologically relevant cell-based systems. The extension to cells involves manipulation of the CM factor, and the appropriate forms of the CM factor for various

types of cells, such as mammalian cells and protoplasts, have been determined assuming various electrical models [58, 120] and are generally accepted in the community. The accuracy of the models is determined by the extent to which the various parameters describing them (such as membrane capacitance, etc.) are known and homogeneous among a cell population.

### 2.3.2 Parameter-space exploration

A primary use of the modeling environment is to explore the effects of experimental parameters on the interplay of forces. The forces considered in the model all vary differently with such experimental parameters as voltage, frequency, particle radius, etc, which can make it difficult to predict how parametric variations will affect holding. The model allows one to make these predictions easily and quantitatively. One way to visualize the interplay of forces is through the zero-force isosurfaces, which provide a convenient bridge between the vector force fields and the holding points. This can either be used to confirm ones' intuition, as when predicting that "heavier" particles will be "harder" to levitate (Figure 2-10), or can provide insight into situations that are more difficult to grasp initially—such as the interaction between DEP and HD drag forces (Figure 2-11).

This interaction is actually the primary concern in developing DEP-based cell traps that can hold cells against flow. One can expect that for a given situation, a particle will be held in the trap until some threshold destabilizing flowrate (the release flowrate) is applied, whereupon the particle will be released. Figure 2-11 shows this development, where the  $F_x=0$  isosurface "bends" over until holding points cease to exist. Since the system aim of the  $\mu$ DAC is to develop traps where the flow needed to "bend" the isosurface is "large" as determined by some external specification, this amounts to increasing the "stiffness" of the isosurface.

Since this isosurface represents the interplay between HD drag and DEP forces, I can alter either force to effect greater holding. Realizing that the HD drag forces increase away from surfaces (Eqn. (2-4)), one sees that keeping the particle close to the substrate will increase the holding. Manipulating the shape of the electric fields to remove the decay in DEP force away from the substrate can also increase holding. This can be done by using an octopole cage [93, 143] or by introducing extruded electrodes that remove the  $z$ -directed DEP variation. This is in fact what I will proceed to do in Chapter 4 when designing the extruded traps. Thus the insights obtained via the modeling environment will guide future microscale DEP design.

### 2.3.3 Limitations

While the modeling environment provides for the types of analyses required by the  $\mu$ DAC, others may encounter limitations. First, the implementation of rigid surfaces, such as might be found in hybrid DEP-mechanical traps, is difficult to do. This requires more sophisticated particle-boundary intersection algorithms than the simple one implemented for the substrate surface. Second, algorithms have not been optimized for memory usage, and thus analyses using large (or very fine) grids can quickly command  $>100$  Mb of memory. If this is larger than the available physical memory, the time needed to swap in and out of the hard disk will dramatically slow the analysis.

Another limitation concerns the use of discrete grids and polygons. This discretization introduces numerical "noise" into the isosurface intersection algorithms. The "noise" makes the location algorithms very sensitive where two non-smooth isosurfaces are intersecting. The most pronounced case of this is when the particle is on the substrate, because the  $F_z=0$  isosurface has a

sharp corner near the origin in this case (Figure 2-10C). This effect is seen in the holding characteristics of both systems later in this thesis.

An additional limitation is the inability to perform analyses of non-linearly-polarized DEP excitations (such as for electrorotation and traveling-wave DEP studies), although this was not the intent of the modeling environment and could be implemented since the relevant multipolar theories have been worked out [60]. Also, dynamic analyses cannot be performed, although the force matrices allow the determination of force streamlines (and hence particle trajectories in certain situations). Finally, electrohydrodynamic forces, which can be substantial in some experimental situations [144], are not incorporated. This would require the calculation of the temperature and charge distribution in the fluid, which is not a simple addition to the code. EHD forces will become important in the analysis of the planar quadrupole in the next chapter.

## **2.4 Conclusion**

In this chapter I have presented an integrated modeling environment for the development of DEP-based single-particle traps. The modeling environment can take user-supplied electric field data and other experimental parameters and determine the efficacy of DEP-based cell traps. I have shown that the modeling environment gives insight into the interplay between forces in DEP-based microsystems, such as those describing the balance between DEP and HD drag forces. In addition, the use of an iterative DEP force calculation makes it easy to compute the DEP forces to arbitrary order, allowing for exact analyses of arbitrarily complex electrode geometries. Experimental validation of the modeling environment is presented in the next chapter. With these modeling tools it is now possible to perform *a priori* quantitative designs of various DEP traps for high-performance applications, which is what I will do in Chapter 4.

## Chapter 3: Holding forces of the planar quadrupole

Much information can be learned by experimentally determining the holding forces of planar quadrupole traps. First, the results can be used to validate the modeling environment and determine the parameter space within which its predictions are valid. Second, the results can be used to gain insight into the functioning of the planar quadrupole and DEP-based single-particle traps in general, as well as to determine whether the planar quadrupole can meet the requirements of the  $\mu$ DAC. In this chapter I will describe experiments with planar quadrupole traps, varying the trapped particle size, the applied voltage, the applied frequency, and the solution conductivity, to determine this information.

### ***3.1 Experimental vehicle—the planar quadrupole***

I have decided to use the planar quadrupole shown in Figure 2-2 as the experimental vehicle for the following reasons. First, the planar quadrupole is perhaps the most commonly used DEP trap, and there thus exists a rich set of comparisons to make. Second, correct modeling of the planar quadrupole demands that one use at least the 2<sup>nd</sup>-order multipole (quadrupole), thus providing the ability to demonstrate the ease to which these multipoles can be calculated. Third, the planar quadrupole is easy to fabricate for experimental verification of the model.

Instead of using living cells as the test particle, I have used beads for the verification studies. The reason for this is that during the verification stage it is important to minimize variations in the test parameters so that the true accuracy of the models can be rigorously determined. This is possible by using latex beads, which have precise and accurately determined physical and electrical properties.

### ***3.2 Experimental methods—fab, packaging, test setup, methodology***

In this section I will describe in detail the materials and methods used in the verification experiments.

#### **3.2.1 Stock Solutions**

Solutions of two different conductivities—0.01 S/m and 0.75 mS/m—were made by taking DI water with 0.05% Triton X-100 (Sigma, St. Louis, MO) added and adding appropriate amounts of Hank's Balanced Salt Solution (HBSS, GibcoBRL, Grand Island, NY), also with 0.05% Triton X-100, until the nominal conductivity was reached, as indicated by a Orion Model 125 conductivity meter (Beverly, MA). Solutions were filtered through a 0.45-micron filter (Micron Separations, Inc., Westborough, MA) and their conductivity measured before each use.

#### **3.2.2 Beads**

Polystyrene beads (incorporating 2% divinyl benzene), with density 1.062 g/cm<sup>3</sup>, in three diameters—7.58  $\mu$ m (0.08  $\mu$ m std. dev.), 10.00  $\mu$ m (0.09  $\mu$ m std. dev.), and 13.20  $\mu$ m (0.89  $\mu$ m std. dev.)—packaged as 10 % solids in water were purchased from Bangs Laboratories (Fishers, IN). 15  $\mu$ L of each bead solution was washed twice in 1.5 mL of the appropriate conductivity

stock solution and finally resuspended in 1.5 mL of stock solution. All bead solutions were refrigerated and used within two months.

### 3.2.3 Electrode Traps

Thin-film quadrupole electrodes were fabricated using conventional microfabrication processes. Standard (25 mm x 75 mm) microscope slides were cleaned for 10 minutes in a Piranha solution (3:1 H<sub>2</sub>SO<sub>4</sub>:H<sub>2</sub>O<sub>2</sub>) and blow dried. Photolithography was then performed using the image-reversal photoresist Hoechst AZ-5214 (Somerville, NJ)—which gives re-entrant resist profiles—to define the electrode patterns. 200 Å of chrome and 5000 Å of gold were then evaporated onto the slides followed by resist dissolution and metal liftoff in acetone. Finally, the slides were cleaned in methanol and isopropanol and blow-dried. An image of the completed electrodes is shown in Figure 3-1A, along with relevant dimensions.

### 3.2.4 Packaging

The packaging scheme is shown in Figure 3-1B. Fluid inlet and outlet holes were drilled in the glass slides with 0.75-mm diamond drill bits (C.R. Laurence, Los Angeles, CA). Poly(dimethylsiloxane) gaskets, cast in machined molds from monomer (Sylgard 184, Dow Corning, Midland, MI), above and below the slide functioned as the spacer material and bottom sealing gasket, respectively. The top of the chamber consisted of a glass slide that had been cut to a width of 16 mm and clamped down using an aluminum block. With this setup, the flow chamber sustained >200 µL/min flows without leaking.

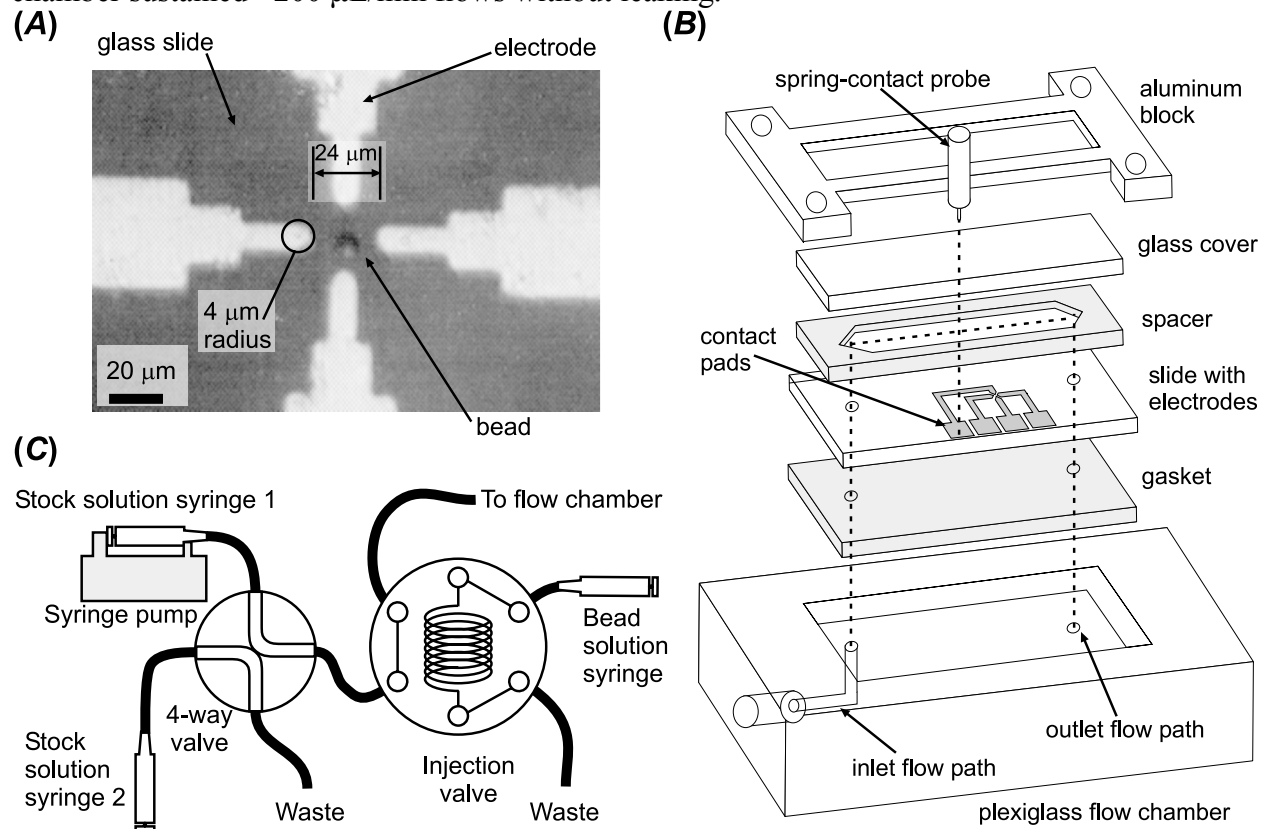


**Figure 3-1:** (A) Photograph of the completed quadrupole electrodes, showing a single 10.00 µm bead captured in trap; (B) Schematic of packaging assembly, showing the stack of layers comprising the flow chamber along with the electrical connections via spring-contact probes; (C) Schematic of fluidic subsystem.

### 3.2.5 Chamber height measurement

The chamber height of the fully assembled unfilled package was measured at various points with an optical interferometer coupled to a z-axis linear gage (543 Series, Mitutoyo/MTI Corp., Aurora, IL) on a Nikon microscope (UM-2, Nikon Inc., Melville, NY). Corrections were made for the indices of refraction of the different materials. The measured chamber height was  $0.73 \pm 0.01$  mm.

### 3.2.6 Electrical Excitation

Sine wave excitation up to 20 MHz and  $10 V_{pp}$  (into  $50 \Omega$ ) was generated by an HP 3314A signal generator (Hewlett-Packard, Palo Alto, CA). This signal was split and sent into 4 high-speed amplifiers (LM7171, Analog Devices, Norwood, MA)—2 non-inverting and 2 inverting—that amplified the signal 2x. The amplifiers delivered  $180^\circ$  phase-shifted signals with negligible gain and phase error up to 10 MHz. The output from the amplifiers was sent via coaxial spring-contact probes (Interconnect Devices, Inc., Kansas City, KS) to the contact pads at the edge of the glass slide (Figure 3-1B).

### 3.2.7 Fluidics

Fluidic connection to the package was made via HPLC connectors and tubing (Figure 3-1C). The fluidic test subsystem consisted of a 4-way valve (V-101D, Upchurch Scientific, Oak Harbor, WA) that allowed the interchange of syringes without introducing bubbles. The bead solution was injected into the flow using an injection valve (V-450, Upchurch Scientific, Oak Harbor, WA). Flow was initiated by a syringe pump (KD-101, KD Scientific, Boston, MA) using a 5 mL Hamilton luer-lock syringe (1005TLL, Reno, Nevada).

### 3.2.8 Optics

The beads were viewed using a Microzoom microscope (Wentworth Labs, Brookfield, CT) with long-working distance objectives on a semiconductor probe station. Images could be captured using a Panasonic WV-D5000 video camera (Secaucus, NJ) and a Sony VCR.

### 3.2.9 Release flowrate measurements

Once beads were captured in the quadrupole trap, flow was initiated. In the parallel-plate flow chamber, beads experienced a transverse hydrodynamic force that tended to dislodge them from equilibrium at the center of the trap and thus acted as a destabilizing force (Figure 3-2). If the bead was held in the trap at the end of two minutes, the bead was considered captured. This time was chosen empirically by observing that beads  $>90\%$  of beads held for two minutes would be held indefinitely (tested up to  $\sim 5$ -10 minutes). The flowrate was adjusted to find the minimum flowrate (within  $1 \mu\text{L}/\text{min}$ ) at which the bead was released within two minutes. This is termed the “release flowrate”. The flowrate was adjusted above and below the release flowrate to ensure that the true release flowrate was determined. In practice, a given bead could be used repeatedly by stopping the flow immediately after it was released, in order to pull the bead back into the trap.

### 3.2.10 Modeling

The modeling was performed with the specifications described in §2.2.1, using FEM data obtained from Maxwell 3D (Ansoft, Pittsburgh, PA). For the current work I simulated the upper-

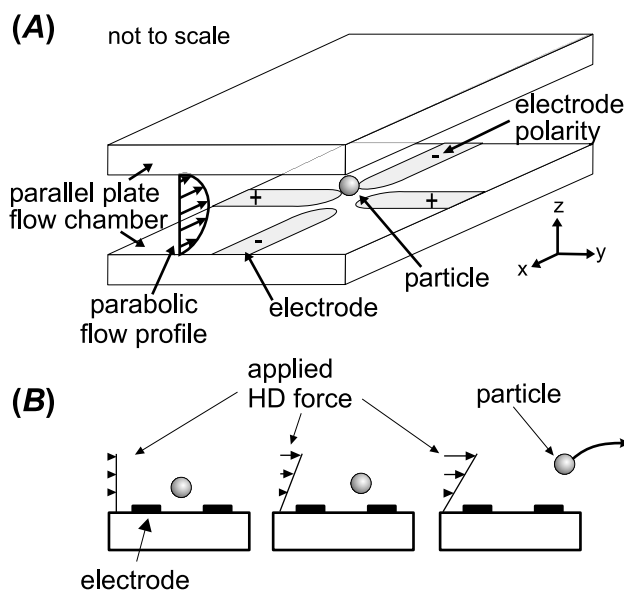


**Figure 3-2:** (A) Schematic of flow chamber, showing a bead in the trap experiencing a parabolic HD drag force; (B) Release flowrate and holding force measurements. The flowrate (force) is increased until the bead is liberated from the trap. The parabolic flow profile is approximately linear at when the particle is close to the substrate.

half of the trap in Figure 3-1A, using symmetry boundary conditions at the glass substrate. Field data from the central portion of the quadrupole was written to a grid, using a grid spacing of 0.5-2  $\mu\text{m}$ , and smoothed using a three-dimensional Gaussian low-pass filter with the following parameters: three-grid-point convolution kernel (in each direction) with a standard deviation of 1.3 grid points. The filtering was used in lieu of long simulation times to reduce high-spatial frequency noise. The modeling performed in this chapter used an older version of the simulation program that represented the isosurfaces not only with triangles but also with 4-, 5-, and 6-sided polygons. All computations on these isosurfaces are as described in Chapter 2. This representation was later abandoned in favor of the simplicity of using only 3-sided polygons.

### 3.3 Results

#### 3.3.1 Single-bead holding

Figure 3-1A shows a trap holding a single 10.00- $\mu\text{m}$  bead. This shows that the traps do work, at least rudimentarily. Interestingly, even with these un-optimized traps, I have demonstrated single-bead capture: when two beads are captured in a trap, the second bead will be held with less force than the first, meaning that I can apply a flowrate that will selectively remove the second bead while still holding the first. Thus, I can get single-particle trapping, which is a necessary requirement for the  $\mu\text{DAC}$ . In practice this discriminating flowrate is determined empirically because the modeling tools are unable to accommodate the interactions of two particles in a trap. Schematically, the number of particles held in a trap varies with the imposed flowrate as in Figure 3-3. One way to think about it is that the size of the potential-energy well that comprises the trap decreases as the flowrate is increased. Thus, there will exist a range of flowrates such that the size of the well is larger than one but less than two particles. In this flow regime, only one particle can be held per trap. Empirically, this occurs at approximately 90% of the release flowrate for a given set of experimental parameters.

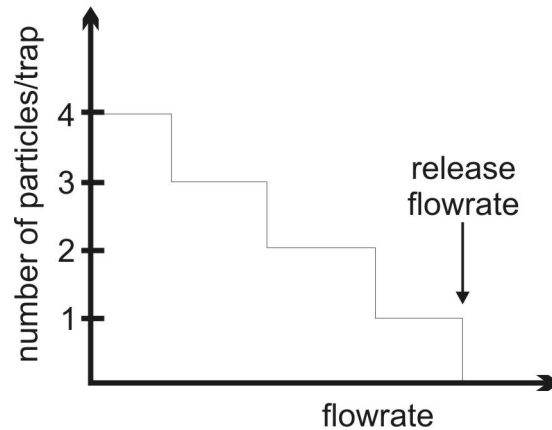


**Figure 3-3:** Schematic showing how the number of particles per trap varies with applied flow. Close to but below the release flowrate only one particle can “fit” in the trap.

### 3.3.2 Release flowrate as the voltage is varied—the holding characteristic

By varying the voltage and measuring the release flowrate, I can generate what I call the holding characteristic of the trap for a particular set of experimental conditions. By comparing the shape and absolute values of the measured holding characteristic with the predictions based upon the modeling environment, I can evaluate the accuracy and completeness of the modeling environment.

The typical shape of the holding characteristic for these traps is shown in Figure 3-4A for 7.58- $\mu\text{m}$  beads in 0.01 S/m solutions at a frequency of 1 MHz. The characteristic behavior in these traps is that the release flowrate increases from zero until a maximum release flowrate (the peak release flowrate) is achieved (at the peak voltage), after which it decreases quickly and then reaches a plateau (the baseline release flowrate). To validate the model, I have compared the match between these three parameters, as they define the shape of the holding characteristic.

To get a sense of the scatter in the experimental results, I repeatedly took data for the 10.00- $\mu\text{m}$  beads using more than  $\sim 10$  different beads over three months. Individual release flowrates were measured between one and nine times, with each measurement being double-checked. I have included this scatter and the flowrate discretization error in Figure 3-4B. The other data shown in the rest of the chapter can be assumed to possess similar scatter over this time frame. I then used these results as an internal control when acquiring the rest of the data presented in this paper. I did this by taking data from equivalent conditions during subsequent runs to establish experimental precision. When this was inconvenient (as with different solution conductivities) I used the prior knowledge that the curves should not greatly shift to check against the previous data. In addition, equivalent data points were taken before and after each experimental run to estimate any short-term drift (usually  $< 5\%$ ). I did observe a long-term downward drift (towards lower release flowrate) in the release characteristic of  $\sim 16\%$  (which therefore accounts for the majority of the scatter). Several factors could account for this trend, such as changes in the chamber geometry, experimental solutions, or room temperature.

Turning back to Figure 3-4A, I also show the predicted holding characteristics calculated including either only the dipole ( $n=1$ , ‘...’) or dipole and quadrupole (—) DEP force terms. One sees that the computing only the dipole term gives a monotonically increasing holding characteristic (‘...’) because the  $z$ -directed force from the dipole term is unable to induce levitation near the field null, where the particle is located. As described below, this levitation is the key to

the shape of the holding characteristic. Including the quadrupole term accurately models the problem, since it correctly accounts for the levitation force in quadrupole traps, in agreement with previous work [133, 145, 146]. Incorporating the octopole term does not qualitatively or quantitatively change the results, indicating that induced octopoles are negligible in this situation (data not shown).

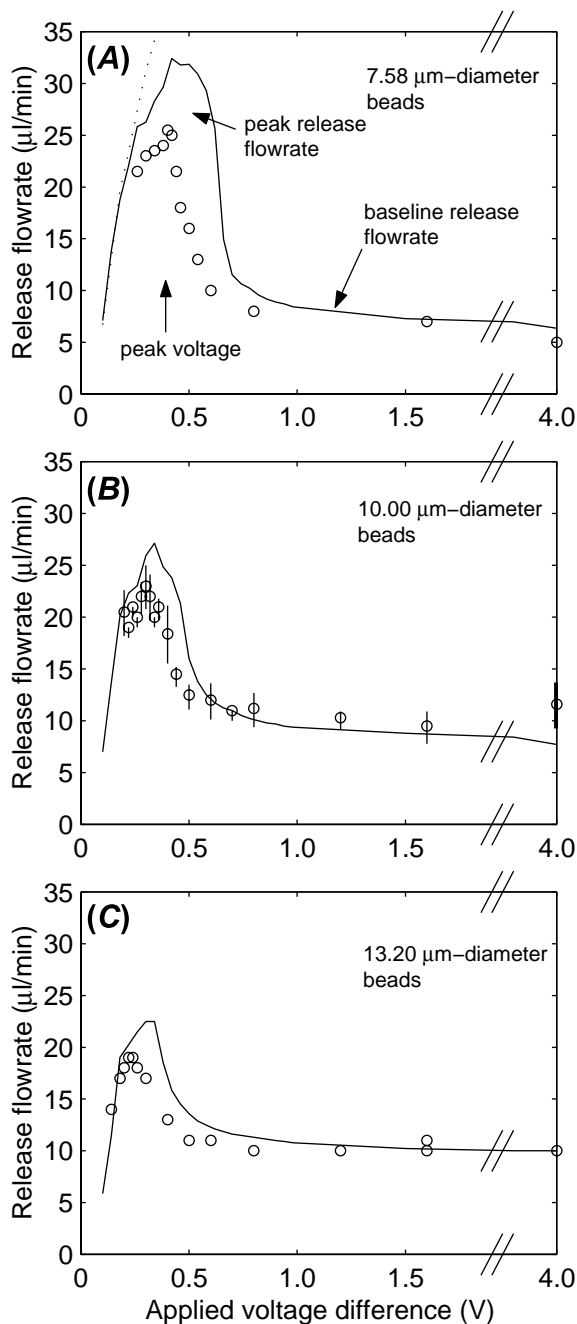


**Figure 3-4:** Experimental ( $\circ$ ) and simulated ( $—$ ) holding characteristics for beads in the planar quadrupole trap of Figure 3-1A as the bead diameter was varied. Bead diameters were  $7.58\ \mu\text{m}$  (A),  $10.00\ \mu\text{m}$  (B), and  $13.20\ \mu\text{m}$  (C), respectively. Subplot (B) shows the long-term scatter in the data, which can be taken as typical of the other curves. Also shown in (A) are the simulated holding characteristics including only dipole DEP force terms ( $\cdots$ ). The frequency is 1 MHz and the solution conductivity is 0.01 S/m. Note the break in the voltage axis.

The match between the experiment and the 2<sup>nd</sup>-order simulations is significant, especially considering that there are *no* adjustable parameters. All parameters needed in the model have come from either measurements, company data, or literature values. The simulations predict a higher release flowrate (27%) at the peak voltage, a higher peak voltage (5%), and a higher baseline release flowrate (8%).

The trend in release flowrate as the voltage is varied (Figure 3-4A) is initially non-intuitive, but becomes apparent when one recognizes that the DEP force influences the height of the particle. This is shown in Figure 3-5, where I plot the predicted release flowrate along with the predicted holding force and the predicted height of the particle at release for a 7.58- $\mu\text{m}$  bead in the quadrupole trap.

When no voltage is applied, there is no confining force, and neglecting any stiction effects between the bead and the surface of the glass slide—which have been measured at less than 1-2  $\mu\text{l}/\text{min}$ —the release flowrate should be zero. As the voltage is increased, the DEP forces will create a confining well (Figure 3-5A). In this pre-levitation regime, the  $z$ -directed component of this force, which serves to levitate the bead, will initially not be large enough to overcome the gravitational force and thus the bead will remain on the slide surface. The force pushing the bead from the trap—the fluid flow—varies linearly with height of the bead and volume flow rate (Eqn. (2-4)). Thus, if the bead height does not change but the confining forces increase, the release flowrate will also increase.

At some threshold voltage, the  $z$ -directed DEP force will exactly balance the gravitational force and the bead will start to be levitated (Figure 3-5B). This voltage corresponds to the peak voltage and peak flowrate. Any increase past this voltage and the bead will be levitated upwards and then experience larger HD drag forces (Eqn. (2-4)). As can be seen from Figure 3-5, the height of the particle (---) increases quickly with voltage once it is levitated, and particle will

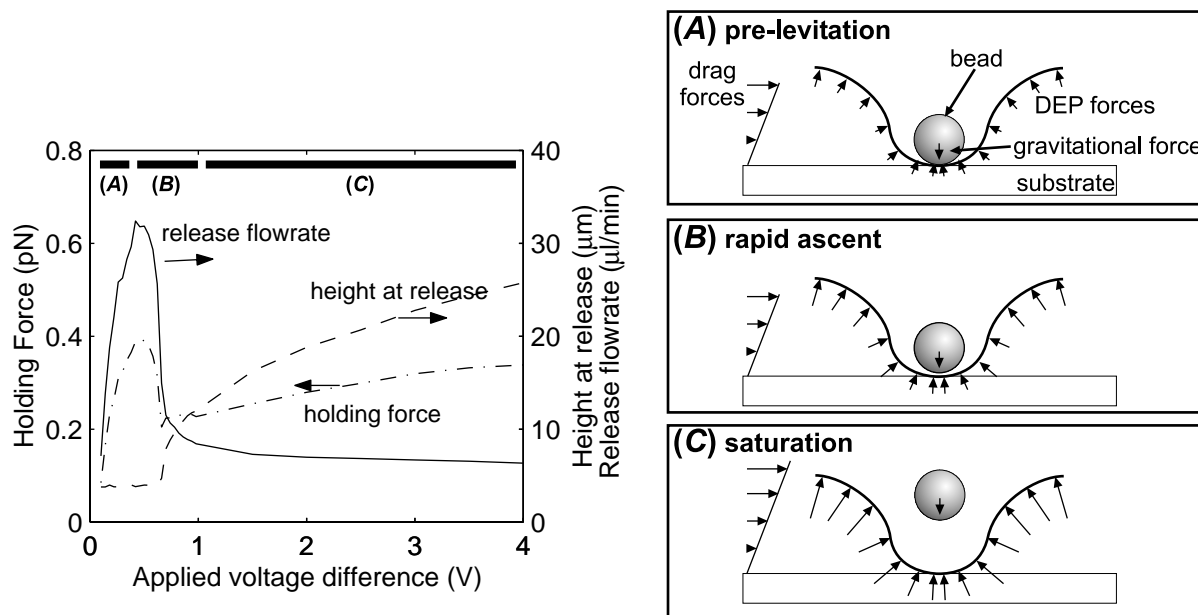


**Figure 3-5:** Explanation of holding characteristics as voltage is varied, showing the simulated release flowrate (—), the holding force (---), and the height of the particle when it is released (---). (A) Pre-levitation. At very low voltages, the gravitation force cannot overcome the  $z$ -directed DEP force, and the bead is not levitated; (B) Rapid ascent. At a certain voltage the bead will just become levitated and the holding characteristics will peak; (C) Saturation. At high voltages, the increase in holding force is balanced by the increased particle levitation height, resulting in a flat release flowrate profile.

experience a rapid ascent. Therefore, the increased exposure to the HD drag forces with little increase in the DEP force causes the release flowrate characteristic to decrease. This can be contrasted with simulations involving only the dipole DEP-force term (Figure 3-4A, ‘...’) where the release flowrate never decreases because the particle never becomes levitated.

Observing the particle height versus voltage curve (Figure 3-5, ---), one sees that after an initial rapid ascent, the slope of the curve decreases and saturates because the  $z$ -directed DEP forces decrease rapidly as the bead is levitated away from the electrodes. This is in accord with the measured height versus voltage characteristics of other researchers [92]. At this point, the holding force increases with voltage (Figure 3-5, ‘---’) are matched by the increases in the HD drag forces due to the increased particle height (Figure 3-5, ‘---’). They thus balance each other and give a saturated flat release-flowrate characteristic (Figure 3-5C, ‘—’).

### 3.3.3 Holding characteristic as the particle diameter is varied

Since the DEP forces vary as  $R^3$  (dipole) and  $R^5$  (quadrupole), the gravitational force varies with  $R^3$ , and the HD drag forces vary with  $R$ , I can use differing particle sizes to evaluate the accuracy of the modeling environment to see if it predicts the correct particle size effects. This will help determine whether the model accounts for these forces adequately and whether other forces are significant. I have performed experiments with three different bead sizes to explore this trend. The results are shown in Figure 3-4, along with the predicted results (simulated including up to the  $n=2$  DEP force term). Although all three bead diameters show the same characteristic peaking-declining-plateau response, the values of the peak release flowrate, peak voltage, and baseline release flowrates all differ as the bead diameter changes.

These differences are shown Figure 3-6, where the three parameters that define the holding characteristic have been extracted from the simulation and experimental results. In making this comparison I extracted parameters from only one data set consisting of three runs at

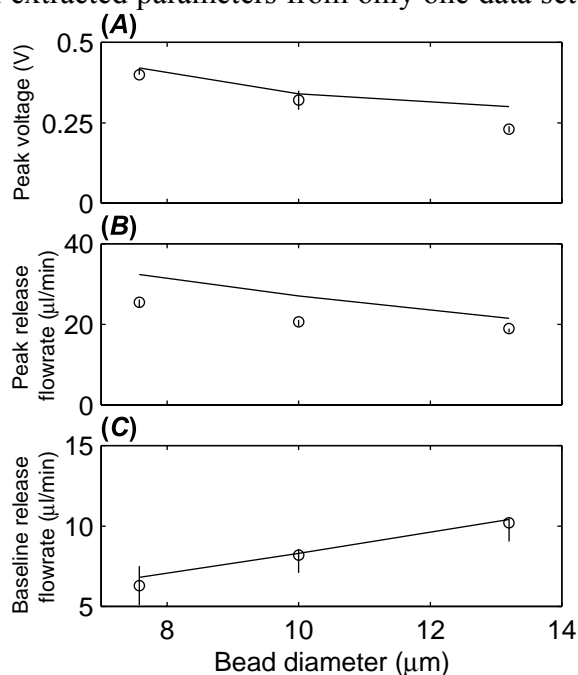


**Figure 3-6:** Comparison of extracted experimental (○) and simulated (—) peak voltage (A), peak release flowrate (B), and baseline release flowrate (C) from one data set. The frequency is 1 MHz and the solution conductivity is 0.01 S/m.

different bead diameters to eliminate the long-term drift seen in Figure 3-4B (and thus I only use a subset of the data displayed in Figure 3-4B). The scatter was estimated from the uncertainty in the peak height ( $n=7$  data points for 10.00- $\mu\text{m}$  beads,  $n=2$  for other diameters) and position ( $n=5$  for 10.00- $\mu\text{m}$  beads,  $n=2$  for others) during these runs and from the release flowrates collected at voltages greater than 0.8 V for the baseline ( $n\geq 6$  for each diameter). In all cases, the scatter was  $<17\%$  and usually was  $<5\%$ .

As the bead diameter is increased, the baseline release flowrate (Figure 3-6C) increases while both the peak voltage (Figure 3-6A) and peak release flowrate (Figure 3-6B) decrease. The agreement between simulations and experiment is good, with the dependencies captured quantitatively—the maximum differences are 30% for the peak voltage, 27% for the peak flowrate, and 9% for the baseline release flowrate.

The trends (Figure 3-6) can be explained in accordance with DEP theory. As the bead diameter is increased, the voltage necessary to initially levitate the bead (which corresponds to the peak voltage) will decrease because the levitation forces increase with bead diameter. These smaller voltages cause the bead to experience smaller DEP confining forces before being levitated. This leads to the decrease in peak release flowrate with bead diameter. Finally, the increasing baseline release flowrate with diameter is due to the fact that while the HD drag forces increase only linearly with diameter, the DEP confining forces increase as  $R^3$  and  $R^5$ .

### 3.3.4 Holding characteristic changes with frequency

While the first two trends (voltage and bead diameter) evaluate the spatial aspects of our model, the frequency trends are a test of the CM factor of the DEP force, which is the only frequency-dependent component that I have included. The CM factor (Eqn. (1-2)) for 10.00- $\mu\text{m}$  diameter beads is shown in Figure 3-7. Although only the dipole term of the CM factor is shown, the quadrupole and higher terms display similar behavior, although at slightly different dispersion frequencies and smaller ranges (e.g., the quadrupole term can only vary between  $-1/3$  and  $+1/2$ ). To generate Figure 3-7, the conductivity of the beads was estimated by using very-low-conductivity stock solutions and measuring the n-DEP to p-DEP transition frequencies, when the beads would switch from being repelled to being attracted to the electrodes, respectively. Fitting these to the zeros of the CM factor gave a conductivity estimate of  $2e-4$  S/m, which is in accord with literature values for unmodified polystyrene beads of this size [147].

As the frequency is decreased, the CM factor goes from being permittivity dominated to conductivity dominated (Eqns. (1-4) & (1-5)). For the high-conductivity solution (0.01 S/m), no dispersion is apparent because the CM factor is dominated by the properties of the stock solution.

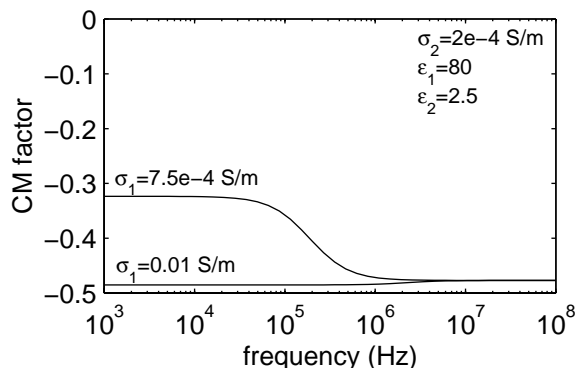


Figure 3-7: Calculated CM factor (dipole term) for a polystyrene bead in salt solution.

For the low-conductivity solution (0.75 mS/m), the CM factor decreases in magnitude as the frequency is decreased. Since the CM factor directly multiplies the DEP force equation (Eqn. (1-1)), changes in the CM factor will cause corresponding changes in the DEP force at a given voltage. Thus, I expect little frequency dependence of the forces at 0.01 S/m and some dependence at 0.75 mS/m. In essence, the CM factor changes are equivalent to scaling along the voltage axis, and should thus only shift the holding characteristic along that dimension.

Two frequency sweeps were performed, at both high (0.01 S/m) and low (0.75 mS/m) solution conductivities. Both of the 1 MHz holding characteristics (Figure 3-8A,D) agree well with predictions, although the peak flowrates and peak voltages are smaller than predicted. While these predictions can be partly explained by the sensitivity of the simulations around the peak flowrate, they could also be due to temperature changes in the measurement room—causing the chamber height and experimental properties to change—or experimental observations of neglected forces. The 100 kHz holding characteristics (Figure 3-8B,E) for both solutions also have the predicted shape, although the low conductivity characteristic (Figure 3-8E) deviates more from predictions than the 0.01 S/m characteristic (Figure 3-8B). The 10 kHz holding characteristics (Figure 3-8C,F) for both solution conductivities exhibit very different shapes that cannot be explained by our modeling environment.

The only frequency dependence included in the model is through the CM factor. The 10 kHz curves, which show completely different holding characteristics, can clearly not be explained through manipulation of the CM factor. The 100 kHz curve at the low conductivity solution has the same characteristic shape, but is shifted towards lower voltages and release flowrates. As explained before, the release flowrate shift cannot be caused by changes in the CM factor. For the voltage shift to be caused by changes in the CM factor, the CM factor would have to decrease (become more negative) at low frequencies. Not only would this require an extremely small (and physically dubious) bead conductivity ( $\sim 1e-6$  S/m), but because the CM factor is already near its theoretical minimum, the increase in the magnitude of the CM factor would be much too small to account for the experimental observations (data not shown).

The shifts in the 100 kHz (and also possibly the 1 MHz) holding characteristics can be more readily explained by the existence of an upward destabilizing force on the bead. The 10 kHz characteristics are consistent with the existence of an extra confining force on the bead. Thus, I conclude that the cause of the discrepancies is due to other forces that are not accounted for in the model, as discussed below.

## **3.4 Discussion**

### **3.4.1 DEP force measurements**

The development of the multipolar DEP theory coupled with the decreasing cost of computing power and the increasing sophistication of microscale DEP researchers has led to several recent attempts to construct quantitative DEP microdevices that are amenable to modeling. Recent work [143, 148] has even started to concentrate on the interaction between DEP and HD forces, in their case determining the flow needed to break through a DEP barrier, similar to our case. The difference between their situation and the one presented here is that the particles in that work are located at the centerline of Poiseuille flow, and thus the drag force is well-defined by the Stokes drag on a sphere. This allows them to derive analytical representations for the force balance. As particles approach surfaces, this analytical formulation becomes hopelessly complicated, necessitating a numerical approach as taken here.

The experimental approach—the determination of release flowrate—has many advantages over direct measurements of the DEP force. First, the efficacy of particle traps in many applications *will* be the ability of the trap to hold a particle against fluid flow. Thus, this measurement, even if not correlated to theory, would still be valuable. The comparison with theory, however, is ultimately more useful, since the validation of the modeling environment allows for future trap design with confidence that the fundamental physics in a specific operating

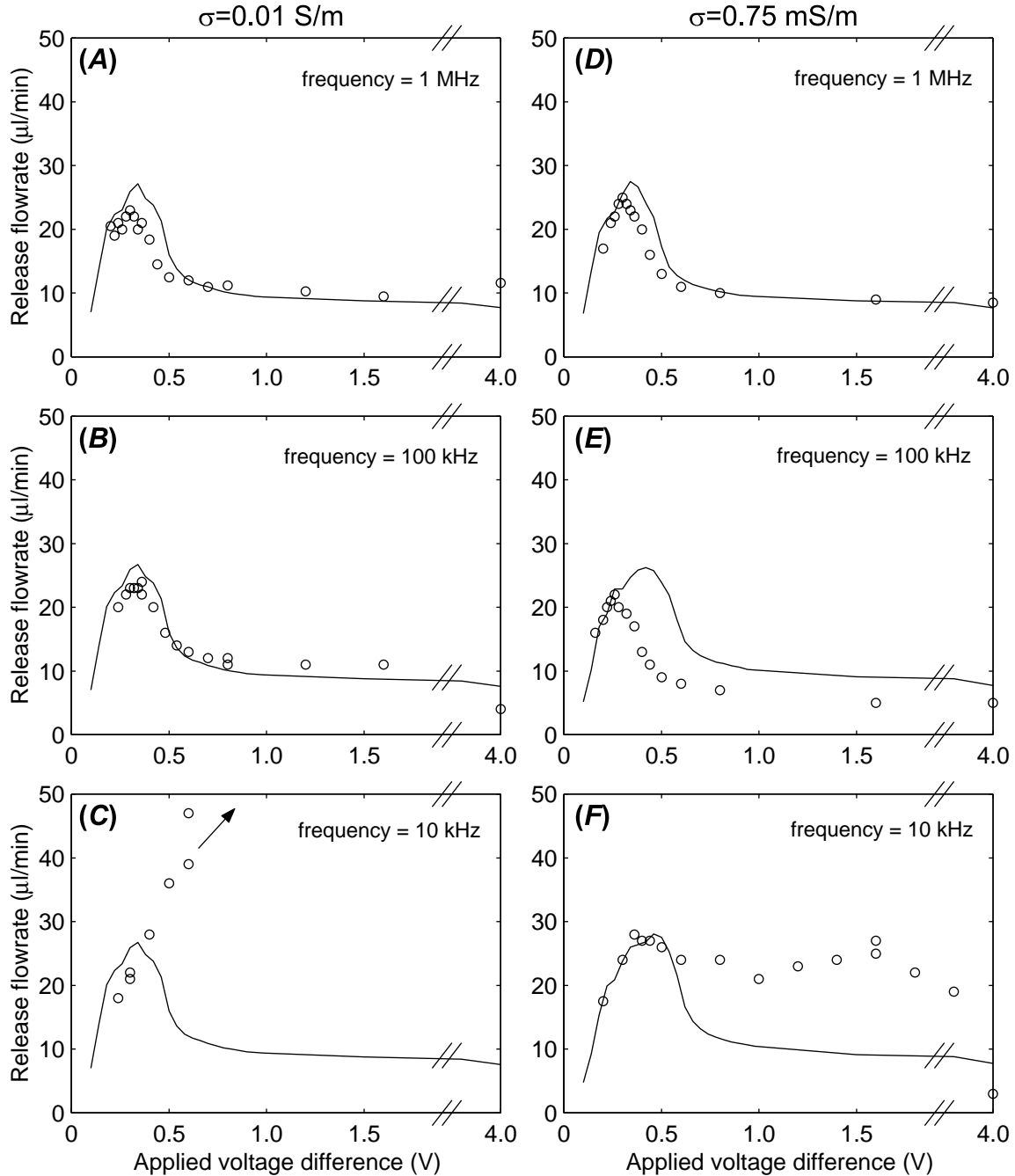


**Figure 3-8:** Experimental ( $\circ$ ) and simulated ( $—$ ) holding characteristics for 10.00  $\mu\text{m}$  beads for three different frequencies at solution conductivities of 0.01 S/m (A-C) and 0.75 mS/m (D-F). Results are shown for frequencies of 1 MHz (A,D), 100 kHz (B,E), and 10 kHz (C,F). The 10 kHz holding characteristic at 0.01 S/m (C) increases quickly with voltage and so is truncated in the plot. Note the break in the voltage axis.

regime of interest are being accounted for.

There are several implications of these results for such future trap design. First, larger voltages are not necessarily better; optimal holding occurs in our structures at  $\sim 0.3\text{V}$ . The best trapping occurs when particles are “deep” in a potential energy well. For these planar quadrupole traps, this occurs when the particles are on the substrate or just barely levitated. Second, planar quadrupoles are quite weak traps (holding at  $<20\ \mu\text{l}/\text{min}$ ), and so exploring alternate geometries may lead to much higher holding forces. While operating at low frequencies is one route to higher holding (Figure 3-8C,F), this regime most likely involves forces other than those accounted for in the model, complicating such designs. If these forces could be understood and harnessed, however, they might themselves provide routes to higher holding.

The agreement with predictions also allows one to extract DEP forces, which themselves are useful for testing the DEP theory itself or determining the electrical properties of particles. Other researchers testing the theory have used particle levitation [88, 145], flow-induced particle displacement in DEP traps [143, 149], and particle velocity measurements in DEP force fields [150]. The release flowrate method described represents a new addition to this list. The close coupling with our numerical modeling environment removes limits that other methods may have with respect to electrode geometries or experimental conditions.

Finally, examining Figure 3-5, one sees that the forces are in the sub-pN range. This gives an indication to the sensitivity of the measurement methodology. This is comparable to the force sensitivities of optical tweezers [151, 152], which is the most closely related biophysical measurement. The agreement in shape and actual value of the predicted and measured holding characteristics gives strong validation that the model correctly accounts for the DEP, HD drag, and gravitational forces in our system.

### 3.4.2 Shear flow approximation to Poiseuille flow

I have used shear-flow drag forces instead of Poiseuille flow (which actually exists within the parallel-plate flow chamber) to compare predictions to experiments. At the bead heights encountered in these experiments, the deviation between the shear and parabolic flow profiles is less than 2%, and thus both models should be expected to give the same drag force and thus holding characteristic. I checked this assumption by comparing predictions using analytically solved drag forces for each flow profile [138, 139]. The two drag force formulations gave release flowrates that differed by 10%, which was found to be due to a 10% difference in drag forces predicted by the two theories near the substrate. The reason for the differences is not entirely clear, but I have chosen to use the shear flow model for the following reasons: 1) it involves interpolating within a 1-D parameter space, versus 2-D for the Poiseuille flow; 2) the regions of operation are well within its parameter space, whereas I am at the asymptotes of the Poiseuille flow model; and 3) it predicts release flowrates that agree better with experiments. Regardless of the flow profile chosen, the predictions are only affected by 10%.

### 3.4.3 Agreement between predictions and experiments

The agreement between predictions and experiments in Figure 3-4 and Figure 3-6 is remarkable, especially since *no* fitting parameters were used. This leads to the conclusion that the model accurately accounts for the DEP, gravitational, and HD drag forces. One possible cause of the existing discrepancies that one can rule out would be errors associated with physical and experimental parameters such as bead radius, chamber width, etc. Using the modeling

environment to perform sensitivity analyses shows that reasonable errors in these quantities would not result in the observed deviations between prediction and experiment.

Other causes of error include the sensitivity of the release flowrate determination around the peak height due to noise in the numerics, brownian motion of the particle into lower force-confining regions [78], and electrohydrodynamic (EHD) flows, as discussed below. In addition, although the symmetry of the ideal quadrupole electrode structure precludes any substrate-liquid material interface or charge relaxation effects from affecting the electric fields, the actual physical situation could have asymmetries that cause these effects to appear. A final source of error is that heat generation will cause inhomogeneities in the electrical properties of the system, which could alter the electric fields.

To remove this final source of error and to include the interfacial effects properly in non-symmetrical electrode geometries, the electric field would need to be calculated self-consistently including frequency and temperature effects, as others have done [148]. Here one sees the benefit of the arbitrary choice of field solver, as it allows easy implementation of such a change.

#### **3.4.4 Forces responsible for anomalous frequency effects**

The experimental results agree with predictions at high frequencies, but as the frequency is lowered, anomalies surface that cannot be explained by manipulating the model. The source of the discrepancies most consistent with observations is forces unaccounted for in the model, which I conclude are induced by EHD flows. I have ruled out flow-induced lift forces and linear polarization effects; calculated flow induced-lift forces for this experimental situation are much too small ( $\sim 10^{17}$  N) [153], and linear polarization effects, which would reduce the electric field in the medium [57], would affect predictions much as the CM factor does and thus only shift the curves toward higher voltages.

EHD flows, induced by the interaction between either thermally generated or double-layer charge with electric fields in fluids [154-156], can impart either confining or destabilizing forces. The type of force is dictated by the origin of the charge (thermal or double-layer) and the applied frequency relative to the relaxation frequency of the medium (which has the form  $\sigma/\epsilon$ ) [144, 154].

Several lines of evidence are consistent with EHD flows being the cause of the release flowrate deviations. First, flows not predicted by DEP theory alone (and attributed to EHD phenomena) have been observed repeatedly by DEP researchers working on microscale electrodes [77, 94, 97, 144, 154, 157-160]. Second, small debris ( $\sim \mu\text{m}$ ) inadvertently introduced into the chamber will flow in circulatory patterns (reminiscent of other reported EHD flow patterns) around the electrodes at various voltages and frequencies. Third, the observed increases (Figure 3-8C,F) and decreases in the holding forces (Figure 3-8E) with frequency are consistent with frequency-dependent changes in the magnitude and direction of the EHD flows (for systems such as the planar quadrupole that possess both thermally induced and double-layer charge). Future work could incorporate these effects into the modeling environment.

Thus, based on both the experimental observations and a plausible rationale for frequency-related deviations between model and experiment, I conclude that the modeling environment accounts for DEP, HD drag, and gravitational forces, and thus is valid under conditions where other forces are negligible. Avoiding possible EHD effects necessitates design at relatively high frequencies or for relatively large particles. For the cell-based single-particle DEP traps, such as would be used in the  $\mu\text{DAC}$ , this regime provides a great deal of latitude in design since one

would normally like to operate at high frequencies to minimize induced transmembrane potentials (§1.5.2).

### **3.5 Conclusion**

In this chapter I have used a microfabricated planar quadrupole as an experimental vehicle for evaluating modeling tools that can quantitatively predict DEP-based trap performance. I have been able to compare the predicted and experimental results and found them to be quite close, with no adjusted parameters. In addition, I have determined HD and DEP forces at the sub-pN level. Anomalous frequency-dependent behaviors were observed, most likely caused by electrohydrodynamic flows, and do not affect the validity of the modeling environment, but rather provide bounds on the design space where the environment is valid. The combination of modeling and experiments gives insight into the nature of DEP traps and can act as a guide in the design of stronger single-particle traps for various biological applications. The design of such stronger traps is the focus of the next chapter.

## Chapter 4: Extruded trap design

Now that I have demonstrated the validity of the modeling environment for modeling the relevant forces (DEP, gravity, HD drag) in these microsystems, the next step is to design a trap that can meet the system requirements of the  $\mu$ DAC, where the strength of the trap is paramount. The design will start by motivating the use of a quadrupole trap, but this time using extruded electrodes, as opposed to the planar electrodes described earlier. I will continue the design by determining the exact geometry of the trap—post diameters, spacings, etc.—and how to electrically connect the trap to the outside world while maintaining holding. After choosing the trap dimensions, I will conclude with a system-level design to determine the chamber geometry and operating conditions necessary to meet the requirements of the  $\mu$ DAC.

### 4.1 Materials and Methods

#### 4.1.1 Modeling

All modeling performed in this chapter used the modeling environment described in Chapter 2. Drag forces were computed using a parabolic (as opposed to shear) flow profile, to better represent the physical situation. Unless noted otherwise, the simulations were performed on beads with  $f=20$  MHz,  $R=10$   $\mu\text{m}$ ,  $\rho_p=1.062$  g/cm<sup>3</sup>,  $\epsilon_p=2.5$ ,  $\sigma_p=10^{-4}$  S/m,  $\sigma_m=1$  S/m (to approximate physiological saline),  $w=5$  mm,  $h=150$   $\mu\text{m}$ , and simulating the dipole and quadrupole force orders ( $n_{max}=2$ ). All extruded traps had 50- $\mu\text{m}$ -tall posts unless noted otherwise. Although the final traps will use cells, beads are appropriate for the *relative* design employed throughout much of the chapter.

#### 4.2 The extruded trap - introduction

The major reason for the weakness of the planar trap is that the electric field (and hence the confining force) decays away from the substrate. One approach for making a stronger trap, therefore, is to eliminate this decay. Another problem with the planar trap is that increases in voltage cause the particle to levitate higher, exposing it to stronger drag forces. Designing a trap where the height does not increase with voltage will increase its strength.

An extruded three-dimensional trap solves both of these problems and is amenable to microfabrication. First, extending the electrodes in the  $z$ -direction can eliminate the field decay away from the substrate. Second, extruded traps add an element of axial symmetry to the field, which to a first approximation (away from the electrode top & bottom) eliminates  $z$ -directed DEP forces. Given that bioparticles will have weight, the absence of any  $z$ -directed DEP force means that the particle will always be found on the substrate. Since the drag force is smallest near the substrate, the particle is effectively “shielded” from the drag forces. As I will show, deviations from perfect axial symmetry will affect this, but the conclusions remain—the extruded trap may be an avenue towards meeting the  $\mu$ DAC system requirements.

### 4.2.1 Electrode number

The next major issue to deal with is the electrode structure. Several questions arise. How many electrodes are necessary? How should they be shaped? How should they be arranged? I will answer these in turn.

Minimizing the number of discrete electrodes to hold a single cell directly minimizes the number of interconnections and is therefore desirable. The question that presents itself is whether strong three-dimensional confinement can be achieved with two electrodes. Several lines of argument lead to the conclusion that it is difficult, if not improbable. The approach is to start from one-dimension and determine how many electrodes are necessary for one-dimensional holding. I can then extrapolate to three-dimensions, making the necessary corrections.

In order to get DEP confinement, one needs a non-zero electric field (to induce the dipole) and a variation in that field (to get a non-zero  $\nabla|E|^2$ ). Figure 4-1 shows the electric field and  $|E|^2$  factor for one and two point electrodes in one dimension. The  $|E|^2$  factor is proportional to the potential energy of the DEP force  $U_{DEP}$ ,

$$\begin{aligned} \mathbf{F}_{dep} &= 2\pi\epsilon_m R^3 \cdot \text{Re}[CM \cdot \nabla|E|^2] = -\nabla U_{DEP} \\ U_{DEP} &= -2\pi\epsilon_m R^3 \cdot \text{Re}[CM \cdot |E|^2] \end{aligned} \quad (4-1)$$

and so plotting  $|E|^2$  gives the profile of the potential energy. One sees that Figure 4-1B exhibits a well in the DEP potential energy around  $x=0$ , while the single-electrode case (Figure 4-1A) does not, and thus only the two-electrode configuration results in confinement.

Now imagine the two point electrodes on a two-dimensional plane (Figure 4-2). The holding in the  $x$ -direction, along the  $x$ -axis, will be similar to the above. Since the field and its

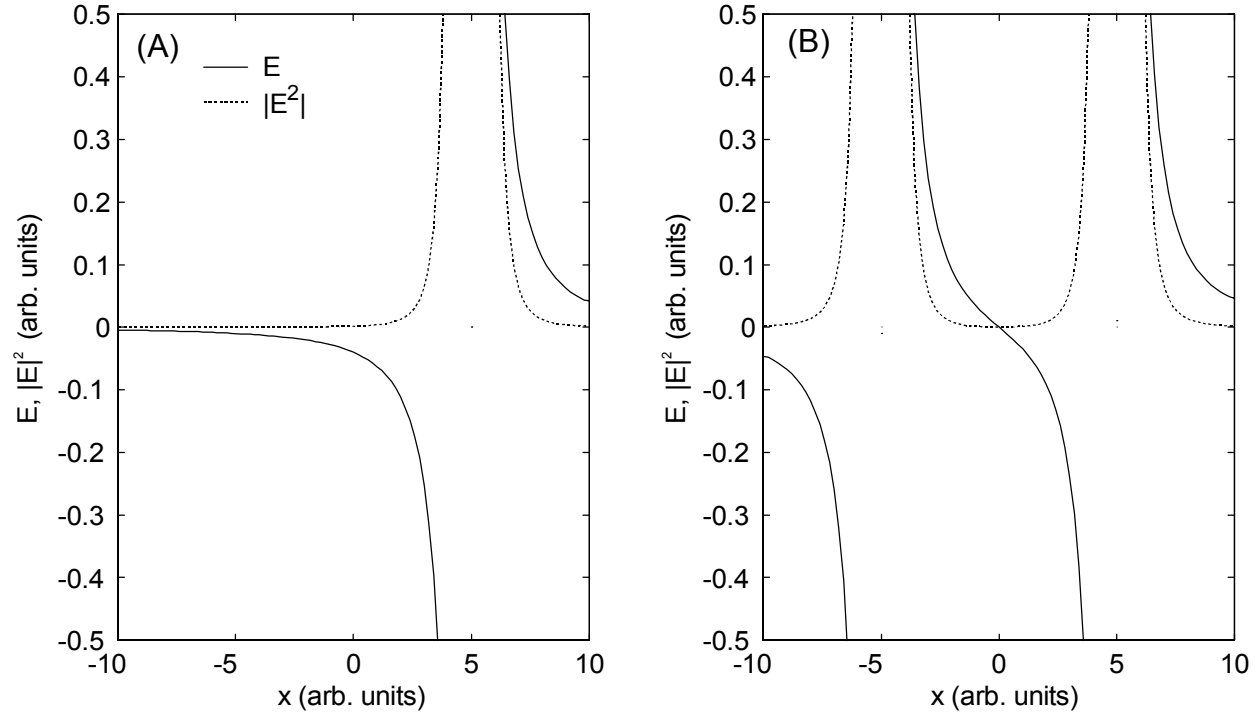
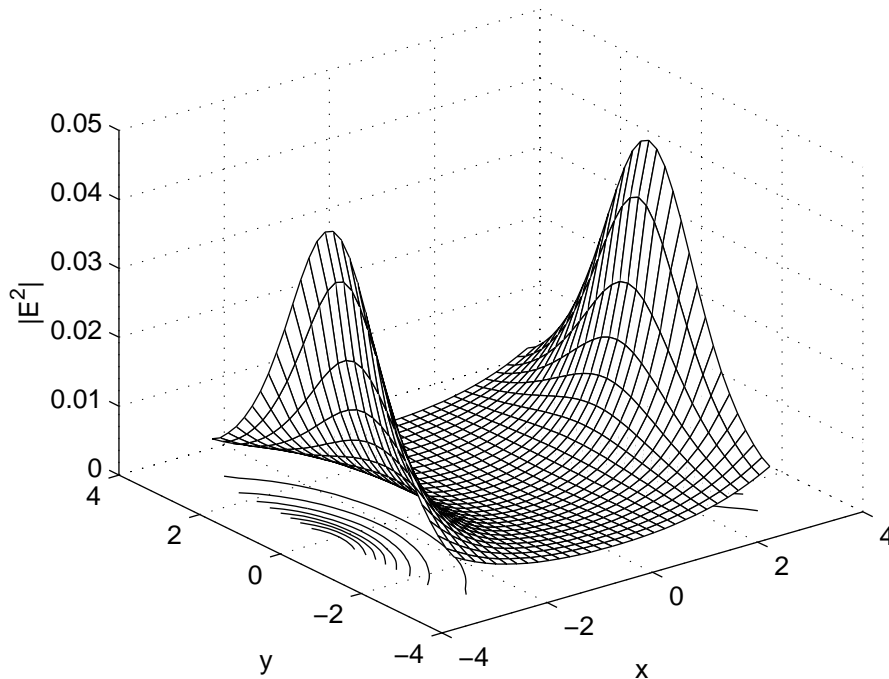


Figure 4-1: DEP holding in one dimension. (A) Plots of the electric field  $E$  (—) and  $|E|^2$  (---) in arbitrary units due to one point electrode at  $x=5$  in one dimension. (B) Same as (A), but for two point electrodes ( $x=-5,+5$ ) in one dimension. With two electrodes, a potential energy well appears (---) around  $x=0$  and thus would provide one-dimensional holding.



**Figure 4-2:** DEP holding in two dimensions. A surface plot of  $|E|^2$  near two point electrodes. Two electrodes give an effective potential well in the  $x$ -direction only. There is negligible confinement in the  $y$ -direction.

slope go to infinity in the vicinity of the electrodes, the  $x$ -directed holding will also go to infinity. In a real device, this means that the  $x$ -directed holding will be large with this configuration. The  $y$ -directed holding, on the other hand, will be much smaller because there are no electrodes on the  $y$ -axis to cause an infinite force. Thus, the cage will be orders of magnitude large in  $x$  than in  $y$ , and one can regard the two electrodes as possessing one dimension of holding. (In actuality, there is a small  $y$ -directed confining force on the  $y$ -axis at  $x=0$ , but this will be negligible compared to the  $x$ -directed confining force).

From the above discussion, one learns that two electrodes are necessary for one-dimensional confinement, while more are needed for two-dimensional confinement. Extrapolating, I can see that to get strong holding in  $n$ -dimensions requires  $2n$  electrodes, arranged two per direction. This is consistent with the planar quadrupole, which with 4 electrodes holds in two dimensions; it does not by itself hold in the  $z$ -direction—the weight of the particle counterbalances the destabilizing  $z$ -directed DEP force.

One could imagine a trap involving three electrodes arranged triangularly to give two-dimensional confinement. However, it is not trivial in this case to determine the proper voltages to apply to the electrodes—more than two discrete potentials are needed. This is not to say that three electrodes arranged in some fashion cannot meet these requirements. However, it is a difficulty that can be easily circumvented by going to a  $2n$  electrode configuration.

For the  $\mu$ DAC, I am primarily concerned with strong trapping in two dimensions, and thus four electrodes will be sufficient. Trapping in the  $z$ -direction can be handled by the weight of the particle, as with the planar quadrupole.

A few caveats must be mentioned as per the above discussion. First, the above discussion concerns highly symmetric charge distributions on each axis. For actual extruded

structures, the tops and bottoms of the electrodes will break axial symmetry and affect the holding. For the extruded traps used in this thesis, these effects will be beneficial. Careful design exploiting these effects could possibly lead to even better traps, as defined by some metric.

### 4.2.2 Electrode shape/arrangement

If I now assume that the trap will have four electrodes, how should they be arranged and how should they be shaped? The two questions can be answered together by noting that almost any arrangement of four electrodes will result in a field minimum somewhere, and that near that minimum the field will look quadrupolar. Since the particle will be trapped at the field minimum, arrangement and shaping of the electrodes, while drastically affecting the fields near the electrodes, will only slightly affect the fields near the minimum.

Since the shaping and electrode arrangement are second-order effects, I have not shaped the electrodes at all (apart from making them cylindrical) and have only slightly disturbed the true quadrupole arrangement, as described below. If one desires additional functionality besides trapping, such as fluid guiding then shaping of the electrodes may be appropriate.

One final point, related to the aforementioned questions, concerns the proper driving voltages and phases. One could make a cage by applying  $+V$  to all electrodes, as opposed to the alternating ( $+/-$ ) voltages applied to quadrupoles. In general, it is beneficial to alternate voltages on the quadrupole since it tends to enhance the fields—and hence the holding—inside the trap. One way to see this is to note that if one applies  $+V$  to all the electrodes and increases the number of electrodes, the field will eventually decrease to zero inside the trap—for the same reason that there is no field inside an infinite cylinder of charge.

### 4.3 The extruded trap—optimization

Up to now I have demonstrated that a good trap—for the  $\mu$ DAC—can be achieved by using four extruded cylindrical electrodes, arranged and excited in a quadrupole configuration. Thus, the trap looks as in Figure 4-3A. Further optimization can now be used to improve the performance of the trap.

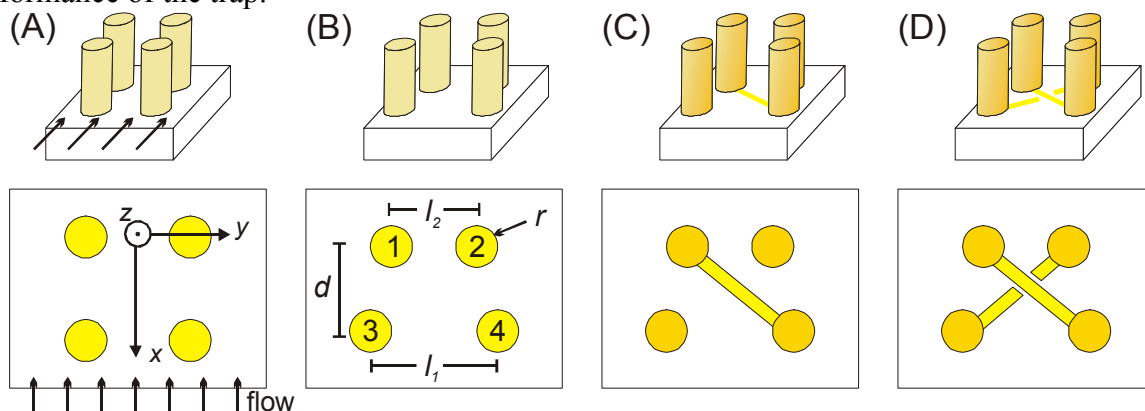


**Figure 4-3:** Evolution of the extruded trap. (A) Four cylindrical electrodes arranged in a square, along with the reference axes and the direction of flow. (B) Four cylindrical electrodes arranged trapezoidally. Also shown are the geometric variables used in the trap optimization simulations and numerical labels for individual electrodes. (C) Introduction of wiring between two electrodes. (D) Final electrode configuration, showing the two shunts that restore the symmetry to the trap. For all these configurations, flow is applied as in (A). The axes shown in (A) also apply to the other three traps.

### 4.3.1 Electrode height

For perfectly cylindrical electrodes, the electrodes need to be at least as high as the diameter of a cell and additionally encounter a good fraction of the cells in the flow. The constraint is that high-aspect-ratio posts will be fragile and difficult to fabricate. Later on in this chapter I will perform a system-level design of the chamber, the result being that the chamber will be 150  $\mu\text{m}$  high. I have thus chosen an electrode height of 50  $\mu\text{m}$ , which is  $>4x$  as high as the cell radius, and 1/3 of the chamber height. Thus, this height should allow traps to encounter at least 1/3 of the cells in the flow (more if the cells are allowed to settle) and be much taller than the cell size, so that a cell can fit within the trap.

### 4.3.2 Electrode arrangement/diameter

The next characteristic to pin down is the electrode arrangement. I want to have a low barrier for entry into the trap, but a high barrier to exit. This will make it easy to load the traps but still result in strong traps. The entry barrier field is in large measure determined by electrodes 3 & 4, while electrodes 1 & 2 largely determine the exit barrier (see Figure 4-3B). Thus, by increasing the separation of electrodes 3 & 4 with respect to the separation between 1 & 2, the trap should be easier to load and still remain strong.

Indeed, this is the case. Figure 4-4 shows a plot of the  $|E|^2$  term (proportional to the DEP potential energy) along the  $y$ -axis for two differently asymmetric trap geometries under the same experimental conditions. The change in the entrance-electrode spacing from 50  $\mu\text{m}$  to 70  $\mu\text{m}$

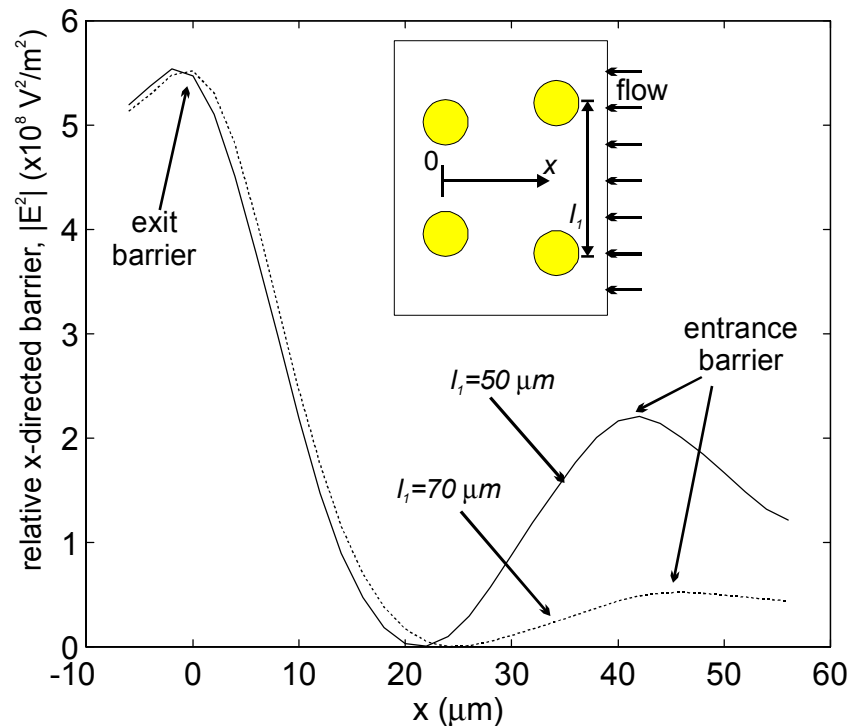


**Figure 4-4:** Comparison of  $x$ -directed barriers for two trap geometries. The first geometry (—) is only slightly asymmetrical, with an entrance-electrode separation ( $l_1$ ) of 50- $\mu\text{m}$  and an exit-electrode separation ( $l_2$ ) of 40- $\mu\text{m}$ . The second geometry (---) has the same exit-electrode separation but a 70- $\mu\text{m}$  entrance-electrode geometry. Plotted is the  $|E|^2$  factor along the  $y$ -axis at a height of 16  $\mu\text{m}$ . The height of the rightmost peak (at  $x=40 \mu\text{m}$ ), corresponding to entrance barrier, is lowered more than the second peak upon changing to more asymmetric trap geometry. The axes are as defined in the inset.

barely affects the exit barrier height (at  $x=0$ ) but lowers the entrance barrier height  $\sim 5x$ , making the trap much easier to load.

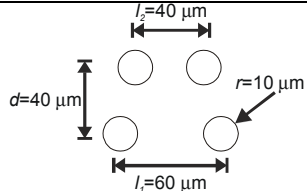
For a final optimization of the trap geometry—electrode diameter, absolute spacings, etc.—I performed a series of simulations within a matrix of variations (Table 4-1), varying each parameter while holding the others constant, to determine the final geometry. The simulations are all for beads in these traps, and so the absolute release flowrates predicted will not be the same as when using cells. In fact, the traps can be expected to be weaker with cells because of their smaller CM factor. However, since I am only interested here in the *relative* performance of the different trap designs, simulations with beads are appropriate. In the system-level design section later on, I will perform simulations with cells to converge to an *absolute* design.

The results are shown in Figure 4-5, where I plot the calculated release flowrate and imposed electric field at 3V. This choice of parameters is because the release flowrate is an indicator of performance whereas the imposed electric field is a variable that must be minimized, as I will discuss below in the system-level design section. Knowing that all traps have monotonic holding characteristics with the same basic shape, only one simulation point is necessary to compare them.

In agreement with the result in Figure 4-4, the variation of  $l_1$  has a negligible effect on performance (Figure 4-5B), as does the variation of the trap length  $d$  (Figure 4-5D). Changes in the post radius  $r$  and the exit-barrier separation  $l_2$  dramatically affect both the holding and the electric field in fairly linear manners. This makes sense by noting that the inner distance between the posts is  $l_2 - 2r$  and that this is the primary variable that will affect the imposed electric field (at a given voltage) near the exit and thus the trap strength. Choosing an electrode radius of  $10\ \mu\text{m}$  for fabrication ease, I have chosen an overall exit-post spacing ( $l_2$ ) of  $40\ \mu\text{m}$  to give clearance for the cells, a trap length  $d=40\ \mu\text{m}$ , and an entrance-electrode spacing of  $l_1=60\ \mu\text{m}$ . The final electrode arrangement is shown in Figure 4-3B and in the figure in Table 4-1.

### 4.3.3 Trap switching

The  $\mu\text{DAC}$  requires the ability to individually control trap sites. To minimize external connections, it would be advantageous if only one electrode needed to be switched to “turn off” a whole trap. One way to accomplish this is to switch the polarity of one electrode in the quadrupole, thus eliminating the symmetric arrangement of potentials. The result of doing this is shown in Figure 4-6. Here I plot the vector force fields in the  $xy$ -plane at the height of  $16\ \mu\text{m}$  when the quadrupole is stimulated with alternating polarities (Figure 4-6A), and when the

Initial geometry	
Variable	Range of variation
$r$	5 $\mu\text{m}$ , <b>10 <math>\mu\text{m}</math></b> , 15 $\mu\text{m}$
$l_1$	50 $\mu\text{m}$ , <b>60 <math>\mu\text{m}</math></b> , 70 $\mu\text{m}$
$l_2$	30 $\mu\text{m}$ , <b>40 <math>\mu\text{m}</math></b> , 50 $\mu\text{m}$
$d$	30 $\mu\text{m}$ , <b>40 <math>\mu\text{m}</math></b> , 50 $\mu\text{m}$

**Table 4-1:** Matrix for trap optimization. Shown is a top-down view of the initial trap geometry. Below that are the variables that were varied, one at a time, to trace out the design space. Bold numbers indicate the starting trap geometry on which the variations were made.

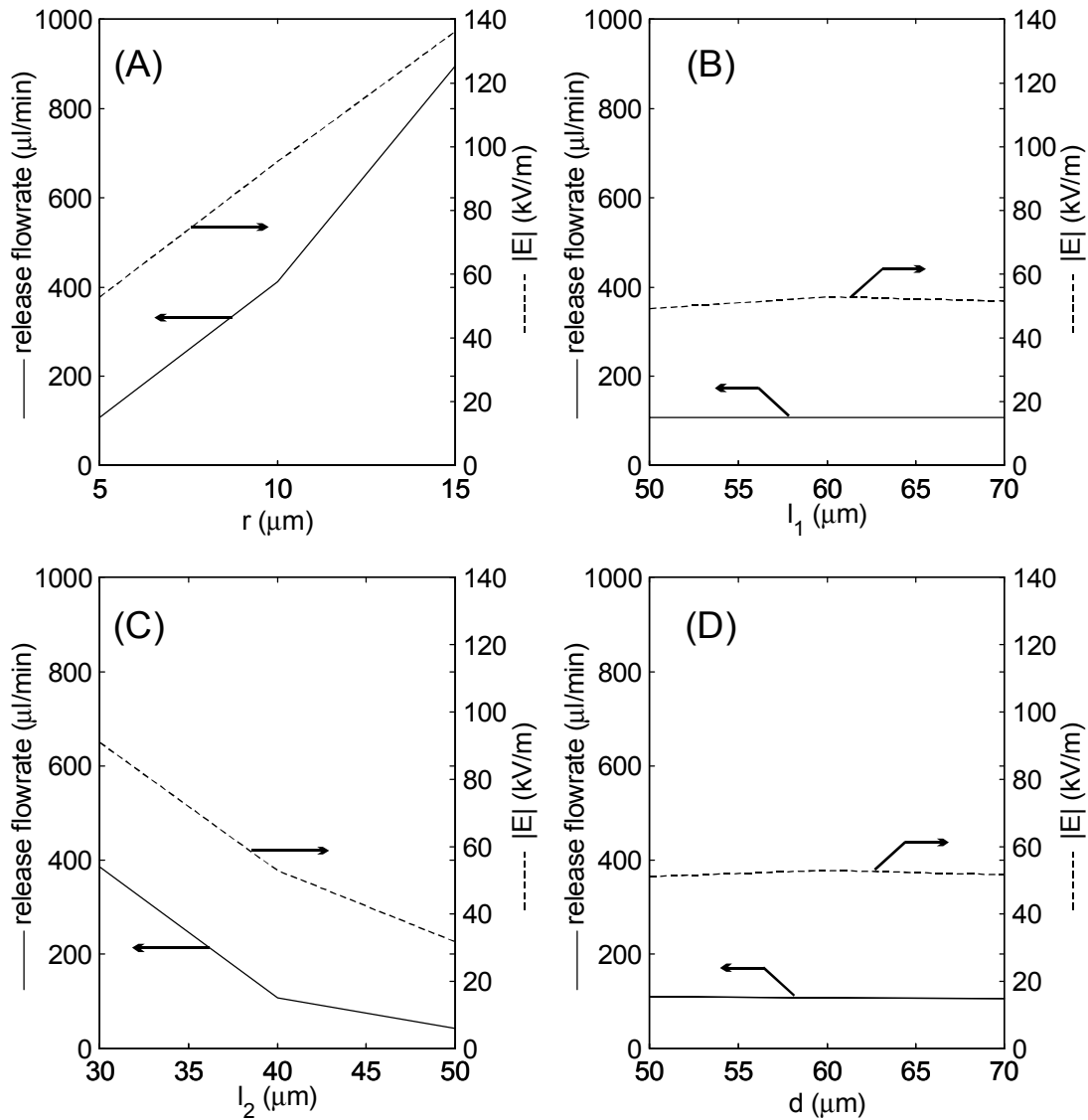


**Figure 4-5:** Results of trap optimization simulations. Plotted are the release flowrate (—, left y-axis) electric field experienced by the particle at release (---, right y-axis) for various trap geometries defined in (Table 4-1) under identical experimental conditions. Shown are variations in (A) electrode radius  $r$ , (B) entrance-electrode spacing  $l_1$ , (C) exit-electrode spacing  $l_2$ , and (D) trap length  $d$ .

polarity of electrode #2 is reversed (Figure 4-6B). The change in polarity of one electrode is enough to disrupt the potential energy well and eject the particle. Thus, in the final trap design this electrode is wired to be switchable in this way. The imposition of flow during release would change the trajectory of the ejected particle. Although it is unclear in this analysis what exactly that trajectory will be, the particle will be ejected in either situation, which is the goal.

#### 4.3.4 Wiring

For ease of fabrication, I have chosen to limit metalization to one layer with no dielectric insulation between the metal and the fluid. The following discussion of how to compensate for this becomes moot if multilayer metalizations and/or insulators can be used.

The optimal way to wire an array of traps within a small area and keep the lead count low is to tie one pair of electrodes to the same potential by connecting them through the middle of the

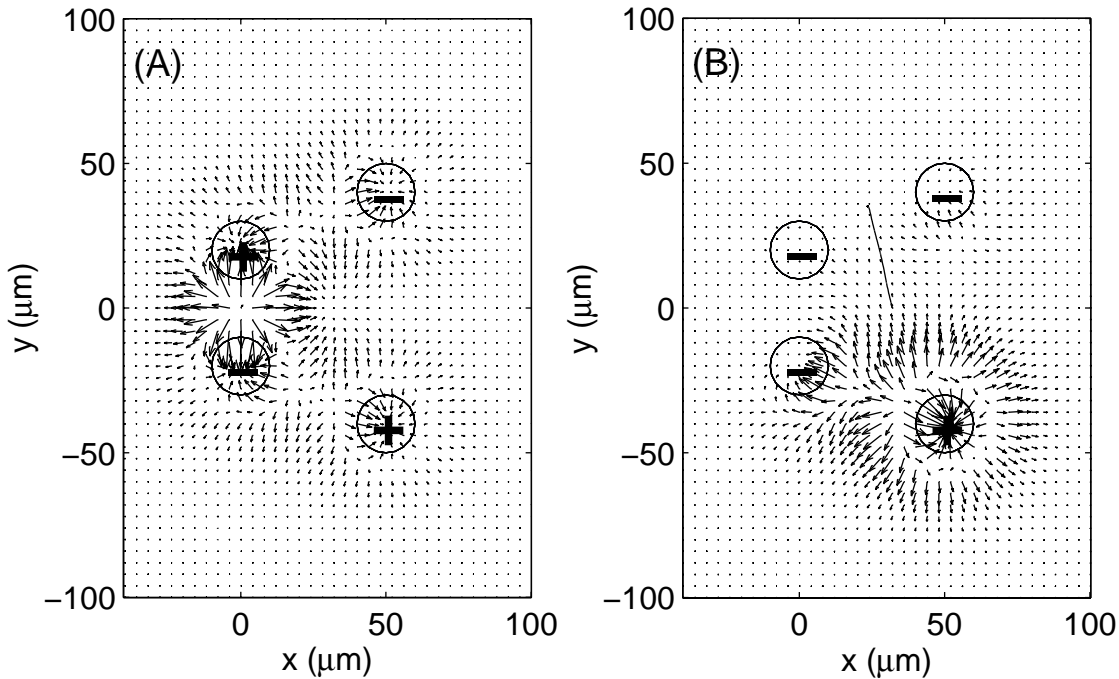


**Figure 4-6:** Trap switching via one electrode. (A) A vector plot of the DEP force in the  $xy$ -plane at a height of 16  $\mu\text{m}$  when the trap is excited conventionally (as shown in the figure). Within the trap, all arrows point to the center, indicating that a particle will be trapped in this circumstance. (B) Plot of the same situation when the polarity of the top-left electrode is changed from  $+V$  to  $-V$ . There is no longer a trapping region in this configuration. The black line shows the trajectory of a particle at the trapping point in (A) upon initiation of the excitation pattern in (B). The particle is ejected from the trap. This particular trap had 100- $\mu\text{m}$ -tall posts with  $d=50 \mu\text{m}$ ,  $l_1=40 \mu\text{m}$ , and  $l_2=80 \mu\text{m}$ .

trap, as shown in Figure 4-3C. Simulating the holding characteristic of this trap, I show in Figure 4-7 that the trap is much weaker than the ideal trap with no wiring (Figure 4-3B). This figure also reinforces the monotonic nature of the holding characteristic for the extruded trap regardless of the specific trap geometry. The reason that the interconnected trap is much weaker than the “ideal” trap is that the interconnect disrupts the symmetry of the trap, reducing its quadrupolar nature and thus its strength. One approach towards restoring the strength of the trap given the need for the interconnect would be to restore its symmetry.

I empirically designed and simulated a number of possible wiring schemes to try to restore the trap strength. To efficiently compare the wiring schemes, I simulated their behavior at one voltage under identical experimental conditions ( $R=10 \mu\text{m}$  bead,  $f=20 \text{ MHz}$ ,  $w=5 \text{ mm}$ ,  $\sigma_m=1 \text{ S/m}$ ). The designs and simulated release flowrates are shown in Figure 4-8. Although several wiring schemes (#4-#6) perform equally well in restoring the trap strength, wiring scheme #4 delivers the most restoration of the holding while minimizing the encountered electric field. As described below in the system-level design, minimizing the electric field encountered by the particle is essential for optimal performance. I have thus chosen wiring scheme #4 for these traps, shown in Figure 4-3D.

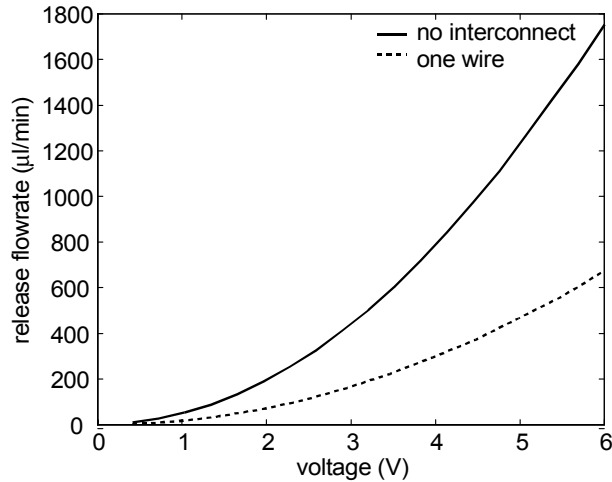


**Figure 4-7:** Holding characteristic of the single-wire trap. Plotted is the release flowrate versus voltage for the trapezoidal trap with (---) and without (—) a substrate interconnect between electrodes #1 & #4. The introduction of the substrate interconnect drastically reduces the holding in the trap and thus its performance.

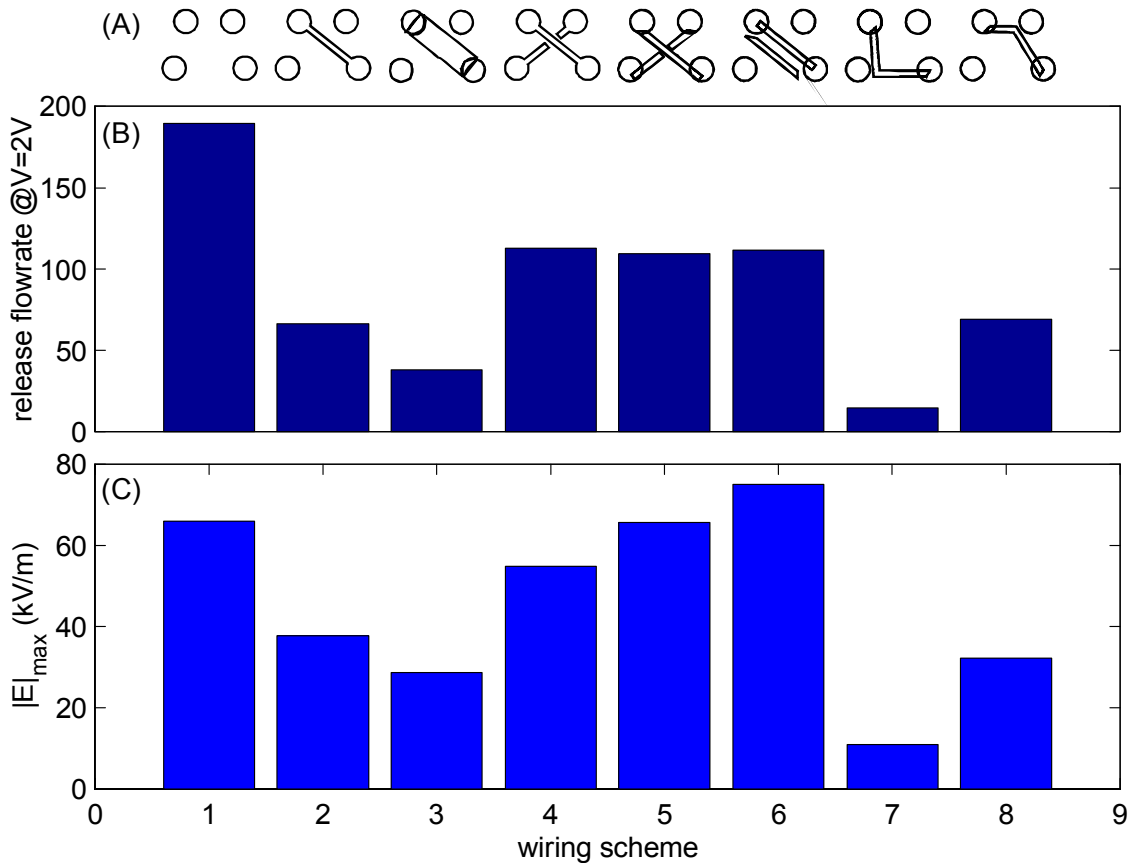


**Figure 4-8:** Results from various wiring schemes. (A) Shown are various empirically designed wiring schemes. The two left-most schemes are, from left to right, no internal wiring and a single interconnect. The rest of the schemes are designed restore the performance of the trap. (B) The release flowrate at 2V due to the wiring schemes in (A). The left-most result, from a trap with no interconnect, possesses the highest release flowrate and is the ideal trap. (C) The electric field encountered in the various traps in (A) at 2V. The schemes that improve the symmetry of the trap tend to restore most of the holding. Wiring scheme #4 is most effective at restoring holding while minimizing the encountered electric field.

To ensure that the wiring does not affect cross-wise holding, I have plotted the  $x$ - and  $y$ -directed holding forces for this wiring scheme at a height of  $16\ \mu\text{m}$  under the same conditions as above in Figure 4-9. The surfaces display both the  $x$ -directed (similar to Figure 4-4) and  $y$ -directed barriers to the particle. Even though the  $x$ -directed barrier is high ( $\sim 500\ \text{pN}$  along the central axis) as expected, the  $y$ -directed barrier is also quite substantial ( $300\text{-}500\ \text{pN}$ ). Thus, optimizing the  $x$ -directed barrier height does not affect  $y$ -directed barrier for this trap. One can expect that any cross-flows necessary to remove the particle from the trap would have to be of the same magnitude as the imposed ( $x$ -directed) flow, and thus not likely to occur.

#### 4.4 System-level design

I can now undertake a system-level design to determine the chamber geometry and operating regimes for the final trap design. This step will move the design from a *relative* comparison between geometries to an *absolute* analysis of holding with cells in defined situations. The system-level requirements are to find an acceptable flowrate and operating voltage such that trap operation with the  $\mu\text{DAC}$  is feasible. In essence, these two requirements are even more important than the holding force; if it was possible to find a trap with a low holding force but that was able to meet the system requirements, then this trap would be acceptable for the  $\mu\text{DAC}$ . As described in Chapter 3, the planar quadrupole, which is such a weak trap, could not meet the system requirements, and it is this fact that motivated the search for a higher-performing trap.

The primary quantitative requirements, as described in Table 4-2, are that the time needed to introduce reagents into the chamber be less than 2 minutes, the maximum shear on the cells be less than  $0.1\ \text{Pa}$  ( $1\ \text{dyne}/\text{cm}^2$ ), and the maximum externally imposed transmembrane potential by the cells be  $<70\ \text{mV}$ . In addition, it requires one-electrode electrical switchability

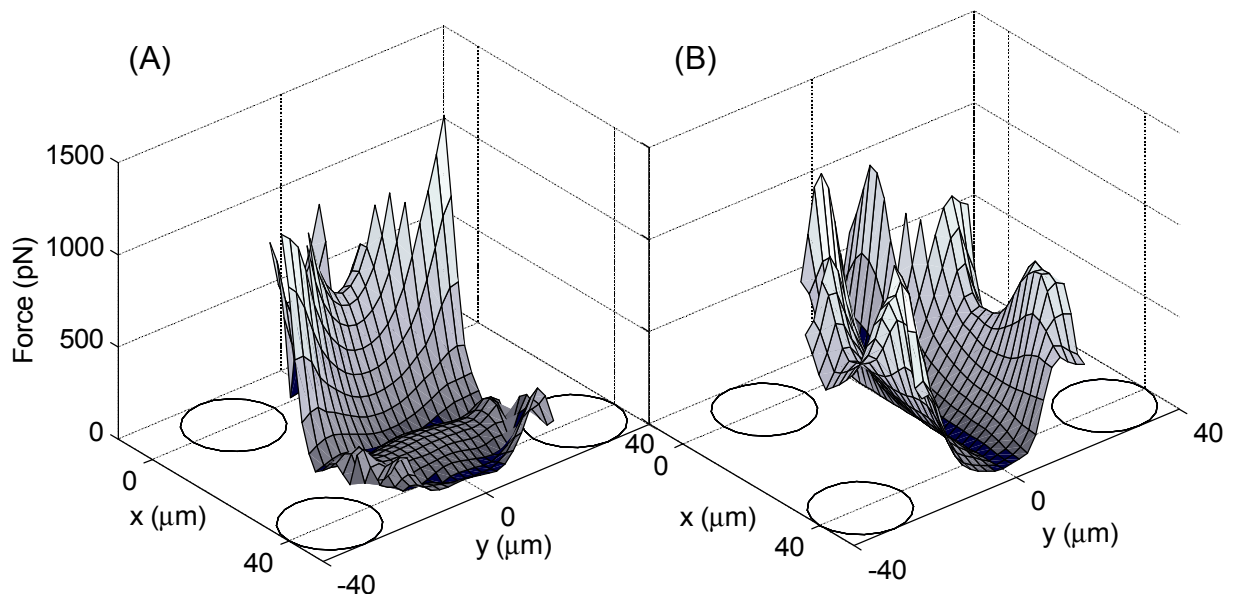


**Figure 4-9:** In-plane holding of selected wiring scheme. Shown are surface plots of the magnitude of the  $x$ - and  $y$ -directed DEP forces at a height of  $16\ \mu\text{m}$  for wiring scheme #4. The results were obtained for beads at  $V=2\ \text{V}$ . The placement of the posts is indicated by the circles. The  $x$ - and  $y$ -directed holding are adequate with this design.

Parameter	Target
Fill time	120 s
Maximum shear stress	0.1 Pa
Maximum transmembrane potential	70 mV
Electrical switchability	One electrode
Arrayability	Yes

**Table 4-2:** System-level specifications of the  $\mu$ DAC.

and a trap geometry that is easily arrayable. Most of these parameters are more strongly dependent on chamber height than width because the flow approximates plane Poiseuille flow—the width simply sets the volume flowrate.

#### 4.4.1 Fill time

In order to operate the  $\mu$ DAC in a timely manner, it must not take too long to introduce reagents into the chamber. For the  $\mu$ DAC, I have chosen 120 s as an appropriate fill time. This fill time will be dependent on the void volume of the system and the maximum flowrate that the trap can withstand. Thus, I can trade off void volume for flowrate if the fill time is fixed (as it is). For a rectangular chamber, the volume flowrate ( $Q$ ) needed is

$$Q = (wlh + V_0) / t_f \quad (4-2)$$

Where  $w$ ,  $l$ , and  $h$  are the chamber width, length, and height, respectively,  $V_0$  is the void volume of the tubing, and  $t_f$  is the fill time. The chamber will be approximately 8x2x0.15 mm or 2.4  $\mu$ l, and thus its volume will be dwarfed by any tubing void volume. In this case, Eqn. (4-2) can be approximated as

$$Q \cong V_0 / t_f \quad (4-3)$$

and to 1<sup>st</sup> order the chamber dimensions do not affect the fill time. A reasonable void volume to expect is 20  $\mu$ l, which corresponds to about 10 cm of standard 0.020"-diameter HPLC tubing. This gives a target flowrate of 10  $\mu$ l/min that the trap must withstand.

In many respects these parameters—fill time, chamber volume, and void volume—are extrinsic to the performance of the trap itself. One can always redesign the experimental setup and protocol to vary these parameters.

#### 4.4.2 Shear on cells

Stationary cells in the traps will experience shear forces from the flow. The maximum shear experienced by the cells must be less than that which will cause any physiological disturbance. Arterial shear stress is about 1.5-2.0 Pa (15-20 dyne/cm<sup>2</sup>) [161], and so I want to keep shear stress levels well below that value, or about 0.1 Pa (1 dyne/cm<sup>2</sup>). To get an estimate of the shear, two extreme cases can be considered—1) the cell against the substrate, and 2) the cell in the center of flow.

Against, the substrate, the cell will feel approximately the wall shear resulting from plane Poiseuille flow, which is

$$\tau = 4U_c \eta / h = \frac{4}{h} \left( \frac{3Q}{2A} \right) \eta = \frac{6Q}{wh^2} \eta \quad (4-4)$$

where  $\tau$  is the shear stress,  $U_c$  is the centerline flow velocity,  $A$  is the cross-sectional area and  $\eta$  is the viscosity of the water.

At the centerline of the chamber, the cell will experience shear due to the Stokes' flow around it, which at its maximum is given by

$$\tau = \frac{3V_c}{2R} \eta = \frac{3}{2R} \left( \frac{3Q}{2A} \right) \eta = \frac{9Q}{4whR} \eta \quad (4-5)$$

Thus I see that the centerline shear will be  $\sim h/3R$  larger than the wall shear. It is better therefore to keep the cell near the wall, rather than in the flow. For our situation, where the cell is about 1/5 of the distance between the substrate and the centerline, the first (and smaller) expression for the shear is appropriate. In this case the shear is strongly dependent on the chamber height ( $1/h^2$ ) if the flowrate ( $Q$ ) is independent of chamber height (Eqn. (4-3)). As described below, the final design will result in an imposed shear of 0.03 Pa, which is within the goals.

#### 4.4.3 Transmembrane potential

As discussed in §1.5.2, the imposed electric field can directly affect cell physiology by perturbing the cell's endogenous transmembrane potential. To minimize such effects one must limit imposed transmembrane potential, in this case to  $<70$  mV (Table 4-2). This feeds back into the design because I can calculate the imposed transmembrane load for a nominal electric field at a given frequency. Since that load will scale linearly with the electric field (Eqn. (1-10)), this will directly limit the maximum electric field that the cell can be exposed to, which is a parameter that can be extracted from the models. In Figure 4-10A I have plotted the computed

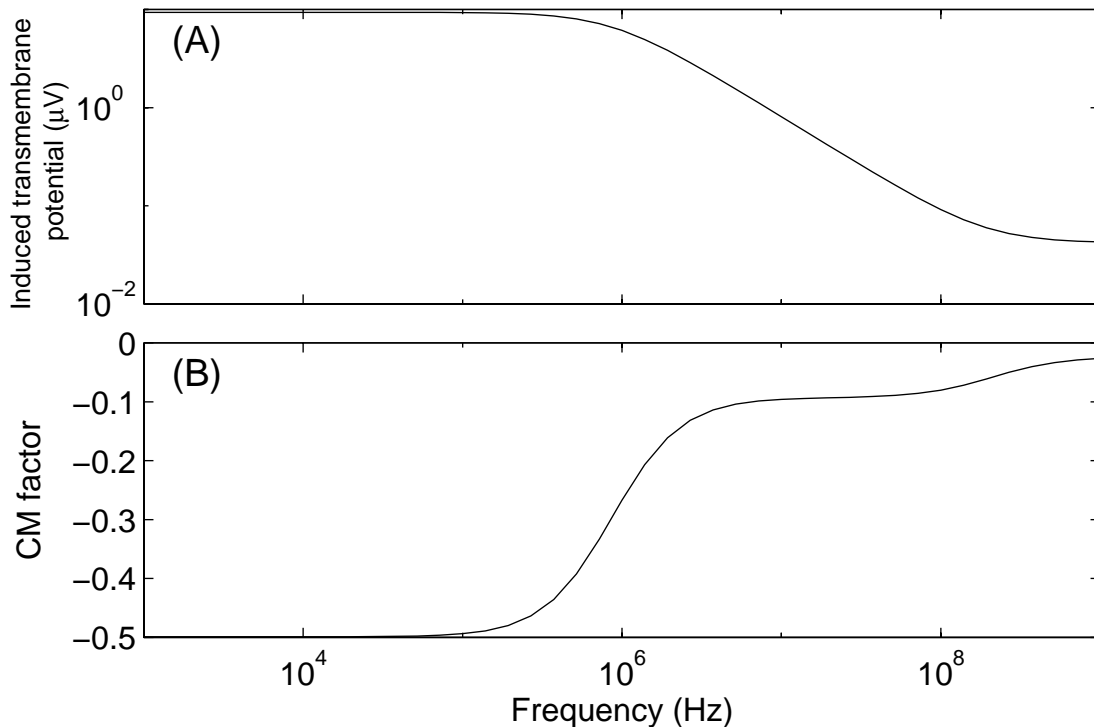


**Figure 4-10:** (A) Transmembrane potential of HL-60 cells. Plotted is the transmembrane potential imposed on HL-60 cells for an incident field of 1 V/m as the field frequency is varied. The transmembrane potential decreases logarithmically above a critical frequency and saturates at a yet higher frequency. (B) The dipole term of the CM factor for the same cells. The CM factor is saturated at  $-0.5$  for low frequencies and experiences two dispersions as the frequency increases.

transmembrane load imposed on HL-60 cells using Eqn. (1-10) but including the high-frequency dielectric saturation effect. I have used parameters for HL-60 cells described by the Gascoyne group [81] with radius  $R=6.25 \mu\text{m}$ , membrane capacitance and conductance  $C_m=1.6 \mu\text{F}/\text{cm}^2$  &  $G_m=0.22 \text{ S}/\text{cm}^2$ , membrane thickness  $\Delta=1 \text{ nm}$ , and cytoplasmic permittivity and conductivity of  $\epsilon_{cyto}=75 \text{ F}/\text{m}$  &  $\sigma_{cyto}=0.75 \text{ S}/\text{m}$ . The solution conductivity (of HBSS) was measured as  $1.0 \text{ S}/\text{m}$ . The figure shows that frequencies above  $1 \text{ MHz}$  are necessary and that operation at  $20 \text{ MHz}$  (at the limit of our signal generator) is preferable. At this latter frequency, the transmembrane voltage is  $0.4 \mu\text{V}$  for a  $1 \text{ V}/\text{m}$  field, and thus a  $70 \text{ mV}$  maximum transmembrane potential leads to a maximum electric field in the vicinity of the cell of  $\sim 1.8 \times 10^5 \text{ V}/\text{m}$ .

In Figure 4-10B I show the dipole term of the CM factor for the same cell, which, in analogy to Eqn. (1-2), is given by

$$CM = \frac{\underline{\epsilon}_p - \underline{\epsilon}_m}{\underline{\epsilon}_p + 2\underline{\epsilon}_m} \quad (4-6)$$

where  $\underline{\epsilon}_p$  refers to effective complex permittivity of the cell (Eqn. (1-3)) and  $\underline{\epsilon}_m$  is the complex permittivity of the medium. The transmembrane voltage and CM factor experience dispersions at the same frequency, which isn't surprising since they both represent time-constants of charging on either side of the membrane. The CM factor does not go to zero after the dispersion, however. This is because while the transmembrane voltage is across the membrane RC pair, the CM factor is due to the voltage across the network compared to the voltage across the medium in the absence of the cell; in effect, the CM factor represents the disturbance in the field due to the cell [119]. This disturbance exists whether the voltage is dropped across the membrane or the cytoplasm.

To get an estimate of how the electric field (and thus transmembrane potential) scales with the chamber height, I can use the fact (see Figure 4-7) that the release flowrate characteristic for the extruded traps has approximately the form

$$Q_{rf} = \alpha V^2 \quad (4-7)$$

where  $Q_{rf}$  is the release flowrate and  $\alpha$  is some fitting parameter. In essence, the release flowrate is dependent on the square of the voltage. This makes sense if one considers that the dipole term of the DEP force also goes as  $V^2$ . I can introduce chamber height as a parameter, using the linearity of flow with chamber height, by

$$Q_{rf} = \alpha V^2 h/h_0 \quad (4-8)$$

where  $h_0$  is some nominal chamber height. Thus, if a given  $Q_{rf}$  is needed to meet the system parameters then the voltage needed will scale as

$$V = \sqrt{\frac{Q_{rf} h_0}{\alpha h}} \quad (4-9)$$

which goes as  $1/\sqrt{h}$ . Thus, increasing the chamber height should decrease the voltage needed, and thus the electric field experienced by the cells.

From the calculated holding characteristics for HL-60 cells, I can determine the chamber height and width that meet the system parameters along with an operating voltage and flowrate. The design is iterative, in that I simulate the characteristics for some chamber geometry and then use those results to optimize the chamber geometry. The program can easily record the electric field experienced by the cell at the point of release. Then, using the chamber height as a parameter, I can calculate the flowrate needed from Eqn. (4-2), the voltage that is therefore

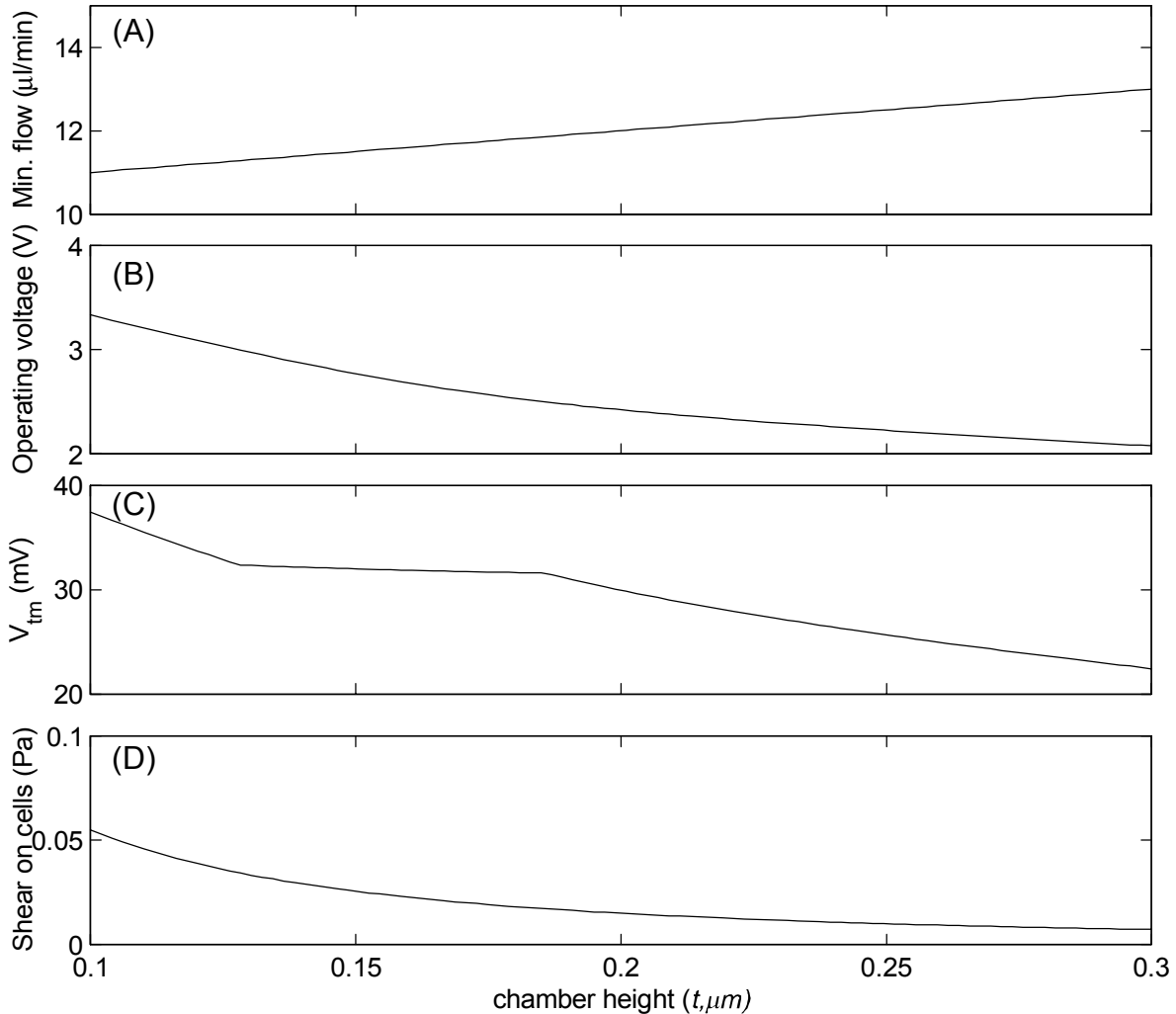
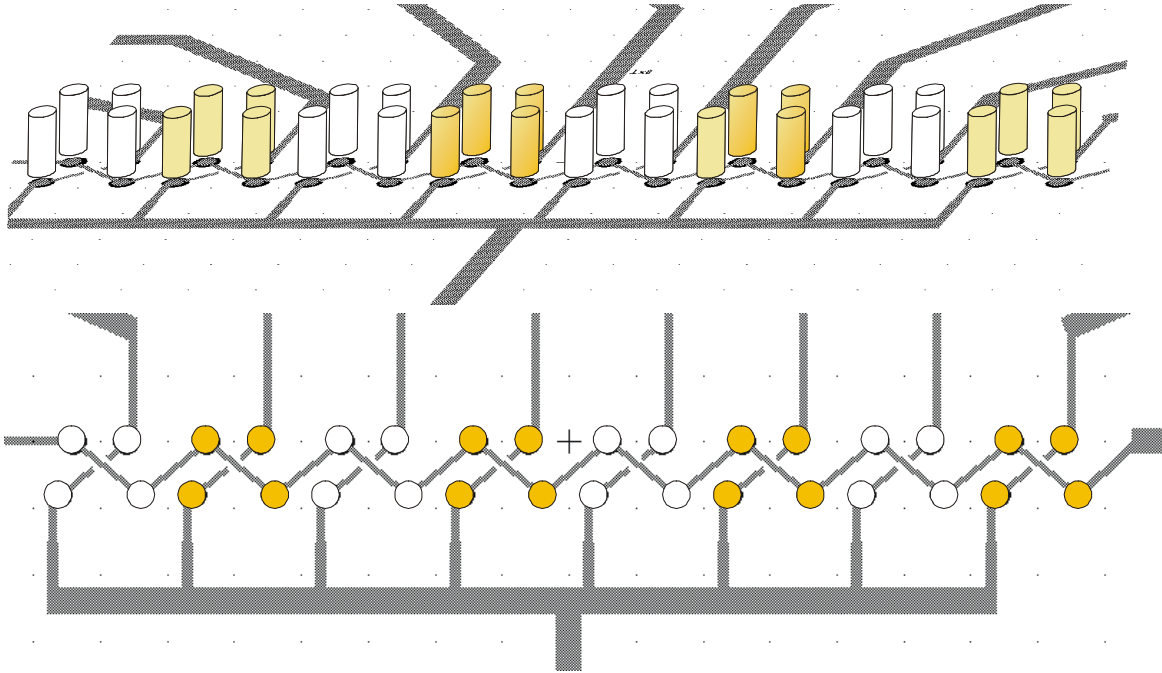


**Figure 4-11:** System-level design of chamber height. (A) Plotted is the minimum flowrate needed to fill the chamber in 120s (from Eqn. (4-2)) as the chamber height, and thus chamber volume, varies. (B) The voltage, obtained from the holding characteristic (Figure 4-13), needed to sustain the flowrate in (A). (C) The transmembrane potential encountered by the cell at the voltage in (B). (D) The shear on the cells at the operating flowrate in (A), from Eqn. (4-4). All values are for HL-60 cells in a chamber width ( $w$ ) of 2 mm and an applied frequency of 20 MHz.

required (from the holding characteristic), and thus the transmembrane potential experience by the cell. The result of this analysis is shown in Figure 4-11. The figure confirms the behaviors predicted above; the flowrate needed (Figure 4-11A) is fairly insensitive to the chamber height (and thus volume), while the operating voltage, induced transmembrane potential, and shear on the cells decrease with increasing chamber height. In all cases the transmembrane potential is  $<70\text{mV}$  and the shear on the cells is less than  $0.1\text{ Pa}$ . Thus, there is an operating point that will meet the system specifications of Table 4-2. I chose a chamber height of  $150\ \mu\text{m}$  to satisfy these requirements, giving an operating voltage of  $\sim 3\text{V}$  and a release flowrate of  $\sim 12\ \mu\text{l}/\text{min}$ .

#### 4.5 Final design

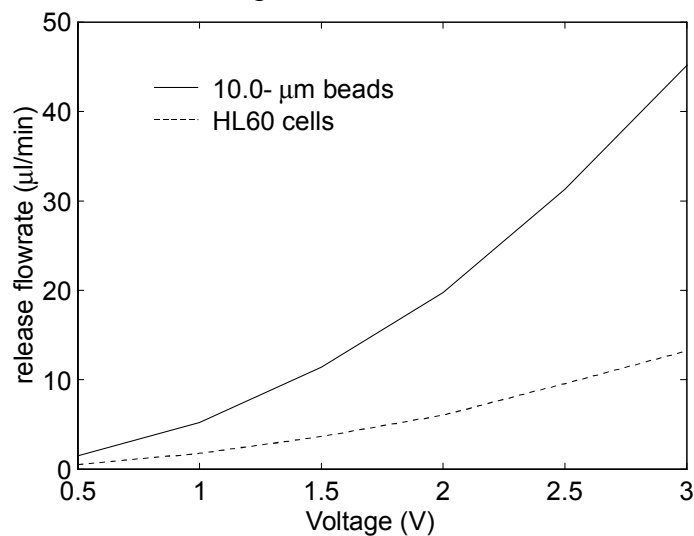
The final designed trap geometry is shown in Figure 4-3D and a schematic of a  $1 \times 8$  array is shown in Figure 4-12. The trap, with the chamber geometry described above, exhibits the



**Figure 4-12:** Schematic of a 1x8 array of traps, showing the interconnects and posts.

holding characteristic shown in Figure 4-13 for 10.0- $\mu\text{m}$  beads and HL-60 cells. The characteristic is indeed monotonic and approximately quadratic with voltage (again confirming the validity of Eqn. (4-7)). The actual release flowrates are much smaller than those shown during the relative design employed in the previous part of the chapter, even for the beads. The primary reason for this is that those simulations used 20- $\mu\text{m}$  beads, while these use 10- $\mu\text{m}$  beads, which gives an  $\sim 8\text{x}$  difference between the two (due to the  $R^3$  factor).

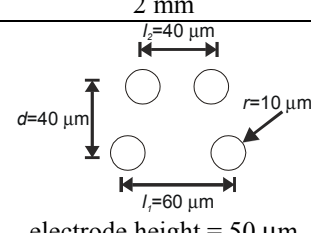
The differences in holding between the beads and cells shown in Figure 4-13 is almost entirely directly due to the differences in the CM factors ( $\sim 0.1$  for the cells,  $\sim 0.5$  for the beads) while the rest is due to differences in the particle sizes.



**Figure 4-13:** Holding characteristic for final trap (Figure 4-3D) in the finalized trap geometry, for 10.0- $\mu\text{m}$  beads (—) and HL-60 (---) cells at 20MHz. The holding characteristics are monotonic and are roughly proportional to  $V^2$ .

The extracted system-level parameters for the final design are shown in Table 4-3. As shown, the trap and chamber geometry meets all the system parameters for the  $\mu$ DAC.

I can compare the behavior of the final trap design with that of the planar quadrupole described in 0. For this comparison I have “placed” both traps in the same flow chamber (width, height), so that a fair comparison can be obtained. In Figure 4-14 I show the results of this comparison. Both the predicted release flowrates and holding forces of the extruded traps are much larger than for the planar quadrupole. In addition, the monotonic behavior of the extruded

Parameter	Target Value	Final Value
Time to load chamber	120 s	120 s
Shear on cells	<0.1 Pa	0.03 Pa
Transmembrane load	<70 mV	~30 mV
Electrical switchability	Y	Y
Arrayability	Y	Y
Operating voltage ( $V$ )	3 V	
Operating frequency ( $f$ )	20 MHz	
Release flowrate	12 $\mu$ l/min	
Chamber height ( $h$ )	150 $\mu$ m	
Chamber width ( $w$ )	2 mm	
Trap dimensions		

**Table 4-3:** Final system-level design parameters. Shown are the target and final values for the five system parameters in the design. Below that are displayed the trap dimensions and operating characteristics necessary to obtain those values.

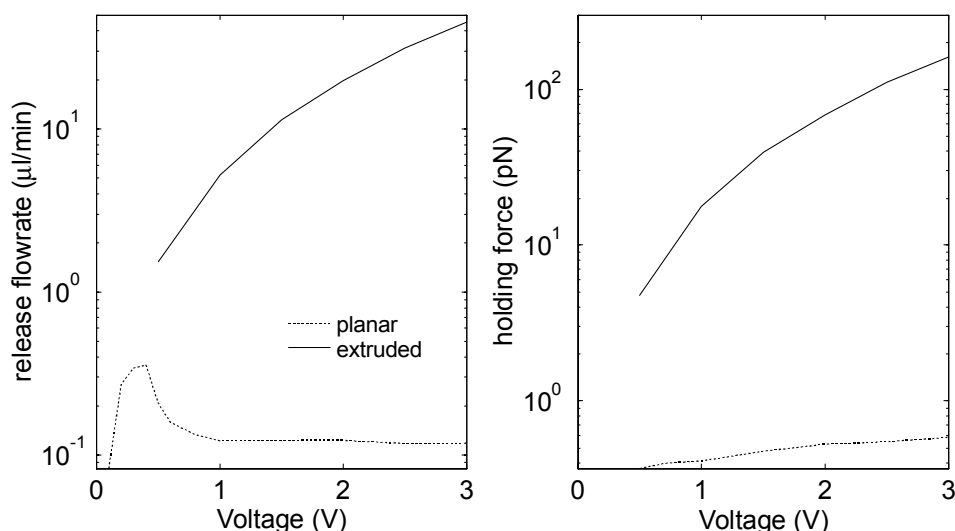


**Figure 4-14:** Comparison of the holding characteristics of the finalized trap design with the planar quadrupole of 0 for 10.0- $\mu$ m beads, both simulated with the finalized chamber geometry. (A) Plotted is the release flowrate versus voltage for the extruded (—) and planar quadrupoles (---). (B) Plotted is the extracted holding force versus voltage for the extruded (—) and planar quadrupoles (---). The extruded trap is at least an order of magnitude stronger than the planar trap.

trap allows the user to “turn up the voltage” if more holding is desired.

#### **4.6 Conclusion**

In this chapter I have undertaken the design of an improved DEP-based single-particle trap with characteristics that can meet the system requirements of the  $\mu$ DAC. Through extensive use of the modeling tools developed in Chapter 2, I have designed a trap that is an extruded quadrupole with an asymmetric trapezoidal geometry. It can be easily arrayed and is electrically switchable. The trap also incorporates substrate shunts to improve holding when only one layer of metal is used with no dielectric. Through the evaluation of the design in terms of the system parameters for  $\mu$ DAC operation, I have determined operating characteristics and chamber geometries that will result in successful operation.



## Chapter 5: Array fabrication, packaging & test setup

In this chapter I will describe the fabrication process for making the extruded trap arrays as well as the packaging and setup needed to test them. Various type of arrays were fabricated—1x4, 2x4 & 1x8—examples of which are shown throughout the chapter. The fabrication process is mostly concerned with obtaining a set of extruded posts by electroplating gold into an SU-8 mold. Other process steps form substrate interconnects and a fluidic chamber around the electrode arrays. The latter part of the chapter describes the packaging scheme needed to obtain electrical, optical, and fluidic connection to the chips, and finally the test setup used in the final two chapters of this thesis.

### 5.1 Fabrication

The fabrication process for making the extruded traps essentially involves fabricating extruded posts via electroplating into a mold and then encapsulating the array within a photoresist channel. The fabrication process flow for the making the extruded arrays is shown in Figure 5-1.

#### 5.1.1 Substrate interconnect

The first step in the process flow is to pattern the interconnect layer that resides on the substrate. I have chosen to use gold for the interconnect layer due to its biocompatibility [162] and because of the availability of differential etchants between it, titanium, and glass, the need for which is explained below.

The process starts with 100-mm-diameter 1-mm thick pyrex wafers. The thickness was chosen simply because of material availability. I cleaned the wafers with a 10-min Piranha clean and then used an e-beam evaporator to deposit 1700 Å of titanium and 5000 Å of gold (Figure 5-1A).

I chose to use titanium under the gold for several reasons. First, it serves as an adhesion layer between the glass and the gold. Second, the titanium can be etched with dilute HF, which has high selectivity to gold and glass. Finally, and most importantly, the SU-8 molding material that I will use later adheres fairly well to the titanium. I determined this last property by performing a series of experiments testing the adhesion of SU-8 to various metals (Cr, Ti, Ni, Pt)

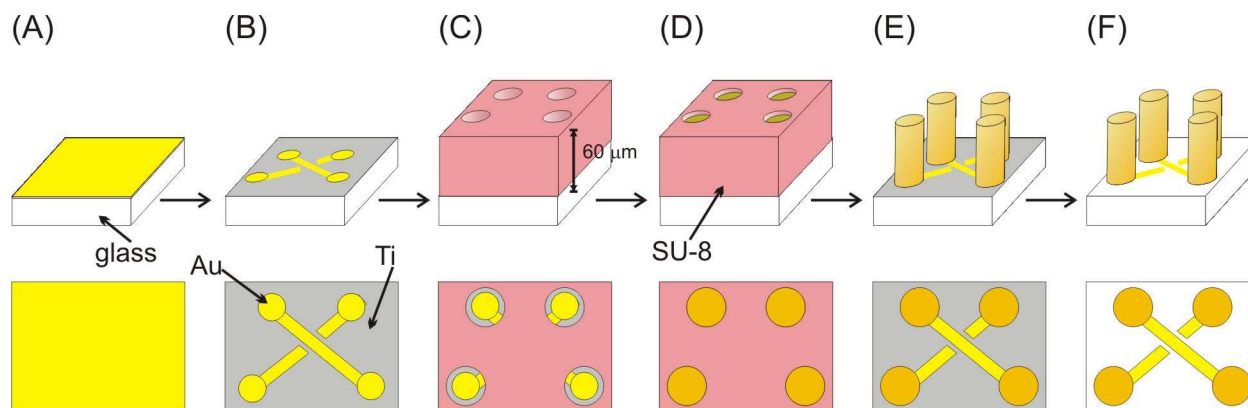


Figure 5-1: Fabrication process flow for the extruded traps.

and found that titanium performs best.

Following deposition, I performed standard contact lithography and pattern etching of the gold to define the substrate interconnect (Figure 5-1B). I used a potassium iodide-based etchant (Gold Etchant Type-TFA, Transene, Danvers, MA), which displays high selectivity to titanium and glass, to etch the gold. The availability of this selective etchant enables the use of this gold/titanium/glass tri-layer system, as described above. The etchant severely undercuts photoresist (although much less than aqua regia), so the as-drawn mask features were biased to account for this. The nominal undercut for perfect isotropy would be 5000 Å, but the actual undercuts were closer to 2 μm. Thus I used 8-μm linewidths on the mask to achieve 4-μm features. In practice, however, the undercut was a bit more, and final features varied from entirely undercut (Figure 5-2A) to ~3-4-μm linewidths (Figure 5-2B). Different etchant formulations (manufactured by Transene) could be used in the future to reduce this undercut.

The best way to obtain well-defined metal lines is by lift-off, so the question arises as to why I chose not to use that process. The reason is that it is impossible with lift-off to obtain a Ti-Au metal bilayer and have patterns on only one of the layers. The unpatterned Ti layer is needed for the electroplating process (described below). Thus, pattern etching of the gold is the best alternative.

### 5.1.2 SU-8 mold deposition

The extruded electrodes are fashioned from posts electroplated into SU-8 (Figure 5-1C & Figure 5-1D). SU-8 is an epoxy-based negative photoresist developed by IBM in the 1980's [163, 164]. It is useful because it can be patterned with conventional contact lithography into high-aspect-ratio microstructures. The photoresist can be spun with single coats into layers ranging from a few microns to 100's of microns thick (depending on the formulation), and is extremely conformal. In addition, the developed photoresist is quite robust and can be fashioned into structural layers. Essentially, the photoresist enables one to do LIGA with conventional equipment.

SU-8 has been used as a mold for electroplating by several researchers [163-165]. The challenges lie in (1) getting it to adhere to the substrate, (2) patterning sufficiently high-aspect-ratio structures, and (3) removing the SU-8 following electrodeposition.

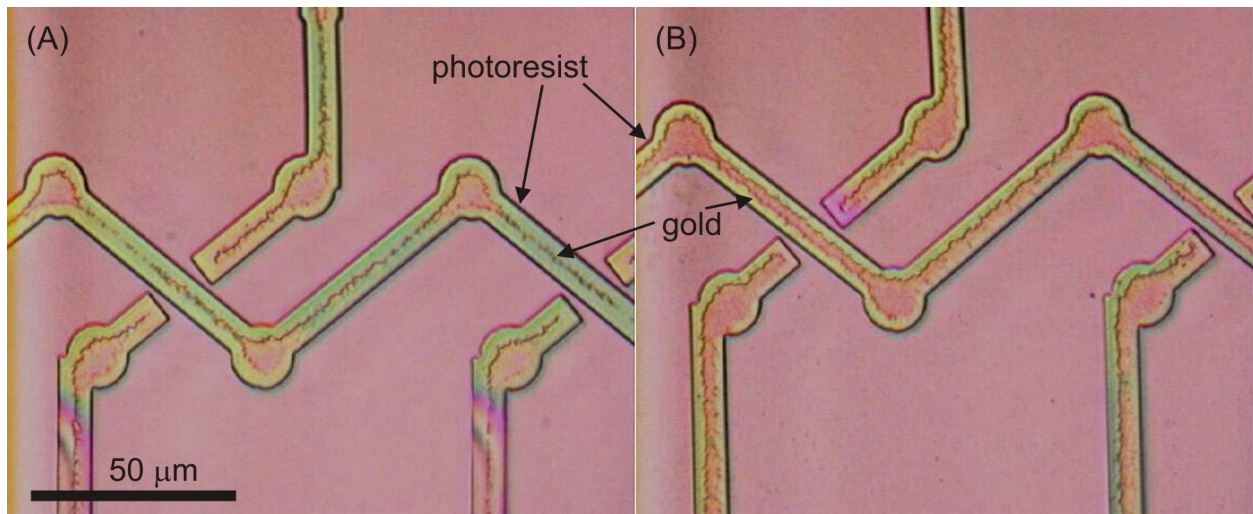


**Figure 5-2:** Top-down view of the substrate interconnect following Au etching. Shown is an example of excessive undercut (A) and an acceptable specimen (B).

The first challenge was overcome by both using Ti as the contact layer and formulating a strict fabrication protocol to clean and prepare the surface for the SU-8. The protocol, described in Appendix B, essentially consists of first cleaning the wafer in Nanostrip (because the titanium layer cannot withstand Piranha), followed by a long dehydration bake on a hotplate and then a short UV ozone exposure. This is used in lieu of an adhesion promoter, since HMDS (hexamethyldisilazane) is incompatible with SU-8 and the commercial adhesion promoter (SMAD, Sotec Microsystems, Renens, Switzerland) was unavailable. This substrate preparation leaves the wafer sufficiently clean and hydrophobic for proper SU-8 adhesion.

Following the preparation, I spun SU-8 50 (Microchem Corp., Newton, MA) onto the wafer with a three-step coating cycle. The SU-8 was first deposited onto a stationary wafer, followed by a slow spread, a faster spin, and then a final short high-speed spin, resulting in a nominally 60- $\mu\text{m}$  thick layer. The reason for the final spin step was not to adjust the layer thickness but rather to control the edge bead. SU-8 50 is highly viscous and under these conditions forms a thick (15  $\mu\text{m}$ ) and wide (7  $\mu\text{m}$ ) edge bead around the wafer (Figure 5-3A). This edge bead prevents proper mask contact with the wafer. Without proper mask contact, I end up essentially doing a proximity exposure, which is terrible when trying to pattern high-aspect ratio structures. The final spin does not change the thickness of the edge bead but concentrates it around the periphery of the wafer, making it easier to subsequently remove (Figure 5-3B).

Following coating, I perform a relaxation step by letting the wafer rest on a leveled room-temperature hot plate for 30 min. This step is thought to reduce stresses in the as-spun SU-8 [166], which is important for getting good adhesion to the substrate. Leveling the hotplate is key to this and the prebake step to limit any thickness non-uniformities due to gravity-induced flow of the SU-8. After relaxation, the wafer is prebaked using a ramped temperature profile (to minimize thermal stress), where the final temperature and time are minimized. This minimization aids subsequent removal of the SU-8. I allow the wafer to cool to below 40° C before removing it from the hotplate in order to minimize any thermal shocks.

The next step is to remove the edge bead. I managed this by lightly rubbing the perimeter of the wafer with a PGMEA-coated cleanroom swab (PGMEA is the SU-8 developer). Careful rubbing could reduce the thickness of the edge bead without merely pushing the edge bead closer to the wafer center and creating a large ridge (Figure 5-4). This method is certainly sub-optimal but resulted in edge beads that averaged <10  $\mu\text{m}$  thick rather than the originally deposited 15

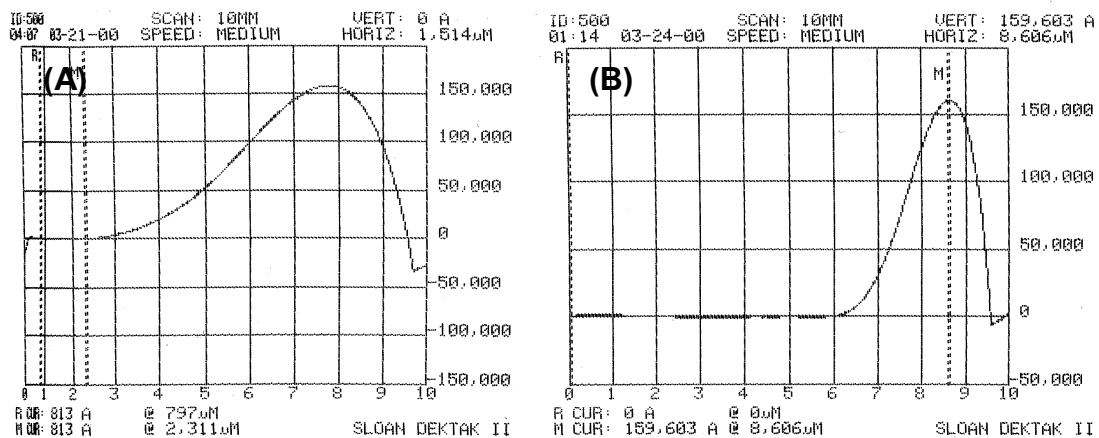


**Figure 5-3:** Dektak measurements of the edge bead from SU-8 coating without (A) and with (B) a final high-speed spin. The edge bead width reduces from ~7  $\mu\text{m}$  to ~3  $\mu\text{m}$  following the high-speed spin.

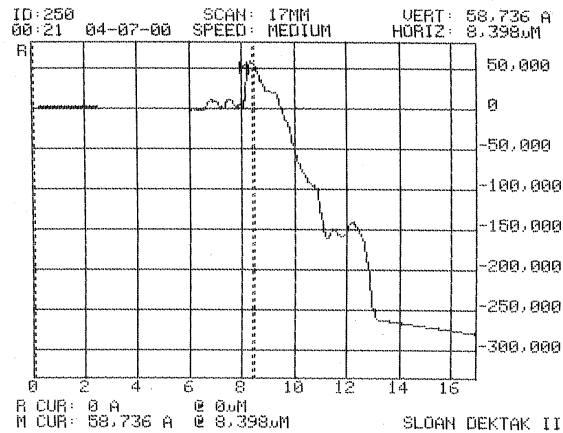


**Figure 5-4:** Dektak measurements of the SU-8 edge bead following PGMEA treatment of the edge. The edge bead has decreased to ~6 μm in this example. A spike appears where the edge of the swab has created an SU-8 ridge.

μm. One cannot simply perform a wafer-perimeter photo exposure step to remove the edge bead because the SU-8 is not a positive resist. Perhaps a more optimal technique would be to prebake the SU-8 with a cylindrical Teflon weight on the wafer that had a hole in it to permit SU-8 solvent fumes to escape. Such a jig would not adhere to the SU-8 and might significantly reduce the edge bead. Of course, the best method would probably be to use a coater with an integrated edge-bead removal system.

Following prebake, I performed contact lithography to define the holes in the SU-8 for the electrodes. The key to performing this lithography step is to obtain good contact between the mask and the SU-8 by minimizing any airgap. To do this, it's important to both remove the edge bead and use the vacuum contact mode on the aligner. Despite the thickness of the SU-8 one can see thru it well enough to achieve a few microns of alignment tolerance, which is sufficient for this application.

I chose the minimum exposure that would harden the photoresist without overexposing into the electrode holes—usually 40 seconds. When high-aspect-ratio features are desired, optimizing (and usually minimizing) the exposure is crucial. After exposure comes a ramped postbake on a hotplate, again minimizing the bake time to aid in future SU-8 removal.

The final step is to develop the SU-8 in PGMEA. This developer will remove the unexposed regions of the photoresist. Five minutes was sufficient to open up the electrode holes, followed by cycles of coating the wafer with PGMEA and spin-drying it to try to remove residue from the bottoms of the holes. Removal could be seen by a clearing of the bottoms of the holes a viewed under a microscope, although the thickness and small diameter of the holes made it difficult to see into them easily.

I eventually learned that simply rinsing the SU-8 in PGMEA is insufficient for removing all organic debris at the bottom of the holes and thus allowing electroplating initiation to occur. The solution to this was to introduce an oxygen ashing step after the development step and immediately before the electroplating. Ashing was performed in a barrel asher for 20-40 minutes, where the endpoint was that the bottoms of the holes across the wafer would appear clear under the microscope. This step drastically improved the yield of post initiation. Overashing will reduce the adhesion of the SU-8 to the substrate and cause underplating, so minimizing the ashing time is important.

After this step, the wafer looked as in Figure 5-6. The cracks in the SU-8 are due to shrinkage in the developer and are confined to the surface, thus not affecting the SU-8's suitability as a mold. These cracks result from stress can affect adhesion to the substrate and cause subsequent underplating, depending on the pattern and total stress involved. This was not a problem for the circular patterns, but has been a problem for rectangular regions, especially near corners.

### 5.1.3 Electroplating the electrodes

The next step is to electroplate the posts into the SU-8 mold (Figure 5-1D). As for the interconnects, I wanted to use gold for the electrode posts because of its biocompatibility. I performed the electroplating in a cyanide-based gold plating solution (Orotemp 24, Technic Inc., Anaheim, CA). Literature reports, however, suggest that non-cyanide gold plating solutions may actually function better in the presence of photoresists [167].

The electroplating setup is shown in Figure 5-5. It consists of a closed-loop hotplate-stirrer to heat and stir the plating solution, a power supply to apply current, and a jig to hold the wafer and anode in the solution. I used an insulated dip-style thermocouple to measure the solution temperature without affecting the electrochemistry. The power supply was a pulse-plating supply (Dynatronix, Amery, WI) capable of forward and reverse pulse plating. I used a

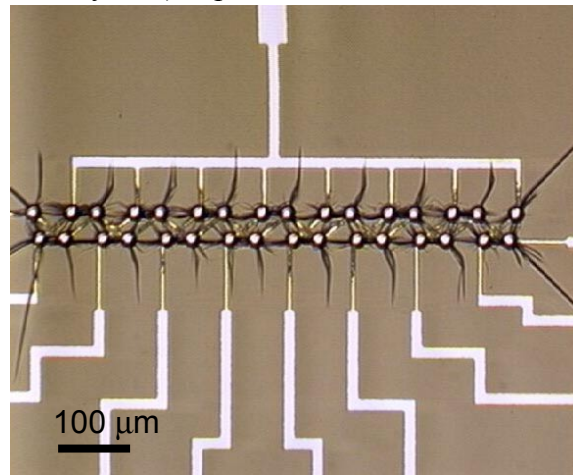


Figure 5-6: Image of a 1x8 array after SU-8 development and ashing.

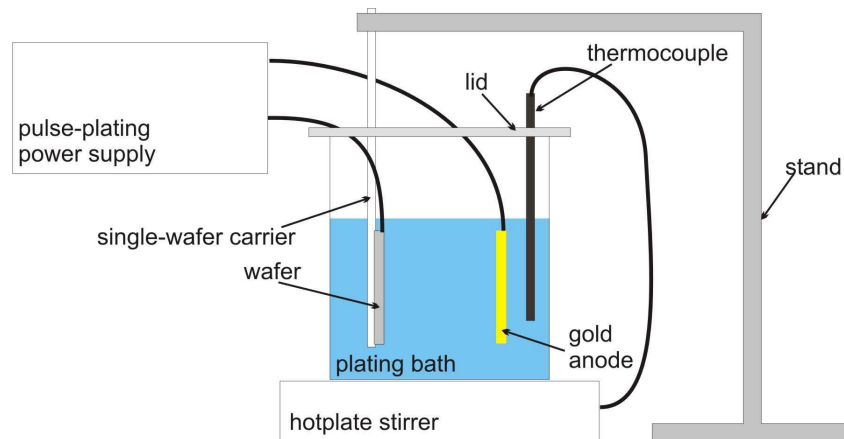


Figure 5-5: Schematic of the electroplating setup.

1-mil-thick 100x100 mm gold sheet as the anode and held the wafer (cathode) in the solution with a single-wafer carrier clipped at one end to complete the electrical circuit.

Electroplating works by forcing a constant current through the circuit composed of the power supply, anode, cathode, and plating bath. The faradaic current at the electrode/electrolyte interfaces oxidizes and reduces the species at the anode and cathode surfaces, resulting in solubilization of the gold foil (anode) and deposition of metal at the cathode [168]. Because of the availability of the pulse-plating supply, I used 1 ms forward-going pulses with a 10% duty cycle. The pulsing helps to refresh the concentration of electroactive species at the interface and thus increase the efficiency of the plating and reduce the time. With this setup, the manufacturer quoted plating rates of 0.1-0.3  $\mu\text{m}/\text{min}$  with 1-3  $\text{mA}/\text{cm}^2$  of current and this is what I obtained in practice. The current density needed to obtain these rates was difficult to measure because the small plated area introduced large errors, and so these parameters were determined via trial and error.

The need for the continuous titanium layer becomes apparent now. I used it to form a continuous electrode connecting all plated posts to the clip. I could not simply use the patterned gold layer for this connection as the patterns are not all connected together. In addition, the continuous nature of the titanium layer gives a low resistance to the layer, which minimizes voltage drops and enhances plating uniformity.

As noted above, I found it necessary to ash the wafers before electroplating. I originally tried electroplating without ashing, and found that the plating was difficult to initiate and that the yield was low. After trying several things (addition of surfactant, overnight developing of the SU-8) I realized that there was an organic layer at the bottom of the electrode holes that was extremely difficult to remove by developing alone. Upon introduction of the ash step, electroplating initiated readily.

One other potential problem with electroplating into a photoresist mold is underplating of the photoresist pattern due to delamination of the photoresist from the substrate. This can be induced by thermal expansion mismatch between the photoresist and substrate, inherent stresses in the photoresist, and chemical attack of the photoresist by the plating solution. This was not a problem for these circular structures, although other geometries may be more susceptible.

In practice I electroplated for a few hours and then measured the thickness with a microscope-coupled z-axis interferometry system to determine the deposition rate. Then I would obtain an approximate endpoint time and check the thickness every few minutes as the time approached to obtain the desired electrode height of 50- $\mu\text{m}$ . In addition, I would rotate the wafer every few hours to even out deposition-rate differences due to temperature and current-density gradients. With these techniques I was able to obtain post heights that varied  $\sim 10\%$  across the wafer. Figure 5-7A shows an array structure after electroplating.

#### **5.1.4 SU-8 mold removal**

After forming the extruded electrodes, I need to remove the SU-8 mold (Figure 5-1E). The resistance of SU-8 to chemical attack becomes a problem now because there is as of yet no standard procedure to remove the films. Various approaches have been tried, from high-temperature ashing [169] to NMP-based resist strippers [170]. Piranha solutions will remove the SU-8 but will also remove most metals, including the Ti adhesion layer that I used here. I have developed a three-step technique involving a wet stripper, an oxygen ash, and a wet chemical clean that seems to work fairly well.

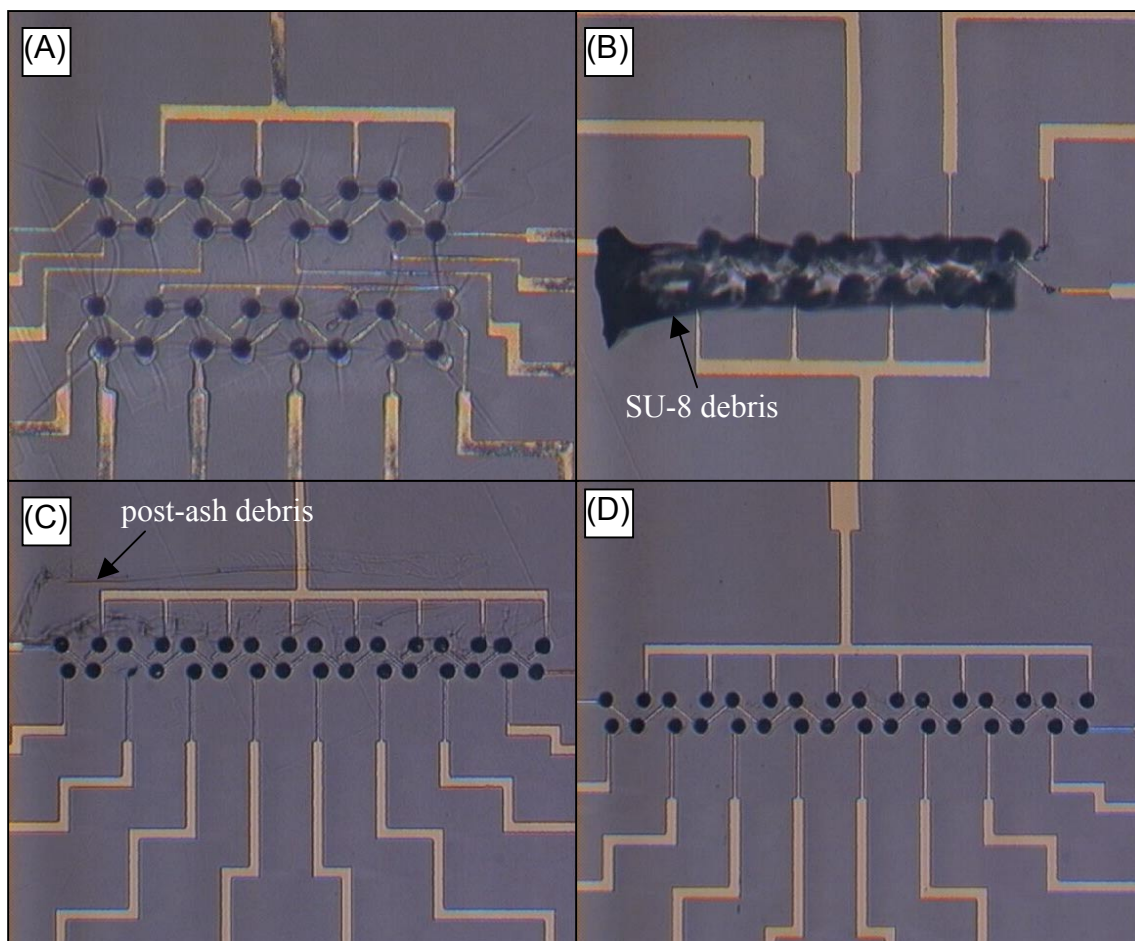


**Figure 5-7:** Electroplating & SU-8 stripping process. (A) A 2x4 electrode array after electroplating. The black circles are the electroplated posts, while the SU-8 cracks can also be seen. (B) A 1x4 array after stripping in the wet stripper, showing the SU-8 debris still attached to the posts. (C) A 1x8 array after ashing, showing that the majority of the debris is gone except for wispy post-ash debris. (D) A 1x8 array after Nanostrip, showing that all the debris has been removed.

For all stripping procedures, judicious handling of the SU-8 will ease the removal process. Minimizing prebake/postbake times and temperatures helps, as does limiting the total time that the SU-8 stays on the wafer [170]. For this process, I usually had the SU-8 on the wafer for 2-3 days before stripping, which worked well.

The first step in the removal process is the use of a DMSO-based (dimethylsulfoxide) stripper (ACT-691, Ashland Chemical Co., Pueblo, CO). I used the stripper in a glass beaker on an explosion-proof hotplate with an explosion-proof stirrer at 90 °C. At this temperature, the stripper swells the SU-8 and causes it to delaminate from the wafer and shred itself. The SU-8 is not actually dissolved in the stripper but exists as a suspension in the solution. Following this step I rinsed the wafer in cold stripper and then water. 45-90 minutes was sufficient to remove the vast majority of the SU-8, especially from the open areas of the wafer. SU-8 debris was still left around the posts, as shown in Figure 5-7B.

To remove this final debris, I put the wafer in a barrel asher until this debris was ashed away. While ashing is not practical for removing the complete 60- $\mu\text{m}$  SU-8 layer, I could effectively remove the SU-8 debris in 1-2 hrs (Figure 5-7C). Following ashing, there would

often be wispy debris in and around the posts (but off the substrate). A quick 5-min Nanostrip treatment removed these, most likely by simply dragging them away during rinsing. The final electrode structure is shown in Figure 5-7D.

### 5.1.5 Titanium adhesion-layer removal

The next step is to remove the Ti layer that had served to provide electrical contact for the electroplating (Figure 5-1F). If left in place, it would electrically short the posts together, preventing operation of the traps. Removal was straightforward with a dilute HF:H<sub>2</sub>O etch, which did not attack the gold and at these timescales and concentrations did negligible damage to the glass wafer. I endpointed the etch by looking to see when the wafer became transparent, indicating the loss of the titanium layer. Careful endpointing was necessary to prevent undercutting and lift-off of the gold lines. After Ti layer removal, the electrode structure looked as in Figure 5-8A. An underside view (Figure 5-8C) shows how the gold layer is undercut. This reinforces the need to start with gold lines that are as wide as possible and to endpoint the etch accurately. Failure to do this can result in lift-off of the gold lines if the titanium layer is entirely etched away. This two-step undercut (first gold, then titanium) was a major source of yield loss.

I found that a very thin film of unknown origin would be left over following the stripping process (Figure 5-8). The film could be distinguished under optical microscopy because of its

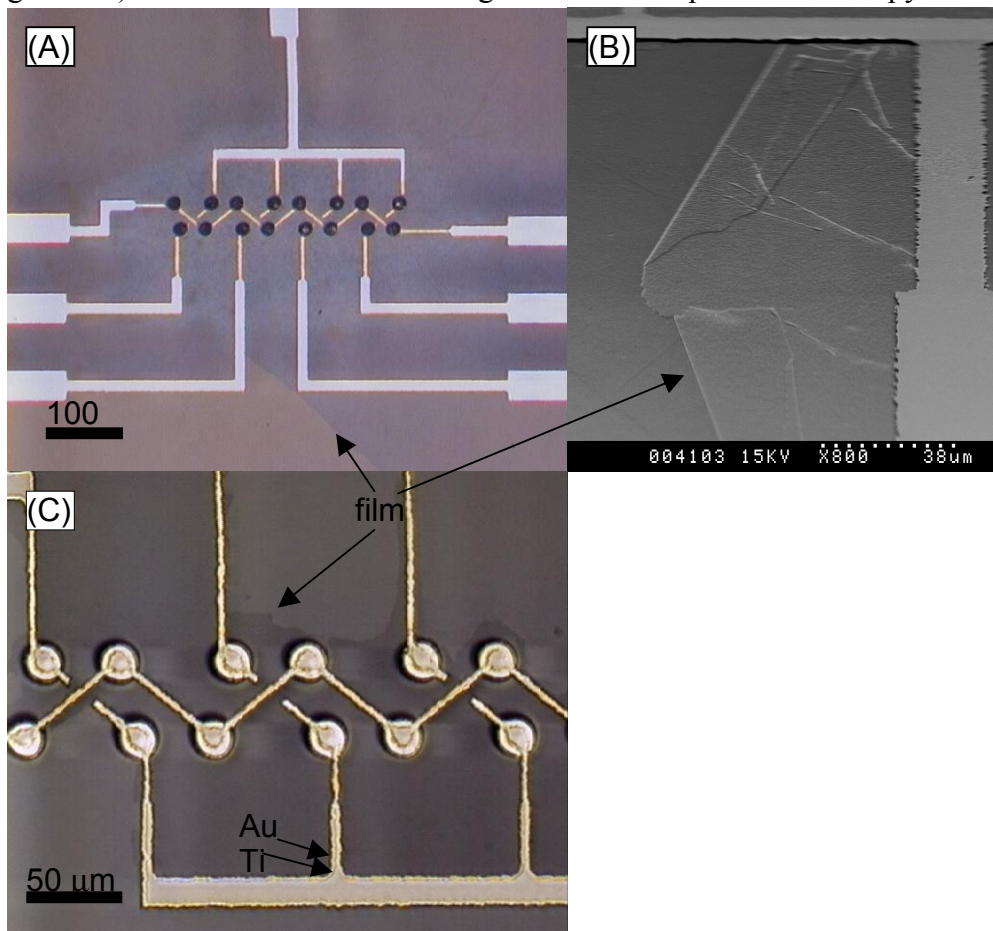


**Figure 5-8:** Electrodes after titanium removal. (A) Top-down optical micrograph of a 1x4 array (B) SEM closeup of a gold line, showing the attached residue film. This film can also be seen in (A) and (C). (C) Underside view of the posts, showing the titanium undercut during etching.

thin-film interference effects. Fluoroscope examination revealed that the film was not fluorescent, and thus probably not an organic residue such as photoresist. Dektak and SEM measurements showed it to be much thinner than 1  $\mu\text{m}$ . Careful SEM analysis indicated that the film was actually attached to the underside of the gold, but not to the substrate (Figure 5-8B), suggesting that the film was present on top of the titanium, and only became apparent following Ti removal. This further suggests that the film is the result of some reaction between the Ti and the SU-8, induced by either light, temperature, or the SU-8 stripper. As the film was non-conductive (tested with a probe station), I did not investigate its properties further, although it is probably a Ti/organic compound.

### 5.1.6 Forming the SU-8 channel

I decided to form the channel out of SU-8 (Figure 5-9A). I did not use PDMS (polydimethylsiloxane), which has the advantage of being removable & reusable because the validation experiments require accurate knowledge of the channel height, which may be difficult to control given the compliance of the PDMS under pressure. In addition, for fluorescence microscopy I reasoned that using a standard coverslip as the look-thru medium may result in less distortion than looking through PDMS.

The SU-8 channel formation is a straightforward SU-8 lithography step. I varied the spin cycle to obtain a thicker film and varied the exposure, bake, and develop times, but otherwise the process was the same as described above. There were no apparent problems with the SU-8 causing the posts to deform during application and the film thickness near the electrodes was not affected by their presence.

In Figure 5-10 I show SEMs of a completed 1x8 array device. One sees that the yield is excellent within the array, and was approximately 30% across the wafer (with yield defined as percentage of devices with all traps intact). The major yield-loss mechanisms were loss of posts during the wet etching of the substrate interconnects or during handling after SU-8 mold

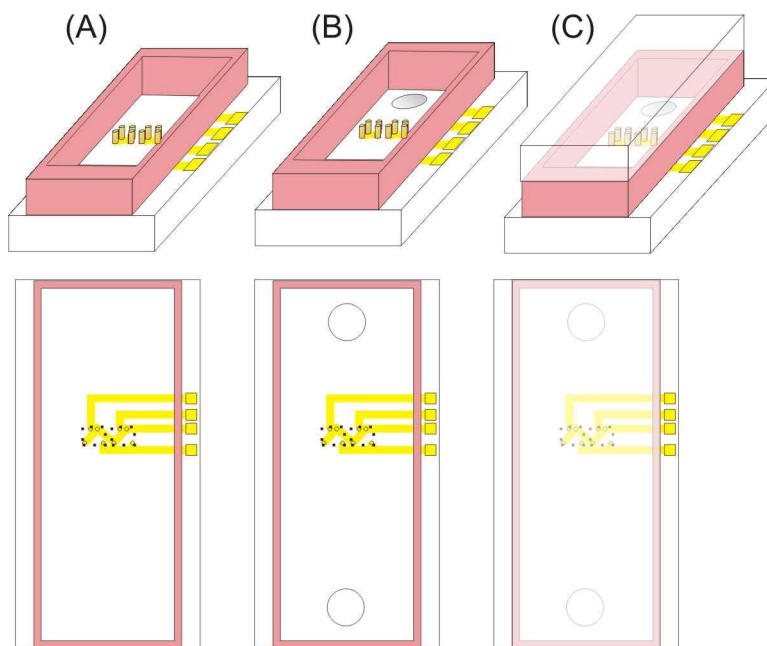


**Figure 5-9:** Final fabrication steps. (A) Forming the SU-8 channel. (B) Dicing and drilling the fluidic access holes. (C) Capping the channel with a coverslip.

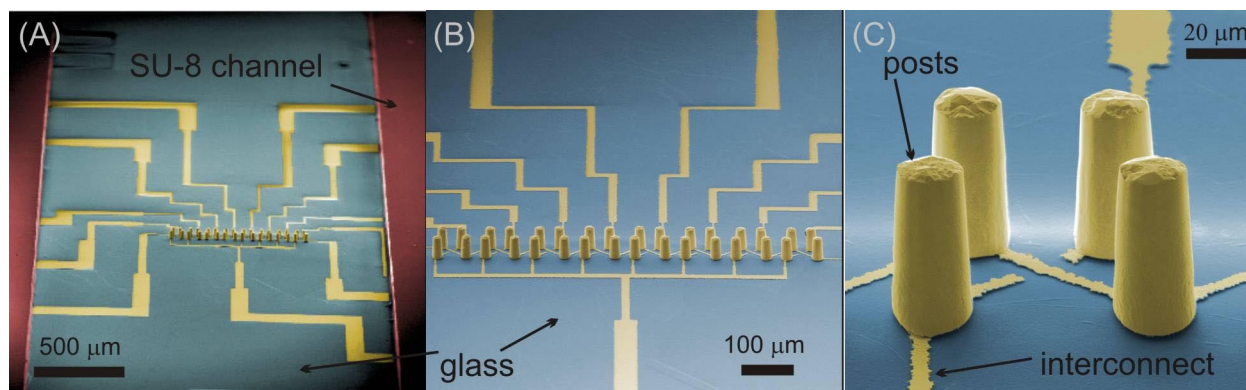


**Figure 5-10:** Final SEMs of the completed chips. (A) a 1x8 array in an SU-8 channel. (B) a close-up of the array. (C) A closeup of a single trap.

removal. The final electrodes have a tapered geometry and slightly domed tops (Figure 5-10C).

### 5.1.7 Final fabrication

The final steps, after channel formation, were to dice the wafers (Figure 5-9B), drill fluidic access holes (Figure 5-9B), and cap the channel (Figure 5-9C). I'll describe the first two steps in this section; capping the channel is done during packaging. The dicing was performed with a conventional diesaw. I protected the posts during dicing by backfilling the channels with AZ4620 photoresist. After dicing, I soaked the chips in acetone to remove the photoresist.

Access holes were drilled into the glass with a 0.75-mm diamond-tipped drill bit (C. R. Laurence, Los Angeles, CA) registered to gold marks formed on the slide during the first lithography step. The drilling of the holes usually resulted in a slightly tapered hole that was wider at the bottom of the chip, which actually eased in aligning the chip during packaging.

## 5.2 Packaging

The packaging requirements for the small array are three-fold. Electrically, I need to bring 20-MHz signals of a few volts to the electrode tips. Optically, I need to be able to perform fluorescence microscopy of cells held in the traps. From a fluidics standpoint, I need to introduce cell-containing liquids onto the chip at around 1 psi.

The packaging solution that meets these needs is shown in Figure 5-11. The electrical connections start from the electrodes, go under the SU-8 channel out to the chip periphery, and are finally wire-bonded to a ceramic package that fits on a ZIF-socket and is connected to a printed-circuit board. The optical solution is to use a coverslip to attain a high-fidelity optical transfer system that would be compatible with coverslip-corrected objectives. The package is low-profile, in that there are no protrusions above the plane of the coverslip, which makes it easy to mount the package under a conventional microscope. In addition, since the cells are at most ~300 μm away for the objective, low-working-distance objectives with high numerical apertures can be used. The fluidic connections are made with an aluminum block that has a protrusion which rises up through the middle of the ZIF socket and carries fluidic channel to the chip. Locking the ceramic carrier into the ZIF socket with o-rings in-between ensures a leak-proof seal.

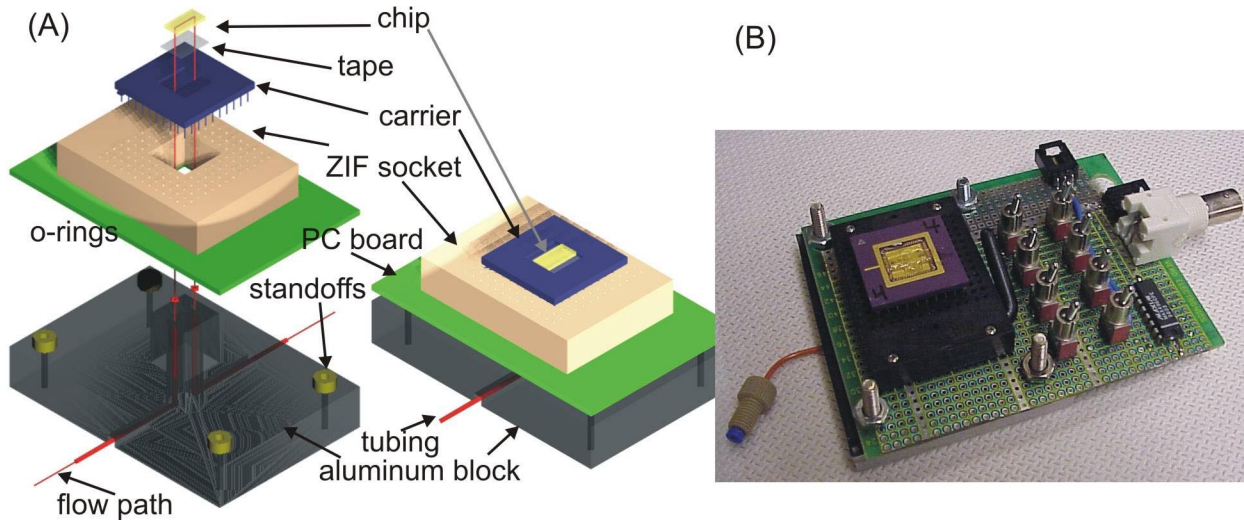


**Figure 5-11:** Packaging of the extruded array. (A) Schematic and (B) photograph of the packaging assembly. An aluminum block serves as the substrate. It has cutouts to carry the flow within tubing . The flow path continues through o-rings and mates with the bottom of the ceramic carrier, thru double-sided tape, and into the channel on the chip.

### 5.2.1 Assembling the package

The packaging assembly starts with the diced chips (Figure 5-12A). The first step is to drill the fluidic access holes, as described above. Concurrently, I take a 64-pin ceramic carrier package with a 0.4"x0.4" die area (Spectrum Semiconductor Materials, Inc., San Jose, CA) and drill holes in it (with the diamond drill bit) that will line up with the holes in the chip and the holes in the aluminum package (Figure 5-12B). To mount the chip onto the ceramic carrier and make fluid-tight seals, I use double-sided tape with openings cut in it for each of the holes.

At this point I gold wirebond the connections from the chip to the ceramic carrier. Wirebonding will ensure that I can reliably transfer the signals necessary for operation to the electrodes.

Following wirebonding, I attach the coverslip top to the channel. The top is a coverslip

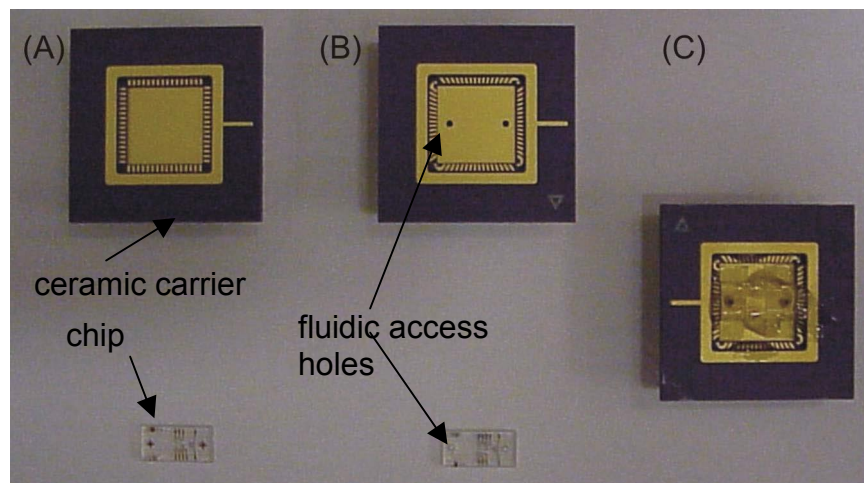


**Figure 5-12:** Assembling the packaging. (A) Naked chip and ceramic carrier, (B) with holes, (C) mounted together with double-sided tape & the coverslip.

that has been scribed and cleaved to the approximate size of the outer channel dimensions. I mechanically clamp the coverslip on top of the channel and then apply five-minute epoxy to the assembly to create a fluidic seal (Figure 5-9C). One drawback to this assembly method is that the distance between the coverslip and the channel will vary depending on how much epoxy flows into the gap, which means that a secondary measurement of the channel height is necessary. More importantly, it means that the coverslip and substrate may not be perfectly parallel, which will introduce optical aberrations.

At this point the ceramic carrier is ready to mate with the rest of the package. This consists of an aluminum block that has been shaped to have a protrusion (Figure 5-11 & Figure 5-13). The bottom of the block has cutouts that carry 0.020" (I.D.) PEEK tubing (Upchurch Scientific, Oak Harbor, WA). The tubing has been permanently bent with a heat gun and glued onto the aluminum block with Ducco cement. The tubing serves as a low-void-volume fluidic carrier from the edge of the block almost to the chip itself. The fluidic path briefly goes through the aluminum and then emerges on the top of the protrusion at a groove for a size #001 o-ring (Parker Hannifin Co., Lexington, KY).

A printed circuit board, which contains a simple circuit to drive the electrodes and a ZIF socket (3M, St. Paul, MN) for the ceramic carrier to sit in, is mated to the aluminum block so that the protrusion goes through an opening machined out of the ZIF socket. Clamping the chip into the ZIF-socket automatically aligns and seals the fluidic connections and makes the electrical connections to the circuit board, completing the package. This makes it relatively easy to interchange ceramic carriers, and hence chips, during testing.

The driving circuit is shown in Figure 5-14. The signal from the signal generator goes to a quad buffer (MAX496, Maxim Integrated Products, Sunnyvale, CA). Two of the electrodes on each trap are wired to ground, while one is permanently wired to the output of the buffer. The other is wired to the output of the buffer but through a SPDT switch, which allows switching of the electrode to ground, thereby controlling the trap. The four outputs of the quad buffer are equally shared between the permanently wired and controlled electrodes. While this circuit is not electrically ideal, in that the SPDT switches are not designed to switch these types of signals, it works adequately for my purposes, and can send 20-MHz 5 V<sub>pp</sub> signals with good fidelity to the electrodes. Occasional ringing of the circuit occurs, but this is accompanied by an increase in the supply current to the buffer and can be easily detected with the current monitor integrated into the power supply. Switching the SPDT switches back and forth removes the ringing.

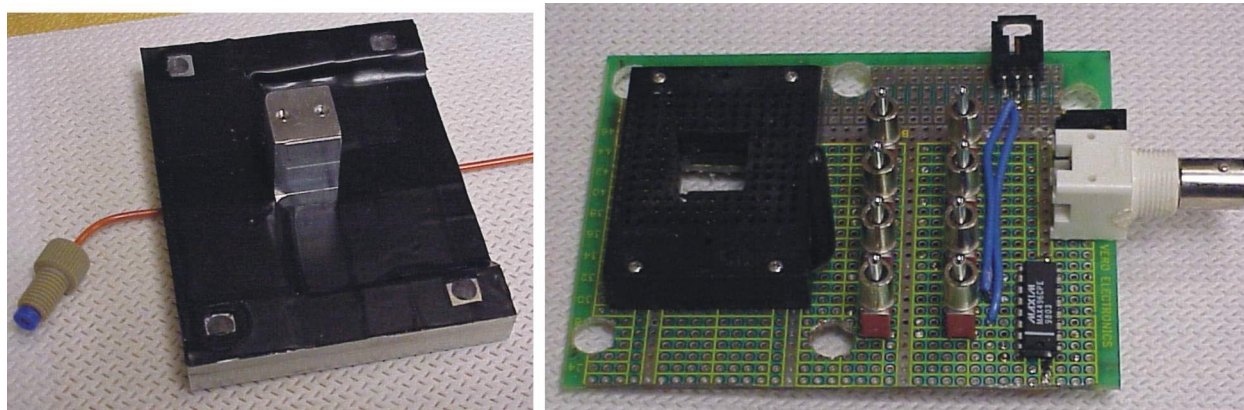


**Figure 5-13:** The aluminum fluidic carrier and printed circuit board.

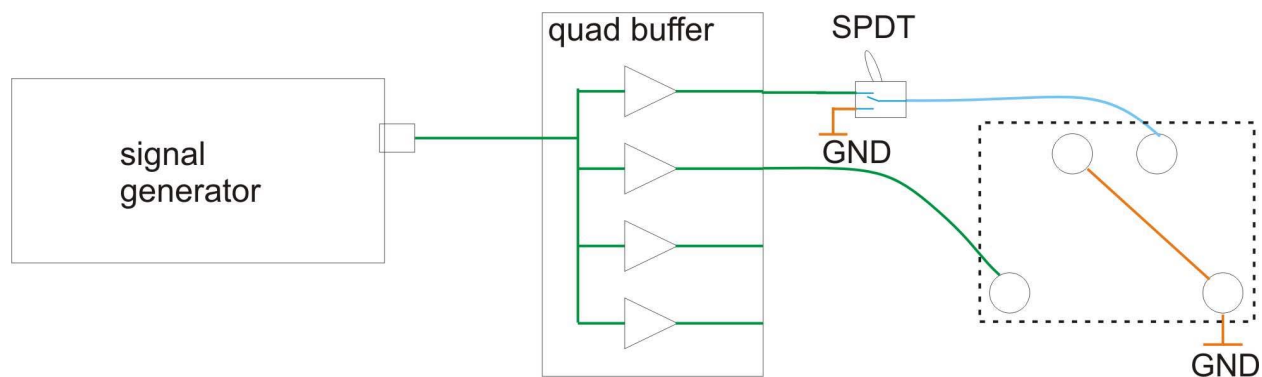


Figure 5-14: Electrical driving circuit.

### 5.3 Test setup

The test setup is identical to the one used in Chapter 3 except that it resides on a Zeiss Universal upright fluorescence microscope (Figure 5-15). The microscope is equipped with a fluorescent slider permitting four filter combinations. The microscope has been modified to allow the use of both reflected brightfield and epi-fluorescence by re-directing the brightfield lightpath from the transmitted to the reflected mode. This requires the use of a half-silvered mirror in one slot of the filter slider. The microscope uses a halogen lamp for its brightfield source and a 150W Xenon lamp for its fluorescent source. It is equipped with both a monochrome video CCD camera (TM-7CN, Pulnix America, Inc., Sunnyvale, CA) and a cooled color-CCD imager (SPOT-RT Color, Diagnostic Instruments, Sterling Heights, MI). Unfortunately, I was unable to install an automatic shutter system because of the physical

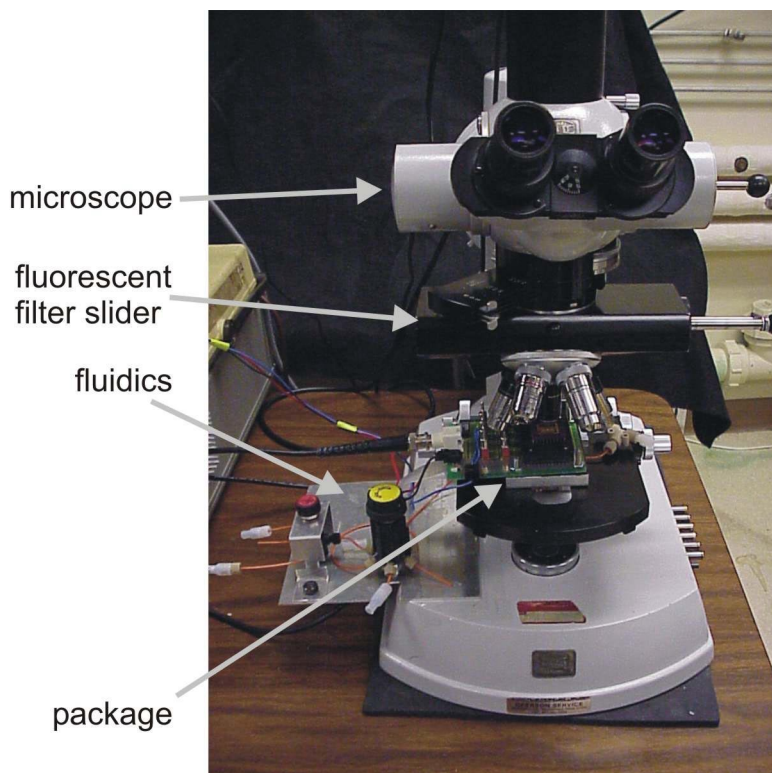


Figure 5-15: Photographs of the test setup.

constraints of the microscope, and so performed all shuttering manually.

## **5.4 Conclusion**

In this chapter I have described the fabrication process flow, packaging, and test setup needed to fabricate, package, and test the extruded trap arrays. The process flow uses electroplating into an SU-8 mold to define the posts that are necessary for the new trap design. This process had to overcome the challenges of using and removing SU-8, which can be both difficult to apply and to remove. In addition, the process used wet etching of the gold substrate interconnects and the use of an SU-8 chamber to ease the process complexity. The packaging design allows for easy assembly and interchangeability of individual chips, while meeting the stringent requirements for electrical input, optical access, and fluidic connection.

## Chapter 6: Trap validation

The first objective upon completion of the array was to validate that the improved DEP traps do indeed exhibit stronger holding. To do this, I followed a similar testing protocol as for the planar quadrupole traps—measuring the release flowrate of beads under different conditions—and compared the results to the model predictions, now using the as-fabricated rather than ideal geometries. As described below, the results do validate the predictions of superior trap strength.

### 6.1 Materials and Methods

#### 6.1.1 Materials

All beads and solutions were prepared as in Chapter 2. I used the same three bead sizes as before—7.58  $\mu\text{m}$ , 10.00  $\mu\text{m}$ , and 13.20  $\mu\text{m}$ —although with fresh 0.01 S/m HBSS solutions containing 0.5% (v/v) Triton X-100.

#### 6.1.2 Test methodology

The methodology was similar to what I used for the planar quadrupole traps: trap a bead at a given voltage and measure the minimum flowrate needed to dislodge the bead from the trap. I slightly modified the testing procedure for use with the extruded traps. First, I considered a one-minute hold time as constituting holding to speed up the data-taking procedure. Initial tests showed that the vast majority of beads held for one minute were indefinitely held. Second, instead of varying the applied flow to find the “true” release flowrate for a given voltage, I increased or decreased the flow monotonically and measured all release flowrates that I found. I believe that this more closely approximates the true errors in the measurements and made the error analysis much easier. Third, I obtained data from any of the three working traps in the 1x4 array that I used, dictated by which trap(s) happened to be holding beads then. This gives a better estimate of the variations within an array. Finally, I performed three runs on different days (over 2 weeks) to get a sense of the drift.

#### 6.1.3 Modeling

Simulations were performed using the modeling environment described in Chapter 2. Simulations encompassed both as-designed (no taper, and with as-drawn geometries) and as-fabricated geometries (described below). Bead simulations used the experimental parameters for the holding experiments -  $\rho_p=1.062 \text{ g/cm}^3$ ,  $\sigma_m=0.01 \text{ S/m}$ ,  $\sigma_p=2 \times 10^{-4} \text{ S/m}$ ,  $\epsilon_p=2.5$ ,  $f=1 \text{ MHz}$  or  $20 \text{ MHz}$ ,  $w=2 \text{ mm}$ . The chamber height ( $h$ ), as described below, was  $159.5 \mu\text{m}$ . Dipole and quadrupole force orders were simulated. Cell simulations used the same parameters, except that  $\sigma_m=1 \text{ S/m}$ . The nominal values for HL-60 cells were from [81], with  $C_m=1.6 \mu\text{F/cm}^2$ ,  $G_m=0.22 \text{ S/cm}^2$ ,  $\Delta=1 \text{ nm}$ ,  $\epsilon_{cyto}=75 \text{ F/m}$  &  $\sigma_{cyto}=0.75 \text{ S/m}$ .

### 6.2 As-fabricated geometries

In order to be able to compare experiments to predictions, I must know what the device dimensions as fabricated really are. I performed measurements on the device and package to

extract parameters that would affect the modeling, so that I could perform simulations with the as-fabricated devices to accurately predict the trap strength.

### 6.2.1 Trap geometry

Figure 6-1 shows SEMs of fabricated traps. While these traps are not the specific traps used in the experiments, they are from the same wafer and so constitute a representative sample. In Figure 6-1A I show comparisons to the as-drawn geometries. The interconnect lines are significantly narrower ( $3.7\ \mu\text{m}$  wide instead of  $8\ \mu\text{m}$ ) than drawn, due to the gold-etch undercut, and slightly narrower than the anticipated width of  $4\ \mu\text{m}$ . The values that I used for the wiring geometry in the revised simulations are shown in the figure and Table 6-1.

The negative tone of the SU-8 confers a conical shape to the posts, and modeling this taper is necessary to accurately predict trap strength. This is because the taper breaks the axial symmetry of the trap, creating a divergence in the field in the  $z$ -direction and thus a positive  $z$ -directed DEP force. As can be seen in Figure 6-1B, the taper is actually a compound taper, with

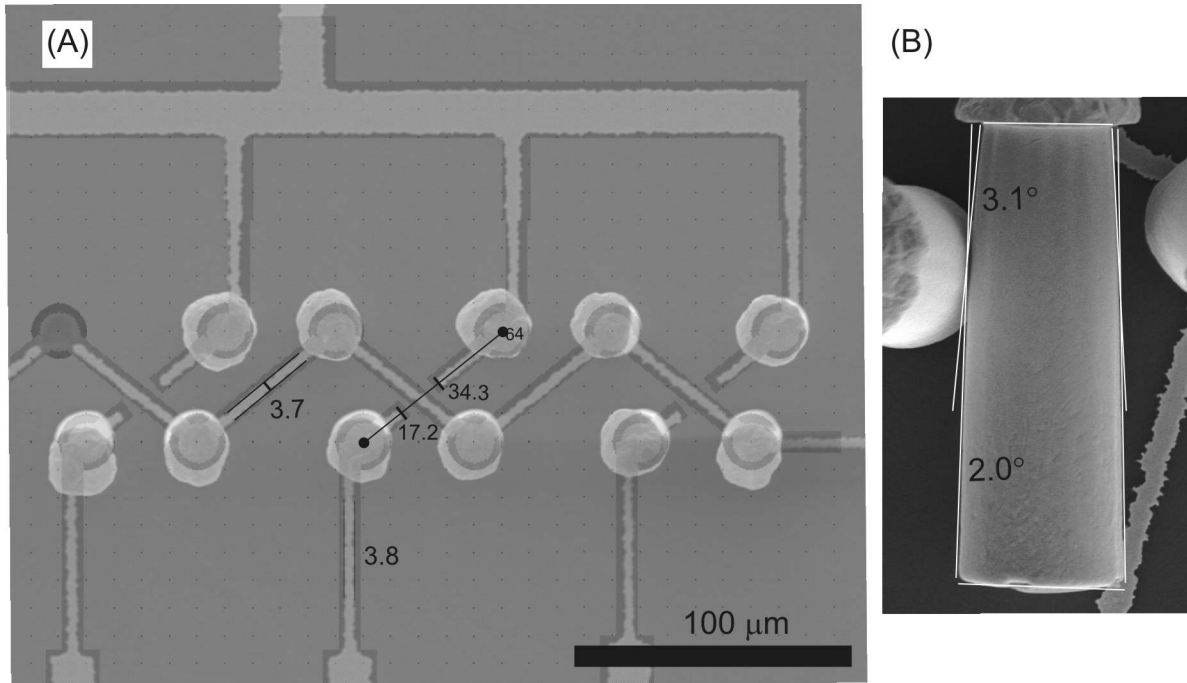


**Figure 6-1:** (A) SEM of a completed trap overlaid with the mask drawing. The post tops appear larger than the drawn geometries because this particular array was electroplated too long and mushroomed at the top of the posts. The numbers refer to lengths (in microns) of the various segments of the interconnect geometry that were subsequently used in the electric-field modeling. (B) SEM of a fallen post, showing the taper angle along the length of the post. The taper varies between  $2.0^\circ$  and  $3.1^\circ$ .

Dimension	As-designed	As-fabricated	Modeled
Electrode height	$50\ \mu\text{m}$	$47\text{-}50\ \mu\text{m}$	$50\ \mu\text{m}$
Electrode diameter	$20\ \mu\text{m}$	$18\text{-}20\ \mu\text{m}$ at top with a $2^\circ\text{-}3^\circ$ taper	$18\text{-}20\ \mu\text{m}$ at top with a $3.5\ \&\ 4.0\ \mu\text{m}$ taper
Substrate interconnect width	$8\ \mu\text{m}$ drawn, $4\ \mu\text{m}$ designed	$3.7\ \mu\text{m}$	$3.7\ \mu\text{m}$
Chamber width ( $w$ )	$2\ \text{mm}$	$1.983 \pm 0.003\ \text{mm}$	$2\ \text{mm}$
Chamber height ( $h$ )	$150\ \mu\text{m}$	$157\text{-}162\ \mu\text{m}$	$159.5\ \mu\text{m}$

**Table 6-1:** Comparison between as-designed and as-fabricated geometries for the traps used in this chapter.

an upper-section taper of  $3.1^\circ$ , a lower-section taper of  $2.0^\circ$ , and an overall averaged taper of  $2.4^\circ$  using values from this SEM figure. For a 50- $\mu\text{m}$  high post, the overall taper of  $2.4^\circ$  leads to a 4.2- $\mu\text{m}$  difference in the diameter of the post between the top and bottom. Using a microscope-mounted  $x$ - $y$  micrometer stage I measured the taper of this post to be 4 $\mu\text{m}$  with approximately 1  $\mu\text{m}$  of error, which is consistent with the SEM angle measurement.

Another measurement that I performed was to use SEMs of top-down views of the posts to get proportions of the diameters at the post top and bottom. From Figure 6-2, the tops of the posts are 81% (Figure 6-2, left) and 84% (Figure 6-2, right) of the diameters of the bottoms. The error in this measurement is due to the difficulty in assigning a diameter to the non-circular profiles of the posts. However, using 18  $\mu\text{m}$  as the diameter at the top of a 50- $\mu\text{m}$ -high post gives an overall taper of between 3.4 (84%) and 4.2 (81%)  $\mu\text{m}$ , which is consistent with the measurements from Figure 6-1B.

As I shall show below, the taper dramatically affects the predicted results. Assembling the above measurements, I can state that the taper angle varies between  $2^\circ$  and  $3^\circ$  and is probably multi-valued along the length of the post.

I measured the height and diameter of the posts from the traps used in the validation experiments. Heights ranged from 47-50  $\mu\text{m}$  ( $\langle x \rangle = 48.1 \pm 2.2 \mu\text{m}$ ,  $n=12$ ), measured with a microscope-mounted  $z$ -axis micrometer, although the domed tops of the posts (Figure 5-10C) make it difficult to precisely define the height. I measured the diameters at the top of the posts with a microscope-mounted  $x$ - $y$  micrometer stage. The values ranged from 18-20  $\mu\text{m}$  ( $\langle x \rangle = 18.8 \pm 0.8 \mu\text{m}$ ,  $n=5$ ), with the primary errors coming from the resolution of the micrometer stage (1  $\mu\text{m}$ ), the deviations from perfect circularity of the posts, and the domed character of the post tops. I believe the absolute error to be about 1-2  $\mu\text{m}$ .

Assembling all this data, I modeled the traps to have the interconnect geometries as described in Figure 6-1A, posts with 50  $\mu\text{m}$  height, a taper of 3.5  $\mu\text{m}$  ( $2.0^\circ$ ) or 4.0  $\mu\text{m}$  ( $2.3^\circ$ ), and

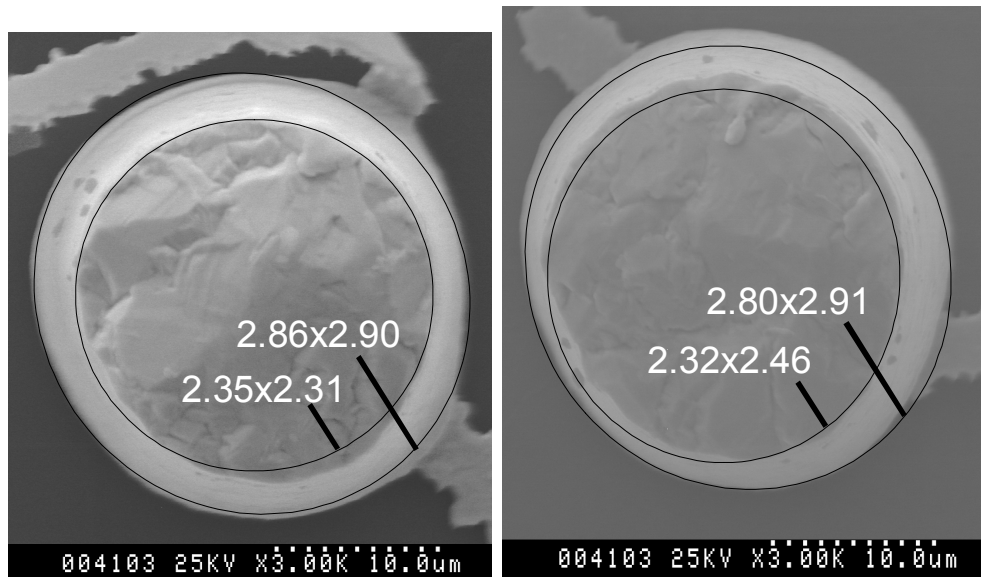


**Figure 6-2:** Top-down SEMs of two posts (different sample than Figure 6-1), with the top and bottom diameters circled. The major and minor axes of the ellipses, in arbitrary units, are given by the two numbers for each ellipse. Approximate circle diameters can be obtained by averaging the values. The figure shows that the top dimensions are smaller than the bottom dimensions. Averaging the dimensions to get an average diameter for each circle, the left subfigure has an 81% ratio of top-to-bottom diameter while the right subfigure has an 84% ratio.

post diameters (at the top) of between 18  $\mu\text{m}$  and 20  $\mu\text{m}$  (Table 6-1).

## 6.2.2 Chamber geometry

The chamber width of the tested device was measured with a microscope-mounted  $x$ - $y$  micrometer stage to be 1.98 mm ( $\langle x \rangle = 1.983 \pm 0.003$  mm,  $n=3$ ), and modeled as 2 mm. The chamber height of the tested device was measured with a microscope-mounted  $z$ -axis micrometer to be 157-162  $\mu\text{m}$  ( $\langle x \rangle = 159.6 \pm 2.4$   $\mu\text{m}$ ,  $n=9$ ), and modeled as 159.5  $\mu\text{m}$ . The chamber height appeared to change over the course of the experiments as evidenced by the change in the appearance of the glue between the coverslip and the SU-8 chamber; by the end of the experiments, water was seeping much farther into the space where the glue was than at the beginning (but not leaking out of the chamber). This drift will affect the holding in an inversely linear manner.

## 6.3 Results

### 6.3.1 Trap switching

I performed experiments to validate the single-electrode switching described in §4.3.3 and Figure 4-6. In Figure 6-3 I show three images of beads held in traps showing that I can turn one trap off independently of the other. Under flow, the released bead flows away when only one electrode is toggled between  $+V$  and ground.

### 6.3.2 Holding characteristics with beads

I performed experiments as described above to obtain the holding characteristics of these traps. The results are shown in Figure 6-4. The error bars represent experimental errors of one standard deviation. All release flowrate measurements were taken 3-8 times and on average 4.3 times. The data demonstrates that the holding in these traps is size selective with larger beads exhibiting stronger holding, as one would predict given the  $R^3$  dependence of the DEP force (dipole term). The stated error includes systematic deviations between individual traps—one trap was consistently weaker than the other two.

In Figure 6-5 I show comparisons between the experimental results and the modeling

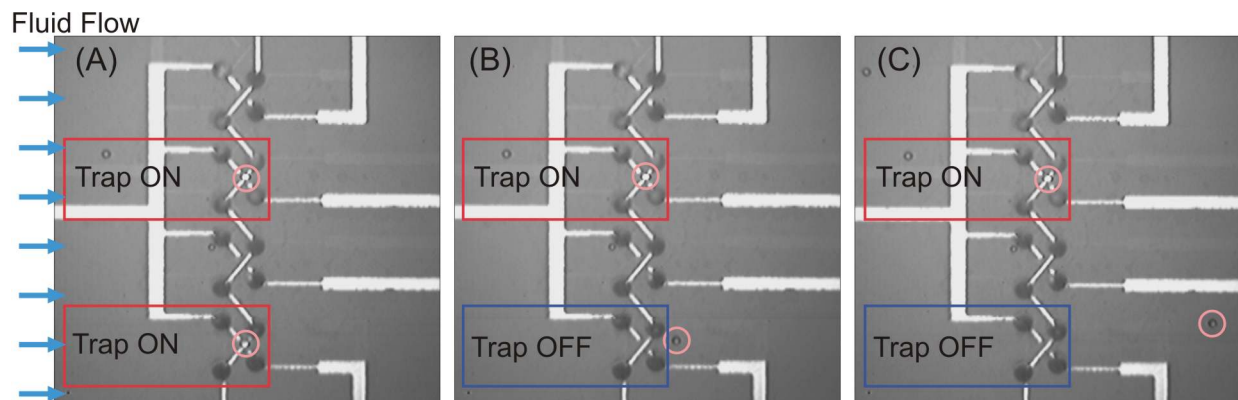


**Figure 6-3:** Movie frames showing electrical control of the traps. (A) Flow (3  $\mu\text{l}/\text{min}$ ) is applied from left to right, with two 10.0- $\mu\text{m}$  beads held in each of two traps. (B & C) The bottom trap is turned off by switching its bottom-right electrode, causing the bead to flow away while the bead in the top trap is held. Traps were energized at 1.5 V and 1 MHz.

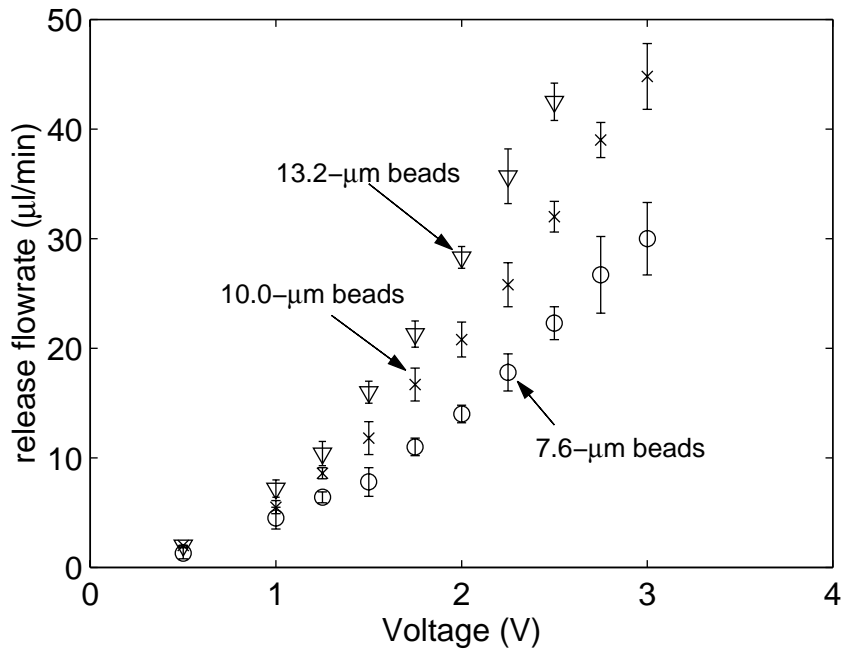


**Figure 6-4:** Superimposed data for holding characteristics. Shown are the results of release flowrate measurements with 7.6- $\mu\text{m}$  (o), 10.0- $\mu\text{m}$  (x), and 13.2- $\mu\text{m}$  ( $\nabla$ ) beads in the extruded trap. Measurements were performed at 1 MHz.

using a 3.5- $\mu\text{m}$  taper. The smaller model prediction in each subplot corresponds to a post diameter of 18-21.5  $\mu\text{m}$ , while the larger model prediction corresponds to a post diameter of 19-22.5  $\mu\text{m}$ . As stated before, this is within the limit of my measurements of the post diameter. The model predictions for the 18-21.5- $\mu\text{m}$  post diameter for the 7.6- $\mu\text{m}$  beads (Figure 6-5A) has some numerical noise in it, similar to the effects seen in the planar quadrupole holding characteristics in Chapter 3. There is no physical significance to this noise.

The first feature to notice is that for all bead sizes the experimental data is bounded by the predictions. Furthermore these are absolute predictions, as for the planar quadrupole. Thus, the model is further validated. Second, the traps are working as predicted, which is a validation of the design methodology.

It is possible to obtain a best fit, within the experimentally measured post diameters, by finding the linearly interpolated post diameter that would minimize the error between the experiments and models. While there is not any absolute knowledge gained by this maneuver, it does allow for easier visual representation and manipulation of the data. Ideally the fit would be independent of which set of data was used to generate it. In other words, fitting to the 7.6- $\mu\text{m}$  bead characteristic should give the same fitted post diameter as a fit to the 13.2- $\mu\text{m}$  bead characteristic. Unfortunately, the modeling is not perfect and this is not the case.

Lacking this, one might fit the data using the 7.6- $\mu\text{m}$  beads and extrapolate the results for the larger beads. The rationale here is that the smallest bead is least likely to be disturbed by 2<sup>nd</sup>-order effects, such as fluid flow, that are not accounted for in our model and therefore those results are likely to be most accurate. Unfortunately, Figure 6-5A shows that the simulations for the two post diameters are not well spread out and so the resultant fit will likely not be precise.

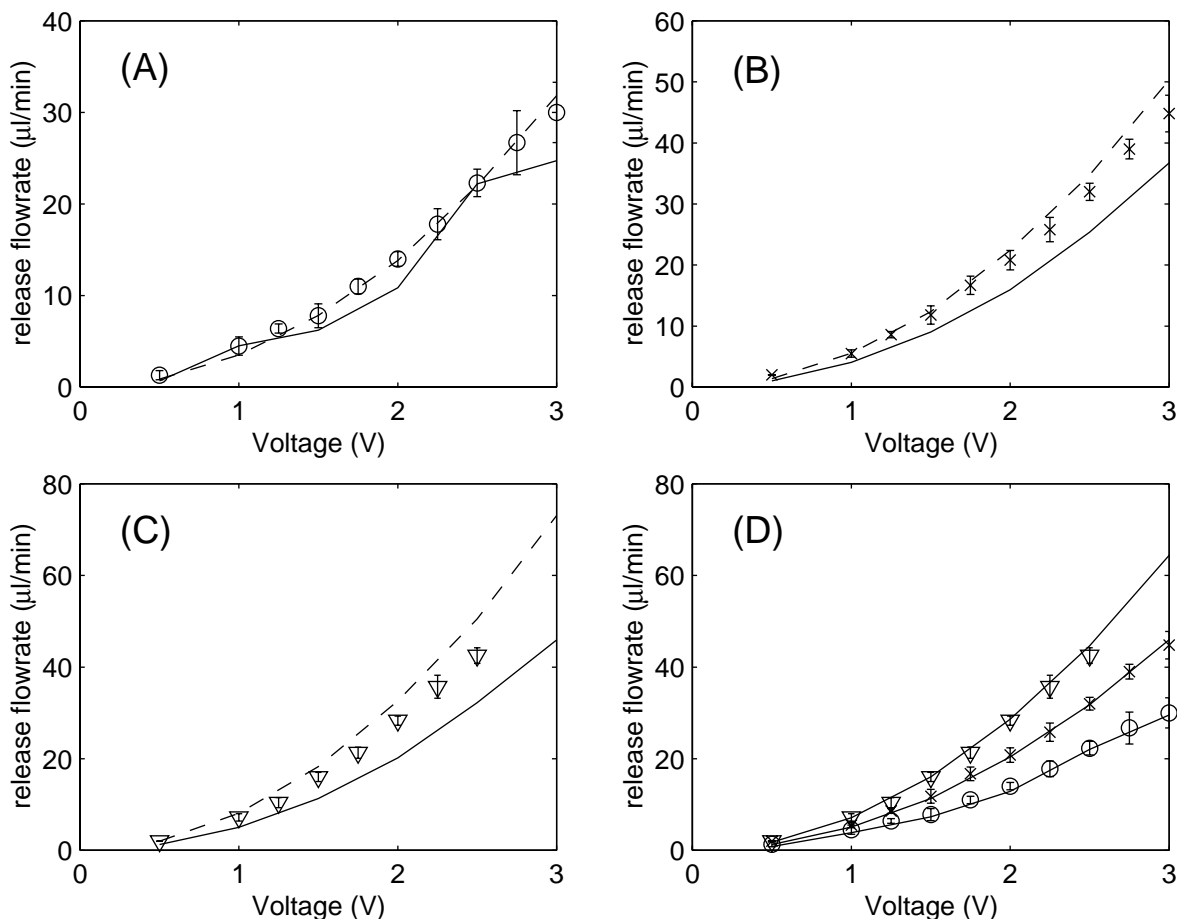


**Figure 6-5:** Model predictions of the holding characteristics. The data is shown as discrete points while the simulation results are shown for 18-21.5- $\mu\text{m}$  (—) and 19-22.5- $\mu\text{m}$  (---) posts. The data and predictions are shown for (A) 7.6- $\mu\text{m}$  (o), (B) 10.0- $\mu\text{m}$  (x), and (C) 13.2- $\mu\text{m}$  ( $\nabla$ ) bead diameters. (D) Plotted is a best-fit interpolation (18.7-22.2- $\mu\text{m}$  diameter posts) of the predictions to the data in (B) and then the use of that fit parameter to predict the holding characteristics for the other bead sizes.

Using the 10- $\mu\text{m}$  bead characteristics for the fit is a good compromise between minimizing the 2<sup>nd</sup>-order effects while maximizing the fitting resolution.

Figure 6-5D shows the results of linearly interpolating the results for the 10.0- $\mu\text{m}$  beads and then extrapolating the extracted post diameter to the other two bead sizes. The post diameter corresponding to this fit is 18.7  $\mu\text{m}$ , which is very close to the measured average post diameter as described above (see §6.2.1). This results in a maximum error between the fit and the data averages of 1.1  $\mu\text{l}/\text{min}$  (4% of full scale (FS)) for the 7.6- $\mu\text{m}$  beads, 1.2  $\mu\text{l}/\text{min}$  (3% of FS) for the 10.0- $\mu\text{m}$  beads, and 2.2  $\mu\text{l}/\text{min}$  (5% of FS) for the 13.2- $\mu\text{m}$  beads. Incorporating the measurement errors, only 7 of 28 simulated values fall outside the  $1\sigma$  measurement errors, with a maximum miss of 0.7  $\mu\text{l}/\text{min}$ . Using a  $2\sigma$  measurement error (corresponding to a 87% confidence level), all predictions fall within the experiments. Two data points whose measured experimental precision was 0  $\mu\text{l}/\text{min}$  will never match predictions without incorporating systematic experimental errors, which I have not done.

With confidence in the model I can extract the holding forces from the simulations, as shown in Figure 6-6. The results show the greatly increased strength of the new trap, as

compared to the planar trap (see also Figure 4-14). For instance, a 10.0- $\mu\text{m}$  bead is held with 65 pN of force at 2V, as opposed to the 0.5-1 pN of the planar quadrupole. The trap is indeed 10-100x stronger, as predicted in §4.5.

### 6.3.3 Holding characteristics with cells

To see if the traps are meeting the system requirements for the  $\mu\text{DAC}$ , I ran simulations with HL-60 cells using the validated as-fabricated geometries. I used parameters for HL-60 cells given in §4.4.3 with an applied frequency was 20 MHz.

In Figure 6-7 I show the holding characteristics and holding forces for the HL-60 cells in this system. These differ from the ideal characteristics given in Figure 4-13 because of the difference between designed and as-fabricated geometries. As can be seen, however, the difference is slight and thus the operating conditions determined in §4.5 are still valid.

## 6.4 Discussion

### 6.4.1 Model and trap validation

The results described above demonstrate the utility of the modeling environment for designing DEP-based traps for bioscience applications. I have been able to *a priori* design a trap geometry that could meet the system applications of the  $\mu\text{DAC}$  without performing any trial-and-error experiments. In addition, the geometry used for the extruded traps is much more complicated than the planar quadrupole, involving an asymmetric electrode placement, exposed wiring within the trap, and the tapered three-dimensional profile of the posts. Despite all of these challenges, the model has been successful in predicting the performance of these traps.

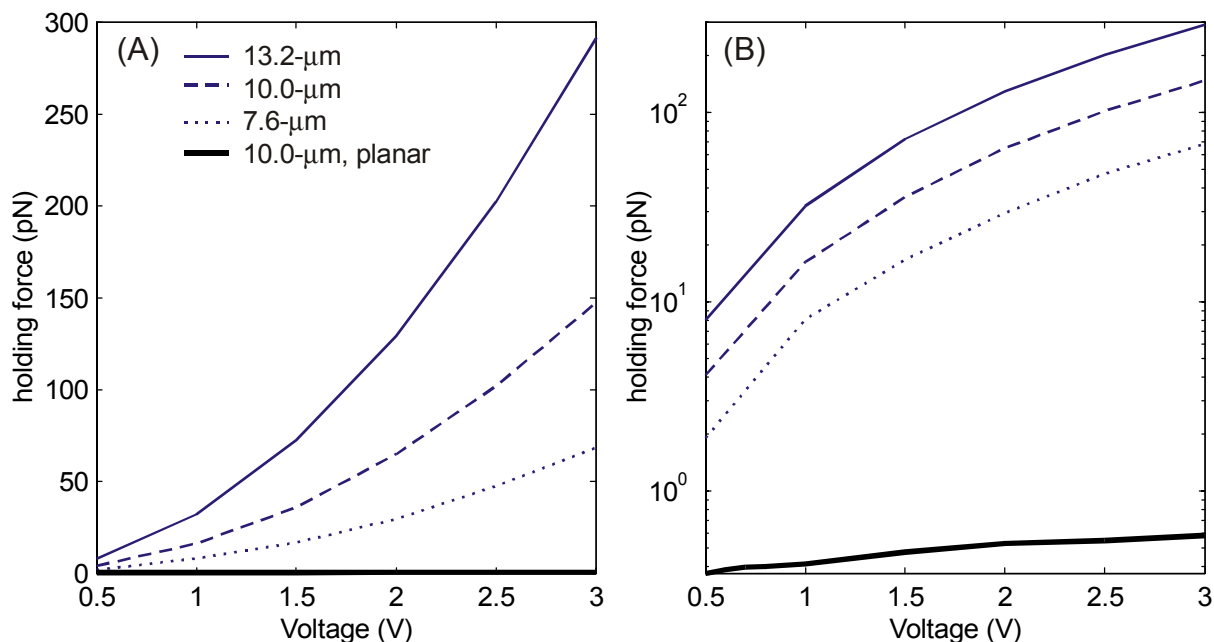


**Figure 6-6:** Extracted holding forces of the extruded quadrupole traps, using the same fit as for the holding characteristics (Figure 6-5D). Plotted are holding forces for 13.2- $\mu\text{m}$  (—), 10.0- $\mu\text{m}$  (---), and 7.6- $\mu\text{m}$  (····) beads using (A) linear and (B) logarithmic scales. Also shown (—) for comparison are the results from Figure 4-14 for 10.0- $\mu\text{m}$  beads in the planar quadrupole. In (A) the results for the planar quadrupole (—) are so small that they lie on the  $x$ -axis.

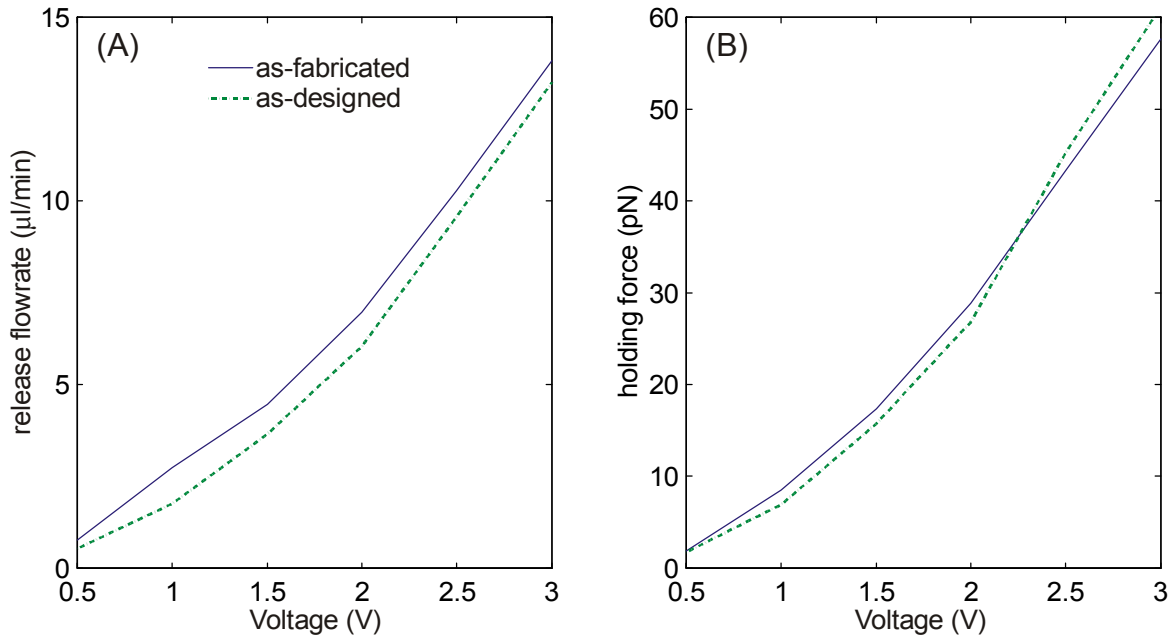


**Figure 6-7:** Simulated holding characteristics for HL-60 cells in the finalized traps, interpolated using the same fit as for the beads and compared to the designed holding characteristics of Figure 4-13. (A) Release flowrate versus voltage for the as-designed (---) and as-fabricated (—) traps. (B) Extracted holding forces versus voltage for the designed (---) and as-fabricated (—) traps.

The results also demonstrate an internal consistency to the design process—the modeling and the trap are both validated by these measurements. This validation, coupled with the results from the planar quadrupole, strongly suggest that such modeling could be useful in the future.

Looking at the dipole form of the DEP force (Eqn. (1-1)), one would expect the trapping to follow an  $R^3$  law. Figure 6-4 shows that the ratio is actually less than that. In fact, the holding goes approximately as  $R^x$  with  $x=1.4-1.5$ . A possible explanation for this can be seen in Figure 6-8, where I have plotted that predicted locations of the particles at release. Although the predicted characteristics contain significant numerical noise at  $V=1V$  and  $3V$  (due to the discretization of the problem space), they do suggest that the particle positions differ for the different bead sizes. If this is true then since all three particles settle into the different release points, the drags and DEP forces experienced will differ, and can account for the observed non-cubed-law behavior. In fact, the discrepancy reinforces the utility of the model in accounting for the complex behaviors in these traps.

#### 6.4.2 Deviation between model and experiment

Although the model certainly has succeeded in predicting the holding characteristics for beads in the extruded quadrupole traps, I can speculate as the origins of the remaining deviations between experiment and model. This is useful in trying to ascertain the appropriate space within which the model has predictive power, which is necessary for future designs. One must reiterate however that the agreement, as depicted in Figure 6-5, is within the experimental error and thus the model predicts the experimental results *extremely* well. This is much better than could be expected in a real-world situation involving cells, whose variable size and electrical properties could swamp any 2<sup>nd</sup>-order effects neglected in the model. For the purposes of real-world operation one must pick an operating regime (flow, voltage, frequency) such that there is a comfortable margin in the holding characteristics for all encountered particle variations. Such a

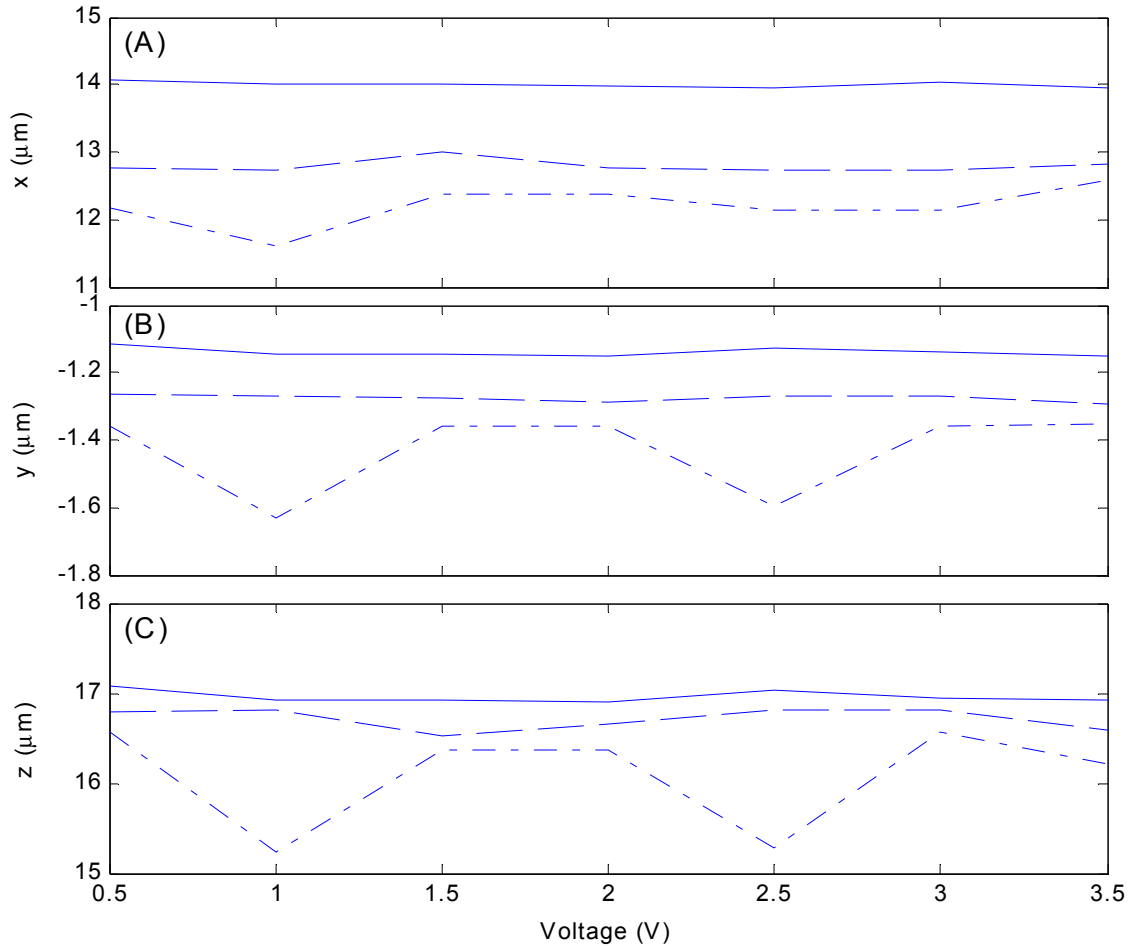


**Figure 6-8:** Predicted particle locations at release using the interpolated results. Plotted are the simulated  $x$ -locations (A),  $y$ -locations (B), and  $z$ -locations (C) of the 13.2- $\mu\text{m}$  (—), 10.0- $\mu\text{m}$  (---), and 7.6- $\mu\text{m}$  (-.-) beads right below the release flowrate. The coordinates are as defined in Figure 4-3A.

design falls outside the scope of this thesis, but the path towards its implementation is clear and the necessary design tools are now in place.

Several effects have been neglected in the model. Besides those described in Chapter 3 (EHD, HD lift forces), several are specific to the extruded geometries. First and foremost, the modeled flow field (Poiseuille) is clearly different from the actual flow pattern, which will be fully three-dimensional in the vicinity of the electrodes. The deviation is insignificant for predictions using the extruded quadrupole, but other geometries that might disturb the flow further would benefit from full CFD modeling. Such modeling could also be used to design the electrode structure to physically control the flow in addition to controlling the electric fields. This would add another “knob” in the design and could lead to higher performance.

Second, care must be taken to ensure that the simulated geometries match what is actually being fabricated. In my case, the deviations in the as-fabricated geometry from the designs significantly affect the predictions. First, the compound taper has not been modeled, nor is the actual taper exactly as modeled. In Figure 6-9 I show the comparisons of simulations using 3.5- $\mu\text{m}$  and 4.0- $\mu\text{m}$  tapers. The different taper angle influences the characteristics for the larger bead sizes dramatically, even though the posts are only 1  $\mu\text{m}$  closer together at the substrate. The 4.0- $\mu\text{m}$  taper reduces the separation between the holding characteristics for the

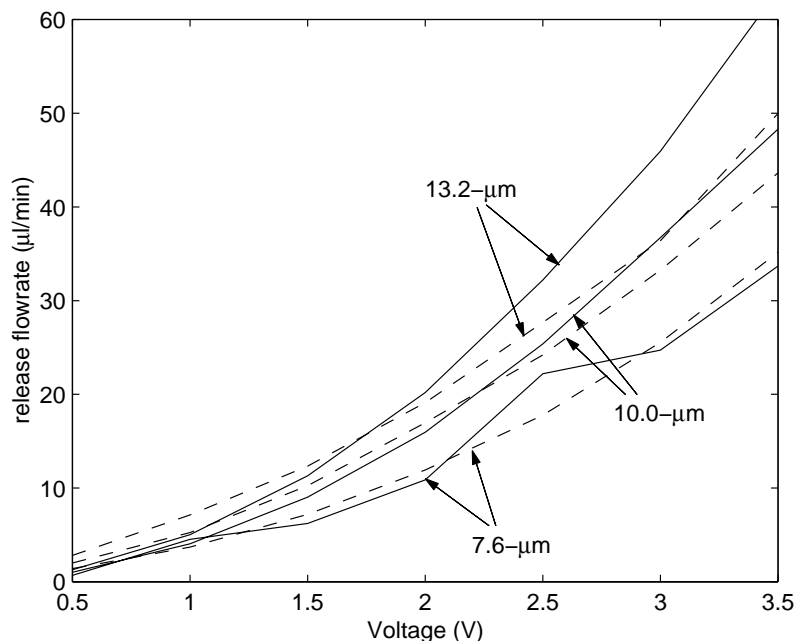


**Figure 6-9:** Comparison between the simulated holding characteristics of beads in traps with 3.5- $\mu\text{m}$  (—) and 4.0- $\mu\text{m}$  (---) electrode tapers. All posts have an 18- $\mu\text{m}$  top diameter and are 50- $\mu\text{m}$  tall. Results from the 3.5- $\mu\text{m}$  tapered traps exhibit a higher slope at large voltages and bead diameters than the 4.0- $\mu\text{m}$  tapered traps. The 3.5- $\mu\text{m}$  tapered traps better represent the data (see Figure 6-5).

10.0- $\mu\text{m}$  and 13.2- $\mu\text{m}$  beads. The 3.5- $\mu\text{m}$  taper, used in the fits in Figure 6-5, gives a better representation of the data. This is consistent with the fact that the beads are to be found near the lower half of the posts (Figure 6-8) where the taper is closer to  $2.0^\circ$  (corresponding to 3.5- $\mu\text{m}$ ), as shown in Figure 6-2. Generating trap designs that are robust to such variations is an interesting future use of the modeling, and a readily conceivable one.

The previous discussion emphasizes that the sensitivity of the predictions with respect to the post geometry could easily result in the deviations. Another geometrical deviation is that some of the posts may not be exactly perpendicular to the substrate. This could be caused during fabrication—a common mechanism for yield loss was non-perpendicular posts. Although the tested devices did not display overt non-perpendicularity, it is still possible to be off a few degrees and remain visually undetectable. A final geometrical discrepancy is that the posts are not perfectly spherical, as demonstrated in Figure 6-2.

### 6.4.3 Comparison to existing traps

Although I have established that this trap holds better than the planar quadrupole described in Chapter 3, it is necessary to compare it to other DEP and non-DEP traps to fairly evaluate it. As described in Chapter 1, the DEP community can be split into researchers who use DEP for separations and those who use it for trapping. As early as 1993, the group at Humboldt University in Berlin described how a three-dimensional electrode configuration in the form an octopole (Figure 1-4) was necessary to “close” the trap and obtain a cage and, presumably, high holding [93]. This group has since exclusively explored this configuration and has recently started performing quantitative trapping experiments. My search through the literature has revealed no other researchers interested in using DEP traps to hold particles against flows.

Among the five reports from the Fuhr group that mention some quantitative measure of trap strength [85, 98, 143, 148, 149], I have chosen to compare the extruded trap to their most recent report [98]. The reason for this is that it contains the most complete description of the experimental parameters, enabling a fair comparison. This report describes the strength of the octopole for holding particles against flow under various electrical excitation schemes. The comparison is summarized in Table 6-2.

The first issue in making a comparison resides in whether to compare the trap performance at equivalent voltages or equivalent electric-field strengths. The former can be viewed as an extrinsic comparison and the latter as an intrinsic one, because the forces fundamentally depend on electric fields, not voltages. Unfortunately, it is difficult to compare electric fields because the non-uniform (i.e. non-spatially constant) nature of the fields in DEP makes it impossible to obtain a single value for their strength. I have thus chosen to compare the trap strengths at equivalent voltages. Because the characteristic electrode separation is similar for both traps, however, the electric fields will be similar and thus the comparison can be viewed as both extrinsic *and* intrinsic.

In addition, since both traps will increase in strength monotonically with voltage, there are no system-level constraints on the maximum voltage applied; the upper limit will be determined by the generation of EHD flows due to heating effects. Thus, both traps can be compared at equivalent voltages.

From the dipole approximation to the DEP force (Eqn. (1-1)), one sees that an accurate comparison requires normalization for different particle radii, CM factors, media permittivities and electric field strengths. The last factor is accounted for by comparing at the same voltage, and the media permittivities are the same because both traps are used in water. Table 6-2 shows that the real parts of the calculated CM factors are nearly identical. This is because at these frequencies the CM factor is dominated by the media conductivity, which is much higher than the particle conductivity. Use in physiological saline would not change the CM factors, and thus the comparison would still hold.

The particle radii are different, so I have normalized their results by the cube of the ratio, using the  $R^3$  dependence of the DEP force. I can perform this normalization for the octopole trap because the particle location will not be dependent on its size—it will always be held at the midstream. For the extruded quadrupole the particle locations change with radius, and thus the strict  $R^3$  dependence does not hold.

The results show that the extruded trap is significantly stronger than the opposed octopole—the holding forces are ~5x larger for similar fields. Although their trap is much easier to fabricate, it is much more difficult to package (because one needs to align the opposed quadrupoles and then make electrical connections to an upside-down substrate). In addition, the height of their chamber is locked to the characteristic dimension of their trap—the separation

Electrode configuration	Electrode spacing (μm)	Particle diameter (μm)	CM factor	Linear flowrate (mm/s)	Volume flowrate (μl/min)	Holding force (pN)	Normalized holding
octopole	40	14.9	-0.47	0.2	0.13	28	20
extruded quadrupole	40	13.2	-0.48	1.3	15	95	95

**Table 6-2:** Comparison of holding against flow between the opposed octopole and the extruded quadrupole trap for beads. The normalized holding for the octopole was obtained from scaling by the cube of the particle radii. The volume flowrate for the octopole results was obtained from the given linear flowrate and the chamber dimensions. The extruded quadrupole exhibits higher holding against volume & linear flowrates and higher holding forces.

between the opposed quadrupoles. The extruded quadrupole relaxes this constraint, adding another variable into the design process. Thus, the work involved in the complex design of the extruded quadrupole is rewarded.

The other comparison to make is to optical tweezers, which may have significant usage overlap. Optical tweezers are advantageous when one needs long-range three-axis control of single particles or when electric access is difficult to achieve. However, if one only needs to localize a particle, wants to trap many particles, or does not have easy optical access, then DEP becomes the trapping method of choice. In terms of strength, optical tweezers usually have holding strengths of a 1-100 piconewtons [151, 152], which are similar to those attainable with the extruded trap.

#### 6.4.4 Holding forces

The extracted holding forces (Figure 6-6) are more than those experienced in conventional traps, and  $\sim 5x$  larger than in the opposed octopole. Although these results were predicted, they still may appear startling. A few simple calculations to show self-consistency demonstrate that these results are indeed reasonable.

First, since the drag force in the trap is less than the drag force at the centerline of the chamber, the holding force of a particle in the trap must be less than the drag force on the same particle along the centerline. This is because the parabolic flow profile necessitates that the particle in the trap is exposed to a flow velocity that is smaller than the centerline velocity (Figure 6-10). In Figure 6-11 I plot, along with the calculated holding forces of 13.2- $\mu\text{m}$  beads in the extruded traps (as in Figure 6-6), the Stokes' drag on 13.2- $\mu\text{m}$  beads in the centerline of the chamber at the release flowrate. The relevant expression is

$$F_{drag,centerline} = 6\pi\eta R U_c = 6\pi\eta R \left( \frac{1.5Q_{rf}}{wh} \right) \quad (6-1)$$

The plot shows that the centerline drag force is indeed always larger than the holding force. A further refinement can be taken by simply correcting the centerline drag to the fluid velocity at the height of the particle

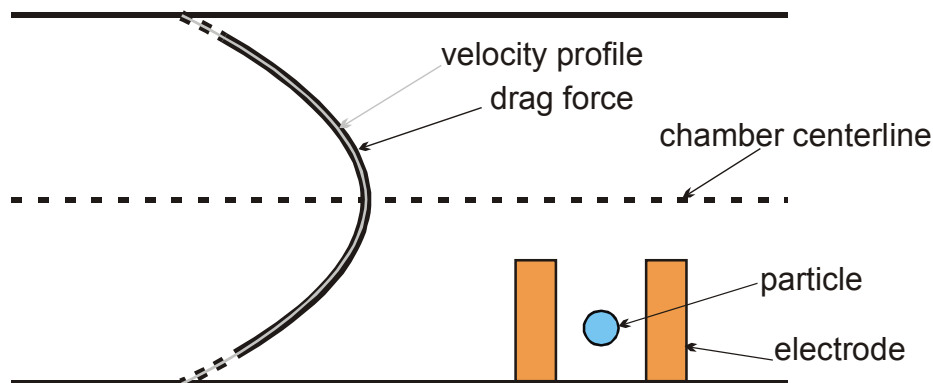


**Figure 6-10:** Depiction of drag force on particles in the chamber. Shown is the parabolic flow velocity profile (in gray) and the drag force profile (in thick black). The drag force follows the velocity profile except near the edges, where particle-wall interactions alter the profile (indicated by dotted black line). The drag on a particle in the trap is smaller than at the centerline because it is near the edge of the parabolic flow profile.

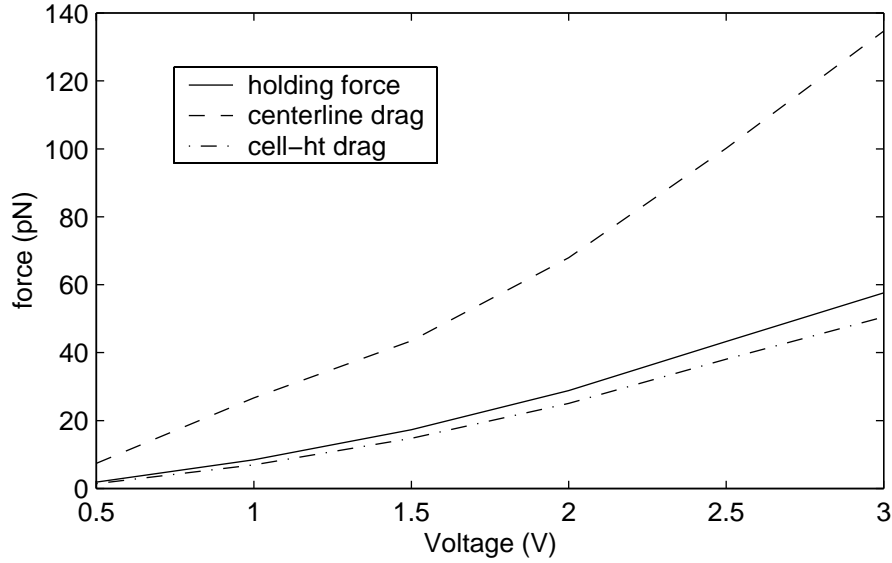


**Figure 6-11:** Holding forces in extruded traps. Plotted is the computed holding force on 13.2- $\mu\text{m}$  beads in the extruded traps as the voltage is varied (—), along with the drag force at the centerline of the flow (---) and at the particle height found using eqn (6-2) (-.-). The computed holding force is always smaller than the centerline drag, as expected, and remarkably close to the results obtained using the flowrate-corrected Stokes’ drag (Eqn. (6-2)).

$$F_{drag,trap} = 6\pi\eta RU(z) = F_{drag,centerline} \left[ 1 - \left( \frac{h/2 - z}{h/2} \right)^2 \right] \quad (6-2)$$

where  $z$  refers to the height of the particle above the substrate. The expression in the brackets is the parabolic velocity profile found in the parallel-plate chamber. The results of this are also shown in Figure 6-11, demonstrating that this simple expression approximates the observed holding forces very well. Thus, the holding forces are in-line with what would be expected at those flows, increasing our confidence in the strength of these traps.

Such good agreement with such a simple model might inspire the question as to why I use a complicated model (described in Chapter 2) for the drag forces. The reason for the good agreement with this simple model is that for the extruded traps the particles are held relatively far away from the wall, and so the 2<sup>nd</sup>-order flow disturbances due to particle-wall interactions are minimized. Since it is not possible to know where the particle will be when designing a new trap, the more complete flow model is necessary. This is seen in the design for the planar quadrupole, where the particle is found on the substrate for low voltages.

#### 6.4.5 Outlook for future trap design

Given the knowledge obtained about trap design, I can give qualitative speculations as to how to make future traps even stronger. I want to stress, however, that strength isn’t everything. Other system parameters, given that the strength is adequate, may become “bottlenecks.” Nevertheless, several things are apparent.

First, one reason for the high trap strength is that the low height of the particle above the substrate shields it from the drag force. An easy way to increase the strength even further is to lower that height. Figure 6-8 shows that the particles average about  $\sim 16 \mu\text{m}$  above the surface and thus could be lowered. Several ways exist to accomplish this. First, the upward DEP force

is due to the slope of the posts and the wiring in the center of the trap. Removing the effect of the wiring by passivating it and tailoring the slope of the posts (perhaps even making them reentrant) could tailor the height of the particle, even pushing it against the substrate, thereby maximally shielding it from the flow.

From a fabrication/packageing standpoint, making robust traps is crucial. The current trap geometry is very stable during operation—not a single post has been damaged after packaging. However, gold is soft, and the posts can easily get bent during fabrication steps, especially wet steps. This can be alleviated by either 1) using a different geometry without posts, 2) increasing the diameter of the posts, 3) encapsulating the posts in SU-8 till after diesaw, or 4) using a harder metal.

Finally, the strong sensitivity of the predicted trap performance on the taper angle suggests that this specific trap geometry is not robust towards processing variations. Designing a trap where taper angle does not affect the position of the particle or the electric field strength, such as a trap that forces the particle to the substrate, should be much more stable in this regard.

## **6.5 Conclusion**

In this chapter I have described initial tests with the extruded traps demonstrating that they indeed operate as designed. Similar to the experiments performed in Chapter 3, I have used beads as surrogate cells to quantitatively determine the holding forces in these traps. The predicted holding characteristics, once adjusted for the actual geometries of the fabricated device, are very close to the observations. This demonstrates that the modeling environment can be used for predictive design of traps much different than those it was validated with, and that it thus is a truly useful tool. In addition, these results introduce the extruded quadrupole trap into the literature, which, although more difficult to fabricate over planar traps, has numerous advantages.

## Chapter 7: Cell-based operation

Up to this point, I have designed and fabricated an array of extruded quadrupole traps that have been shown to hold beads stronger than the planar quadrupole traps. In this chapter, I will demonstrate the use of these traps with cells, showing the proof-of-concept operation of the  $\mu$ DAC. The capabilities that constitute proof-of-concept operation are: holding with cells, single-cell discrimination, independent trap control, and dynamic fluorescent assays.

### 7.1 Materials and Methods

#### 7.1.1 Cell culture

HL-60 cells were obtained from ATCC (Manassas, VA). They were cultured in T25 or T75 flasks in RPMI-1640 (BioWhittaker, Walkersville, MD) with 5% (v/v) fetal bovine serum (JRH Biosciences, Lenexa, KS), 2 mM L-glutamine (Sigma, St. Louis, MO), 100 IU/ml penicillin, and 100  $\mu$ g/ml streptomycin (Sigma Cell Culture, St. Louis, MO) in a 95% O<sub>2</sub>/5% CO<sub>2</sub> atmosphere at 37 °C. Cultures were maintained between 10<sup>5</sup> and 10<sup>6</sup> cells/ml. They were subcultured approximately every 7 days by gently pipetting the media up and down to break up clumps and adding cell suspension to fresh media to obtain a cell density of 10<sup>5</sup> cells/ml (determined by Trypan Blue dye exclusion with a hemacytometer).

#### 7.1.2 Assay buffer

The assay buffer was made by adding 10 mg/ml of bovine serum albumin (BSA, Boehringer Mannheim, Indianapolis, IN) to Hank's Buffered Salt Solution (HBSS, GibcoBRL, Grand Island, NY). The detergent solution was made by adding 100  $\mu$ g/ml of sodium dodecyl sulfate (SDS, GibcoBRL, Grand Island, NY) to the assay buffer.

#### 7.1.3 Cell assay preparation

Aliquots of cells were obtained from the flasks. They were centrifuged for 5-8 min at 125 x g and the supernatant discarded. Fresh assay buffer was added and this procedure was repeated 2x, with the final volume adjusted to obtain a cell concentration of  $\sim 4 \times 10^5$  cells/ml.

#### 7.1.4 Calcein labeling

For calcein labeling or leakage experiments, calcein-AM (Molecular Probes, Eugene, OR) was added to the assay buffer to obtain a concentration of 10  $\mu$ M. Equal volumes of this calcein solution were added to the cells suspended in the assay buffer, to obtain a final calcein concentration of 5  $\mu$ M, and incubated at room temperature for 30-45 minutes. Following incubation, the cells were washed in the assay buffer 2x to remove extracellular calcein from the solution.

Aliquots of the calcein-labeled cell suspensions were added to the chamber via the injection valve (Figure 3-1C). To perform calcein leakage experiments, the detergent solution was subsequently introduced into the chamber via the four-way valve (Figure 3-1C) after the cells had been trapped.

Calcein-loading experiments were performed by injecting unlabeled cells into the chamber, capturing them in the traps, and then using the four-way valve to inject 1  $\mu\text{M}$  or 10  $\mu\text{M}$  calcein in the assay buffer.

### **7.1.5 Electrode Traps**

The extruded quadrupoles were prepared as described in 0. For the holding experiments, I used the same trap array that was used in 0, while other devices were used for the rest of the experiments presented in this chapter. The packaging and test setup are also as described in 0.

### **7.1.6 Chamber purging and cleaning**

Before commencing any cell injections, the chamber was flushed with the assay buffer for  $\sim 20$  min, usually at 50  $\mu\text{l}/\text{min}$ . After experiments were complete, the chamber was cleaned with  $\sim 1$  ml of HBSS/BSA solution, then  $\sim 1$  ml of HBSS/Triton X-100 solution, then  $\sim 1$  ml of DI  $\text{H}_2\text{O}$ , and finally dried with  $\text{N}_2$ .

### **7.1.7 Optics**

The devices were observed under a Zeiss Universal upright microscope, modified for use with both epi-fluorescence and reflected brightfield illumination. A filter set for calcein, comprised of a 485-nm bandpass excitation filter, a 505-nm dichroic filter, and a 530-nm longpass emission filter was obtained from Omega Optical (Brattleboro, VT) and thinned to 3-mm thickness to fit into the microscope's filter slots. Images were recorded with a video camera (TM-7CN, Pulnix America, Inc., Sunnyvale, CA) or a cooled-color CCD (Spot-RT Color, Diagnostic Instruments, Sterling Heights, MI) and stored on a Pentium-class computer. Time-lapse images were manually shuttered because of the difficulty of attaching an automatic shutter to the microscope. Movies were captured with a Pinnacle Systems DC10plus analog capture board (Mountain View, CA) connected to the video camera.

### **7.1.8 Image analysis**

Various still-image analysis operations were performed using either Scion Image (Scion Corporation, Frederick, MI), Adobe Photoshop (Adobe Corporation, San Jose, CA), or the Matlab Image Processing Toolbox (The Mathworks, Natick, MA). Movies were edited using either the DC10plus software or Adobe Premiere (Adobe Corporation, San Jose, CA). Cell diameters for the holding experiments were obtained by converting measured pixel distances to actual lengths via calibrations obtained at different magnifications with a ruled microscope slide.

Fluorescence intensities for the dynamic assays were determined via Matlab. Algorithms found the pixel area comprising each cell in a series of time-lapse images by thresholding the images. From the pixel values, the mean and maximum intensity values could be recorded. Other values, such as cell area (in pixels), could easily be determined from the thresholded image. A swath of nominally dark pixels was used to determine the background intensity level, which was subtracted from the measurements. Changes in the exposure time or gain of the camera were compensated for by linearly scaling the measured pixel values.

Multicolor images were created by adding the grayscale fluorescence images to the green channel of color brightfield images in either Photoshop or Matlab.

### 7.1.9 Release flowrate measurements

The release flowrate measurements were performed identically to those in Chapter 3. Briefly, after trapping a cell, an image was taken so that its diameter could be subsequently determined. Flow was initiated, and if the cell stayed in the trap for 60 sec, the cell was considered captured. The flowrate was increased in 1  $\mu\text{l}/\text{min}$  steps until the cell was ejected, and this flowrate was termed the release flowrate.

### 7.1.10 Modeling

All modeling to compare to the measured holding characteristics used the as-fabricated geometries, as described in Chapter 6. Although the cell membrane capacitance varied in the simulations (described below), the nominal values for HL-60 cells were from [81], with  $C_m=1.6 \mu\text{F}/\text{cm}^2$ ,  $G_m=0.22 \text{ S}/\text{cm}^2$ ,  $\Delta=1 \text{ nm}$ ,  $\epsilon_{\text{cyto}}=75 \text{ F}/\text{m}$  &  $\sigma_{\text{cyto}}=0.75 \text{ S}/\text{m}$ .

## 7.2 Results

### 7.2.1 Qualitative operation

#### *Array loading*

Array operation with cells was fairly straightforward. After warming up the electronic equipment and purging the chamber with  $\sim 1 \text{ ml}$  of the assay buffer run at  $50 \mu\text{l}/\text{min}$ , I would inject a  $\sim 50\text{-}55 \mu\text{l}$  plug of cells. After the cell-containing aliquot had started to enter the chamber, I would turn off the flow for  $\sim 1\text{-}2 \text{ min}$  to allow the cells to settle to the chamber bottom. At this point I would restart the flow, but at a flowrate that was less than the release flowrate for a given voltage & frequency. Cells near the surface of chip would flow by the array and be trapped, while cells far above the substrate would simply flow over the traps. The use of BSA in the assay buffer was advantageous here in that it prevented cells from adhering to the substrate after they had settled.

A typical example of array loading is shown in Figure 7-1, which shows the loading of a  $1 \times 8$  array with calcein-labeled HL-60 cells. The first image (Figure 7-1A) was taken 5 sec after the application of flow, but before any cells were loaded into the array. One cell (solid arrow) is nearing trap #6, while two other cells (dotted arrows) approach trap #3. In Figure 7-1B, the first cell has been trapped, and by Figure 7-1D, 9.5 sec after the start of the flow, the two cells denoted by the dotted arrows have been loaded into trap #3. Figure 7-1F and Figure 7-1G show a similar situation with two cells being loaded into trap #5. Figure 7-1D and Figure 7-1E show a cell (solid arrow) that is being repelled from the post and is driven crosswise against the flow into trap #4. 23 seconds after the start of flow, six of the eight traps have been loaded with cells. Since one trap (#2) does not work, this means that six of seven functional traps have been loaded in 23 seconds.

This loading sequence, which is typical, demonstrates a few common themes in operating these traps. First, in the loading phase, when the applied flow is much less than the release flowrate for the given operating conditions, it is likely that more than one cell will be loaded into a given trap. Second, the actual loading time will vary with cell concentration and flowrate—introducing a high concentration of cells will load the trap very quickly, but will also make it much more probable that  $>1$  cell will be trapped in a given site. Obtaining one cell-per-trap, after loading, is the topic of the next section. Third, the trapezoidal structure of the posts aids the

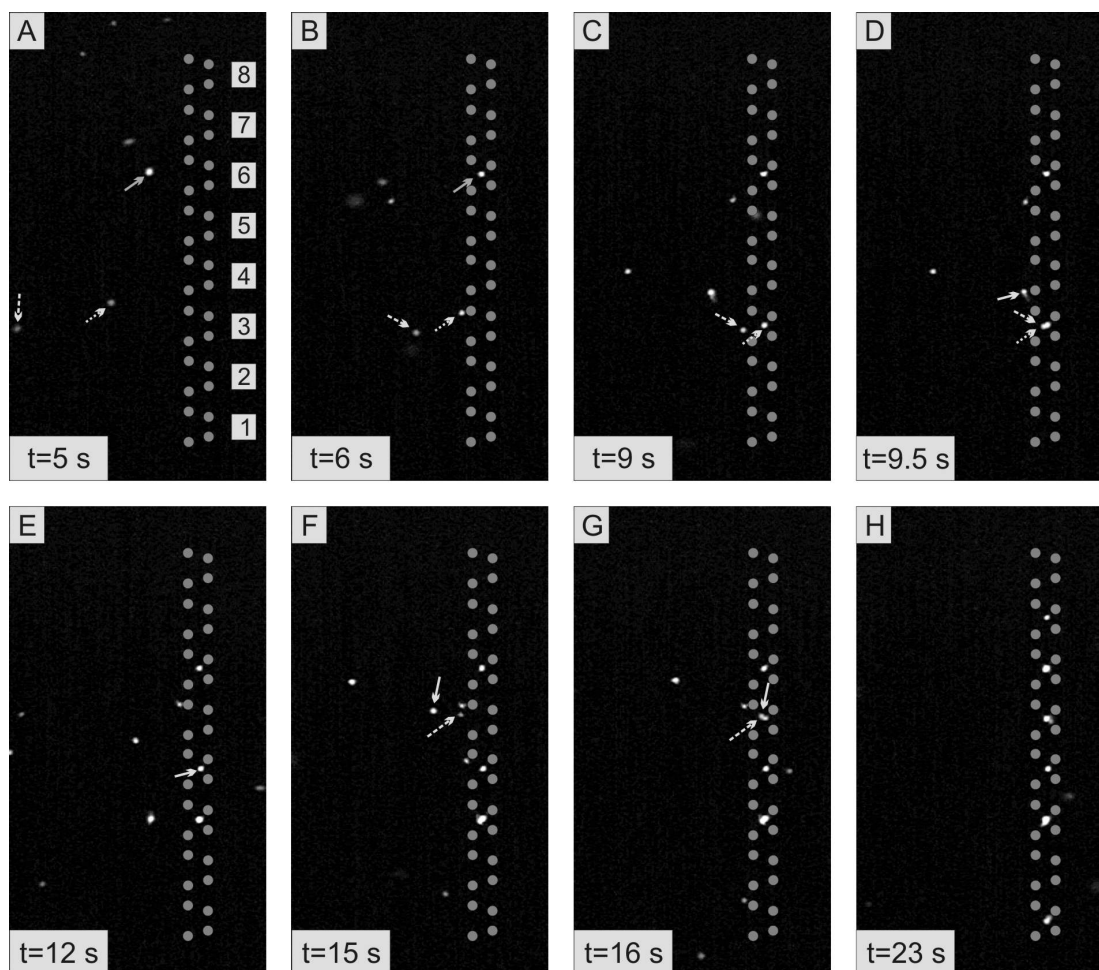


**Figure 7-1:** Loading a 1x8 array of traps with calcein-labeled HL-60 cells. Shown are fluorescence images extracted from video with the post locations superimposed and denoted by gray circles. The cell intensities were scaled and gamma-shifted to make them easier to visualize. The flowrate was 10  $\mu\text{l}/\text{min}$  from left to right while the electrodes were energized at 3V and 20 MHz. The time stamp of the frames (after the initiation of flow) is given in the bottom left of each frame.

loading process—both physically by the obstruction of the posts and also electrically due to the lower loading barrier (Figure 4-4).

#### *Single-cell discrimination*

One of the requirements of the  $\mu\text{DAC}$  is that the traps must be able to be set to hold *only* one cell per site. In Figure 7-1, I show that after loading it is possible that some traps will hold more than one cell. Single-cell discrimination can be performed after loading by applying a flowrate that is close to but less than the release flowrate for a given set of conditions. Starting with a loaded trap, I can effect single-cell discrimination by now applying a higher flowrate than during loading. As shown in Figure 7-2, this causes the cells to revolve around each other. The maximum separation between the cells increases as the flowrate increases, until one of the cells is released. This is seen happening in Figure 7-2D at a flowrate of 12  $\mu\text{l}/\text{min}$ , 30 seconds after the 2<sup>nd</sup> cell was caught.

While the operating conditions needed to obtain discrimination are obtained empirically, they still follow the pattern shown in Figure 3-3. One additional complication of using cells is that the operating window for obtaining single-cell discrimination is smaller than with beads, for

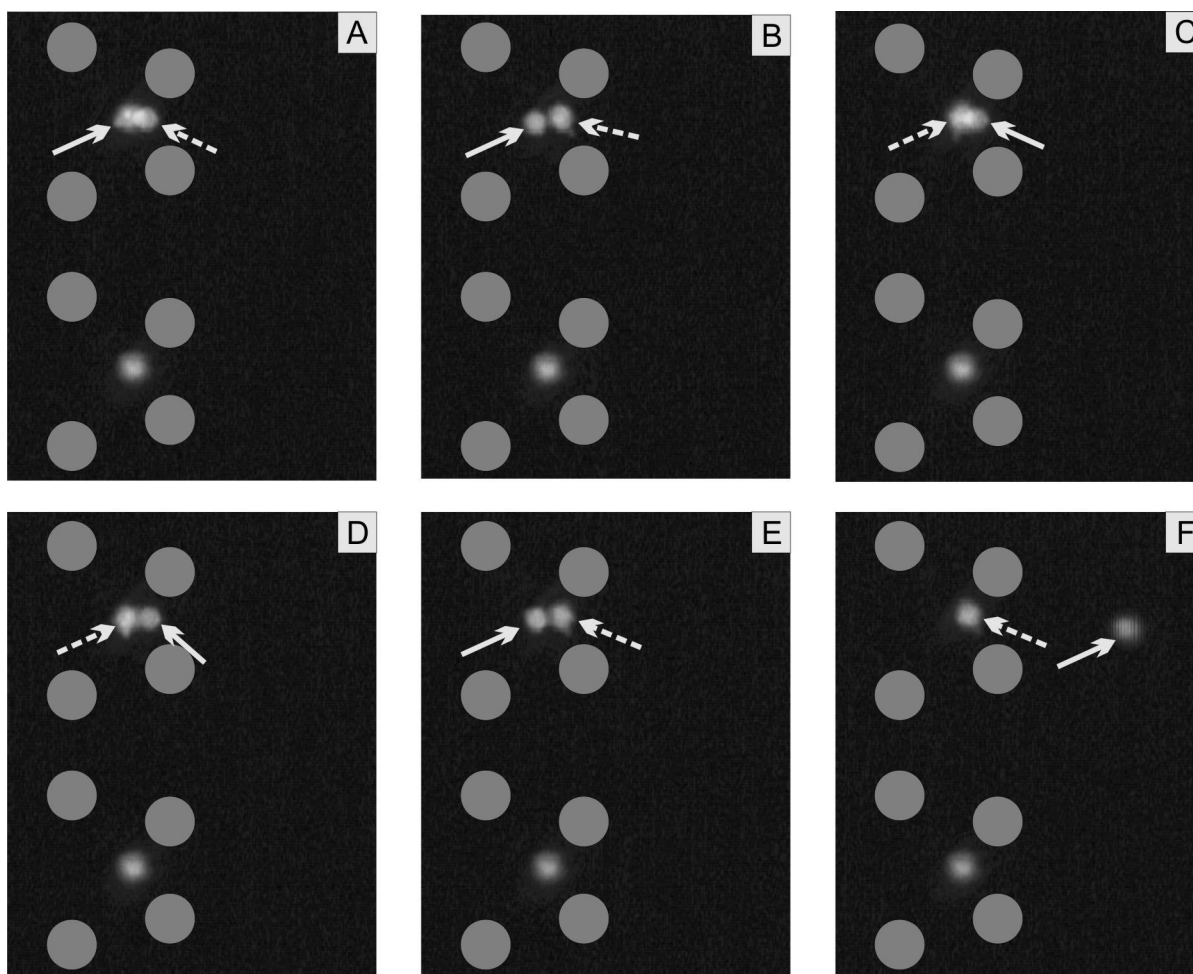


**Figure 7-2:** Single-cell discrimination. Shown is a time sequence of fluorescence images extracted from video with the superimposed post locations denoted by gray circles. The arrows follow a particular cell over time, illustrating the back-and-forth motion of the cells around each other. The cell intensities were scaled and gamma-shifted to make them easier to visualize. The flowrate was 12  $\mu\text{l}/\text{min}$  from left to right while the electrodes were energized at 3V and 20 MHz. The total time from 2<sup>nd</sup>-cell capture to release was 30 sec.

several reasons. First, the cells are not as monodisperse as the bead solutions, and thus flowrates that work well for single-cell discrimination for a given pair of cells could be too small or too large for another pair. In addition, cells have larger distributions of electrical properties, narrowing the window even further. However, the ability to perform single-cell discrimination on a given trap with a given pair of cells is fairly robust, being repeated many times with many different sets of cells over the course of using these devices.

#### *Independent trap control*

Another designed property of these trap arrays is the ability to independently toggle traps on and off by varying the potential on only one electrode. In Figure 7-3 I show an implementation of this with a 1x8 array of electrodes that has been loaded with seven calcein-labeled HL-60 cells at 3V and 20 MHz under a flow of 10  $\mu\text{l}/\text{min}$ . One-by-one, I have turned off each trap, and the cells in those traps have been released and have flowed away. While this is not significantly different than the experiment depicted in Figure 6-3, the demonstration with cells is a necessary step toward validation of the  $\mu\text{DAC}$ .

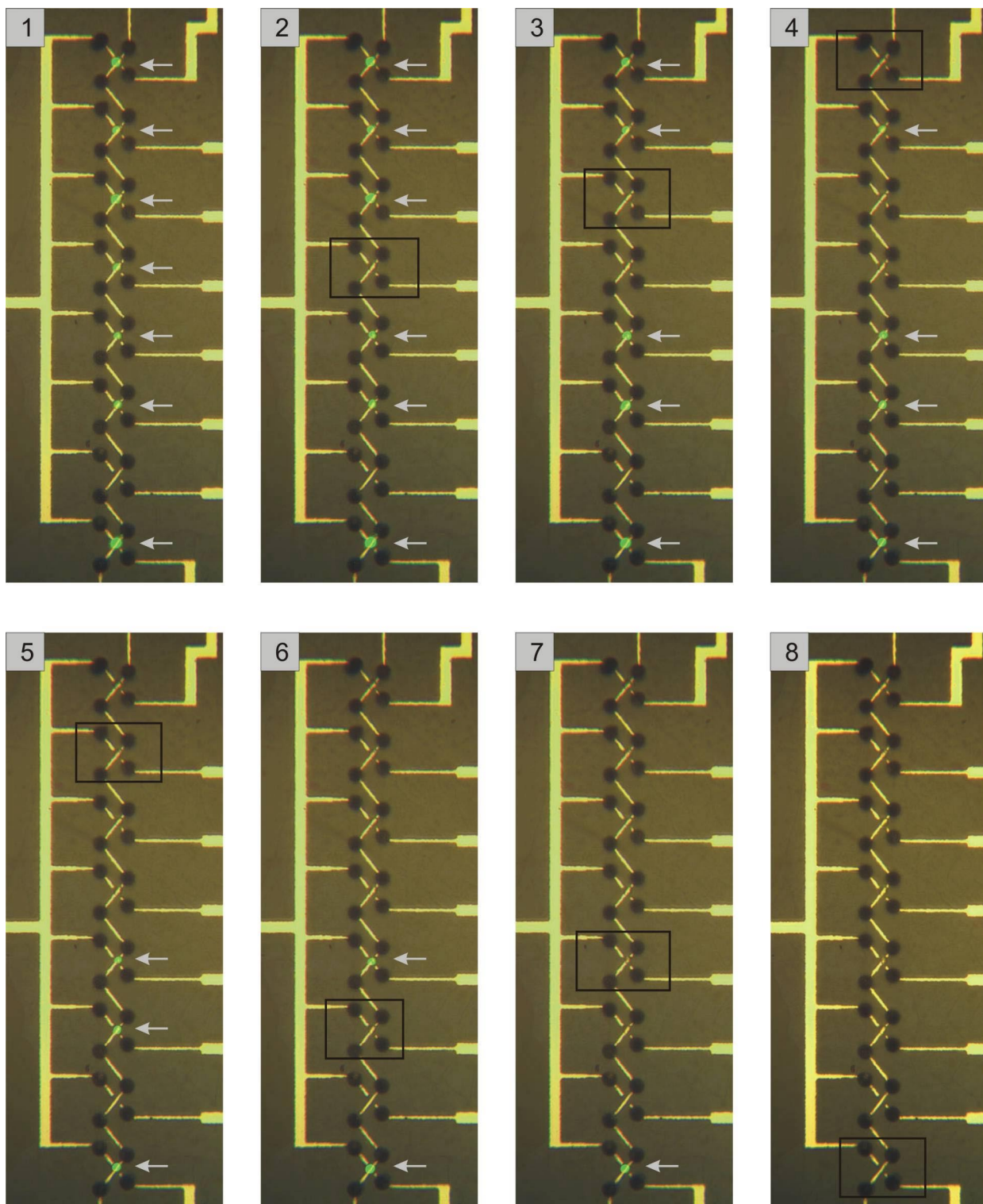


**Figure 7-3:** Independent trap control. Shown are a series of composite brightfield and fluorescence images illustrating selective and independent trap control. Seven calcein-labeled HL-60 cells, trapped in a 1x8 array, are individually released in a defined yet arbitrary manner in Panels 1 to 8. The arrows indicate the cell locations, while the black box indicates the trap that was just turned off. Electrodes were energized with 3V at 20 MHz and flow was from left-to-right at 10  $\mu$ l/min.

## 7.2.2 Quantitative operation

### *Holding with cells*

Following qualitative validation of the operation of the small array with cells, the first quantitative experiments sought to determine if Figure 6-7 gives a correct representation of the holding characteristics of cells. Given the validation experiments performed with beads in Chapter 6, the idea here was not to validate the modeling but rather to determine if the electrical model of the cell that I used was reasonable. The reason for this is that the difference between beads and cells will only manifest itself in the CM factor (and, if they are different sizes, in the  $R^3$  factor). Thus, if the bead experiments compare well with the model predictions, which they do, then any deviations with cells can be isolated to an incorrect model for the CM factor.

I performed holding experiments with ten different unlabeled cells in one of the traps of the same device used in Chapter 6. I varied the frequency between 1 MHz, 10 MHz, and 20 MHz, and chose three voltage points 1V, 2V, and 3V. Each cell was used for between one and four data points, depending on whether I could retrieve it after it was released, for a total of 14 data points. I obtained the diameters of each of the cells from images taken with the CCD camera. The average cell diameter was 11.4  $\mu\text{m}$ , with a range of between 9.3 and 14.4. This is fairly close to the cell diameter of 12.5  $\mu\text{m}$  that I used in the model predictions.

In Figure 7-4 I show the results of the holding *experiments at various frequencies* superimposed on top of the holding *predictions at one frequency*—20 MHz (from Figure 6-7). Even though the predictions were made using a single cell size and a single frequency, they can be useful in orienting the comparison. Two features are apparent in the comparison. First, the predicted results at 20 MHz are fairly close to the actual data at all frequencies, indicating that the model for the CM factor is not too far off. Second, there is no significant frequency trend amongst the data taken in Figure 7-4. However, the CM factor that I used for these cells, and shown in Figure 7-5, has a large difference between the lowest frequency of 1 MHz (CM=-0.32) and the two higher frequencies—10 MHz (CM=-0.10) and 20 MHz (CM=-0.09). This difference would cause the predicted holding characteristics at 1 MHz to be much larger than all the data shown in Figure 7-4. The fact that the data match the  $f=20$  MHz predictions well suggests that the predicted CM factor at that frequency is accurate, and that the dispersion at  $\sim 1$  MHz (Figure 7-5) needs to be shifted to lower frequency to increase the size of the plateau between 10 and 50

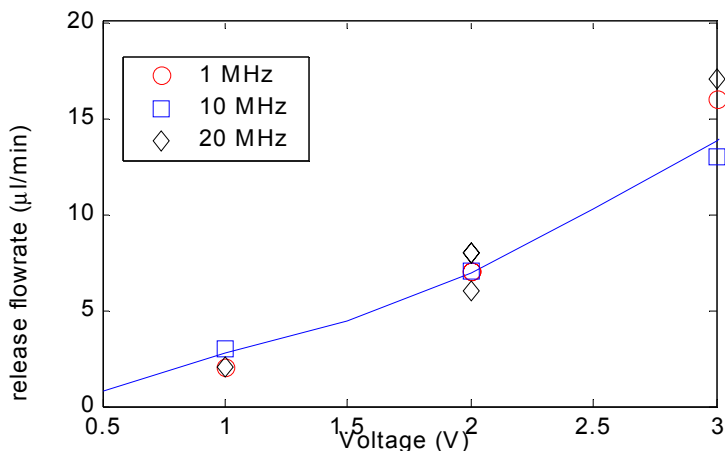


**Figure 7-4:** Results of cell-holding experiments at various frequencies superimposed on the predicted holding characteristics for 12.5- $\mu\text{m}$  diameter HL-60 cells at 20 MHz (from Figure 6-7, using  $C_m=1.6 \mu\text{F}/\text{cm}^2$ ). Plotted is data for cells taken at 1 MHz (○), 10 MHz (□), and 20 MHz (◇).

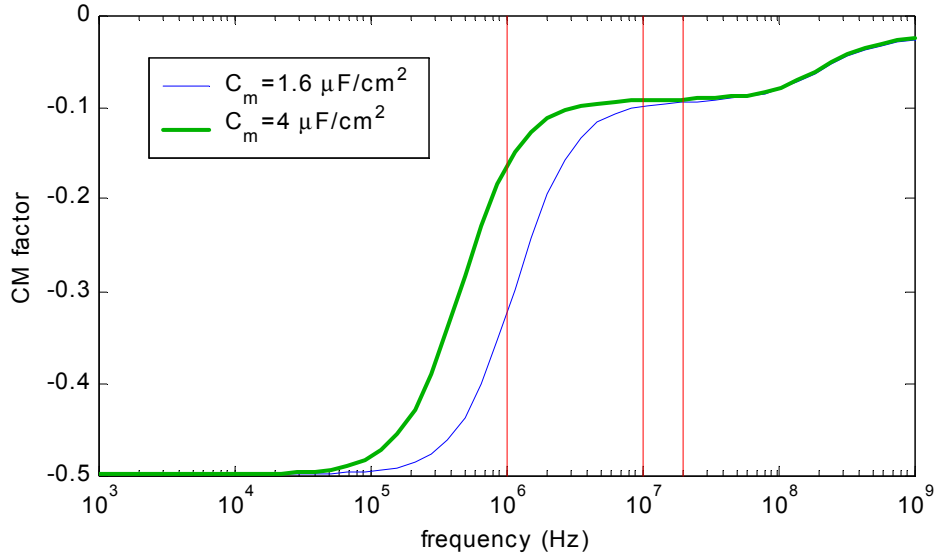


**Figure 7-5:** CM factor for 9.3- $\mu\text{m}$  HL-60 cells when the membrane capacitance is 1.6  $\mu\text{F}/\text{cm}^2$  (—) and 4.0  $\mu\text{F}/\text{cm}^2$  (—). The calculated CM factor for  $C_m=1.6 \mu\text{F}/\text{cm}^2$  is similar to that of Figure 4-10B. Also indicated on the plot are vertical lines representing the three frequencies where experimental holding data were taken.

MHz.

To determine which parameters in the model for the CM factor influence this plateau, one can take the appropriate limits of the CM factor expression of Eqn. (1-3). One simplifying assumption is that in most cases (including here) the membrane conductance ( $G_m$ ) can be neglected. With this assumption, the approximations for the frequency dependencies of the CM factor for cells in highly conductive media are shown in Figure 7-6. A quick check of the approximate dependencies shows them to be plausible. For instance, at low frequencies, the situation is conductivity dominated (Eqn. (1-4)), with the cell conductivity being represented by its surface conductance and cell radius. At high frequencies, the situation is permittivity dominated (Eqn. (1-5)), with the permittivity of the cytoplasm representing the cell. The CM factor at MHz frequencies, in the region of interest, is also conductivity dominated but this time with the cell represented by its cytoplasmic conductivity.

Examining the 1 MHz dispersion, one sees that its frequency is controlled by the membrane capacitance ( $C_m$ ), since the medium conductivity ( $\sigma_m$ ) is fixed and the cell radius ( $R$ ) is known. Thus, to decrease the dispersion frequency, one must increase the membrane capacitance. Increasing this value from 1.6  $\mu\text{F}/\text{cm}^2$ , used in the predictions of Figure 6-7, to 4.0  $\mu\text{F}/\text{cm}^2$ , does indeed move the dispersion to lower frequency without disturbing the plateau levels (Figure 7-5). In addition, modeling the CM factor for the smallest measured cell size gives a worst-case scenario, since the dispersion frequency will be highest for the smallest cells (Figure 7-6). With this membrane capacitance, there is still a difference in the CM factors at 1 MHz and 20 MHz, but it is much smaller— $CM=-0.16$  at 1 MHz and  $CM=-0.09$  at 10 MHz and 20 MHz. Increasing the membrane capacitance further would reduce this difference even more. However, increasing the value too much would lead to overoptimization past the limits of the measurements and possibly to a non-physical membrane capacitance.

Is  $C_m=4.0 \mu\text{F}/\text{cm}^2$  itself a reasonable result? Huang et al.'s measurements found a membrane capacitance for HL-60 cells of  $1.6 \pm 0.95 \mu\text{F}/\text{cm}^2$  [81], and which is lower than the that being considered here. The chosen value of  $C_m$  is still plausible, however, because 1) it is in

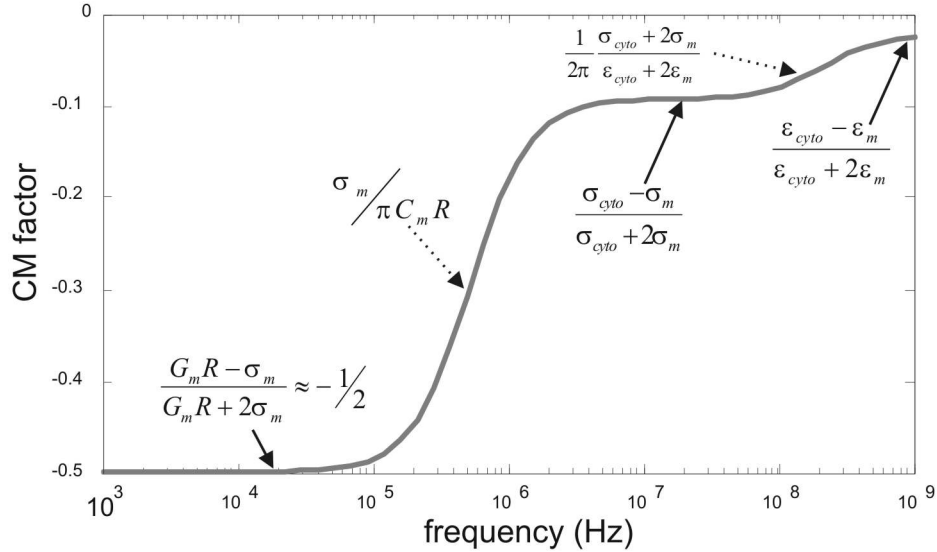


**Figure 7-6:** CM factor HL-60 cells with the approximations for the various frequency dependencies indicated. The solid arrows indicate approximations to the CM factor in various frequency regimes, while the dotted arrows indicate the approximate dispersion frequencies separating those regimes.

the  $\mu\text{F}/\text{cm}^2$  range typical of cells, 2) different cell populations cultured under different conditions can be expected to yield diversity in their electrical properties, and 3) Huang et al.'s values were determined for cells in low-conductivity media, and the membrane electrical properties may be dependent on the suspension medium. Thus, the value of  $4.0 \mu\text{F}/\text{cm}^2$  is plausible. More extensive experiments could refine these values, leading possibly to an alternate hypothesis, but is beyond the scope of this thesis.

In Figure 7-7 I plot the effects of this change in the membrane capacitance on the predicted holding characteristics. Here I have only simulated the characteristics at  $V=1\text{V}, 2\text{V},$

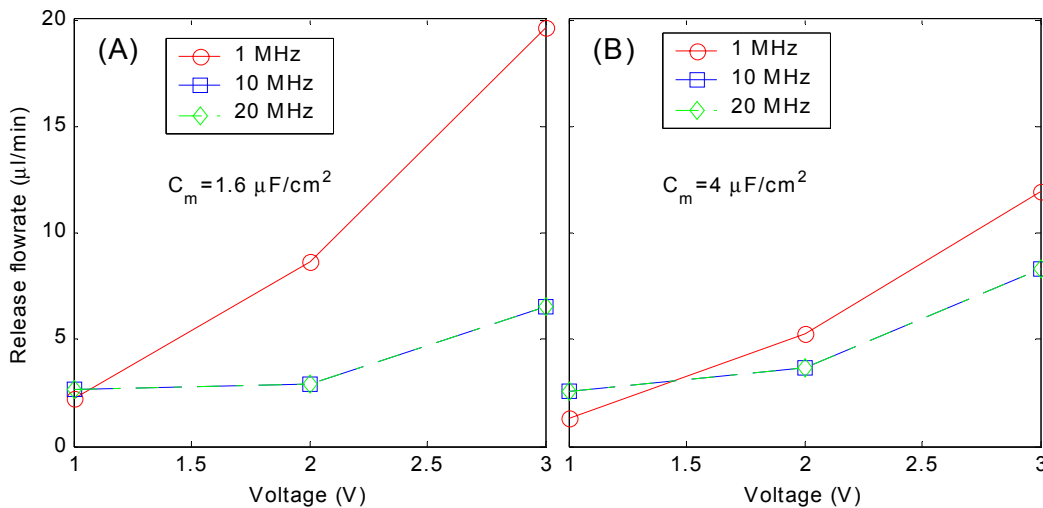


**Figure 7-7:** Effects of changes in the membrane capacitance on the predicted holding characteristics of  $9.3\text{-}\mu\text{m}$  HL-60 cells when their membrane capacitance ( $C_m$ ) is (A)  $1.6 \mu\text{F}/\text{cm}^2$  or (B)  $4.0 \mu\text{F}/\text{cm}^2$ . Plotted are the predicted holding characteristics at 1 MHz ( $\text{---}\circ\text{---}$ ), 10 MHz ( $\text{---}\square\text{---}$ ), and 20 MHz ( $\text{---}\diamond\text{---}$ ), for cells in traps with  $19\text{-}22.5\text{-}\mu\text{m}$  diameter posts. The results at 10 MHz and 20 MHz are indistinguishable and thus overlap. Increasing the membrane capacitance lessens the difference between the holding characteristics at different frequencies.

3V, and so the results are not as smooth as for finer simulations performed elsewhere in this thesis. The results clearly indicate that increasing the membrane capacitance decreases the differences between the holding characteristics at higher frequencies (10 MHz and 20 MHz) versus those at 1 MHz, which is what was predicted. Specifically, the maximum difference in holding characteristics versus frequency goes from 13  $\mu\text{l}/\text{min}$  for  $C_m=1.6 \mu\text{F}/\text{cm}^2$  to 4  $\mu\text{l}/\text{min}$  for  $C_m=4.0 \mu\text{F}/\text{cm}^2$ . The results for  $C_m=4.0 \mu\text{F}/\text{cm}^2$  still have some frequency dependence, but the magnitude is small enough to be within the experimental uncertainties.

Figure 7-8 shows the final results of superimposing the experimental cell holding data on top of the extents of simulations encompassing the parameter space. For these results I performed simulations across the measured cell diameters (9.3  $\mu\text{m}$  to 14.4  $\mu\text{m}$ ), the experimentally applied frequencies (1 MHz to 20 MHz), as well as the two post profiles that I determined in Chapter 6 spanned the as-fabricated geometries. The minimum and maximum limits of all these simulations were extracted and comprised the predicted space.

All the cell-holding results fall within the predicted space, lending credence to the chosen form of the CM factor. Further optimization could be employed to reduce the size of the design space, but would not be appropriate here given that there is not much data and thus not much statistical significance. The goal of these experiments was to verify that the cell holding characteristics were not radically different than predicted, and this has been accomplished.

#### *Calcein loading*

One of the most interesting properties of the  $\mu\text{DAC}$  is the ability to monitor the fluorescent dynamics of multiple individual cells. To demonstrate this, I used a simple calcein-loading assay, whereby the non-fluorescent precursor calcein-AM is passively loaded into cells through the cell membrane. Once inside a viable cell, the calcein-AM will be cleaved by cytoplasmic esterases to form a non-cell-membrane permeant fluorophore, thus turning live cells green.

I performed this assay by introducing unlabeled HL-60 cells into the chamber and trapping them in the array. After they were trapped, I introduced calcein-AM in the assay buffer

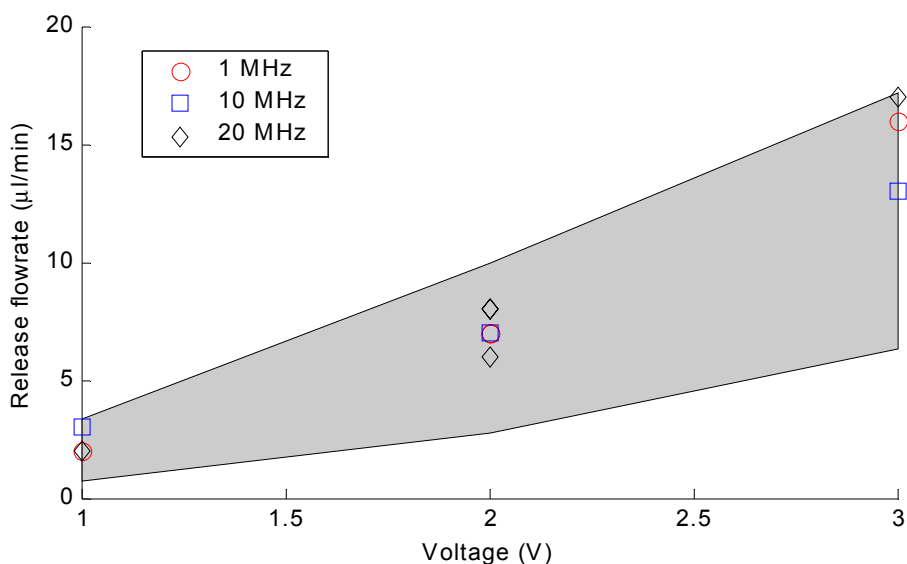


**Figure 7-8:** Cell holding data overlaid with a patch (light gray) denoting the extents of the predicted parameters. The predictions spanned the measured cell sizes of 9.3-14.4  $\mu\text{m}$ , frequencies of 1 MHz—20 MHz, and post top diameters of 18.5-19  $\mu\text{m}$ . All the data lies within the predicted space.

into the chamber, at a concentration of 10  $\mu\text{M}$  and a flowrate of 10  $\mu\text{l}/\text{min}$ , and monitored the cells' fluorescence over time.

Figure 7-9 shows four time-sequence images of the loading of five traps from one run. Image analysis at the end of the experiment, upon releasing the cells, indicated that traps #2 and #3 contained two cells at the end of the experiment. Other image analysis, using a high-magnification objective, suggested that trap #5 contained two cells at the beginning but not at the end of the experiment (it is unclear when the 2<sup>nd</sup> cell was released from that trap). It appears that traps #1 and #4 contained only one cell for the entire experiment. The images clearly indicate that the cells are getting brighter over time. The last panel, Figure 7-9D, shows that cells in two of the traps (#2 & #3) have disappeared because I toggled their traps to release them. Thus, this figure shows the observation of fluorescence information over time on a minimum of two individual cells—and possibly up to five, depending on when the 2<sup>nd</sup> cells entered/exited the traps—followed by sorting.

One can also extract quantitative fluorescence information from these images. The choice of which fluorescent parameter to follow—mean fluorescence, maximum fluorescence, or some other parameter—would presumably be dictated by the particular assay being performed; for these assays I simply monitored the mean and maximum intensities of the cells.

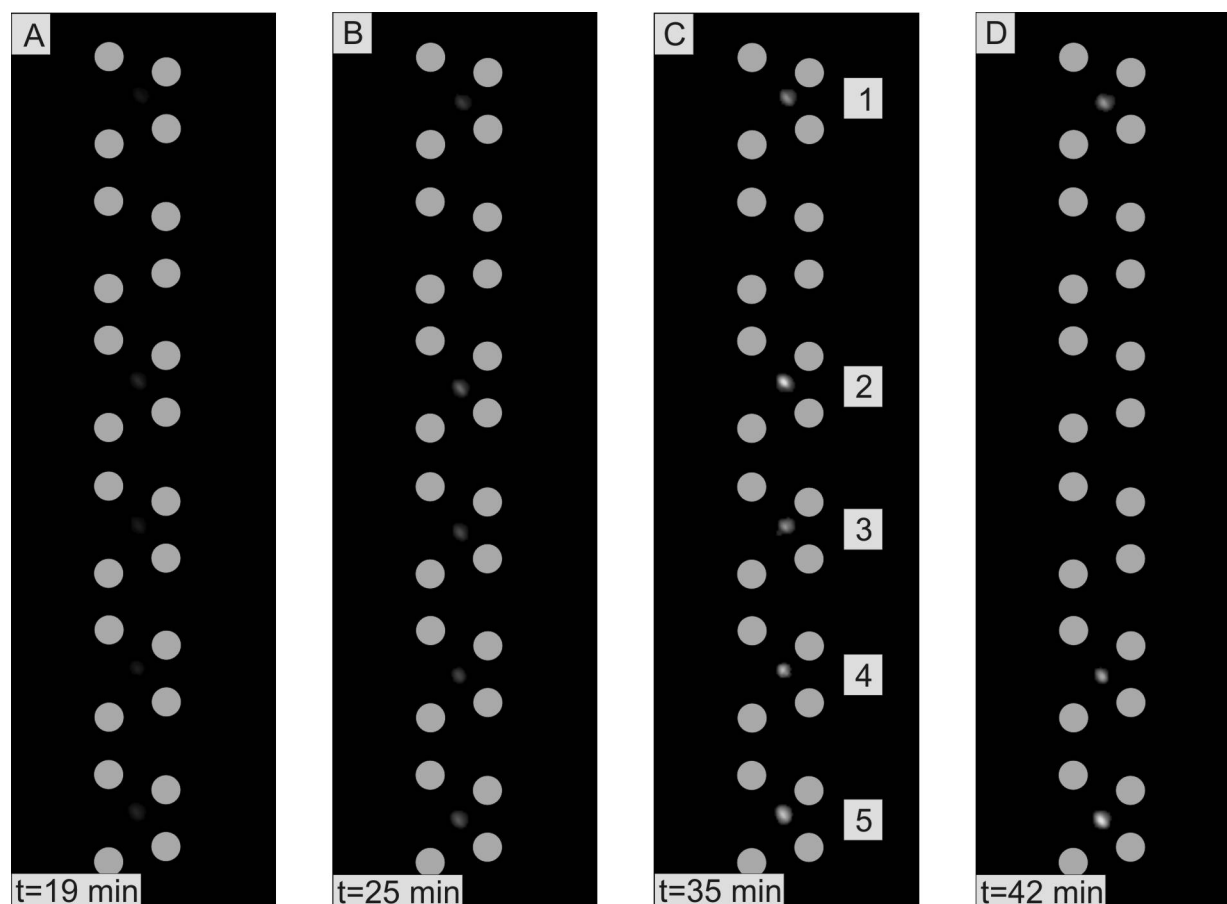


**Figure 7-9:** 10  $\mu\text{M}$  calcein loading of HL-60 cells. Shown is a time sequence of fluorescence images with the superimposed post locations denoted by gray circles. The timepoints of the images are shown in the lower left corners. The experimental parameters were  $V=3\text{V}$ ,  $f=20\text{ MHz}$ , flowrate=10  $\mu\text{l}/\text{min}$ . The image pixel values were linearly adjusted to maximize the intensity of (C), with the same transform subsequently applied to panels A, B, & D.

Figure 7-10 shows the results of extracting this information from the sequence of images. In these plots I show the mean (Figure 7-10A) and maximum (Figure 7-10B) intensities in each of the traps over time, as well as the normalized mean intensity (Figure 7-10C) and the cell area (Figure 7-10D). The mean intensities of each of the curves have been shifted relative to each other to ease comparison. The normalized mean intensities (Figure 7-10C) were determined for each site by normalizing the mean intensities to the minimum and maximum encountered intensities during the experimental time course.

One can see that the mean fluorescence intensities of the cells in the five traps increases over time, following similar kinetics, with a 50% rise time of ~20 minutes (Figure 7-10C). The mean intensities of the cells increase approximately 800 units over the background. Although it appears as though the cells' fluorescence saturates near the end of the experiment, this could also be due to the saturation of the camera at that exposure setting—the maximum intensities of some of the cells flatten out at that time period. Since I did not run the experiments longer it is impossible to determine if the cellular fluorescence saturated or not. In practice, I found that cells loaded with calcein in tubes for up to ~50 minutes displayed only marginally higher fluorescence intensities, suggesting that the cellular fluorescence is indeed saturating.

Also apparent in the figure are discontinuities in the fluorescence intensities, e.g., Figure 7-10C at 23 minutes. This is due to the fact that several times during the experiment (at  $t=13$ , 17, & 23 minutes) I had to reduce the camera sensitivity to avoid saturation. Although the pixel values can be linearly scaled to account for this, the information extracted from the images does not follow these simple rules. The reason for this is depicted in Figure 7-11. The difficulty is that the background noise level does not change 2x when the gain is changed 2x, and since the cell will have some intensity distribution due to the different optical path lengths across its diameter, the cutoff of this distribution will not scale perfectly, leading to the discontinuities in the extracted data, most notably in the extracted cell areas (Figure 7-10D).

The extracted cell area for trap #5 shows a very large spike at 13 minutes. The reason for this is that the setup was not properly shielded from the light at this timepoint, leading to a much larger background level and thus a significant deviation in the cell intensity. Since the cell(s) was fairly dim at this timepoint, however, it did not affect the extracted intensities. In addition, there is a general dip in the intensity values for all the cells at  $t=37$  minutes. The cause of this is unclear, although the fact that it occurred in all the cells suggests that it was an experimental artifact, perhaps due to a short-term decrease in lamp intensity.

These last few issues are experimental artifacts that could easily be corrected. The result of the experiment, however, remains undiminished. There has been a marked increase in fluorescence due to the introduction of a “stimulus”, in this case calcein, followed by sorting after the experiment was complete.

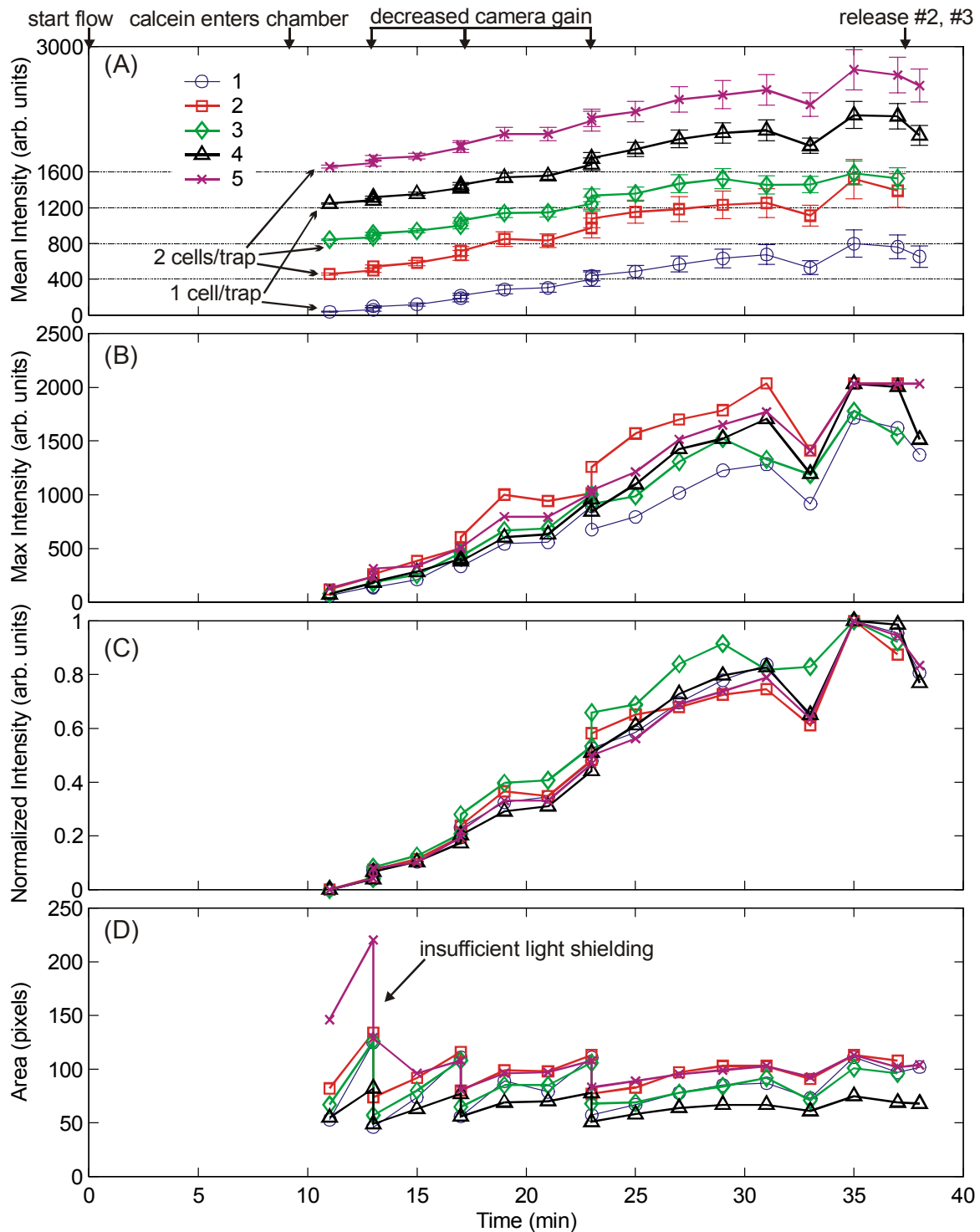


**Figure 7-10:** Calcein loading at 10  $\mu\text{M}$ . Plotted is the time course of fluorescence of cells in the five traps shown in Figure 7-9 due to injection of 10  $\mu\text{M}$  calcein solution. Shown are the (A) mean intensity over the cell area, (B) maximum intensity, (C) normalized mean intensity, and (D) cell area. The mean intensities in (A) are each offset 400 intensity units for clearer display. The error bars denote the standard deviations of the mean intensities across the cell area. The normalized mean intensity (C) was determined by normalizing the mean intensity values (A) to the minimum and maximum values over the time course. A threshold value of 35 was used to extract these results. Flow was initiated at  $t=0$  minutes. The values are all adjusted for a camera exposure time of 3 sec and a gain of 4.

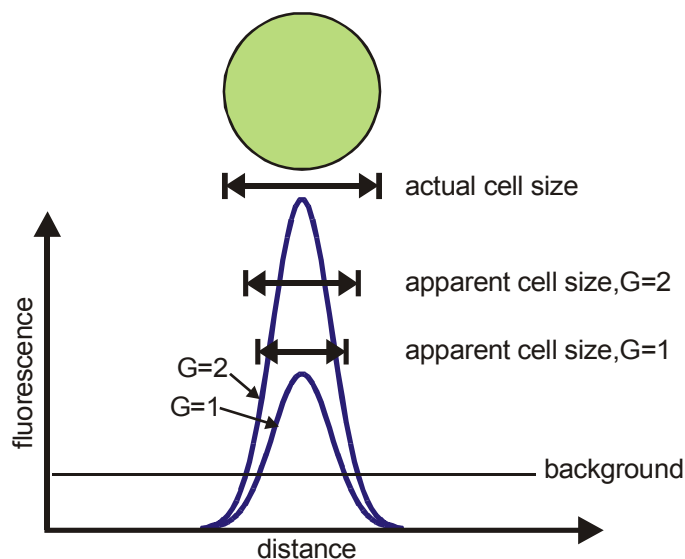


**Figure 7-11:** Effect of changing the camera sensitivity on the extracted parameters. Depicted are the recorded fluorescence pixel values over the cell area when the camera gain is changed from  $G=1$  to  $G=2$ . Since the intensities increase but the background level does not, the apparent cell size changes.

Although the fluorescence intensities of the cells in Figure 7-10 increase over the threshold 11 minutes after the start of flow, examination of the actual images shows that their fluorescence is visible 8 minutes after the initiation of flow. Their intensity at this timepoint is lower than the threshold used in the data extractions, which is why that point is not included in Figure 7-10. The lag time between start of the flow and the initiation of fluorescence is appropriate given that the measured volume between the 4-way valve and the chamber is  $\sim 94 \mu\text{l}$ , and the flow rate was  $10 \mu\text{l}/\text{min}$ . This gives a mean time of entry of the calcein of approximately 9.5 minutes. Due to the parabolic flow profile, however, the calcein will disperse as it is being convected, and should arrive somewhat earlier than 9.5 minutes, which is consistent with these observations.

Decreasing the void volume would decrease this lag. Actually, the  $\mu\text{DAC}$  design specified a  $20 \mu\text{l}$  void volume to meet the system requirements. The reason for the much larger void volume in the actual device is simply a constraint of the current experimental setup. Optimization of this setup could easily reduce the void volume to the appropriate value.

In Figure 7-12 I show the results of a similar experiment, except that this time the calcein concentration was  $1 \mu\text{M}$ . In this experiment I have trapped cells in four traps—2 cells in each of traps #1 and #4 and 1 cell/trap in trap #2 and #3—under the same conditions as before. Two features distinguish these results. First, the mean intensity values are much lower than with the  $10 \mu\text{M}$ -calcein injection (200 units, versus 800 units for the  $10 \mu\text{M}$  injection), which is consistent with a lower intracellular concentration due to the higher extracellular concentration. Second, the loading kinetics are slower, since the time to achieve 50% of the maximum fluorescence is  $\sim 35$  min for the  $1\text{-}\mu\text{M}$  injection (Figure 7-12C) and  $\sim 20$  min for the  $10\text{-}\mu\text{M}$  injection (Figure 7-10C).

Again there is a discontinuity in the measurements at  $t=37$  minutes due a reduction in the camera gain.

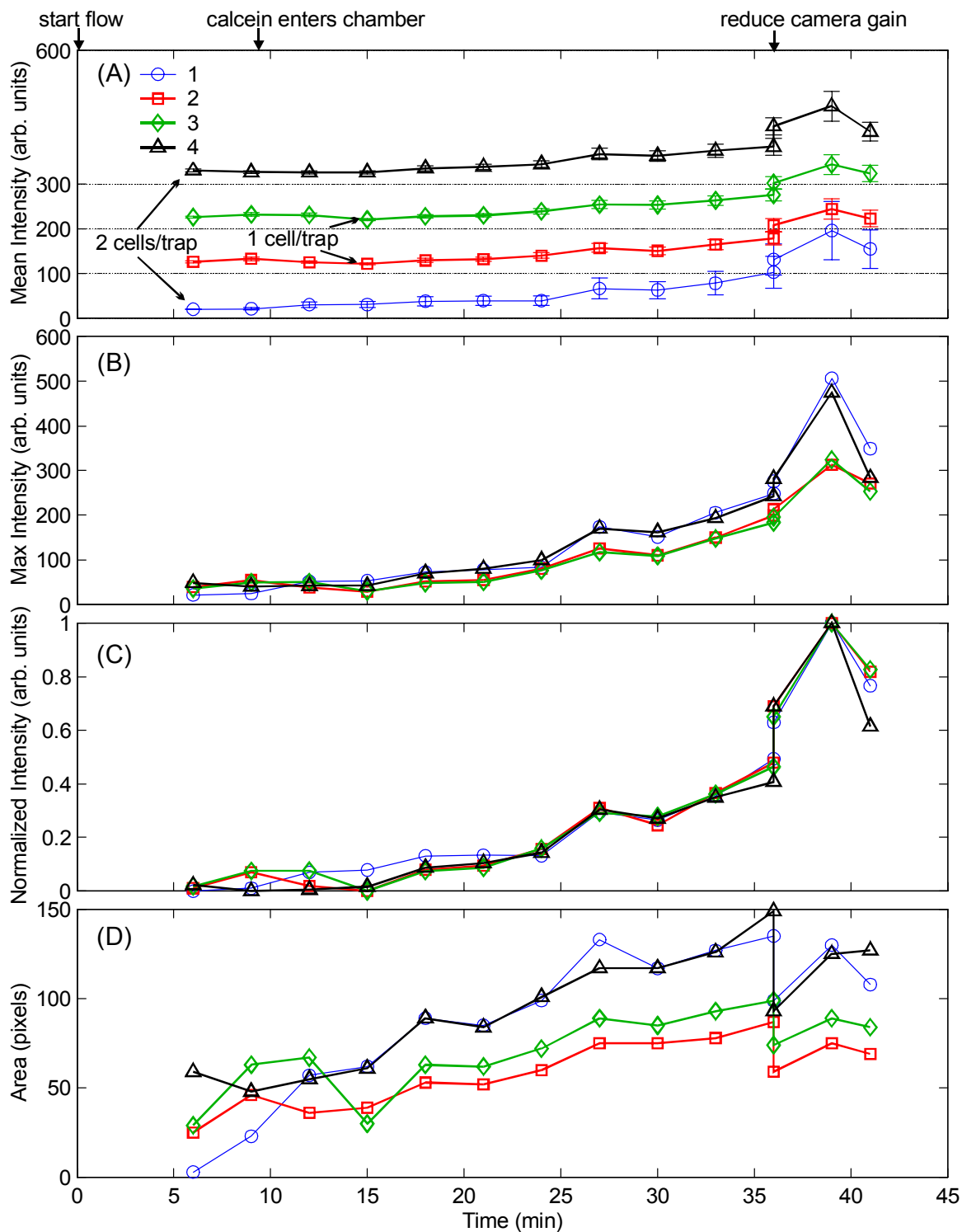


**Figure 7-12:** Calcein loading at  $1 \mu\text{M}$ . Plotted is the time course of fluorescence of four cells due to injection of  $1 \mu\text{M}$  calcein solution. Shown are the (A) mean intensity over the cell area, (B) maximum intensity, (C) normalized mean intensity, and (D) cell area. The mean intensities in (A) are each offset 100 intensity units for clearer display. The error bars denote the standard deviations of the mean intensities across the cell area. The normalized mean intensity (C) was determined by normalizing the mean intensity values (A) to the minimum and maximum values over the time course. A threshold value of 20 was used to extract these results. Flow was initiated at  $t=0$  minutes. The values are all adjusted for a camera exposure time of 3 sec and a gain of 4.

### *Fluorescence intensity calibrations*

In order to compare the fluorescence intensities between the two experiments (and even over the course of one experiment), I need to demonstrate that the optical setup does not drift over the course of an experiment and over different days. The factors that could change are the camera gain and exposure-time settings and the Xenon lamp intensity. The fluorescence intensity should be linear with camera gain and exposure time, and so changes between these two factors can be correlated by simply ratioing the pixel values. This is what was done over the course of the two experiments, and worked well apart from difficulties with the background levels.

The Xenon lamp intensity is more likely to be a source of error. If the lamp intensity varies then the measured calcein intensities need to be corrected for this in order to make comparisons between runs and even during runs. Since I do not have the ability monitor the Xenon lamp intensity with the current setup, I performed a surrogate experiment to examine the short- and long-term variations in the lamp intensity. Using a set of fluorescein-labeled microspheres, I took identical images of the same field of data over several days under identical exposures. Performing data analysis (similar to that done on the dynamic assays) on several beads in the fields, the variations in the mean intensity values over a period of seconds were 1-2%, while over 2 hours it was ~18% and between two different days was ~35%.

Thus, since both reported experiments were performed over the course of a few hours, variations in the optical setup are unlikely to account for the differences in the measured intensities. This correlates with my visual inspections, which indicated that the 10- $\mu$ M injection became much brighter and had faster kinetics than the 1- $\mu$ M injection. Therefore, I conclude that the experimental results represent real differences in calcein loading due to the changes in the calcein concentration.

### *Calcein leakage*

The inverse experiment to calcein loading is calcein leakage. In this experiment, I take HL-60 cells that have been preloaded with calcein and permeabilize their membranes with a detergent solution. Increasing the permeability of the membrane allows the calcein to leak out, decreasing the cellular fluorescence intensity.

Figure 7-13 shows the results of an experiment demonstrating calcein leakage. The holding parameters— $V=3V$ ,  $f=20$  MHz, and a flow of 10  $\mu$ l/min—are the same as for the calcein loading experiments. The three cells' areas and mean fluorescence intensities are fairly constant over the course of the experiment until the cells disappear, which occurs between 19 and 25 minutes after the start of flow. Specifically, the cells' mean fluorescence declines 50% for cell #1, 5% for cell #2, and 14% for cell #3 from the initial intensity values. None of the values reach the background intensity value before the cell is lost.

One reason for this is that as the permeability of the membrane increases due to SDS incorporation, it becomes more difficult for the cell to keep its cytoplasmic electrical conductivity different than that of the extracellular medium. As these two compartments equilibrate, the CM factor will decrease (Figure 7-6) and the cell will be released. A second reason for the rather shallow decline is that I observed that individual cells experienced a sharp fluorescence loss over a period of seconds directly before release. Images were taken every two minutes, however, which is too slow to capture these dynamics.

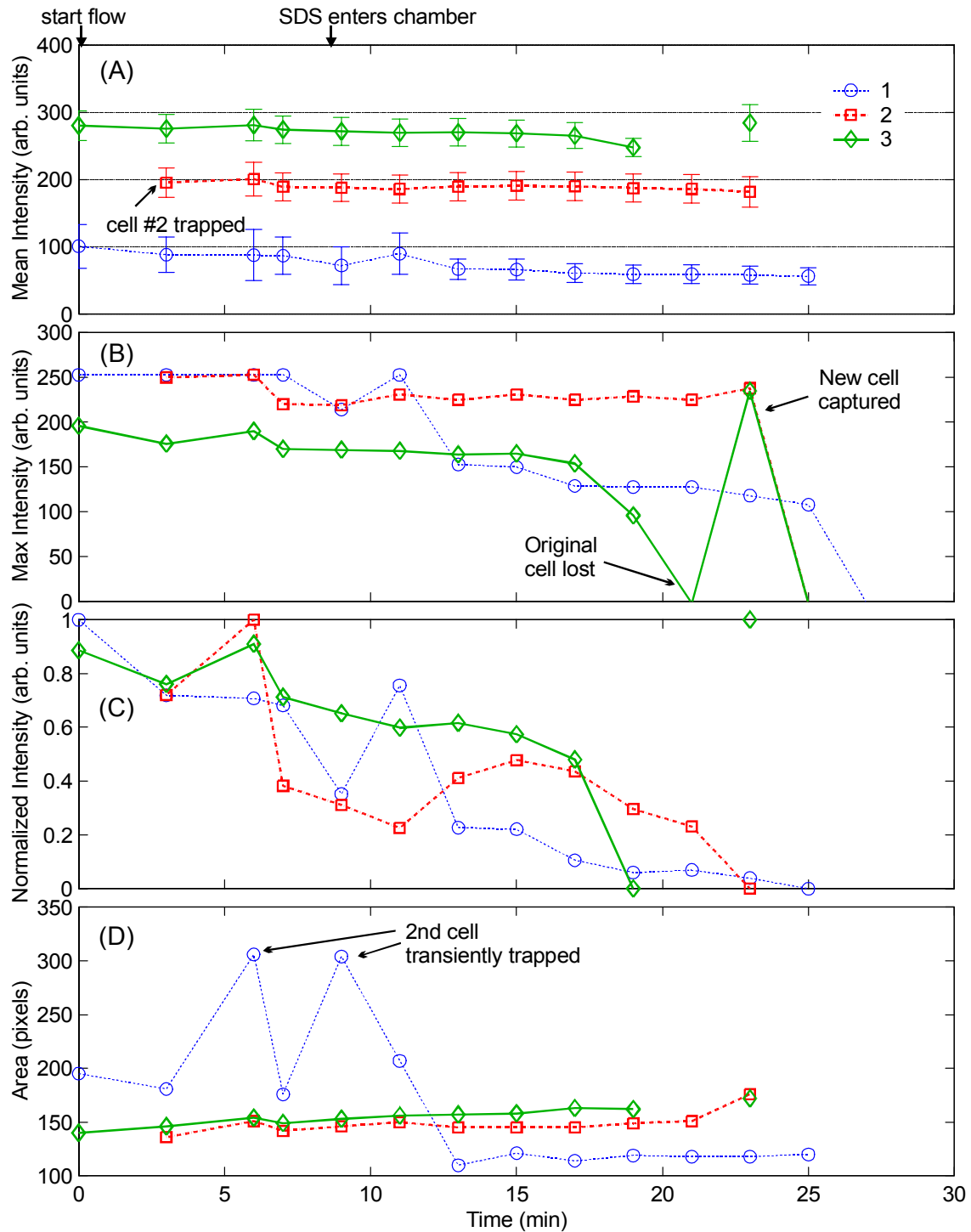


**Figure 7-13:** Calcein leakage at 100  $\mu\text{g/ml}$ . Plotted is the time course of fluorescence of three cells due to injection of SDS solution. Shown are the (A) mean intensity over the cell area, (B) maximum intensity, (C) normalized mean intensity, and (D) cell area. The mean intensities in (A) are each offset 100 intensity units for clearer display. The error bars denote the standard deviations of the mean intensities across the cell area. The normalized mean intensity (C) was determined by normalizing the mean intensity values (A) to the minimum and maximum values over the time course. A threshold value of 15 was used to determine the cell areas. Flow was started at  $t=0$  minutes. The images were obtained at a camera exposure time of 1 sec and a gain of 1.

As with the calcein loading, the leakage experiments contain a few experimental artifacts. The area and normalized fluorescence of cell #1 have peaks at 6 and 9 minutes. Direct observation of the images suggests that this is due to 2<sup>nd</sup> cells being transiently trapped during those timepoints. Cell #2 only became trapped after the first image was taken, which is why it does not appear for the  $t=0$  timepoint. Cell #3 appears to be lost after 19 minutes, but then reappears at 23 minutes. This is no doubt due to a second cell that was trapped in this site after the first was lost.

Instead of calcein leakage, the decline in cell intensity could be due to field-induced cell death, random cell death, or just stochastic loss of a cell from a trap. This is unlikely, however, for several reasons. First, a control experiment under the same conditions but without SDS did not result in a significant decrease in calcein intensity nor loss of cells from traps over a period of 34 minutes (data not shown). Second, I have held both labeled and unlabeled cells in traps for >90 minutes without cell loss. Third, repeating this experiment resulted in a similar behavior on another set of cells, with loss of fluorescence occurring stochastically ~15-21 minutes after the onset of flow (data not shown).

These results represent a second validation of the ability to monitor dynamic fluorescence information on multiple single cells. They demonstrate that it is possible to perform a variety of assays with these trap arrays, with both increasing and decreasing fluorescent responses. They also expose the challenges in having a robust optical setup.

## **7.3 Discussion**

### **7.3.1 Single-cell manipulation**

The results presented in this chapter demonstrate that these traps are well suited for manipulating multiple single cells. The main results are three-fold. First, it is straightforward to load the array with cells—it does not take special, tedious procedures to accomplish this. This is primarily a result of the strong as-designed holding strength and the trapezoidal orientation of the traps, which “focus” cells into the traps. Second, the ability to turn traps on-and-off by toggling one electrode has again been validated, a feature that would probably have not been anticipated without the results of the modeling. Third, the measured holding characteristics for these traps are close to what was predicted, with the predicted window encompassing the measurements. Thus, the *a priori* design has been extended to the desired endpoint; I needed a trap that operated with cells in a certain fashion, and with the modeling tools was able to design a trap that met those requirements.

The trap operation at 10  $\mu\text{l}/\text{min}$  with 3V applied at 20 MHz for the majority of the results shown in this chapter was not random—it lies directly within the calculated operating window of Figure 7-8. It is also the operating condition that was determined in Chapter 4 at the conclusion of the trap design to be the one that would meet the system requirements of the  $\mu\text{DAC}$ . Thus, again the modeling environment has shown that it can absolutely predict trap performance in a variety of experimental situations.

Single-cell discrimination is not a designed feature of these traps—nowhere in the modeling can I determine the operating conditions necessary for this. However, this step is crucial to successful operation of the trap array, and optimizing this variable will be necessary in the next generation of traps. It is plausible to imagine that many trap geometries will operate in such a fashion that conditions will exist where only cell could be held. However, determining

how to manipulate the geometries such that this operating window is large and resistant to changes in cell size and electrical properties will be crucial for robust operation of large arrays.

An alternative approach would be to keep the single-cell operating window fixed and use the loading step of the array to select for large cells and favorable electrical properties. For example, by setting the flowrate during loading to be relatively high, say 13  $\mu\text{l}/\text{min}$  with a 3V and 20 MHz excitation, I would only allow the largest of cells to be trapped in the array, and thus achieve a relatively monodisperse trapped population. This would be useful if one were to perform subsequent electroporation of trapped cells, since the optimal electroporation conditions change with cell size. However, for other biological assays, performing this selection at the beginning of the assay might select out cells that display interesting phenotypes.

The task of ensuring that only one cell was in a given well was difficult to perform for the dynamic assays reported in this chapter. For the calcein loading assays, releasing the cells at the end of the experiment allowed me to determine how many cells were in a given site, and by observing cells revolving around each other under flow I was sometimes able to determine the number of cells/site before or during an experiment. Unfortunately, this is not a practical procedure as the number of sites is scaled up. The extracted fluorescence data also does not give a clear indication of which traps contain  $>1$  cell. The maximum intensities and cell areas of the 1- $\mu\text{M}$  calcein loading experiment (Figure 7-12) show that traps #1 and #4, which contained two cells, were clearly higher than the other two traps. However, the 10- $\mu\text{M}$  calcein loading experiment (Figure 7-10) contains no such clear correlation between the extracted information and traps that contained two cells (#2, #3, and #5). Correct loading and monitoring of the single-cell traps will be a necessary step for the next generation of traps.

Understanding the behavior of the cells revolving around each other, observed in Figure 7-2, will be crucial to designing single-particle traps. Although I am not able to provide a definitive explanation for the phenomenon at this point, I can speculate as to its origin. When two similar polarizable particles are placed close to each other in an electric field, their induced dipoles will attract each other. Thus, the revolving could be due to attraction between these induced dipoles or due to movement of the dipoles within the potential energy well of the trap. The latter seems more probable, as the attraction between the induced dipoles decreases with separation, and thus would probably not cause such revolving to occur. As the particles pass by each other, however, the dipolar attractive forces would affect the dynamics of the process. A proposed mechanism for the revolving is that the variation in drag force with height introduces a non-zero curl into the system—the higher particle being pushed more strongly. This will send it to the back of the trap, where it feels a stronger restoring pushing it back to the center.

### 7.3.2 Lag time to stimulus entry

A major challenge with using pressure-driven flow is that the parabolic flow profile causes the solute to disperse faster than due to diffusion alone. The phenomenon is known as Taylor dispersion [171], and the end result for the movement of solute in a circular tube—like the HPLC tubing used here, is that the diffusion coefficient for calcein can be replaced by a dispersion coefficient, still obeying the diffusion equation, but given by

$$K = D \left( 1 + \frac{\text{Pe}^2}{192} \right) \quad (7-1)$$

where  $K$  is the dispersion coefficient,  $D$  is the diffusivity of the solute, and  $\text{Pe}$  is the Peclet number, which is a non-dimensional quantity that represents the interplay between convection and diffusion, and for a circular tube is given by

$$\text{Pe} = \frac{2UR}{D} \quad (7-2)$$

where  $U$  is the mean flow velocity and  $R$  is the tube radius. Thus, as the Peclet number increases, convective effects dominate diffusive effects.

Calcein's diffusivity in water is  $3.3 \times 10^{-6} \text{ cm}^2/\text{s}$  [172]. A volume flow rate ( $Q$ ) of 10  $\mu\text{l}/\text{min}$  through the 0.015"-diameter HPLC tubing gives  $U=1.5 \text{ mm/s}$ , which leads to  $\text{Pe} \approx 1700$ —a convection-dominated regime. In this regime, the dispersion coefficient can be approximated by

$$K \approx \frac{U^2 R^2}{48D} \quad (7-3)$$

For the experiments performed in this chapter, where I am flowing through a defined length of tubing ( $L$ ), I can determine how the dispersion length (the length over which the concentration will be smeared out) will be affected by the chosen flowrate. The dispersion length ( $l_d$ ), as for diffusion, is approximately  $l_d = \sqrt{Kt}$ , where  $t$  is the elapsed time. The time can be determined from the measured void volume (94  $\mu\text{l}$ ) and the volume flowrate  $Q$ . Inserting  $K$  into this expression and using the relationship between the volume flowrate and the average flow velocity  $U$ , one obtains that

$$l_d = \sqrt{\frac{QL}{48\pi D}} \quad (7-4)$$

and thus the dispersion length increases with the square root of the tube length and the flowrate. Inserting the appropriate values leads to a dispersion length of 5.3 cm. In other words, the beginning of the plug will be  $\sim 5.3 \text{ cm}$  downstream than would be expected from the average flowrate alone. This means that the calcein will arrive in the chamber  $\sim 35$  seconds before expected, or after 8.8 minutes, rather than the 9.4 minutes that is expected.

This arrival time is approximate, since it represents the characteristic dispersion length but lower calcein concentrations will be present in the chamber at earlier times. Thus, the onset of dynamic events should be  $\sim < 8$  minutes, which is indeed what is observed in the experiments.

### 7.3.3 Dynamic assays

The calcein loading and leakage assays are perhaps the culmination of this thesis. Starting from the desire to do these assays, I first determined why planar quadrupole traps could not be used and then designed traps that could be used for such assays. In this chapter I have finally used these traps for such assays, closing the loop.

The significance of these results is large. I have made a small array of traps that can 1) observe fluorescence information on 2) multiple individual cells 3) over time, and 4) sort based upon that information. This is the idea behind the  $\mu\text{DAC}$ , and its feasibility has now been demonstrated.

The dynamic assays demonstrate that introducing various “stimuli” into the system cause measurably different changes in the both the values as well as the dynamics of the responses, and thus that sorting based upon dynamic response is a viable option; the extension to biologically relevant assays does not involve any new fundamental developments.

These dynamic assays also illustrate some of the challenges involved in designing the next set of traps and the assays to use with them. First, it can be difficult to determine absolutely whether a cell in a given image is the same as the one in an image taken at a later timepoint. This

is exacerbated by the challenge of obtaining and maintaining only one cell/site. Because of photobleaching effects, it is not practical to monitor the cells continuously over the course of an experiment. Other ways must be found to secure this information. Two are apparent—electrical monitoring of the electrode impedance, which may be able to detect the presence of a cell, and development of an electrical “fence” to prevent cells from approaching the array once it is loaded. The impedance technique would have the added advantage of being able to detect when two cells are in a trap, which is difficult to do now purely from fluorescence images. A third option would be the development of a trap whose electrical characteristics could be tuned such that one set of conditions would make it easy to load (much like the current trapezoidal trap), while another set of conditions would make it very difficult to load. The modeling environment can aid in the design of these improvements.

Another issue is that the cells rotate under the imposition of flow. This means that subcellular localization of the fluorescence would be extremely difficult. While it is conceivable that one could differentiate between membrane-bound and nuclear fluorescence, investigating trafficking within the cell is very difficult at this stage. In addition, even observing fluorescence from the total cell is affected by the rotation. Since most cells are not perfectly spherical, the rotation induces a time-varying change in the fluorescence intensities and measured cell diameter, which could lead to misleading data.

Another interesting challenge in using these traps is in performing the data analysis. Much like DNA microarrays, collecting the data is only half the battle. Making sense of a large number of spots, especially to extract meaningful dynamic information, is nontrivial. The challenge is to determine whether deviations result from “real” population inhomogeneities or whether they are experimental artifacts or uninteresting biological noise. Thus, posing the correct question and including the proper controls will be crucial for the proper use of such arrays. In-depth investigation of each cell at each time point, while manageable at the proof-of-concept stage, will not scale well. Again, however, working at the microscale helps deliver solutions to these problems. For instance, one could use parallel-flowing low-Reynolds number flows to perform multiple simultaneous experiments on a side-by-side cell population, thus including the proper controls.

## **7.4 Conclusions**

In this chapter I have demonstrated the use of the small trap arrays with cells. I have demonstrated general operation of the arrays—loading, single-cell discrimination, independent trap toggling, cell holding—and dynamic fluorescent assays using calcein loading and leakage as two model systems. The results demonstrate proof-of-concept operation of the  $\mu$ DAC and that the modeling tools developed earlier can indeed be used for real-world trap design based upon a set of system parameters.



## Chapter 8: Conclusions

In this chapter I will conclude with a discussion of the major contributions of this thesis. I will then give my outlook on the future, the challenges that need to be addressed, and in turn possible avenues of future work to address those challenges.

### 8.1 Thesis contributions

The contributions of this thesis span several disciplines. The “big picture” accomplishment is the development and implementation of the  $\mu$ DAC concept—a planar array of single-cell traps coupled with sorting based upon dynamic assays. The results in Chapter 7, demonstrating dynamic calcein assays on a 1x8 array of DEP-based traps, are the synthesis of this contribution. Its proof-of-concept operation opens the door to a whole set of previously unavailable assays—namely, those based upon dynamic information content.

In the field of dielectrophoresis, this thesis greatly extends the state of sophistication of DEP-based traps. I have developed modeling tools that for the first time allow for *a priori* design of DEP-based particle traps based upon a set of system parameters—in this case, operation under a certain flowrate while minimizing the shear stress and electric fields to which the cells are exposed.

The modeling tools also introduce a number of contributions. The first is that the modeling gives general insight into the interplay between the gravitational, DEP, and HD drag forces operating on particles in these traps at the microscale. Second is the incorporation of an algorithm that allows for the computation of arbitrary DEP force orders, removing limitations of the trap geometries that can be simulated. Third is the open nature of the modeling environment, in that it can use as inputs HD forces and electric fields computed using specialized tools. Finally, the use of a force formulation (rather than potential functions) makes it straightforward to add in any other forces, such as EHD flows.

The experiments with the planar quadrupole introduced a new quantitative measurement for examining DEP-based single-particle traps—namely, the release flowrate. Not only is this a robust measurable parameter, but it will also often be *the* parameter of interest in microfluidic systems. In addition, the experiments, when coupled with the model, illustrate the deficiencies in the planar quadrupole for strong holding against flow.

The end result of the use of the modeling tools has been the development of the extruded trap and the demonstration of its stronger holding. The extruded trap has many novel characteristics—it is a batch-fabricatable, extruded-electrode trap design incorporating a trapezoidal structure and substrate shunts to improve holding. In addition, the trap is electrically switchable and easily arrayable. It represents a vast increase in the sophistication of DEP-based single-particle traps.

Although the fabrication process did not require any groundbreaking advances, the experience gained in learning to use SU-8 as a removable mold for electroplating will be useful for other researchers. In addition, the packaging scheme employed for the extruded traps solves many problems encountered in these systems—that of interfacing electrical, optical, and fluidic inputs to a microfabricated device with a package that is easy-to-use and robust.

Demonstrating that the trap is as strong as predicted, within the limits of the measurements, presents a second validation of the modeling tools and the proof that the modeling can be used to actually design real traps that meet system parameters *on the first try*.

Finally, showing proof-of-concept operation with cells validates that DEP-based particle traps such as these can be useful to bioscience, and that really the end of this thesis presents the beginning of a rich vein of research that can be both intellectually and practically rewarding.

## **8.2 Outlook, challenges and future work**

The culmination of this thesis represents the genesis of a new field of inquiry—electric field-mediated cellular assay systems. The system application described throughout this thesis—the  $\mu$ DAC—has been realized in proof-of-concept form. In addition, the *idea* of cell sorting based upon dynamic response, even if implemented in a form widely divergent of the  $\mu$ DAC, is extremely powerful.

Nonetheless, several significant challenges exist in bringing the  $\mu$ DAC from the 1x8 array depicted in Chapter 7 to a truly useful device. These can be divided into issues related to manufacturing a useable device, operating it, and finally how to verify it to obtain biologically relevant information. I conclude with thoughts on likely applications of the  $\mu$ DAC.

### *$\mu$ DAC manufacturing*

Improvements need to be made in manufacturability. The design was not optimized with respect to expected variations in the manufacturing process. The holding characteristics have been shown to be fairly sensitive to trap diameters and electrode taper angles, and since it is difficult to control these parameters, the design is thus not tolerant to manufacturing variations. In addition, the released posts were fairly fragile during processing and packaging (although not during operation). These issues could be overcome by either using a different trap geometry or changing the post dimensions to make them more stable.

In addition, for large-scale trapping (e.g., >20), it may be necessary to use a simpler fabrication process and thus a radically different trap geometry. Robust operation with biological materials is extremely challenging even on blank substrates, and thus a simple design will be crucial. The results in Chapter 3 conclusively show that the planar quadrupole is inadequate, but perhaps a simpler trap than the extruded quadrupole exists. For instance, one could position the planar quadrupole over a well in the substrate such that field was pushing the particle into the well but that turning off the field would eject the particle.

### *$\mu$ DAC operation*

One must also solve challenges related to operating a large-scale array. First, one must improve the system to obtain robust single-cell holding. As described in Chapter 7, while it is possible to get single-cell discrimination in any given trap, obtaining such discrimination across an array of traps, given biological variability, is extremely difficult. Fortunately, there are several possible ways to overcome this. The most direct route is by implementing close-loop control of the trap loading and operating conditions. One could imagine time-multiplexing the applied voltage with an impedance-sensing circuit that would be able to determine when a particle had entered the trap. After sensing the cell's entry, the electrical excitation could be changed to prevent other cells from entering the trap. Such a trap could be designed using the modeling tools so that one excitation would facilitate loading while another would prevent it. Optical techniques, using either a generic fluorescence marker (e.g., viability) or even brightfield detection, could serve the same purpose and possibly add specificity to the trapping. Likely

issues are to make sure that only one cell is captured—not a doublet—and that debris in the solution isn't mistakenly captured.

Another way towards robust single-particle loading is to design a trap and operating conditions such that single-particle trapping is highly favored over multi-particle trapping. Such a step would require the implementation of modeling to determine the single-particle operating regime for a given trap, etc. This modeling may be complicated because of the need to simulate dynamic events—whether an incoming particle can be captured, rather than whether a captured particle can be held—with deformable particles. With this model extension in place, however, one could then optimize for single-particle operation. Using steric effects and fluid-structure guiding, it might be possible to design a trap where the capture of one particle served to “close” the trap to others. Since this technique would have simpler electronics (no control system), it is advantageous to close-loop control.

After the ability to load traps with only one particle has been demonstrated, the next challenge is to load an array of traps, keep all the cells there over time without exchanging cells with the incoming flow, and then release cells so that they can be collected. The challenge in loading a two-dimensional array of traps is in loading the downstream rows, because they would be shielded from incoming cells by the upstream rows. Close-loop control would allow one to load the back row first and then move forward. Alternately, one could have the traps arranged two-dimensionally but have the flow meander through the traps and then load them serially. This would also need close-loop control. Other approaches, significantly different than presented here, may also solve this problem. The ultimate goal would be a trap geometry that would “pull” a cell out of the flow when unloaded but then be transparent to other cells when loaded.

Ensuring that the cells at one timepoint are the same as at the next timepoint is fairly straightforward. The most significant cause of this uncertainty with the current design is that there is no way to “turn off” the incoming flow of cells without turning off the flow. DEP provides an elegant solution here, because it can move particles without affecting flows. Thus, one could have a main DEP barrier at the chamber inlet, and once the traps were loaded this would divert all incoming cells to waste without affecting the reagent flow.

The final operational challenge is to collect released cell populations. The issue here is how to actually transfer the cell or cells released from the array to an external container (e.g., 384-well plate) without losing the cell(s) or exchanging it with another. The first issue is to get the cells into the flow stream without affecting the cells in other traps. This could be done by either having a dedicated sort channel or ejecting the cells in the  $z$ -direction so that they were above the traps (for the extruded quadrupole). Then the cells must be directed to an outlet and captured. Here one could use DEP barriers to direct released cells to a chamber where a DEP multi-particle trap would concentrate the cells and then release the cell plug into the outlet. Nonetheless, ensuring that single micron-sized cells in flow correctly traverse a  $>$ mm-length path is extremely challenging.

Directly related to collecting released cells is obtaining individual trap addressing with passive electronics. Two layers of metal will almost certainly be needed due to the wiring complexity, but to minimize external connections one would still like row-column trap addressing. The direct way to implement this requires active electronics at each trap site, which would prohibitively increase the fabrication complexity. Alternatively, one may either use a limited number ( $\sim 100$ ) of directly addressed traps or implement a passive row-column

addressing scheme. It's unclear how the latter would work, but I am not convinced that it is impossible.

Other challenges exist. Imaging the arrays will become nontrivial as the number of traps increases. The optimal solution will capitalize on the fact that one knows the cell locations in the  $\mu$ DAC to simplify the optics and thus permit high-throughput optical monitoring. One can imagine perhaps an array of microlenses to direct light from each trap to its own individual CCD pixel. Such research has much synergy with that involved in imaging microarrays, and thus would have wide-ranging significance. While I have not examined these issues in depth, conversations with optical engineers have indicated that the problems are tractable.

#### *$\mu$ DAC verification*

Several issues need to be addressed to be able to extract biologically useful information from assays performed with the  $\mu$ DAC. First, investigating the heating in these microsystems will be crucial because the biological community will require proof that the temperature excursions are small. Even though I can assume that the small scale limits induced temperature gradients, the results in Chapter 3 strongly suggest that heating can be a major factor in these systems and presents one upper limit to the voltages that one can apply at the microscale. Fortunately, it should not be too difficult to take the electric field data and flow information and port that to modeling to calculate temperature distributions. Such investigations would also include an experimental component to measure the actual temperature distributions.

In addition, more research needs to be undertaken to determine the effects of the traps on cells, either directly thru the electric fields or indirectly due to heating effects. Given the availability of microarray technology, one should be able to determine which pathways are being affected in cells exposed to given situations. With careful experimental design to obtain generalizable data, it would then be possible to set operating windows for different assays to protect against field-induced artifacts. This could also feed back into the trap design and array implementation itself, creating a  $\mu$ DAC scheme that is tolerant to such effects.

Using the  $\mu$ DAC for biological assays would also benefit from allowing use with adherent cells and or extending it to allow intracellular imaging. The two challenges are similar, in that performing intracellular imaging requires that one stabilize the cell against flow-induced rotation, as would be achieved by using adhered cells. The challenge then is to remove the cell. This might done by first trapping the nonadhered cells in the traps, lowering them to the substrate so they can attach, performing the assay, and then introducing trypsin into the chamber to cause them to detach and be trapped in suspension again. While attached, the cells are amenable to intracellular imaging, although such imaging would slow the throughput of the optics. One might also be able to use polymers whose hydrophobicity is electrically programmable, allowing the attachment/detachment process to occur without enzymes. The question of how to intracellularly image nonadhered cells is more challenging, and would require somehow pinning the cell down to prevent rotation. It's unclear how to do this easily.

#### *$\mu$ DAC applications*

Finally, investigations into biologically relevant dynamic assays to be performed with the  $\mu$ DAC are warranted. One simple yet nontrivial experiment that provides new biological information—differentiating between two alternate mechanisms in a pathway, for example—would provide an ideal vehicle with which to get biologists' attention.

Examining the proposed assays discussed in §1.2.2 in light of the course of the thesis, I can speculate as to where the  $\mu$ DAC might actually be useful for answering real biological

problems. I believe that one of the most powerful applications will be in using luminescent assays to tease out the quantitative operation of the cell, resulting in information suitable for incorporation into predictive cellular models. Biological modeling—to understand how decisions are made in the cell and then to affect those decisions to attain useful behaviors—is in need of assay technologies that can be used to probe model predictions. Results are needed on populations of single cells to get both the mean and the distribution. Predictions can come in the form of time-responses of behavior due to a stimulus, and thus dynamic information is important. Where the  $\mu$ DAC has its most power, however, is by allowing the researcher to sort those cells that are *not* responding as desired and investigate their genome to determine how DNA variation affects phenotype.

Another field of inquiry that I find particularly exciting is how dynamic signals convey information in the cell. The idea that the time-course of a signal, rather than its steady-state values, *is* the signal is extremely interesting. This research is more difficult, however, than analyzing cellular models because the questions here are not well defined. This is because although there are examples of signaling thru dynamic information content (e.g., EGF), assay technologies to investigate such behavior are not readily available, and thus this field is immature. It is likely, however, that other such pathways exist. The  $\mu$ DAC, because it can sort based upon dynamics, is well suited for probing these problems.

Other useful modes of inquiry might take advantage of different features of the  $\mu$ DAC or may be used in conjunction with the previously described assays. For instance, one can perform concurrent differential experiments by introducing different liquid streams. This would allow parallel assays if the streams contained different reagents. Or it is possible to use the  $\mu$ DAC as a vehicle for applying pN forces to an array of suspended objects. One could also use the electrical nature of the forces to probe for electrical changes in the cell due to changes in physiology. While not discounting these ideas, they are not as inherently interesting to me.

#### *DEP technology*

DEP technology has other uses for biology. Given the demonstration that I can design high-strength traps, it may be possible to design DEP structures to impose strong forces on cells and thus move them around quickly. Such a system could be used as a cell sorter and possibly approach the high sorting rates that other microfabricated devices have been unable to achieve. Alternatively, single DEP traps, not encumbered by the requirements of scalability, switchability, etc., could be designed to be extremely strong, allowing the probing of forces in the 100's of pN range that are currently unattainable by optical tweezers.

Although many challenges exist, none are fundamentally insurmountable, and thus DEP technology and the  $\mu$ DAC in particular have great potential to impact bioscience.



# Appendix A: Derivation of the DEP force on a homogenous sphere

In this appendix I will derive Eqn. (1-1) & (1-2) using the classical electroquasistatic arguments found in [58, 173]. The situation is as depicted in Figure A-1. The problem involves placing a non-conducting sphere with permittivity  $\epsilon_p$  into a non-conducting medium with permittivity  $\epsilon_m$  and applying a slightly non-uniform field. If the field is only slightly non-uniform, I can assume that the induced dipole is that which would be found in a uniform field and that the DEP force is the force on that induced dipole. Extension to lossy particles/media and sinusoidally time-varying fields simply involves introducing phasor notation and replacing the static permittivities with their complex (frequency dependent) counterparts.

The first step is to find the magnitude of the dipole induced in a sphere in a uniform field (Figure A-1B). The potential due to a uniform field  $\mathbf{E} = E_0 \hat{\mathbf{i}}_z$  in spherical coordinates is given by

$$\Phi = -E_0 r \cos \phi \tag{A-1}$$

where  $r$  and  $\phi$  are defined in Figure A-1B. The problem now involves solving Laplace's equation  $\nabla^2 \Phi = 0$  for the potential everywhere due to the sphere. There are two regions, and I can try the following solution forms

$$\Phi = \begin{cases} Ar \cos \phi & r < R \\ -E_0 r \cos \phi + \frac{B}{r^2} \cos \phi & r > R \end{cases} \tag{A-2}$$

Where  $A$  and  $B$  are constants to be determined. Inside the sphere, the field is uniform, but outside the sphere the field is a superposition of the original uniform field and a dipole field. This formulation already meets the boundary condition at large  $r$ , which is that the field should reduce to the imposed uniform field. The boundary conditions at the surface of the sphere are that the potential and the normal component of the  $\mathbf{D}$  field should be continuous.

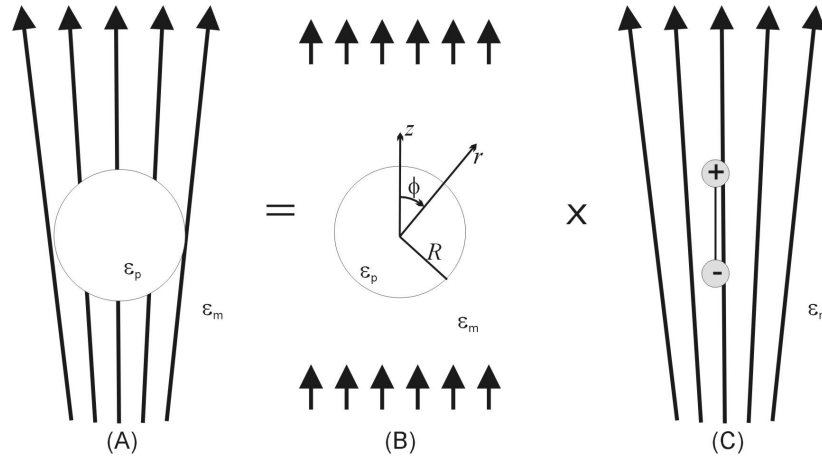


**Figure A-1:** (A) A uniform sphere with permittivity  $\epsilon_p$  is placed in a slightly nonuniform field in a medium with  $\epsilon_m$ . The problem is decomposed into finding the dipole moment of a sphere in a uniform field (B) and then finding the force on a dipole in a non-uniform field (C).

Mathematically, this means that

$$\begin{aligned}\Phi|_{r=R^-} &= \Phi|_{r=R^+} \\ AR \cos \phi &= -E_0 R \cos \phi + B/R^2 \cos \phi \\ AR^3 &= -E_0 R^3 + B\end{aligned}\tag{A-3}$$

and

$$\begin{aligned}\mathbf{D} \cdot \mathbf{n}|_{r=R^-} &= \mathbf{D} \cdot \mathbf{n}|_{r=R^+} \\ \epsilon_p E_r(r=R^-) &= \epsilon_m E_r(r=R^+) \\ \epsilon_p \frac{\partial \Phi}{\partial r}|_{r=R^-} &= \epsilon_m \frac{\partial \Phi}{\partial r}|_{r=R^+} \\ \epsilon_p A \cos \phi &= -E_0 \epsilon_m \cos \phi - 2B\epsilon_m/R^3 \cos \phi \\ \epsilon_p AR^3 &= -E_0 \epsilon_m R^3 - 2B\epsilon_m\end{aligned}\tag{A-4}$$

From (A-3) & (A-4) I can solve for  $A$  and  $B$  and thus the potential everywhere. The second term in the potential for  $r > R$  (Eqn. (A-1)) has the form of the potential due to a dipole, with  $B$  relating to its strength. Since this is what I am interested in, I need only solve for  $B$  and put it in a form from which I can extract its dipole moment. Solving for  $B$  I get

$$B = E_0 R^3 \frac{\epsilon_p - \epsilon_m}{\epsilon_p + 2\epsilon_m}\tag{A-5}$$

One sees the origin of the Clausius-Mossotti factor coming about by solving the boundary conditions.

The potential due to a dipole in a medium with permittivity  $\epsilon_m$  is

$$\Phi = p / 4\pi\epsilon_m r^2 \cos \phi\tag{A-6}$$

Equating this with the potential due to the induced dipole gives the strength of the induced dipole as

$$\begin{aligned}p / 4\pi\epsilon_m &= B = E_0 R^3 \frac{\epsilon_p - \epsilon_m}{\epsilon_p + 2\epsilon_m} \\ p &= 4\pi\epsilon_m E_0 R^3 \frac{\epsilon_p - \epsilon_m}{\epsilon_p + 2\epsilon_m}\end{aligned}\tag{A-7}$$

Now the problem reduces to finding the force on a dipole  $p$  in a non-uniform field (Figure A-1C). This is easiest illustrated in one-dimension, as shown in Figure A-2, and then generalized to three. Two point charges placed along the  $x$ -axis a distance  $d$  apart are subjected to an electric field  $\mathbf{E} = E(x)\hat{\mathbf{i}}_x$ . The Coulomb force on the dipole is

$$F_x = qE(x_0 + d) - qE(x_0)\tag{A-8}$$

If the field is only slightly non-uniform, I can represent the field at  $x_0 + d$  by a two-term Taylor expansion

$$E(x_0 + d) = E(x_0) + d \left. \frac{dE}{dx} \right|_{x_0}\tag{A-9}$$

Plugging this into Eqn. (A-8), one gets that the force on the dipole is

$$F_x = q \left( E(x_0) + d \left. \frac{dE}{dx} \right|_{x_0} \right) - qE(x_0)$$

$$F_x = qd \left. \frac{dE}{dx} \right|_{x_0} \quad (\text{A-10})$$

$$F_x = p_x \left. \frac{dE}{dx} \right|_{x_0}$$

where I have substituted in the dipole moment for a dipole oriented along the  $x$ -axis is  $p_x=qd$ . Thus Eqn. (A-10) shows that a point dipole will only have a force in a non-uniform field, and that this force is proportional to the field gradient and the magnitude of the dipole.

Eqn. (A-10) is for a one-dimensional dipole & field. To generalize to three dimensions, the dipole and the field become vectors and a vector Taylor series is needed for the derivation. The result is

$$\mathbf{F}_{\text{dep}} = \mathbf{p} \cdot \nabla \mathbf{E} \quad (\text{A-11})$$

where one can perform the gradient operation on  $\mathbf{E}$  first, generating a tensor, or dot  $\mathbf{p}$  into  $\nabla$ , generating a scalar that acts on  $\mathbf{E}$ .

Now that I have the form of the force on a dipole in a non-uniform field (Eqn. (A-11)) and the induced dipole in a uniform field (Eqn. (A-7)), I can combine the results to find the DEP force. The force is

$$\mathbf{F}_{\text{dep}} = \mathbf{p} \cdot \nabla \mathbf{E}$$

$$\mathbf{F}_{\text{dep}} = 4\pi\epsilon_m R^3 \frac{\epsilon_p - \epsilon_m}{\epsilon_p + 2\epsilon_m} \mathbf{E} \cdot \nabla \mathbf{E} \quad (\text{A-12})$$

In an electroquasistatic field, the factor  $\mathbf{E} \cdot \nabla \mathbf{E}$  can be simplified to  $\frac{1}{2} \nabla |\mathbf{E}|^2$ , giving the force

$$\mathbf{F}_{\text{dep}} = 2\pi\epsilon_m R^3 \frac{\epsilon_p - \epsilon_m}{\epsilon_p + 2\epsilon_m} \nabla |\mathbf{E}|^2$$

$$\mathbf{F}_{\text{dep}} = 2\pi\epsilon_m R^3 CM \cdot \nabla |\mathbf{E}|^2 \quad (\text{A-13})$$

Generalizing to sinusoidally varying fields and lossy particles & media, one gets the form of

$$\mathbf{F}_{\text{dep}} = 2\pi\epsilon_m R^3 \text{Re}[CM(\omega) \cdot \nabla |\mathbf{E}|^2(\mathbf{r})] \quad (\text{A-14})$$

where now the CM factor has an explicit frequency dependence and the real parts of the field & CM factor must be taken to get the force. This equation is identical to Eqn. (1-1).

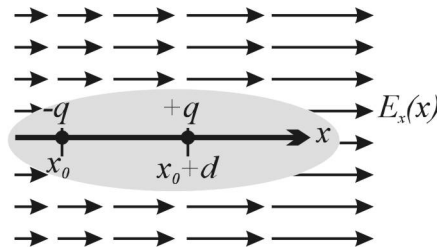


**Figure A-2:** Force on an  $x$ -oriented dipole in an  $x$ -directed non-uniform electric field.



## Appendix B: Fabrication Process flow

starting material: 1-mm thick 100-mm Pyrex wafers

all processing in TRL or diesaw room

Step	Description	Machine	Parameters
<b>Deposit Ti/Au layer</b>			
1	clean wafer	acid-hood	Piranha: 3:1 H <sub>2</sub> SO <sub>4</sub> :H <sub>2</sub> O <sub>2</sub> , time = 10 min
2	deposit Ti/Au	ebeam	pump down to 1e-6 torr deposit 1700 Å Ti: ramp 1-4 Å/s for first 1200 Å, 5 Å/s for next 500 Å deposit 5000 Å Au: ramp 1-5 Å/s for first 1000 Å, 5 Å/s for next 4000 Å
<b>Define Au interconnect layer</b>			
3	HMDS	HMDS	
4	coat wafer	coater	standard photoresist, standard recipe
5	prebake	prebakeoven	90 deg. C, time=30 min
6	expose photoresist	KS2	time=40 sec
7	develop photoresist	photo-wet-r	OCG934 3:2, ~4 min
8	postbake	postbakeoven	120 deg. C, time=30 min
<b>Etch Au</b>			
9	etch Au	acid-hood	1L of KI-based etchant (rate=28 Å/s), time=~210 sec
10	strip photoresist	acid-hood	Nanostrip, time=10 min
<b>Define electrode holes in SU-8</b>			
11	clean wafer	acid-hood	Nanostrip, time=12 min
12	dehydrate	hotplate	200 C, time=60 min
13	uv ozone	uv ozone	time=25 min
	clean & level hotplate & clean spacer wafer		
14	coat wafer	pispinner	pour SU-8 50 onto stationary wafer until there is ~2" circle 500rpm 15s, 1.1krpm 10s, 6krpm 5s
15	relax	hotplate	1 hr at room temp, turn wafer 90 deg. every 15 minutes
16	prebake	hotplate	ramp from room temp to 105 deg. C, total time=25 min, let cool to <40 deg. C
17	edgebead removal	pispinner	rub edge of wafer w/ q-tip dipped in PGMEA
18	edgebead removal bake repeat edgebead removal as necessary	hotplate	ramp from room temp to 50 deg. C, total time=20 min, let cool to <40 deg. C
19	expose SU-8	EV1	multiple exposure: 5sec on/5sec wait, repeat 5x vacuum + hard contact
20	post-exposure bake	hotplate	clean back of wafer and spacer wafer w/ PGMEA to ensure good thermal contact ramp from room temp to 105 deg. C, total time=13 min, let cool to <40 deg. C
21	develop SU-8	pispinner	PGMEA, 5min w/ occasional agitation, dry, repeat spray w/ SU-8 & spin dry on spinner 3x

22	ash descum	asher	time=20 min + 4 min right before electroplating
<b>Electroplate posts</b>			
23	electroplate	KOHhood	~1.4L of Orotemp 24 plating bath, 65 deg. C w/ stirring  forward-pulse mode = 0.1 ms on, 0.9 ms off current = 30 mA (~3 mA/cm <sup>2</sup> ), voltage ~0.44V total time ~3 hrs w/ occasional dep rate checks
<b>Strip SU-8</b>			
24	strip SU-8	photo-wet-r	ACT691, 90 deg. C, stirred & heated w/ explosion-proof equipment time=90 min, although only 60 min was needed rinse with DI & N <sub>2</sub> bubbler, blowdry
25	ash SU-8	asher	time=120 min, although only 60 min was needed
26	clean wafer	acid-hood	Nanostrip, time=5min
<b>Etch Ti layer</b>			
27	etch Ti layer	acid-hood	100:1 H <sub>2</sub> O:HF endpoint w/ wafer clearing, time=~110 sec
<b>Form SU-8 channel</b>			
28	nanostrip	acid-hood	time=10 min
29	dehydrate	hotplate	200 C, time=90 min (only 60 min needed)
30	uv ozone	uv ozone	time = 45 min (only 25 min needed)
31	coat wafer	pispinner	pour su-8 50 onto stationary wafer until there is ~2" circle  500 rpm 15sec, 0.95 krpm 30sec
32	relax	hotplate	time=30 min at room temperature
33	prebake	hotplate	ramp from room temp to 105 deg. C, total time=98 min, let cool to <40 deg. C
34	expose SU-8	EV1	multiple exposure: 5sec on/5sec wait, repeat 12x soft contact
35	post-exposure bake	hotplate	clean back of wafer and spacer wafer w/ PGMEA to ensure good thermal contact ramp from room temp to 105 deg. C, total time=23 min, let cool to <40 deg. C
36	develop SU-8	pispinner	PGMEA, 5min w/ occasional agitation, dry, repeat spray w/ SU-8 & spin dry on spinner 3x
<b>Dice wafer</b>			
37	protect wafer	coater	dab AZ4620 into chambers to protect posts
38	dice wafer	hotplate	90 deg. C, time ~45 min
39	release devices	diesaw	use 6-pass setting
		group lab	acetone

## References

- [1] K. D. Wise, J. B. Angell, and A. Starr, "An integrated-circuit approach to extracellular microelectrodes," *IEEE Transactions on Biomedical Engineering*, vol. 17, pp. 238-47, 1970.
- [2] H. K. Wen, J. Hyncek, and S. F. Boettcher, "Development of a miniature pressure transducer for biomedical applications," *IEEE Transactions on Electron Devices*, vol. ED-26, pp. 1896-905, 1979.
- [3] J. Voldman, M. L. Gray, and M. A. Schmidt, "Microfabrication in Biology and Medicine," *Annu. Rev. Biomed. Engr.*, vol. 1, pp. 401-425, 1999.
- [4] E. Jacobs, E. Vadasdi, L. Sarkozi, and N. Colman, "Analytical Evaluation of I-Stat Portable Clinical Analyzer and Use by Nonlaboratory Health-Care Professionals," *Clinical Chemistry*, vol. 39, pp. 1069-1074, 1993.
- [5] D. Vetter, "Miniaturization for drug discovery applications," *Drug Discovery Today*, vol. 3, pp. 404-408, 1998.
- [6] C. H. Mastrangelo, M. A. Burns, and D. T. Burke, "Microfabricated devices for genetic diagnostics," *Proceedings of the IEEE*, vol. 86, pp. 1769-1787, 1998.
- [7] K. D. Wise, "Micromachined interfaces to the cellular world," *Sensors and Materials*, vol. 10, pp. 385-395, 1998.
- [8] Y. N. Shi, P. C. Simpson, J. R. Scherer, D. Wexler, C. Skibola, M. T. Smith, and R. A. Mathies, "Radial capillary array electrophoresis microplate and scanner for high-performance nucleic acid analysis," *Analytical Chemistry*, vol. 71, pp. 5354-5361, 1999.
- [9] C. D. T. Bratten, P. H. Cobbold, and J. M. Cooper, "Single-cell measurements of purine release using a micromachined electroanalytical sensor," *Analytical Chemistry*, vol. 70, pp. 1164-1170, 1998.
- [10] S. N. Bhatia, M. L. Yarmush, and M. Toner, "Controlling cell interactions by micropatterning in co-cultures: Hepatocytes and 3T3 fibroblasts," *Journal of Biomedical Materials Research*, vol. 34, pp. 189-199, 1997.
- [11] S. P. A. Fodor, J. L. Read, M. C. Pirrung, L. Stryer, A. T. Lu, and D. Solas, "Light-directed, spatially addressable parallel chemical synthesis," *Science*, vol. 251, pp. 767-773, 1991.
- [12] A. Guttman, A. S. Cohen, D. N. Heiger, and B. L. Karger, "Analytical and Micropreparative Ultrahigh Resolution of Oligonucleotides by Polyacrylamide-Gel High-Performance Capillary Electrophoresis," *Analytical Chemistry*, vol. 62, pp. 137-141, 1990.
- [13] D. J. Harrison, A. Manz, Z. H. Fan, H. Ludi, and H. M. Widmer, "Capillary Electrophoresis and Sample Injection Systems Integrated on a Planar Glass Chip," *Analytical Chemistry*, vol. 64, pp. 1926-1932, 1992.
- [14] J. R. Sotelo and J. C. Benech, Eds., *Calcium and cellular metabolism: transport and regulation*. New York: Plenum Press, 1997.
- [15] J. C. Lewis, A. Feltus, C. M. Ensor, S. Ramanathan, and S. Daunert, "Applications of reporter genes," *Analytical Chemistry*, vol. 70, pp. 579A-585A, 1998.
- [16] R. Y. Tsien, "The green fluorescent protein," *Annual Review of Biochemistry*, vol. 67, pp. 509-544, 1998.

- [17] L. J. Kricka, "Chemiluminescent and bioluminescent techniques," *Clinical Chemistry*, vol. 37, pp. 1472-1481, 1991.
- [18] G. Zlokarnik, P. A. Negulescu, T. E. Knapp, L. Mere, N. Burren, L. X. Feng, M. Whitney, K. Roemer, and R. Y. Tsien, "Quantitation of transcription and clonal selection of single living cells with beta-lactamase as reporter," *Science*, vol. 279, pp. 84-88, 1998.
- [19] J. E. Gonzalez and P. A. Negulescu, "Intracellular detection assays for high-throughput screening," *Current Opinion in Biotechnology*, vol. 9, pp. 624-631, 1998.
- [20] A. Joyeux, P. Balaguer, P. Germain, A. M. Boussioux, M. Pons, and J. C. Nicolas, "Engineered cell lines as a tool for monitoring biological activity of hormone analogs," *Analytical Biochemistry*, vol. 249, pp. 119-130, 1997.
- [21] G. A. Rutter, H. J. Kennedy, C. D. Wood, M. R. H. White, and J. M. Tavares, "Real-time imaging of gene expression in single living cells," *Chemistry & Biology*, vol. 5, pp. R285-R290, 1998.
- [22] L. A. Kamensky and L. D. Kamensky, "Microscope-based multiparameter laser scanning cytometer yielding data comparable to flow-cytometry data," *Cytometry*, vol. 12, pp. 381-387, 1991.
- [23] K. Sasaki, A. Kurose, Y. Miura, T. Sato, and E. Ikeda, "DNA ploidy analysis by laser scanning cytometry (LSC) in colorectal cancers and comparison with flow cytometry," *Cytometry*, vol. 23, pp. 106-109, 1996.
- [24] E. Bedner, X. Li, W. Gorczyca, M. R. Melamed, and Z. Darzynkiewicz, "Analysis of apoptosis by laser scanning cytometry," *Cytometry*, vol. 35, pp. 181-195, 1999.
- [25] L. A. Kamensky, L. D. Kamensky, J. A. Fletcher, A. Kurose, and K. Sasaki, "Methods for automatic multiparameter analysis of fluorescence in situ hybridized specimens with a laser scanning cytometer," *Cytometry*, vol. 27, pp. 117-125, 1997.
- [26] Z. Darzynkiewicz, E. Bedner, X. Li, W. Gorczyca, and M. R. Melamed, "Laser-scanning cytometry: A new instrumentation with many applications," *Experimental Cell Research*, vol. 249, pp. 1-12, 1999.
- [27] J. F. Dunne, "Time window analysis and sorting," *Cytometry*, vol. 12, pp. 597-601, 1991.
- [28] H. H. McAdams and A. Arkin, "Stochastic mechanisms in gene expression," *Proceedings of the National Academy of Sciences of the United States of America*, vol. 94, pp. 814-819, 1997.
- [29] H. H. McAdams and A. Arkin, "Gene regulation: Towards a circuit engineering discipline," *Current Biology*, vol. 10, pp. R318-R320, 2000.
- [30] T. S. Gardner, C. R. Cantor, and J. J. Collins, "Construction of a genetic toggle switch in *Escherichia coli*," *Nature*, vol. 403, pp. 339-342, 2000.
- [31] K. A. Smith, "Cell growth signal transduction is quantal," *Receptor Activation by Antigens, Cytokines, Hormones, and Growth Factors*, vol. 766, pp. 263-271, 1995.
- [32] C. J. Marshall, "Specificity of Receptor Tyrosine Kinase Signaling - Transient Versus Sustained Extracellular Signal-Regulated Kinase Activation," *Cell*, vol. 80, pp. 179-185, 1995.
- [33] E. M. Fallon and D. A. Lauffenburger, "Computational model for effects of ligand/receptor binding properties on interleukin-2 trafficking dynamics and T cell proliferation response," *Biotechnology Progress*, vol. 16, pp. 905-916, 2000.
- [34] M. Ramanathan, "Flow cytometry applications in pharmacodynamics and drug delivery," *Pharmaceutical Research*, vol. 14, pp. 1106-1114, 1997.

- [35] M. Whitney, E. Rockenstein, G. Cantin, T. Knapp, G. Zlokarnik, P. Sanders, K. Durick, F. F. Craig, and P. A. Negulescu, "A genome-wide functional assay of signal transduction in living mammalian cells," *Nature Biotechnology*, vol. 16, pp. 1329-1333, 1998.
- [36] K. A. Giuliano, R. L. DeBiasio, R. T. Dunlay, A. Gough, J. M. Volosky, J. Zock, G. N. Pavlakis, and D. L. Taylor, "High-content screening: A new approach to easing key bottlenecks in the drug discovery process," *Journal of Biomolecular Screening*, vol. 2, pp. 249-259, 1997.
- [37] R. Kapur, K. A. Giuliano, M. Campana, T. Adams, K. Olson, D. Jung, M. Mrksich, C. Vasudevan, and D. L. Taylor, "Streamlining the drug discovery process by integrating miniaturization, high throughput screening, high content screening, and automation on the CellChip system," *Biomedical Microdevices*, vol. 2, pp. 99-109, 1999.
- [38] D. Sobek, S. D. Senturia, and M. L. Gray, "Microfabricated fused silica flow chambers for flow cytometry," In *Solid-State Sensor and Actuator Work.*, Hilton Head Island, SC, USA, 1994, pp. 260-3.
- [39] E. Altendorf, D. Zebert, M. Holl, and P. Yager, "Differential blood cell counts obtained using a microchannel based flow cytometer," In *Proc. Int. Solid State Sensors and Actuators Conf. (Transducers '97)*, Chicago, IL, USA, 1997, pp. 531-4.
- [40] A. Y. Fu, C. Spence, A. Scherer, F. H. Arnold, and S. R. Quake, "A microfabricated fluorescence-activated cell sorter," *Nature Biotechnology*, vol. 17, pp. 1109-1111, 1999.
- [41] R. M. Moroney, R. M. White, and R. T. Howe, "Ultrasonically induced microtransport," In *IEEE Micro Electro Mechanical Systems*, Nara, Japan, 1991, pp. 277-82.
- [42] J. Wu, "Acoustical tweezers," *Journal of the Acoustical Society of America*, vol. 89, pp. 2140-3, 1991.
- [43] S. Nilsson, S. Santesson, E. Degerman, T. Johansson, T. Laurell, J. Nilsson, and J. Johansson, "Airborne chemistry for biological micro analysis," In *Micro Total Analysis Systems 2000*, Enschede, Netherlands, 2000, pp. 19-24.
- [44] A. Ashkin, K. Schutze, J. M. Dziedzic, U. Euteneuer, and M. Schliwa, "Force Generation of Organelle Transport Measured In vivo By an Infrared-Laser Trap," *Nature*, vol. 348, pp. 346-348, 1990.
- [45] A. Ashkin, "Optical trapping and manipulation of neutral particles using lasers," *Proc Natl Acad Sci U S A*, vol. 94, pp. 4853-60, 1997.
- [46] C. Mio, T. Gong, A. Terray, and D. W. M. Marr, "Design of a scanning laser optical trap for multiparticle manipulation," *Review of Scientific Instruments*, vol. 71, pp. 2196-2200, 2000.
- [47] J. Liesener, M. Reicherter, T. Haist, and H. J. Tiziani, "Multi-functional optical tweezers using computer-generated holograms," *Optics Communications*, vol. 185, pp. 77-82, 2000.
- [48] E. R. Dufresne and D. G. Grier, "Optical tweezer arrays and optical substrates created with diffractive optics," *Review of Scientific Instruments*, vol. 69, pp. 1974-1977, 1998.
- [49] T. N. Buican, "Automated Cell-Separation Techniques Based on Optical Trapping," *ACS Symposium Series*, vol. 464, pp. 59-72, 1991.
- [50] D. J. Odde and M. J. Renn, "Laser-guided direct writing of living cells," *Biotechnology and Bioengineering*, vol. 67, pp. 312-318, 2000.
- [51] R. A. Braff, "Microbubble cell actuator," diss, Cambridge: MIT, 1999.

- [52] K. Sato, Y. Kawamura, S. Tanaka, K. Uchida, and H. Kohida, "Individual and mass operation of biological cells using micromechanical silicon devices," *Sensors & Actuators A-Physical*, vol. A21-A23, pp. 948-53, 1990.
- [53] E. W. H. Jager, O. Ingnas, and I. Lundstrom, "Microrobots for micrometer-size objects in aqueous media: Potential tools for single-cell manipulation," *Science*, vol. 288, pp. 2335-2338, 2000.
- [54] T. D. Brown, "Techniques for mechanical stimulation of cells in vitro: a review," *Journal of Biomechanics*, vol. 33, pp. 3-14, 2000.
- [55] T. B. Jones and G. W. Bliss, "Bubble dielectrophoresis," *Journal of Applied Physics*, vol. 48, pp. 1412-17, 1977.
- [56] A. J. Grodzinsky and M. L. Yarmush, "Electrokinetic Separations," in *Bioprocessing*, vol. 3, *Biotechnology : a multi-volume comprehensive treatise*, G. Stephanopoulos, Ed., 2nd ed. Weinheim [Germany] ; New York: VCH, 1991, pp. 680-93.
- [57] H. P. Schwan, "Linear and nonlinear electrode polarization and biological materials," *Annals of Biomedical Engineering*, vol. 20, pp. 269-88, 1992.
- [58] T. B. Jones, *Electromechanics of particles*. Cambridge: Cambridge University Press, 1995.
- [59] H. P. Schwan, "Dielectrophoresis and rotation of cells," in *Electroporation and electrofusion in cell biology*, E. Neumann, A. E. Sowers, and C. A. Jordan, Eds. New York: Plenum Press, 1989, pp. 3-21.
- [60] M. Washizu and T. B. Jones, "Generalized multipolar dielectrophoretic force and electrorotational torque calculation," *Journal of Electrostatics*, vol. 38, pp. 199-211, 1996.
- [61] T. B. Jones and M. Washizu, "Multipolar dielectrophoretic and electrorotation theory," *Journal of Electrostatics*, vol. 37, pp. 121-34, 1996.
- [62] T. B. Jones and M. Washizu, "Equilibria and dynamics of DEP-levitated particles: multipolar theory," *Journal of Electrostatics*, vol. 33, pp. 199-212, 1994.
- [63] M. Washizu and T. B. Jones, "Multipolar dielectrophoretic force calculation," *Journal of Electrostatics*, vol. 33, pp. 187-98, 1994.
- [64] X. Wang, X.-B. Wang, and P. R. C. Gascoyne, "General expressions for dielectrophoretic force and electrorotational torque derived using the Maxwell stress tensor method," *Journal of Electrostatics*, vol. 39, pp. 277-95, 1997.
- [65] G. Fuhr and S. G. Shirley, "Biological application of microstructures," in *Microsystem Technology in Chemistry and Life Science*, vol. 194, *Topics in Current Chemistry*. Berlin: Springer-Verlag Berlin, 1998, pp. 83-116.
- [66] R. Pethig, "Application of A.C. electrical fields to the manipulation and characterisation," in *Automation in Biotechnology: a collection of contributions based on lectures presented at the Fourth Toyota Conference, Aichi, Japan, 21-24 October 1990*, I. Karube, Ed. Aichi, Japan: Elsevier Science Publishers B. V., 1990, pp. 159-185.
- [67] R. Pethig, "Dielectrophoresis: Using inhomogeneous AC electrical fields to separate and manipulate cells," *Critical Reviews in Biotechnology*, vol. 16, pp. 331-348, 1996.
- [68] J. Cheng, E. L. Sheldon, L. Wu, M. J. Heller, and J. P. O'Connell, "Isolation of cultured cervical carcinoma cells mixed with peripheral blood cells on a bioelectronic chip," *Analytical Chemistry*, vol. 70, pp. 2321-2326, 1998.

- [69] P. R. C. Gascoyne, X.-B. Wang, Y. Huang, and F. F. Becker, "Dielectrophoretic separation of cancer cells from blood," *IEEE Transactions on Industry Applications*, vol. 33, pp. 670-8, 1997.
- [70] G. H. Markx, M. S. Talary, and R. Pethig, "Separation of viable and non-viable yeast using dielectrophoresis," *Journal of Biotechnology*, vol. 32, pp. 29-37, 1994.
- [71] X. B. Wang, Y. Huang, J. P. H. Burt, G. H. Markx, and R. B. U. K. Pethig, "Selective dielectrophoretic confinement of bioparticles in potential energy wells," *Journal of Physics D (Applied Physics)*, vol. 26, pp. 1278-85, 1993.
- [72] M. S. Talary, J. P. H. Burt, J. A. Tame, and R. Pethig, "Electromanipulation and separation of cells using travelling electric fields," *Journal of Physics D (Applied Physics)*, vol. 29, pp. 2198-203, 1996.
- [73] M. S. Talary, K. I. Mills, T. Hoy, A. K. Burnett, and R. Pethig, "Dielectrophoretic separation and enrichment of CD34+ cell subpopulation from bone marrow and peripheral blood stem cells," *Medical & Biological Engineering & Computing*, vol. 33, pp. 235-7, 1995.
- [74] J. Cheng, E. L. Sheldon, L. Wu, A. Uribe, L. O. Gerrue, J. Carrino, M. J. Heller, and J. P. O'Connell, "Preparation and hybridization analysis of DNA/RNA from E-coli on microfabricated bioelectronic chips," *Nature Biotechnology*, vol. 16, pp. 541-546, 1998.
- [75] N. G. Green and H. Morgan, "Dielectrophoretic separation of nano-particles," *Journal of Physics D-Applied Physics*, vol. 30, pp. L41-L44, 1997.
- [76] N. G. Green and H. Morgan, "Dielectrophoretic investigations of sub-micrometre latex spheres," *Journal of Physics D-Applied Physics*, vol. 30, pp. 2626-2633, 1997.
- [77] N. G. Green and H. Morgan, "Separation of submicrometre particles using a combination of dielectrophoretic and electrohydrodynamic forces," *Journal of Physics D-Applied Physics*, vol. 31, pp. L25-L30, 1998.
- [78] M. P. Hughes and H. Morgan, "Dielectrophoretic trapping of single sub-micrometre scale bioparticles," *Journal of Physics D-Applied Physics*, vol. 31, pp. 2205-2210, 1998.
- [79] G. H. Markx, R. Pethig, and J. Rousselet, "The dielectrophoretic levitation of latex beads, with reference to field-flow fractionation," *Journal of Physics D (Applied Physics)*, vol. 30, pp. 2470-7, 1997.
- [80] X.-B. Wang, J. Vykoukal, F. F. Becker, and P. R. C. Gascoyne, "Separation of polystyrene microbeads using dielectrophoretic/gravitational field-flow-fractionation," *Biophysical Journal*, vol. 74, pp. 2689-701, 1998.
- [81] Y. Huang, X.-B. Wang, F. F. Becker, and P. R. C. Gascoyne, "Introducing dielectrophoresis as a new force field for field-flow fractionation," *Biophysical Journal*, vol. 73, pp. 1118-29, 1997.
- [82] P. R. C. Gascoyne, X. B. Wang, and J. Vykoukal, "A microfluidic device combining dielectrophoresis and field flow fractionation for partical and cell discrimination," In *Solid-State Sensor and Actuator Workshop*, Hilton Head Island, South Carolina, 1998, pp. 37-38.
- [83] J. Yang, Y. Huang, and P. R. C. Gascoyne, "Differential Analysis of Human Leukocytes by Dielectrophoretic Field-Flow-Fractionation," *Biophysical journal*, vol. 78, pp. 2680, 2000.
- [84] L. Gorre-Talini, J. P. Spatz, and P. Silberzan, "Dielectrophoretic ratchets," *Chaos*, vol. 8, pp. 650-6, 1998.

- [85] S. Fiedler, S. G. Shirley, T. Schnelle, and G. Fuhr, "Dielectrophoretic sorting of particles and cells in a microsystem," *Analytical Chemistry*, vol. 70, pp. 1909-1915, 1998.
- [86] T. B. Jones and G. A. C. C. O. U. S. A. Kallio, "Dielectrophoretic levitation of spheres and shells," *Journal of Electrostatics*, vol. 6, pp. 207-24, 1979.
- [87] T. B. Jones and J. P. Kraybill, "Active feedback-controlled dielectrophoretic levitation," *Journal of Applied Physics*, vol. 60, pp. 1247-52, 1986.
- [88] K. V. I. S. Kaler and T. B. Jones, "Dielectrophoretic spectra of single cells determined by feedback-controlled levitation," *Biophysical Journal*, vol. 57, pp. 173-82, 1990.
- [89] J. Suehiro and R. Pethig, "The dielectrophoretic movement and positioning of a biological cell using a three-dimensional grid electrode system," *Journal of Physics D-Applied Physics*, vol. 31, pp. 3298-3305, 1998.
- [90] T. Yamamoto, O. Kurosawa, H. Kabata, N. Shimamoto, and M. Washizu, "Molecular surgery of DNA based on electrostatic micromanipulation," *IEEE Transactions on Industry Applications*, vol. 36, pp. 1010-17, 2000.
- [91] M. Washizu, S. Suzuki, O. Kurosawa, T. Nishizaka, and T. Shinohara, "Molecular dielectrophoresis of biopolymers," *IEEE Transactions on Industry Applications*, vol. 30, pp. 835-43, 1994.
- [92] G. Fuhr, W. M. Arnold, R. Hagedorn, T. Muller, W. Benecke, B. Wagner, and U. Zimmermann, "Levitation, holding, and rotation of cells within traps made by high-frequency fields," *Biochimica Et Biophysica Acta*, vol. 1108, pp. 215-223, 1992.
- [93] T. Schnelle, R. Hagedorn, G. Fuhr, S. Fiedler, and T. Muller, "3-Dimensional electric-field traps for manipulation of cells - calculation and experimental verification," *Biochimica Et Biophysica Acta*, vol. 1157, pp. 127-140, 1993.
- [94] N. G. Green, A. Ramos, and H. Morgan, "AC electrokinetics: a survey of sub-micrometre particle dynamics," *Journal of Physics D-Applied Physics*, vol. 33, pp. 632-641, 2000.
- [95] N. G. Green and H. Morgan, "Dielectrophoresis of submicrometer latex spheres. 1. Experimental results," *Journal of Physical Chemistry B*, vol. 103, pp. 41-50, 1999.
- [96] N. G. Green, H. Morgan, and J. J. Milner, "Manipulation and trapping of sub-micron bioparticles using dielectrophoresis," *Journal of Biochemical and Biophysical Methods*, vol. 35, pp. 89-102, 1997.
- [97] T. Muller, A. Gerardino, T. Schnelle, S. G. Shirley, F. Bordoni, G. De Gasperis, R. Leoni, and G. Fuhr, "Trapping of micrometre and sub-micrometre particles by high-frequency electric fields and hydrodynamic forces," *Journal of Physics D (Applied Physics)*, vol. 29, pp. 340-9, 1996.
- [98] T. Schnelle, T. Muller, and G. Fuhr, "Trapping in AC octode field cages," *Journal of Electrostatics*, vol. 50, pp. 17-29, 2000.
- [99] A. S. Bahaj and A. G. Bailey, "Dielectrophoresis of small particles," In *Industry Application Society IEEE-IAS Annual Meeting*, Cleveland, OH, USA, 1979, pp. 154-7.
- [100] X.-B. Wang, Y. Huang, X. Wang, F. F. Becker, and P. R. C. Gascoyne, "Dielectrophoretic manipulation of cells with spiral electrodes," *Biophysical Journal*, vol. 72, pp. 1887-99, 1997.
- [101] X.-B. Wang, Y. Huang, P. R. C. Gascoyne, and F. F. Becker, "Dielectrophoretic manipulation of particles," *IEEE Transactions on Industry Applications*, vol. 33, pp. 660-9, 1997.
- [102] M. Washizu, "Electrostatic actuation of liquid droplets for micro-reactor applications," In *IEEE Industry Applications Conference*, New York, NY, 1997, pp. 1867-73.

- [103] A. Desai, S. W. Lee, and Y. C. Tai, "A MEMS electrostatic particle transportation system," *Sensors & Actuators A-Physical*, vol. A73, pp. 37-44, 1999.
- [104] G. Fuhr and R. Hagedorn, "Cell electrorotation," in *Electrical manipulation of cells*, P. T. Lynch and M. R. Davey, Eds. New York: Chapman & Hall, 1996, pp. 37-70.
- [105] U. Zimmermann, U. Friedrich, H. Mussauer, P. Gessner, K. Hamel, and V. Sukhoruhov, "Electromanipulation of mammalian cells: Fundamentals and application," *IEEE Transactions on Plasma Science*, vol. 28, pp. 72-82, 2000.
- [106] U. Zimmermann, "Electrical Breakdown, Electroporation and Electrofusion," *Reviews of Physiology Biochemistry and Pharmacology*, vol. 105, pp. 175-256, 1986.
- [107] P. Marszalek and T. Y. Tsong, "Cell Fission and Formation of Mini Cell-Bodies by High-Frequency Alternating Electric-Field," *Biophysical Journal*, vol. 68, pp. 1218-1221, 1995.
- [108] G. Fuhr, T. Schnelle, and B. Wagner, "Travelling wave-driven microfabricated electrohydrodynamic pumps for liquids," *Journal of Micromechanics and Microengineering*, vol. 4, pp. 217-226, 1994.
- [109] J. C. Weaver, "Electroporation of cells and tissues," *IEEE Transactions on Plasma Science*, vol. 28, pp. 24-33, 2000.
- [110] I. G. Abidor and A. E. Sowers, "Kinetics and Mechanism of Cell-Membrane Electrofusion," *Biophysical Journal*, vol. 61, pp. 1557-1569, 1992.
- [111] S. Lindquist, "The heat-shock response," *Annu Rev Biochem*, vol. 55, pp. 1151-91, 1986.
- [112] E. A. Craig, "The heat shock response," *CRC Crit Rev Biochem*, vol. 18, pp. 239-80, 1985.
- [113] R. H. Burdon, "Heat-Shock and the Heat-Shock Proteins," *Biochemical Journal*, vol. 240, pp. 313-324, 1986.
- [114] J. R. Subjeck and T. T. Shyy, "Stress Protein Systems of Mammalian-Cells," *American Journal of Physiology*, vol. 250, pp. C1-C17, 1986.
- [115] M. Urano and E. B. Double, *Thermal effects on cells and tissues*. Utrecht, The Netherlands: VSP, 1988.
- [116] J. C. Weaver, T. E. Vaughan, and G. T. Martin, "Biological Effects Due to Weak Electric and Magnetic Fields: The Temperature Variation Threshold," *Biophys. J.*, vol. 76, pp. 3026-3030, 1999.
- [117] S. W. Carper, J. J. Duffy, and E. W. Gerner, "Heat-Shock Proteins in Thermotolerance and Other Cellular Processes," *Cancer Research*, vol. 47, pp. 5249-5255, 1987.
- [118] J. Gimsa and D. Wachner, "A polarization model overcoming the geometric restrictions of the laplace solution for spheroidal cells: Obtaining new equations for field-induced forces and transmembrane potential," *Biophysical Journal*, vol. 77, pp. 1316-1326, 1999.
- [119] J. Gimsa and D. Wachner, "A Unified Resistor-Capacitor Model for Impedance, Dielectrophoresis, Electrorotation, and Induced Transmembrane Potential," *Biophys. J.*, vol. 75, pp. 1107-1116, 1998.
- [120] A. Irimajiri, T. Hanai, and A. Inouye, "A dielectric theory of "multi-stratified shell" model with its application to a lymphoma cell," *Journal of Theoretical Biology*, vol. 78, pp. 251-69, 1979.
- [121] C. Grosse and H. P. T. A. Schwan, "Cellular membrane potentials induced by alternating fields," *Biophysical Journal*, vol. 63, pp. 1632-42, 1992.

- [122] T. Y. Tsong, "Molecular recognition and processing of periodic signals in cells study of activation of membrane ATPases by alternating electric fields," *Biochimica et Biophysica Acta*, vol. 1113, pp. 53-70, 1992.
- [123] W. A. Catterall, "Structure and Function of Voltage-Gated Ion Channels," *Annual Review of Biochemistry*, vol. 64, pp. 493-531, 1995.
- [124] A. Lacy-Hulbert, J. C. Metcalfe, and R. Hesketh, "Biological responses to electromagnetic fields?," *FASEB Journal*, vol. 12, pp. 395-420, 1998.
- [125] L. F. Jaffe and M. M. Poo, "Neurites grow faster towards the cathode than the anode in a steady field," *J Exp Zool*, vol. 209, pp. 115-28, 1979.
- [126] T. A. Ryan, J. Myers, D. Holowka, B. Baird, and W. W. Webb, "Molecular crowding on the cell surface," *Science*, vol. 239, pp. 61-4, 1988.
- [127] C. Polk and E. Postow, *Handbook of biological effects of electromagnetic fields*, 2nd ed. Boca Raton, FL: CRC Press, 1996.
- [128] A. Docoslis, N. Kalogerakis, and L. A. Behie, "Dielectrophoretic forces can be safely used to retain viable cells in perfusion cultures of animal cells," *Cytotechnology*, vol. 30, pp. 133, 1999.
- [129] S. Archer, T. T. Li, A. T. Evans, S. T. Britland, and H. Morgan, "Cell reactions to dielectrophoretic manipulation," *Biochemical and Biophysical Research Communications*, vol. 257, pp. 687-698, 1999.
- [130] H. Glasser and G. Fuhr, "Cultivation of cells under strong ac-electric field - differentiation between heating and trans-membrane potential effects," *Bioelectrochemistry and Bioenergetics*, vol. 47, pp. 301-310, 1998.
- [131] G. Fuhr, H. Glasser, T. Muller, and T. Schnelle, "Cell manipulation and cultivation under AC electric-field influence in highly conductive culture media," *Biochimica Et Biophysica Acta-General Subjects*, vol. 1201, pp. 353-360, 1994.
- [132] X. J. Wang, J. Yang, and P. R. C. Gascoyne, "Role of peroxide in AC electrical field exposure effects on Friend murine erythroleukemia cells during dielectrophoretic manipulations," *Biochimica Et Biophysica Acta-General Subjects*, vol. 1426, pp. 53-68, 1999.
- [133] M. Washizu, T. B. Jones, and K. V. I. S. Kaler, "Higher-order dielectrophoretic effects: levitation at a field null," *Biochimica et Biophysica Acta*, vol. 1158, pp. 40-46, 1993.
- [134] Y. Huang and R. Pethig, "Electrode design for negative dielectrophoresis," *Measurement Science & Technology*, vol. 2, pp. 1142-6, 1991.
- [135] G. Bartsch, M. Baumann, and R. Grebe, "Numerical calculation of electric fields surrounding biological cells in three dimensions," *Bioelectrochemistry & Bioenergetics*, vol. 42, pp. 221-226, 1997.
- [136] R. Holzel, "Electric field calculation for electrorotation electrodes," *Journal of Physics D (Applied Physics)*, vol. 26, pp. 2112-16, 1993.
- [137] M. P. Hughes, X. B. Wang, F. F. Becker, P. R. C. Gascoyne, and R. B. U. K. Pethig, "Computer-aided analyses of electric fields used in electrorotation studies," *Journal of Physics D (Applied Physics)*, vol. 27, pp. 1564-70, 1994.
- [138] A. J. Goldman, R. G. Cox, and H. Brenner, "Slow viscous motion of a sphere parallel to a plane wall - II Couette flow," *Chemical Engineering Science*, vol. 22, pp. 653-60, 1967.
- [139] P. Ganatos, R. Pfeffer, and S. Weinbaum, "A strong interaction theory for the creeping motion of a sphere between plane parallel boundaries. Part 2. Parallel motion," *Journal of Fluid Mechanics*, vol. 99, pp. 755-783, 1980.

- [140] G. A. Korn and T. M. Korn, *Mathematical handbook for scientists and engineers; definitions, theorems, and formulas for reference and review*, 2nd ed. New York: McGraw-Hill, 1968.
- [141] P. Bourke, "Determining whether or not a point lies on the interior of a polygon," vol. 1998, 1987.
- [142] A. Blake, *Handbook of mechanics, materials, and structures*. New York: Wiley, 1985.
- [143] T. Muller, G. Gradl, S. Howitz, S. Shirley, T. Schnelle, and G. Fuhr, "A 3-D microelectrode system for handling and caging single cells and particles," *Biosensors & Bioelectronics*, vol. 14, pp. 247-256, 1999.
- [144] A. Ramos, H. Morgan, N. G. Green, and A. Castellanos, "The role of electrohydrodynamic forces in the dielectrophoretic manipulation and separation of particles," *Journal of Electrostatics*, vol. 47, pp. 71-81, 1999.
- [145] L. F. Hartley, K. Kaler, and R. Paul, "Quadrupole levitation of microscopic dielectric particles," *Journal of Electrostatics*, vol. 46, pp. 233-246, 1999.
- [146] T. Schnelle, T. Muller, and G. Fuhr, "The influence of higher moments on particle behaviour in dielectrophoretic field cages," *Journal of Electrostatics*, vol. 46, pp. 13, 1999.
- [147] W. M. Arnold, H. P. Schwan, and U. Zimmermann, "Surface conductance and other properties of latex particles measured by electrorotation," *Journal of Physical Chemistry*, vol. 91, pp. 5093- 8, 1987.
- [148] T. Schnelle, T. Muller, G. Gradl, S. G. Shirley, and G. Fuhr, "Paired microelectrode system: dielectrophoretic particle sorting and force calibration," *Journal of Electrostatics*, vol. 47, pp. 121-132, 1999.
- [149] G. Fuhr, T. Schnelle, T. Muller, H. Hitzler, S. Monajembashi, and K. O. Greulich, "Force measurements of optical tweezers in electro-optical cages," *Applied Physics A-Materials Science & Processing*, vol. 67, pp. 385-390, 1998.
- [150] J. M. Cruz and F. J. Garcia-Diego, "Dielectrophoretic force measurements in yeast cells by the Stokes method," In *IEEE Industry Applications Conference*, New Orleans, LA, USA, 1997, pp. 2012-18.
- [151] W. H. Wright, G. J. Sonek, and M. W. Berns, "Parametric Study of the Forces On Microspheres Held By Optical Tweezers," *Applied Optics*, vol. 33, pp. 1735-1748, 1994.
- [152] K. Svoboda and S. M. Block, "Biological Applications of Optical Forces," *Annual Review of Biophysics and Biomolecular Structure*, vol. 23, pp. 247-285, 1994.
- [153] G. P. Krishnan and D. T. Leighton, "Inertial lift on a moving sphere in contact with a plane wall in a shear-flow," *Physics of Fluids*, vol. 7, pp. 2538-2545, 1995.
- [154] A. Ramos, H. Morgan, N. G. Green, and A. Castellanos, "Ac electrokinetics: a review of forces in microelectrode structures," *Journal of Physics D-Applied Physics*, vol. 31, pp. 2338-2353, 1998.
- [155] J. R. Melcher and G. I. Taylor, "Electrohydrodynamics: a review of the role of interfacial shear stresses," *Annual review of fluid mechanics*, vol. 1, pp. 111-46, 1969.
- [156] J. R. Melcher, *Continuum electromechanics*. Cambridge, Mass.: MIT Press, 1981.
- [157] G. Fuhr, R. Hagedorn, T. Muller, W. Benecke, and B. Wagner, "Microfabricated electrohydrodynamic (EHD) pumps for liquids of higher conductivity," *Journal of Microelectromechanical Systems*, vol. 1, pp. 141-6, 1992.
- [158] M. P. Hughes, "AC electrokinetics: applications for nanotechnology," *Nanotechnology*, vol. 11, pp. 124-132, 2000.

- [159] N. G. Green, A. Ramos, A. Gonzalez, A. Castellanos, and H. Morgan, "Electric field induced fluid flow on microelectrodes: the effect of illumination," *Journal of Physics D-Applied Physics*, vol. 33, pp. L13-L17, 2000.
- [160] N. G. Green, A. Ramos, A. Gonzalez, H. Morgan, and A. Castellanos, "Fluid flow induced by nonuniform ac electric fields in electrolytes on microelectrodes. I. Experimental measurements," *Physical Review E*, vol. 61, pp. 4011-4018, 2000.
- [161] H.-J. Hsieh, N.-Q. Li, and J. A. Frangos, "Shear stress-induced gene expression in human endothelial cells," in *Tissue engineering: current perspectives*, E. Bell, Ed. Boston: Birkhauser, 1993, pp. 155-66.
- [162] J. C. Wataha, C. T. Hanks, and R. G. Craig, "The In vitro Effects of Metal-Cations on Eukaryotic Cell- Metabolism," *Journal of Biomedical Materials Research*, vol. 25, pp. 1133-1149, 1991.
- [163] H. Lorenz, M. Despont, N. Fahrni, J. Brugger, P. Vettiger, and P. Renaud, "High-aspect-ratio, ultrathick, negative-tone near-UV photoresist and its applications for MEMS," *Sensors & Actuators A-Physical*, vol. A64, pp. 33-9, 1998.
- [164] K. Y. Lee, N. LaBianca, S. A. Rishton, S. Zolgharnain, J. D. Gelorme, J. Shaw, and T. H. P. Chang, "Micromachining applications of a high resolution ultrathick photoresist," *Journal of Vacuum Science & Technology B*, vol. 13, pp. 3012-3016, 1995.
- [165] C. Harris, Y. Desta, K. W. Kelly, and G. Calderon, "Inexpensive, quickly predicable X-ray mask for LIGA," *Microsystem Technologies*, vol. 5, pp. 189-93, 1999.
- [166] C. Hyun-Kee and K. Yong-Kweon, "UV-LIGA process for high aspect ratio structure using stress barrier and C-shaped etch hole," *Sensors & Actuators A-Physical*, vol. A84, pp. 342-50, 2000.
- [167] W. D. Bonivert, J. M. Hruby, J. T. Hachman, C. K. Malek, K. H. Jackson, R. A. Brennen, M. H. Hecht, and D. Wiberg, "Electroplating for LIGA processing," In *Proceedings of the Fourth International Symposium on Magnetic Materials, Processes, and Devices. Applications to Storage and Microelectromechanical Systems (MEMS)*, 1996, pp. 397-403.
- [168] M. J. Madou, *Fundamentals of microfabrication*. Boca Raton: CRC, 1997.
- [169] T. Kawabata and K. Maenaka, "The micromachined accelerometer fabrication using thick resist," In *Technical digest of the 16th Sensor Symposium*, Japan, 1998, pp. 199-202.
- [170] D. McIntosh, Ashland ACT Corp., 2000.
- [171] W. M. Deen, *Analysis of transport phenomena*. New York: Oxford University Press, 1998.
- [172] N. Yoshida, M. Tamura, and M. Kinjo, "Fluorescence correlation spectroscopy: A new tool for probing the microenvironment of the internal space of organelles," *Single Molecules*, vol. 1, pp. 279-83, 2000.
- [173] H. A. Haus and J. R. Melcher, *Electromagnetic fields and energy*. Englewood Cliffs, N.J.: Prentice Hall, 1989.